Kinetic Studies of Gaseous Halogen Oxide Radical Reactions Implicated in Ozone Depletion

A thesis submitted for the degree of Doctor of Philosophy

by

Valerio Ferracci

Department of Chemistry,
University College London
2012

I, Valerio Ferracci, confirm that the work presented in this thesis is my own. Where information has been derived from other sources, I confirm that this has been indicated in the thesis.

Signed,

Alla mia famiglia,

Per esser stati sempre al mio fianco

Acknowledgements

First and foremost, I would like to thank my supervisor David Rowley for his support, guidance, encouragement, advice and ultimately for his friendship during the last four years. With your help, we made all this happen.

I would also like to express my gratitude to other members of the Rowley Group, first of all to Mike Ward. It has been a real pleasure working with you. Special thanks are also extended to Kaori Hino for contributing to the work on the BrO self-reaction, and to Abi Mountain and Jutta Toscano for their valuable help on the experiments on the BrO + ClO cross-reaction.

I would also like to thank colleagues whose input was extremely helpful in developing the work presented in this thesis: Marc von Hobe, for constructive feedback and discussions on ClO dimerisation; Tim Canty, for carrying out atmospheric modelling using our data; Stan Sander and Dave Golden, for their advice on the thermochemistry of Cl_2O_2; John Barker, for his invaluable help on the Multiwell Software and for supplying the preliminary results of his *ab initio* studies on Cl_2O_2. I am also grateful to the EPSRC for funding my research.

I am ever so grateful to all the friends who have made the past four years so enjoyable and who have been a constant source of support through thick and thin: Kevin, Josie, Jess, James, Mike Warwick, Mike Parkes, Leonardo, Giuliana, Sheila, Adam, Gualtiero, Martina, Giorgia, Vivianne, Mefy and David, to all of you, thank you.

Last but by no means least I must thank my boyfriend Michael for his infinite patience and for helping me see this through until the end.

List of Publications as a Result of Studies Reported in this Thesis

V. Ferracci, D. M. Rowley, "Kinetic and thermochemical studies of the ClO + ClO + M ⇆ Cl_2O_2 + M reaction", *Phys. Chem. Chem. Phys.*, **2010**, 12, 11596

V. Ferracci, K. Hino, D. M. Rowley, "Kinetic studies on the temperature dependence of the BrO + BrO reaction using laser flash photolysis", *Phys. Chem. Chem. Phys.*, **2011**, 13, 7997

V. Ferracci, D. M. Rowley, "The Temperature Dependence of the Bimolecular Channels of the ClO + ClO Reaction over the Range T = 298-323 K", *Int. J. Chem. Kinet.*, **2012**, 44, 386

In preparation:
V. Ferracci, D. M. Rowley, "Kinetic Studies of the BrO + ClO Cross-Reaction Using Laser Photolysis with UV Absorption Spectroscopy at T = 246-314 K"

Abstract

Increased atmospheric emissions of photolabile halogen-containing species as a result of human activity over the Twentieth Century have had a dramatic impact on atmospheric ozone. This has generated significant scientific interest in understanding the reactivity of halogens in the gas phase. In particular, the self- and cross-reactions of halogen monoxide radicals, XO (where X = F, Cl, Br, I), which are the first-formed intermediates in the reaction of photolytically released halogen atoms with ozone, have been identified as key processes in ozone-depleting events as they initiate reaction cycles that catalytically destroy ozone. Understanding the kinetics of these reactions is therefore crucial to establishing their potential for ozone destruction. These reactions are, however, complex multichannel processes, with both bimolecular and termolecular components contributing to the overall reaction. As some product channels do not contribute to the catalytic destruction of ozone, an accurate determination of the product branching is also of utmost importance for a comprehensive understanding of the atmospheric ozone budget.

In this thesis, results from studies of the kinetics of the ClO and BrO self-reactions and of the BrO + ClO cross-reaction, carried out under appropriate atmospheric conditions, are presented. These reactions were studied using laser flash photolysis coupled with UV absorption spectroscopy. This technique adopted the rapid generation of the XO radicals of interest following laser photolysis and monitoring their temporal behaviour *via* UV absorption spectroscopy facilitated by charge-coupled device (CCD) detection. The use of a CCD detector allowed broadband time-resolved acquisition of spectra, leading to the unequivocal identification of multiple species and to the accurate quantification of their concentrations *via* the Beer-Lambert law. The desired kinetic information was then obtained from fitting classical or numerical integration simulations to the experimental concentration profiles. Extensive sensitivity analyses of the results obtained were performed to identify the principal sources of uncertainty in these measurements. The results from the present work are compared to those obtained in previous studies and their implications for ozone in the Earth's atmosphere are discussed.

Table of Contents

Table of Figures

Chapter 1

Chapter 2

Chapter 3

Chapter 4

Chapter 5

Chapter 6

Chapter 7

Appendix 1

Appendix 2

Appendix 3

Appendix 4

Table of Tables

Chapter 1

Chapter 4

Chapter 5

Chapter 6

Chapter 7

Chapter 1
Physics and Chemistry of the Earth's Atmosphere

Long before the advent of modern science, Man showed great interest in the atmosphere and its phenomena. Ancient Greek philosophers used to speculate on the very nature of the world; Anaximenes, one of the pre-Socratic philosophers, identified air as the first principle of the cosmos, or *arche*, from which all things in the universe were made of. [1] Throughout the Middle Ages, the ubiquitous Aristotelian tradition asserted that air was one of the four fundamental elements that constituted the physical world, along with earth, water and fire. This belief persisted until the scientific revolution: from the 17th century, a series of discoveries, from atmospheric pressure to the identification of the constituent gases, shone new light on the nature of the atmosphere.

The greatest challenge facing atmospheric scientists today is to assess the impact of human activities on the composition of the planet's atmosphere, often with adverse environmental consequences. This requires an in-depth knowledge of atmospheric physics and chemistry provided by the synergistic efforts of laboratory studies, field measurements and atmospheric numerical modelling.

This introductory chapter aims to illustrate the physical and chemical principles that govern the atmosphere and that constitute the foundations of any scientific approach to understanding it. These concepts provide the framework on which to build a description of atmospheric chemistry, particularly in the context of atmospheric ozone and the role of halogen oxide self- and cross-reactions, the study of which constitutes the main body of the present work.

1.1 Physics of the Atmosphere

The physics and the chemistry of the atmosphere are extremely intertwined: on the one hand, physical properties such as temperature and pressure influence the chemical behaviour of the atmosphere; on the other hand, chemical reactions and chemical composition can also have a profound effect on these physical characteristics.

1.1.1 Pressure Profile

The vertical pressure profile of the Earth's atmosphere is governed by the competition between the gravitational pull of the planet, which attracts gas molecules to the surface, and the kinetic energy of the gas particles, which opposes these gravitational forces.

An expression for the relationship between pressure and altitude can be derived from first principles. Pressure, p, is classically defined as the force exerted per unit area:

$$p = F/A = ma/A \qquad (1.i)$$

where the force F is the weight of the atmosphere, *i.e.* the product of mass m and acceleration a. By expressing the mass in terms of density and volume, and by defining such volume as the product of area A and height z, then equation (1.i) can be written to express the variation in pressure resulting from an incremental increase in altitude dz as follows:

$$dp = -g\,\rho\,dz \qquad (1.ii)$$

where g is the acceleration due to gravity and ρ is the air density. Rearrangement of the ideal gas equation of state then gives an expression for the air density:

$$\rho = \frac{m}{V} = \frac{nM}{V} = \frac{Mp}{RT} \qquad (1.iii)$$

The molar mass of air, M, can be calculated as the weighted average of the molar masses of the component gases in the atmosphere, given that the bulk composition of air, principally N_2 and O_2, is constant (see Section 1.2) and independent of altitude below 100 km as turbulent mixing prevents gravitational separation of atmospheric gases. Substitution of equation (1.iii) into (1.ii) and separation of the variables returns:

$$\frac{dp}{p} = -\frac{Mgdz}{RT} = -\frac{dz}{H} \qquad (1.iv)$$

where the factor $H = RT/Mg$ is defined as the *scale height* and has units of length. Assuming that the temperature and the acceleration due to gravity are constant over the altitude range taken into account, integration of (1.iv) between limits of altitudes 0 and z leads to the *hydrostatic equation*:

$$p_z = p_0 \exp\left(-\frac{z}{H}\right) \qquad (1.v)$$

where p_z and p_0 represent atmospheric pressures at altitudes z and 0 respectively. The hydrostatic equation therefore predicts pressure to fall exponentially as the altitude is increased. From this perspective, the scale height H is defined as the vertical distance over which the pressure falls by a factor of $1/e$. As the temperature is not constant throughout the atmosphere, as discussed in Section 1.1.2 below, the scale height is not a constant value: typically H ranges between ~6 km at $T = 210$ K and ~8 km at $T = 290$ K.

A corollary of the hydrostatic equation is that the majority of the mass of the atmosphere resides at low altitudes; in fact half of the mass of the atmosphere is found below 5.5 km and approximately 99% of the mass lies below 30 km. [2]

1.1.2 Temperature Profile

The temperature structure of the atmosphere appears more complex than its pressure profile: at some heights the temperature decreases with increasing altitude, whilst it increases at others. The sign of the rate of change of temperature with increasing

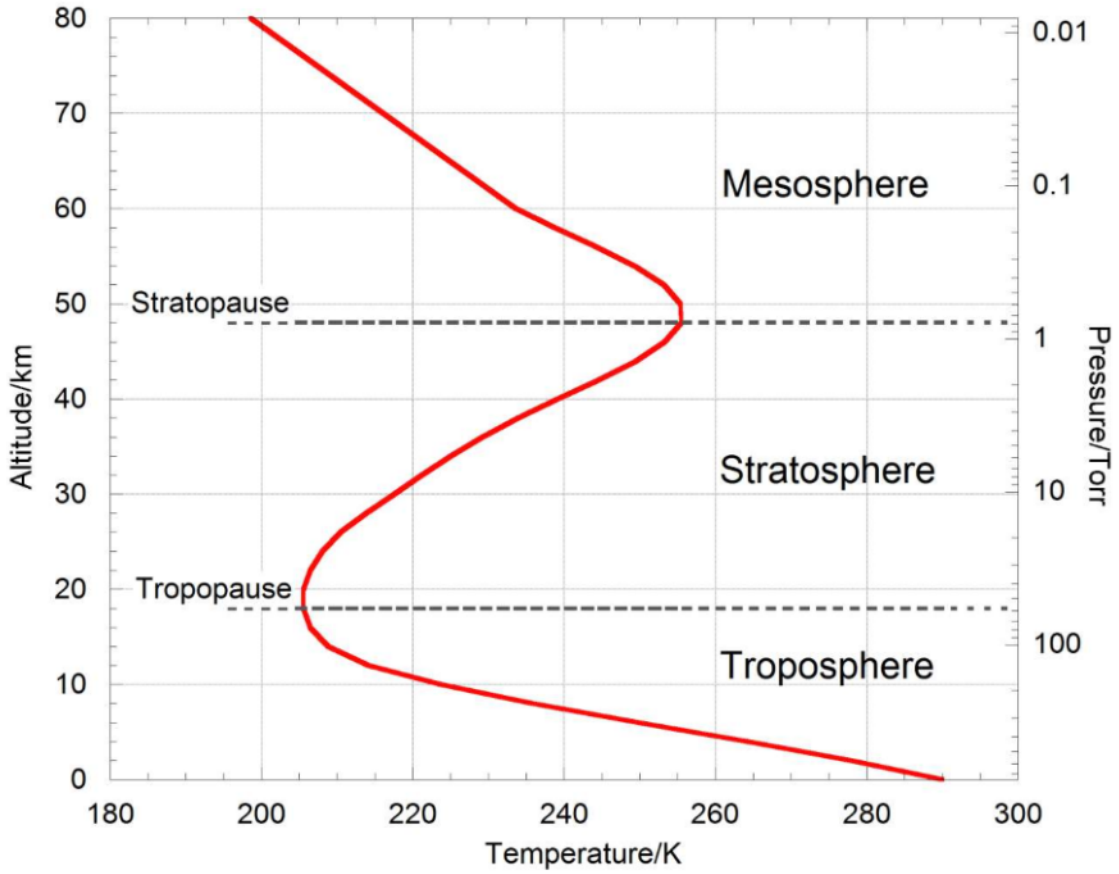

Figure 1.1 : Temperature profile of the Earth's atmosphere. From reference 3.

altitude, the *adiabatic lapse rate*, is used to subdivide the atmosphere in distinct vertical regions, as illustrated in Figure 1.1.

The region closest to the Earth's surface, the *troposphere*, is characterised by a negative adiabatic lapse rate, hence the temperature in this region decreases with increasing altitude. The troposphere can be divided further into two sub-regions: the *boundary layer*, extending from ground level to about 2 km of altitude, and the *free troposphere*. The upper limit of the troposphere, the *tropopause*, occurs typically at an altitude of 15 km, although its exact altitude varies depending on season and latitude. At the tropopause the adiabatic lapse rate changes sign and above this a different region of the atmosphere is encountered, the *stratosphere*. The positive adiabatic lapse rate indicates that the temperature rises with altitude in the stratosphere, in contrast to that observed in the troposphere. The temperature inversion is principally the result the absorption of solar ultraviolet radiation by the ozone present in this region, as discussed in Section

1.3.1, which is ultimately liberated as thermal energy. The upper limit of the stratosphere, the *stratopause*, is found at altitudes of approximately 50 km and marks the turning point where the adiabatic lapse rate becomes negative again. The region above the stratopause, the *mesosphere*, is therefore again characterised by decreasing temperatures with increasing altitudes and it is where the lowest temperatures in the entire atmosphere are found. The temperature stops falling at the *mesopause*, at approximately 90 km of altitude, and effectively starts rising again in the next atmospheric region, the *thermosphere*. The positive adiabatic lapse rate in this region arises from an inefficient thermal equilibration between translational, rotational and vibrational modes of gas molecules. The air density in this region is so rarefied that collisions between gas molecules are very infrequent and energy redistribution between different degrees of freedom (rotational, vibrational) is very inefficient. Therefore absorption of high energy solar radiation in this region leads to high translational velocities and high apparent temperatures.

1.1.3 Atmospheric Stability and Mixing

The stability of the atmosphere towards vertical mixing is an example of how the physical properties of the atmosphere (in this case, temperature and pressure) govern the behaviour of the gaseous mixture it is comprised of (in this case, its dynamical properties).

The concept of the rate of change of temperature with altitude, or adiabatic lapse rate, has already been introduced in the description of the temperature profile of the atmosphere, and is extremely useful to elucidate the principles of vertical mixing. Assuming adiabatic conditions and in the absence of water vapour, the dry adiabatic lapse rate, Γ_d, is defined as:

$$\Gamma_d = \frac{dT}{dz} = -\frac{g}{c_p} \qquad \text{(1.vi)}$$

where g is the acceleration due to gravity and c_p is the heat capacity of air at constant pressure. For tropospheric air, the dry adiabatic lapse rate calculated from equation

(1.vi) is equal to −9.8 K km^{-1}. However, the presence of condensable gases, notably water vapour, implies the release of latent heat upon cooling leading to a higher value of Γ_d of approximately −6.5 K km^{-1}.

Discussion of the stability of the atmosphere with respect to vertical mixing is then facilitated by considering the vertical displacement of a hypothetical volume of air, an air 'parcel'. The fate of this air parcel is dictated by the magnitude of its lapse rate relative to that of the surrounding air. When an air parcel, initially in thermal equilibrium with its surroundings, is vertically displaced upwards in the atmosphere, it expands due to the decrease in pressure. As heat transfer is somewhat inefficient in the gas phase, the expansion is typically adiabatic and results, from the First Law of thermodynamics, in a decrease in the internal energy of the gas, leading to a cooling of the air parcel. Now, if the adiabatic lapse rate of the air parcel is greater (less negative) than that of the surrounding atmosphere, the temperature drop of the surroundings would be greater than the decrease in temperature of the parcel resulting from the expansion, so that the air parcel at the new altitude is warmer and, at the same pressure, less dense then the air around it, and it will continue to rise. Analogously, if an air parcel was displaced downwards under these conditions, it would become cooler and denser than its surroundings and would continue to sink. Under these circumstances convection is readily established and the atmosphere is said to be unstable with respect to vertical mixing. This behaviour is commonplace in the troposphere, as Γ_d in this region is negative, and is reflected in the very name of this region of the atmosphere (*tropos* originates from the Greek for "turning").

On the other hand, when the adiabatic lapse rate of a volume of air displaced upwards is smaller than that of the surrounding atmosphere, the air parcel is colder than its surroundings after vertical displacement and it sinks to its original altitude. Similarly, a gas parcel displaced downwards under the same conditions would be warmer than its surroundings and it would experience a buoyancy force that would cause it to rise back to the initial altitude. Under these conditions the atmosphere is said to be stable with respect to vertical mixing. Given that the very definition of the stratosphere is as a region of positive adiabatic lapse rate, and that the adiabatic lapse rate of a vertically displaced air parcel is always negative (an expanding gas always does work and this

requires energy), this situation is typical of the stratosphere, where very little convection and vertical mixing occur and the air is consequently layered. The name of the region itself is derived from the Greek word for "layered" (*stratos*).

It emerges from the mechanism of vertical mixing elucidated thus far that, notwithstanding diffusion, it is generally difficult for the well-mixed air in the troposphere to access the stratosphere. However, some slow exchange between the two regions does occur as a result of an imbalance between absorbed solar energy and outgoing terrestrial radiation at different latitudes. This is driven by non-adiabatic processes and the resulting circulation, named *meridional* or Brewer-Dobson after its discoverers, transports warm air from the equatorial troposphere into the stratosphere, whereas cold air from the polar stratosphere sinks into the troposphere. Despite this exchange, transport of tropospheric species, including anthropogenic pollutants, into the stratosphere is generally very inefficient. Furthermore, the cold equatorial tropopause ($T < 190$ K) acts as a cold trap, freezing out the majority of the water vapour present in the air; as a result, the stratosphere remains remarkably dry.

1.1.4 Radiative Balance

Solar energy is the principal driving force behind most atmospheric processes. The Earth receives energy from the sun in the form of radiation (*solar flux*), but also releases energy by emitting radiation into space (*terrestrial flux*). An analysis of the energy budget of the planet gives an important insight onto the complex interactions between gaseous species in the atmosphere and both solar and terrestrial radiation. The concept of *radiative balance* is based on the principle that the fluxes of incoming and outgoing energy must be equal for the Earth's temperature to be constant; it therefore offers a simplified but effective approach to calculate the average Earth's temperature.

Incoming energy received from the sun per unit time, R_i, is represented by the solar energy output per unit time per unit area, the solar constant S (typically $S = 1368$ W m^{-2}) multiplied by the cross-sectional area of the beam, which is equal to a cross-section of the Earth with radius r equal to the radius of the planet. Therefore:

$$R_i = S\pi r^2 (1 - A) \qquad \text{(1.vii)}$$

The correction factor $(1-A)$ is applied to the expression for R_i to account for the fraction of solar radiation back-scattered into space that is not absorbed by the Earth's surface. This total reflectivity of a planet is referred to as *albedo*, A, and for the Earth it is usually given a value of 31% [2], indicating that approximately two thirds of the incident solar radiation is absorbed by the Earth.

Our planet releases thermal energy into space and can be approximated to a black-body radiator emitting over its entire surface, *i.e.* approximately the surface of a sphere of radius r, $4\pi r^2$. The amount of energy per unit time per unit area emitted by a black body, R_o, at temperature T is given by the Stefan-Boltzmann law. Thus we obtain:

$$R_o = 4\pi r^2 \sigma T^4 \qquad \text{(1.viii)}$$

where σ is Stefan's constant ($\sigma = 5.67\times10^{-8}$ W m^{-2} K^{-4}). Assuming that R_i and R_o are in equilibrium, and therefore combining equations (1.vii) and (1.viii), we obtain:

$$S\pi r^2 (1 - A) = 4\pi r^2 \sigma T^4 \qquad \text{(1.ix)}$$

Rearranging and solving for the temperature returns a value of T = 255 K. On first inspection, this estimate might seem reasonably close to the actual average surface temperature of the Earth (T = 288 K). However, an average temperature of about 33 K below this would make the planet largely inhabitable. The discrepancy between the temperature predicted by this simple radiative balance model and the measured temperature is even more pronounced for Venus, where the calculated temperature of T = 227 K is dramatically lower than the actual surface temperature ($T \approx 735$ K) [2].

The reason for the observed discrepancy between calculated and measured temperatures lies in the fact that the Earth and the sun emit radiation in different regions of the spectrum and the absorption properties of the atmosphere are strongly dependent on the

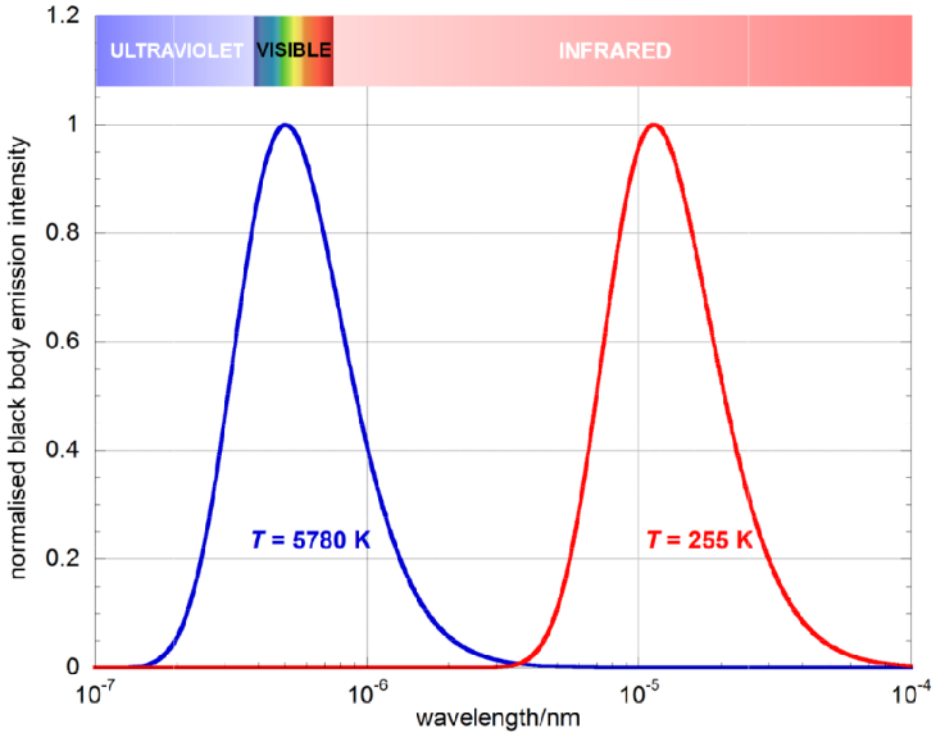

Figure 1.2 : Black body emissions as a function of wavelength for the sun (blue curve) and the Earth (red curve). The magnitude of the emission intensity has been normalised for clarity, as the emission from the sun would be much greater than that from the Earth.

wavelength of the incident radiation. Planets and stars can be reasonably described as black-body radiators. The emission spectrum of a black body depends solely on the temperature of the body itself. Thus solar emissions peak in the visible wavelength region ($\sim\lambda$ = 500 nm) as a result of the mean surface temperature of the sun (T = 5780 K), whereas terrestrial emissions peak in the infrared region of the spectrum ($\sim\lambda$ = 10 μm) as a consequence of the Earth's average emission temperature (T = 255 K). The black-body emission curves for both the sun and the Earth are shown in Figure 1.2. It is important to note that solar emission, though peaking in the visible region, also possesses significant outputs in the ultraviolet and infrared domains.

The principal gases contained in the atmosphere absorb weakly in the UV/visible region of the electromagnetic spectrum, where the bulk of solar radiation lies, with the exception of ozone (see Section 1.3). In contrast, atmospheric trace species absorb in the infrared spectral range of the outgoing radiation emitted by the Earth. In other

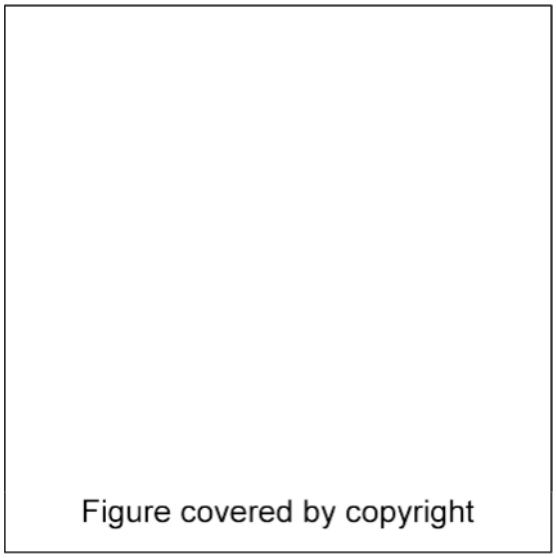

Figure 1.3 : Satellite view of the Earth seen in the infrared region of the electromagnetic spectrum. Taken from reference 4.

words, the atmosphere lets UV/visible radiation in, but does not let infrared radiation out and, as a result, the atmosphere is largely transparent in the visible region of the spectrum but it appears somewhat opaque when observed at infrared wavelengths, as shown in Figure 1.3. The absorption of outgoing radiation is evident from infrared spectra of the terrestrial emission recorded from satellites illustrated in Figure 1.4, clearly showing absorption lines that match the vibrational modes of atmospheric

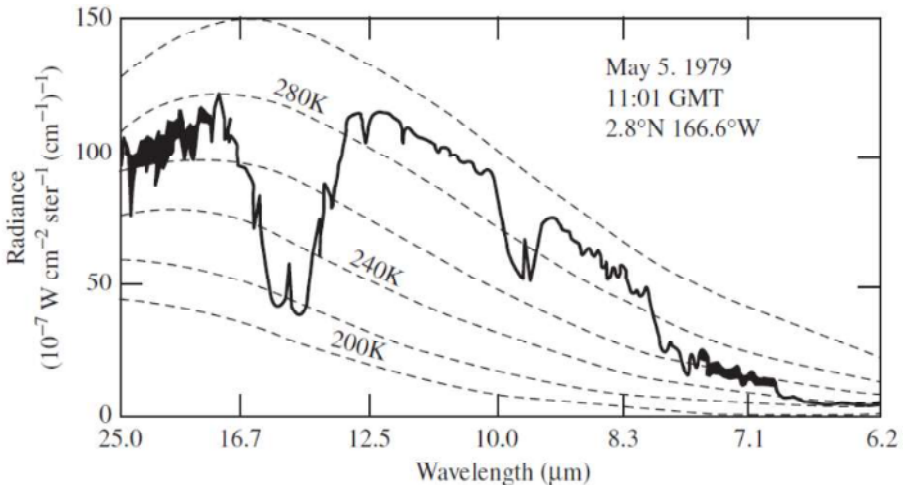

Figure 1.4 : Spectrum of terrestrial infrared emission observed from the satellite (solid line) compared with black-body radiance at different temperatures (dashed lines). Emission minima at λ = 14-15 μm, λ = 9-10 μm and λ < 8 μm arise from absorption of CO_2, O_3 and H_2O respectively. From reference 2.

components. This phenomenon is called the *greenhouse effect* and the atmospheric trace gases that contribute to it are commonly known as *greenhouse gases*, such as CO_2, CH_4, H_2O, O_3, N_2O and chlorofluorocarbons (CFCs). These species absorb outgoing infrared radiation and re-emit it in all directions, with a component directed to the Earth's surface giving rise to surface temperatures higher than predicted by a simple radiative balance model. Furthermore, collisional energy transfer between vibrationally excited molecules and surrounding gas molecules also contributes to increasing the temperature of the lower atmosphere.

Similarly, the disparity between the calculated and the measured surface temperature of Venus can be explained by the greenhouse effect. However, the temperature increase resulting from the greenhouse effect on Venus is dramatically higher than that observed for the Earth due to the higher concentration of infrared-active gases (principally CO_2) in the Venusian atmosphere, coupled with a "runaway greenhouse effect" which precludes the condensation of water. [2]

The greenhouse effect is a natural phenomenon ensuring habitable temperatures on Earth. However, the rapid increase in emissions of greenhouse gases following the industrial revolution threatens to upset the natural radiative balance, potentially leading to higher global temperatures and possibly to climate change. While the scientific consensus on the effects of increased greenhouse emissions is practically unanimous, [5] scepticism is still widespread: the Kyoto protocol (2005) aimed at cutting the emissions of greenhouse gases, but it has not been ratified by a number of countries. [6]

1.1.5 The Photochemical Environment of the Atmosphere

Solar radiation is distributed over the ultraviolet, visible and near-infrared regions of the electromagnetic spectrum as shown in Figure 1.2. However, when describing the photochemical environment of the Earth's atmosphere, usually only the ultraviolet (and to some degree, the visible) section of the solar output are taken into account as only photons at these wavelengths possess sufficient energy to break molecular bonds and initiate chemical reactions.

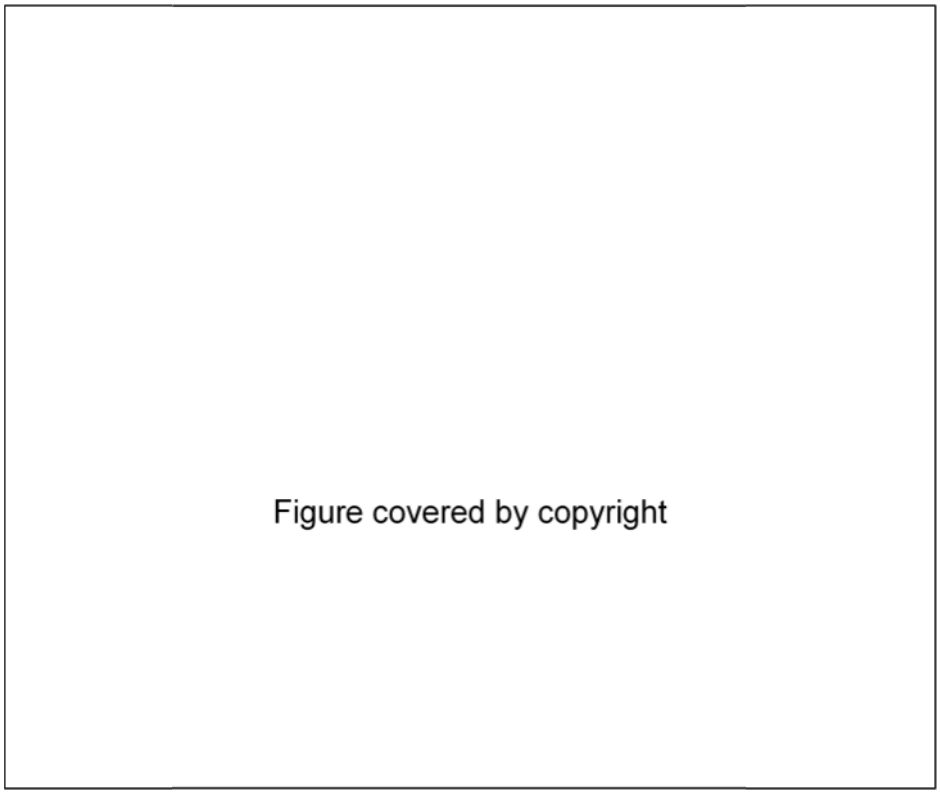

Figure 1.5 : Spectrum showing the intensity of solar emission at the top of the Earth's atmosphere and at ground level (*solid lines*). Also shown is the black-body emission curve for the sun (*dashed curve*). From reference 7.

Molecular oxygen and ozone are the principal UV absorbers in the atmosphere. Oxygen absorbs strongly at $\lambda < 230$ nm so that the vertical distribution of such short-wavelength photons is effectively in anticorrelation with the vertical profile of oxygen. Radiation of wavelength $\lambda > 230$ nm is absorbed by ozone, which exhibits an unusually intense absorption (the Hartley band) in the critical range λ = 230-300 nm. [8] Therefore the majority of the short-wavelength component ($\lambda < 300$ nm) of the incoming solar UV radiation does not reach the surface of the planet, as illustrated in Figure 1.5. The shielding from high energy photons was a crucial step in the evolution of life on Earth as radiation of wavelength $\lambda < 320$ nm is severely damaging for macromolecules fundamental to living cells such as proteins and nucleic acids. Exposure to UV-B radiation (λ = 290-320 nm) has also been associated with conditions such as erythema and cataracts and it is harmful to the biosphere as a whole. Furthermore, radiation at these wavelengths can consequently have disastrous effects on crop yields and marine ecosystems.

Absorption of high energy solar radiation results in photodissociation provided that the wavelength of the incident photon is sufficiently short. The overwhelming majority of gas phase chemistry in the atmosphere is ultimately initiated by photolysis. Stability of gas molecules to photodissociation in the atmosphere is dictated by their bond strength and by the altitude: as some wavelengths are only available at certain altitudes, different regions of the atmosphere exhibit different types of photochemistry. For instance, CFCs are inert in the troposphere but undergo photolysis once they enter the stratosphere (Section 1.4). As the altitude increases, the available solar radiation becomes more energetic and the more complex molecules are broken down to leave only simple species such as N_2, O_2, CO_2, H_2O and the atoms and radicals derived from them. From the upper mesosphere upwards, the incoming solar radiation has enough energy to split neutral species into atoms, and even to ionise atoms and molecules. However, an account of the complex and diverse photochemistry occurring above the stratopause is beyond the scope of this work.

1.2 Atmospheric Chemical Composition

Dry air is principally constituted of nitrogen (78% by volume), oxygen (21%), argon (0.9%) and carbon dioxide (0.039%, as of spring 2012). The water vapour content is highly variable: under conditions of high humidity it can represent up to 4% of the atmosphere by volume. It follows that all other gases combined only account for 0.065% of the total volume of the dry atmosphere: these species are therefore present in trace amounts. A list of key atmospheric trace gases can be found in Table 1.1 along with their natural and anthropogenic sources. Some gases are not evenly distributed throughout the atmosphere: ozone concentrations, for instance, peak in the stratosphere (the so-called *ozone layer*, described in Section 1.3.1), whereas water vapour mainly resides in the troposphere, as the tropopause acts as a barrier to the upward transport of water into the stratosphere as discussed above. Atmospheric concentrations are normally expressed as mixing ratios rather than in units of absolute concentration (*e.g.* molecule cm^{-3}); the concept of mixing ratio is analogous to that of mole fraction and it shows the relative importance of an atmospheric component regardless of the total pressure at a specific altitude. Hence, the mixing ratio of nitrogen is 0.78 and that of carbon dioxide is 3.9×10^{-4}, or 390 parts per million by volume (abbreviated to ppmv or

Compound	Natural sources	Anthropogenic sources
Methane (CH_4)	Enteric fermentation in wild animals; emissions from swamps, bogs, wetlands and oceans	Enteric fermentation in domesticated ruminants; emissions from paddies; natural gas leakage; sewerage gas; colliery gas; combustion
Hydrocarbons (HCs) and volatile organic compounds (VOCs)	Vegetation, aerobic biological processes, forest fires	Natural gas leakage, combustion, vehicle exhausts, paints and solvents.
Carbon monoxide (CO)	Oxidation of natural methane, larger HCs and VOCs; emission from oceans and forest fires	Oxidation of anthropogenic HCs and VOCs; incomplete combustion (especially in motor vehicles); industrial processes; blast furnaces.
Carbon dioxide (CO_2)	Oxidation of natural CO, destruction of forests, respiration by plants	Combustion of fossil fuels; limestone burning
Nitric oxide (NO)	Forest fires; anaerobic processes in soil; electric storms	High-temperature combustion of fossil fuels
Nitrogen dioxide (NO_2)	Forest fires; electric storms	High-temperature combustion of fossil fuels; atmospheric transformation of NO
Nitrous oxide (N_2O)	Emissions from denitrifying bacteria in soil; oceans	Combustion of oil and coal
Ammonia (NH_3)	Aerobic biological processes in soil; breakdown of amino acids in organic waste material	Coal and oil combustion; waste treatment
Hydrogen sulphide (H_2S)	Anaerobic fermentation; volcanoes and fumaroles	Oil refining; animal manure
Sulphur dioxide (SO_2)	Oxidation of H_2S; volcanic activity	Combustion of oil and coal
Methyl chloride (CH_3Cl)	Slow combustion of organic matter; microbial processes in oceans; algae	PVC manufacture and degradation; tobacco consumption
Methyl bromide (CH_3Br)	Aerobic biological processes	Soil fumigation; fire retardants
Methyl iodide (CH_3I)	Aerobic biological processes	None
Carbon tetrachloride (CCl_4)	None	Solvents; fire extinguishers; degradation of tetrachloroethylene
Methyl chloroform (CH_3CCl_3)	None	Electrical insulator
Chlorofluorocarbons (CFCs), halons, HCFCs, HFCs	None	Solvents; aerosol propellants; refrigerants; foam-blowing agents; dry-cleaning agents; degreasing agents

Table 1.1 : Trace gases in the atmosphere and their sources. Adapted from reference 2.

simply ppm).

The atmosphere also contains non-gaseous material. These condensed-phase particles or droplets suspended in air, commonly named *aerosols*, occur in a variety of sizes, ranging from a radius of approximately 1 nm to 1 mm. The sources of these particles are very diverse: they can originate from sea spray or dust due to surface erosion picked up by local weather systems or tropospheric convection, or from material injected into the atmosphere by volcanic eruptions or meteoric debris. Current estimates also attribute approximately 20% of particulate matter entering the atmosphere to human activities. Aerosols have an important effect on the planetary albedo (the reflectivity) and, therefore, on the planet's radiative balance: suspended particles can act as reflecting surfaces, back scattering incoming solar radiation into space, but they can also act as nuclei for cloud condensation, thus increasing the cloud coverage and therefore the Earth's albedo. Aerosols may also provide adsorption sites for gas molecules, initiating heterogeneous chemistry and catalysis of reactions involving trace gases.

The bulk composition of the atmosphere remains largely unaltered in spite of the continuous release of species into the air from both natural and anthropogenic sources. This observation clearly implies the existence of processes that remove the trace gases emitted but do not affect the (largely inert) principal components of the atmosphere. Trace components are removed from the atmosphere when they are deposited or absorbed onto the Earth's surface (*dry deposition*) or dissolved into droplets that eventually precipitate to the ground (*wet deposition*). Solar photolysis not only leads to the direct removal of many trace species, but also initiates important chemical removal processes, for instance *via* formation of the OH radical, discussed in Section 1.3.3.

1.3 Chemistry of Atmospheric Ozone

Although only present in trace amounts, ozone, O_3, is a crucial species in the Earth's atmosphere. Whilst most trace gases are more abundant near ground level, only 10% of the total atmospheric ozone is found in the troposphere. Ozone concentrations exhibit an unusual vertical profile, with the majority of ozone residing in the stratosphere (the so-called *ozone layer*, Figure 1.6). This behaviour is a direct consequence of the

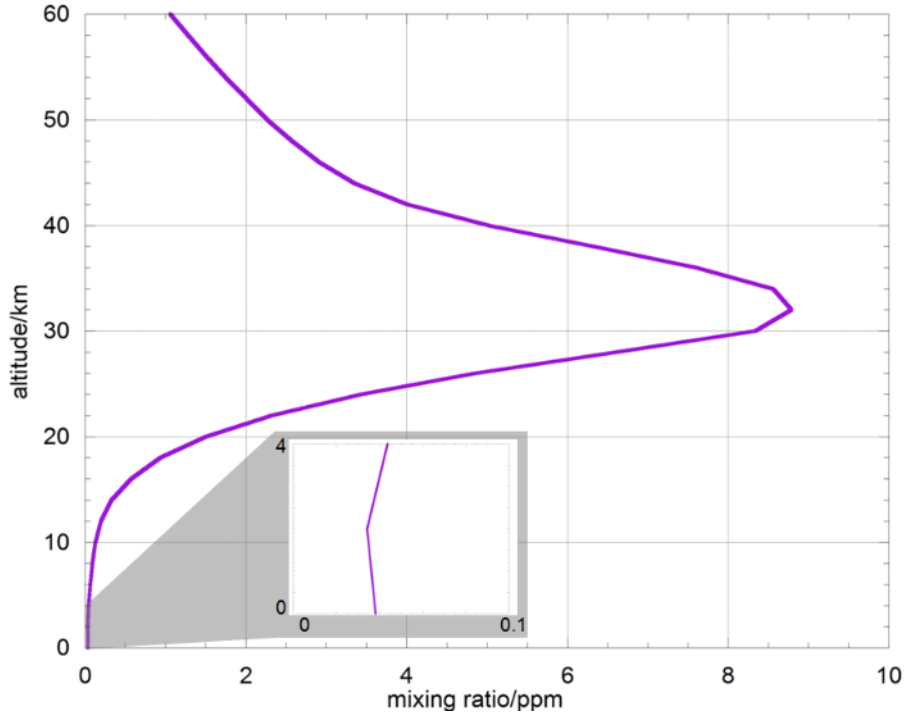

Figure 1.6 : Vertical distribution of ozone showing the characteristic peak (the *ozone layer*) in the stratosphere. Inset, typical ozone mixing ratios in the lower troposphere; ozone abundances in the boundary layer are however highly variable and depend strongly on season and geographical location. Reproduced from reference 3.

interactions between molecular oxygen and the photochemical environment of the atmosphere. Furthermore, as discussed below, the very existence of the stratosphere, as defined by its temperature profile, is due to the presence of the ozone layer.

1.3.1 Stratospheric Ozone

In 1930, Sidney Chapman proposed a mechanism to account for the vertical distribution of ozone in the atmosphere.[9] The so-called Chapman model consists of a series of oxygen-only reactions as follows:

$$O_2 + h\nu\ (\lambda < 242\ \text{nm}) \rightarrow O + O \quad (1.1)$$

$$O + O_2 + M \rightarrow O_3 + M \quad (1.2)$$

$$O_3 + h\nu\ (\lambda < 1180\ \text{nm}) \rightarrow O + O_2 \quad (1.3)$$

$$O + O_3 \rightarrow 2\ O_2 \quad (1.4)$$

$$O + O + M \rightarrow O_2 + M \quad (1.5)$$

where M indicates any other molecule which can act as an energy sink (a *third body*). The Chapman model is successful in explaining the vertical distribution of ozone, arising from the altitude dependence of the rate of process (1.1). Qualitatively, at high altitudes, the intensity of the appropriate short-wavelength radiation is relatively high but oxygen concentrations are too low for O_2 photolysis to be efficient. By contrast, closer to ground level, the number of photons with sufficient energy to dissociate O_2 is somewhat lower, whereas the abundance of oxygen molecules is high. In the stratosphere, where both oxygen molecules *and* radiation of wavelength $\lambda < 242$ nm are abundant, the rate of the photodissociation of O_2 is maximum, leading to the production of ozone in this region.

The proposed model for the formation of ozone also rationalises the temperature inversion observed in the stratosphere. The combination of reaction (1.2) and process (1.3) effectively converts the solar radiation absorbed by ozone in process (1.3) into kinetic energy transferred onto the third body M by increasing the thermal energy of M.

Since the interconversion of ozone and oxygen atoms *via* reactions (1.2) and (1.3) is rapid under stratospheric conditions compared to the other reactions in the cycle, O_3 and O are in effective rapid equilibrium and are usually considered as the *odd oxygen* (O_x) family, where $[O_x] = [O_3] + [O]$. Therefore the Chapman cycle can be described in terms of the steady state between overall odd oxygen production (process 1.1) and odd oxygen loss (reactions 1.4 and 1.5). Furthermore, given the efficiency of reaction (1.2) and the consequent paucity of O atoms in the lower stratosphere, reaction (1.5) has been shown to be too slow to compete with reactions (1.2) and (1.4): the model can be simplified further to a balance between process (1.1) and reaction (1.4).

The rates of processes (1.2) and (1.3) exhibit opposite altitude dependences. As the pressure drops with increasing altitude, termolecular quenching from the third body M becomes less efficient and as a result the rate of reaction (1.2) slows down. On the other hand, photolysis process (1.3) becomes faster at increasing altitudes as more high-energy photons are available in such regions. As a result, the partitioning of odd oxygen is shifted towards ozone at low altitudes and towards atomic oxygen at high altitudes. As shown in Figure 1.7, ozone is the dominant form of stratospheric odd

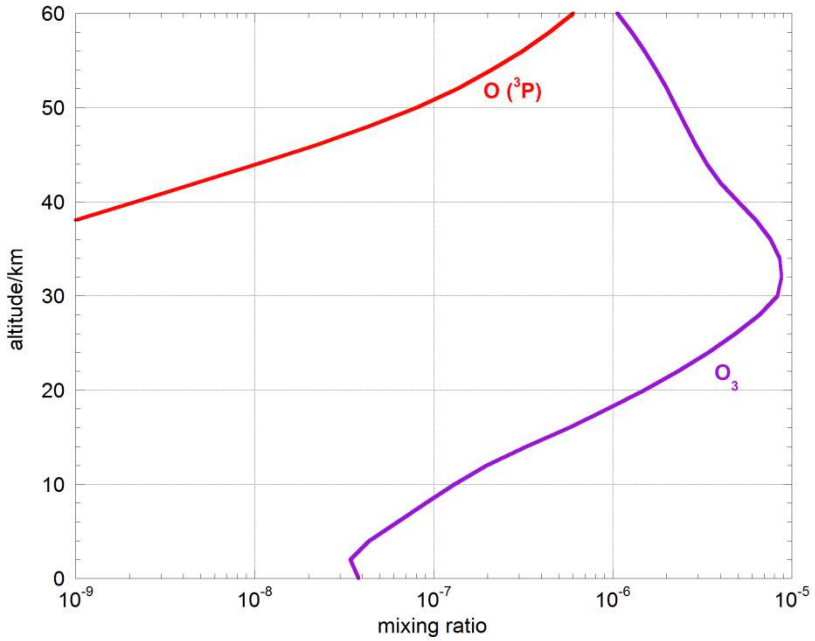

Figure 1.7 : Vertical profile of the partitioning of odd-oxygen into ozone (purple curve) and ground-state oxygen atoms (red curve), known as $O(^3P)$ as discussed in Chapter 2. Reproduced from reference 3.

oxygen below 60 km, and it constitutes approximately 99% of $[O_x]$ in the mid-stratosphere. [3]

Whilst the Chapman model successfully reproduces the overall form of the vertical distribution of ozone, when realistic kinetic and photochemical parameters are introduced, it overestimates the absolute stratospheric concentrations of odd-oxygen by a factor of two or more. Therefore either the rate of odd-oxygen production is overestimated in this model or the rate of its removal is underestimated. The rate of odd oxygen production by photolysis process (1.1) depends on the concentration of O_2 and on the radiation profile at wavelengths $\lambda < 242$ nm, both of which are well constrained by measurements. On the other hand, the rate of odd-oxygen loss *via* reaction (1.4) alone is too slow at stratospheric temperatures to remove sufficient O_3 to account for the observed ozone abundances. This implies that more complex odd-oxygen removal processes are also operating, all proceeding *via* catalytic cycles that can be generalised in the form:

$$X + O_3 \rightarrow XO + O_2 \quad (1.6)$$

$$XO + O \rightarrow X + O_2 \quad (1.7)$$

Net: $O + O_3 \rightarrow 2O_2$

The overall effect of reactions (1.6)-(1.7) is equal to reaction (1.4) and supplements this reaction in removing O_x. Furthermore, since the activation energies of reactions (1.6) and (1.7) are typically lower than that of reaction (1.4) [10], this cycle provides a more efficient route to odd oxygen removal than the direct reaction (1.4) at low stratospheric temperatures. Moreover, the catalytic regeneration of species X indicates that even trace amounts of X (normally in the range of ppb or ppt) may lead to significant loss of ozone (in the order of ppm). Several atmospheric species have been identified as candidates for X and XO, such as OH/HO_2 (HO_x) [11, 12], NO/NO_2 (NO_x) [13], Cl/ClO [14,15], Br/BrO [16], I/IO [17, 18] and H/OH [19].

Different odd-oxygen removing cycles dominate at different latitudes and altitudes. In general, the efficiency of a particular X/XO cycle at removing odd oxygen depends on its competition with other processes involving species X or XO, such as null cycles and (reversible) reservoir formation. Null cycles interconvert X and XO without causing loss of odd-oxygen; for instance, the following null cycle occurs for the NO_x family:

$$NO + O_3 \rightarrow NO_2 + O_2 \quad (1.8)$$

$$NO_2 + h\nu \rightarrow NO + O \quad (1.9)$$

Net: $O_3 + h\nu \rightarrow O + O_2$

The overall effect corresponds to process (1.3) as an ozone molecule is consumed but an oxygen atom is produced with no net effect on the total $[O_x]$.

Alternatively, catalyst X can be sequestered into a so-called *reservoir species* that makes it temporarily inactive with respect to O_x destruction. The most important reservoir species of atmospheric chlorine are, for example, $ClONO_2$ and HCl:

$$ClO + NO_2 + M \rightarrow ClONO_2 + M \quad (1.10)$$

$$Cl + CH_4 \rightarrow HCl + CH_3 \quad (1.11)$$

It is useful to notice how chlorine nitrate, $ClONO_2$, sequesters both active chlorine and NO_x. Formation of reservoir species breaks the X/XO catalytic cycle until the reservoirs themselves are broken down, *e.g.* by photolysis, and the active form of X/XO is re-released. The efficiency with which catalyst X is locked into an inactive form therefore depends ultimately on the formation and stability of the reservoir species. Some reservoirs are very stable and can be removed from the atmosphere *via* deposition processes such as precipitation. Others may be transported to other regions of the atmosphere where photolysis or further chemistry may release the active form of X. This 'partitioning' of species is of key importance: it is currently thought that approximately 70% of stratospheric chlorine exists as the reservoir HCl. On the other hand, bromine reservoir species are so inefficiently formed and short-lived that most atmospheric bromine exists in the 'active' radical forms Br and BrO.

Heterogeneous chemistry occurring on aerosols or cloud particles may also provide an efficient route to the release of the active catalyst from reservoir species. This is the case for chlorine reservoir compounds: their heterogeneous chemistry plays a crucial role in the anomalous and extensive ozone loss observed in recent years over Antarctica, and more recently over the Arctic, at the onset of Polar Springtime, as described in the following section.

1.3.2 Polar Stratospheric Ozone Depletion

Abnormal depletion of stratospheric ozone over Antarctica was first reported in the seminal work of Farman *et al.* [20] in 1985, as shown in Figure 1.8, and since then has been observed at the start of polar spring every year, as illustrated in Figure 1.9. This phenomenon, commonly known as the "ozone hole", is caused by the complex interaction of several factors, but can be attributed ultimately to the initially unexpected chemistry resulting from the unique meteorology of wintertime Antarctica and the enhanced halogen content of the stratosphere as a result of human activities.

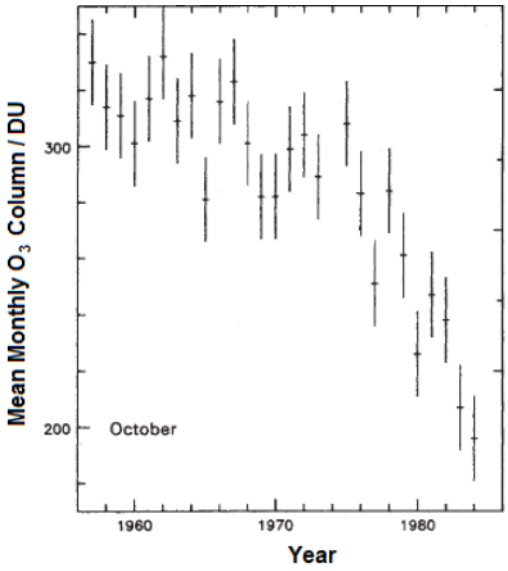

Figure 1. 8 : Mean October values of column O_3 in Dobson Units (DU) over Halley Bay, Antarctica, reported by Farman *et al.* [20] 1 DU is defined as the thickness of the layer (in units of 10 μm) that the total ozone in a column, if pure, would form under standard conditions (T = 273 K and p = 1 atm).

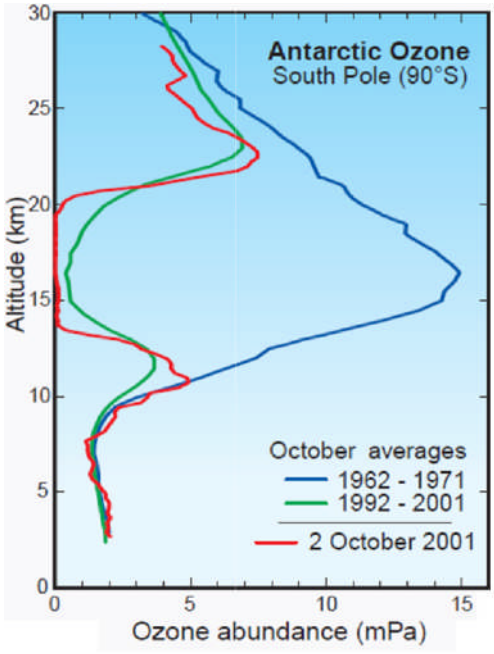

Figure 1.9 : Vertical abundances of ozone over Antarctica during Austral spring. From reference 21.

Understanding the complex mechanism of the anomalous ozone depletion over Antarctica required the joint efforts of field measurements, laboratory study and atmospheric modelling in an unprecedented extensive collaboration between the different fields of atmospheric science.

During winter, strong winds of up to 100 m s^{-1} lead to the formation of a meteorologically isolated region of the stratosphere known as the polar vortex over Antarctica. [2] The vortex is so stable that the cold and dark polar air is effectively isolated from that at the neighbouring latitudes for the whole winter and the beginning of spring. Temperatures at the core of the vortex plummet to values below T = 190 K: at these low temperatures particles of nitric acid trihydrate ($HNO_3.3H_2O$) or even water ice condense to form polar stratospheric clouds (PSCs) in the lower stratosphere. PSCs affect the partitioning of atmospheric chlorine in a two-fold fashion: firstly, they

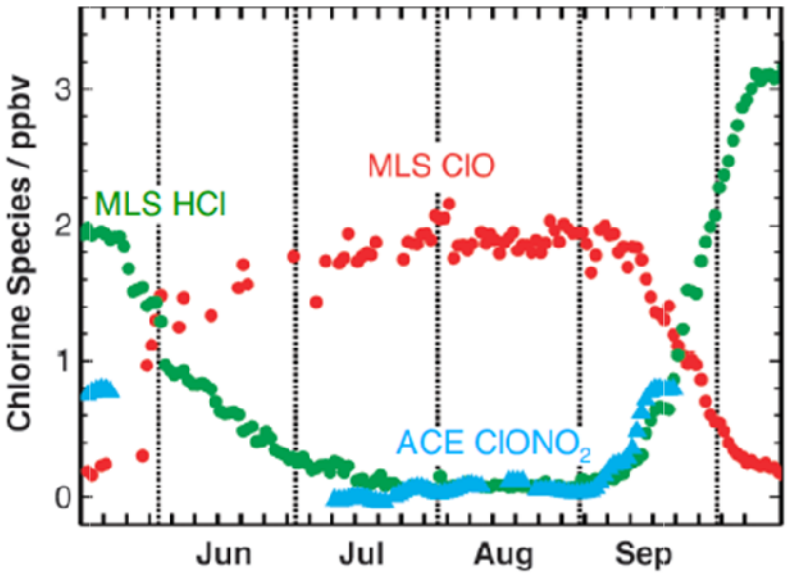

Figure 1.10 : Measurements of ClO and HCl *via* Aura MLS (microwave limb sounder) and $ClONO_2$ *via* ACE-FTS (Atmospheric Chemistry Experiment Fourier Transform Spectrometer) recorded at approximately 20 km of altitude over the latitudes 70-75°S during the Antarctic winter and spring of 2005. Data points represent daily averages. Measurements show the conversion of HCl and $ClONO_2$ reservoirs into active chlorine. At these latitudes, the edge of the polar vortex is exposed to daylight even during polar winter. This explains the presence of ClO during the winter months. From reference 21.

provide a site for heterogeneous conversion of chlorine reservoir compounds into more photolabile species:

$$ClONO_2\,(g) + HCl\,(s) \rightarrow \quad Cl_2\,(g) + HNO_3\,(s) \qquad (1.12)$$

$$ClONO_2\,(g) + H_2O\,(s) \rightarrow \quad HOCl\,(g) + HNO_3\,(s) \qquad (1.13)$$

Secondly, they inhibit the regeneration of the $ClONO_2$ reservoir *via* reaction (1.10) by sequestering up to 90% of the available NO_x into HNO_3.[2] The conversion of chlorine reservoir species into photolabile compounds continues throughout the polar winter and early spring. This is confirmed by satellite measurements, an example of which is shown in Figure 1.10, indicating that the polar stratosphere is impoverished of HCl and $ClONO_2$ reservoirs. In the absence of sunlight typical of the Antarctic winter, photolabile species produced by heterogeneous chemistry accumulate in the stratosphere until polar sunrise at the onset of spring, when solar radiation photolyses

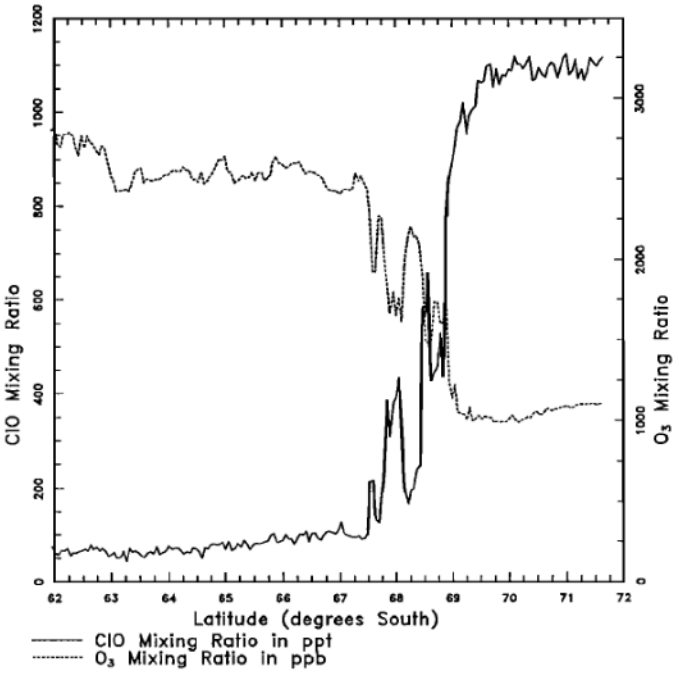

Figure 1.11 : Simultaneous aircraft measurements of stratospheric O_3 and ClO recorded at an altitude of approximately 18 km on 16th Sept 1987, as reported by Anderson and co-workers. [22] As the aircraft enters the vortex region, ClO concentrations increase sharply as ozone abundance plummets. The two data clearly anticorrelate. It is important to highlight that the ozone mixing ratio is given in units of parts per billion (ppb), whereas that of chlorine monoxide is given in parts per trillion (ppt).

Cl_2 and HOCl releasing active chlorine:

$$Cl_2 + h\nu \rightarrow 2\,Cl \qquad (1.14)$$

$$HOCl + h\nu \rightarrow Cl + OH \qquad (1.15)$$

At such elevated abundances of active chlorine, enhanced ozone depletion is inevitable *via* the reaction:

$$Cl + O_3 \rightarrow ClO + O_2 \qquad (1.16)$$

Figure 1.11 shows the evident anticorrelation between stratospheric ozone and chlorine monoxide abundances from aircraft measurements at latitudes typical of the polar vortex. It is crucial to notice, aside from the striking anticorrelation of ozone and ClO,

that the decrease in ozone concentration is approximately three orders of magnitude greater than that of the chlorine mixing ratio. This clearly indicates that a catalytic mechanism, regenerating chlorine atoms from the chlorine monoxide radicals produced in reaction (1.16), must be in place. As illustrated in Section 1.3.1, reaction (1.7) provides a route to the catalytic regeneration of chlorine atoms by reacting the chlorine monoxide radical with an oxygen atom. However the abundance of oxygen atoms is extremely low in the springtime lower stratosphere, especially in polar regions, hence this cycle is not efficient enough to account for the observed extensive ozone loss. Other catalytic cycles are therefore operating. Under the anomalous conditions found at the beginning of polar springtime, the partitioning of atmospheric chlorine is shifted towards ClO to such an extent that the ClO + ClO association occurs, giving rise to an initially unexpected ozone depleting catalytic cycle, first proposed by Molina and Molina in 1987: [23]

	$ClO + ClO + M$	$\leftrightarrows$	$Cl_2O_2 + M$	(1.17, −1.17)
	$Cl_2O_2 + h\nu$	$\rightarrow$	$Cl + ClOO$	(1.18)
	$ClOO + M$	$\rightarrow$	$Cl + O_2$	(1.19)
	$2(Cl + O_3$	$\rightarrow$	$ClO + O_2)$	(1.16)
Net:	$2O_3$	$\rightarrow$	$3O_2$	

This cycle is known as the *ClO dimer cycle* due to the formation and subsequent breakdown of the dimeric species Cl_2O_2. Temperatures in the polar vortex are so low that dimer formation (1.17) is strongly favoured over its thermal dissociation (−1.17) and the equilibration between ClO and Cl_2O_2 is significantly shifted towards the latter.

An additional catalytic cycle operates in the polar vortex, coupling the chemistry of atmospheric chlorine with that of bromine. This mechanism is initiated by the BrO + ClO cross-reaction, a complex multi-channel process, and can be simplified to:

$BrO + ClO$	$\rightarrow$	$Br + Cl + O_2$	(1.20)

	$Br + O_3$	→	$BrO + O_2$	(1.21)
	$Cl + O_3$	→	$ClO + O_2$	(1.16)
Net:	$2O_3$	→	$3O_2$	

The BrO + ClO cycle is thought to contribute to up to 50% of the ozone loss observed in the Antarctic springtime [21, 24], although an accurate characterisation of the efficiency of this cycle depends strongly on the quantification of the inorganic bromine content of the stratosphere and any product channels aside from those shown in reaction (1.20).

Anomalous ozone depletion has also been observed over the Arctic, though not as severe as the Antarctic "ozone hole". This difference arises mainly from the different topology and meteorology of the Northern hemisphere, causing the Arctic vortex to be less stable than its Antarctic counterpart. As a result, the air within the Arctic vortex is not as efficiently isolated from its surroundings as that in the Antarctic vortex, and winter temperatures in the Arctic stratosphere are typically 10-20 K higher than those found in the Antarctic. Consequently, the low temperatures necessary for the condensation of PSCs are reached only for shorter periods of time and the conversion of chlorine reservoir compounds into precursors of active chlorine is not as efficient as in the Antarctic stratosphere. Furthermore, as a result of its reduced stability, the Arctic polar vortex is subject to significant variations on a year-to-year basis, making the extent of Arctic ozone depletion extremely unpredictable. However, the magnitude of ozone loss observed in spring 2011 exceeded that of all previous Arctic ozone depletion events due to unusually long-lasting cold conditions [25]. The unprecedented removal of approximately 80% of stratospheric ozone at altitudes of 18-20 km was, in that winter, comparable to the severe depletion observed in the Antarctic.

Polar ozone depletion also has repercussions on global stratospheric ozone abundances. As temperatures rise throughout polar spring, PSCs break down liberating NO_x species: sequestration of active chlorine into reservoir species can therefore resume and catalytic ozone loss slowly shuts down. Moreover, the polar vortex weakens and polar air mixes with air from mid-latitudes. As polar air is severely ozone-depleted, lateral mixing leads to an overall dilution of global stratospheric ozone.

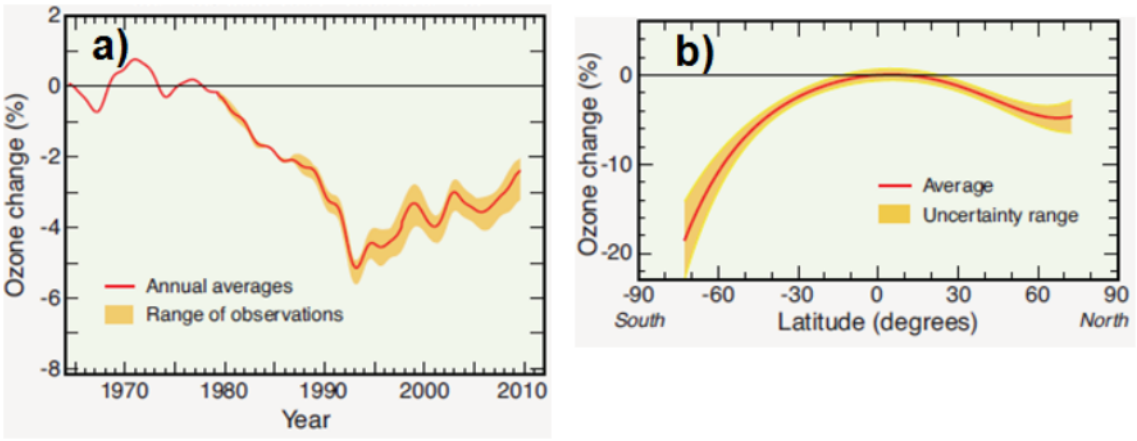

Figure 1.12 : a) Global total ozone change up until 2010 relative to the 1964-1980 average. b) Latitude-resolved changes in global ozone abundance between the 1964-1980 average and the 2005-2009 average. From reference 21.

As a result, measured global ozone abundances have been decreasing since the early 1980s (Figure 1.12a). The thinning of the ozone layer is not uniform around the globe. As shown in Figure 1.12b, the greatest decrease in ozone concentrations is experienced at high latitudes in both hemispheres as a consequence of ozone depletion during polar winter and the dispersion of ozone-impoverished air to mid-latitudes following polar spring. The depletion is not symmetrical in the two hemispheres as considerably less ozone is lost in the Arctic than in the Antarctic. Although ozone depletion occurs at mid-latitudes on a much smaller scale than that at the poles, it constitutes an enhanced environmental threat as these regions are more densely populated. Direct ozone depletion at mid-latitudes, as opposed to that resulting from simple mixing of ozone-deficient air from the poles, has also been observed [21] but it is smaller due to the presence of lower amounts of reactive halogens.

1.3.3 Tropospheric Ozone

Although the majority of total atmospheric ozone is found above the tropopause, the presence of ozone in the troposphere is central to many processes, such as the oxidation of trace species including pollutants and greenhouse gases. However, at elevated concentrations, tropospheric ozone is itself a pollutant and, because of its toxicity, has been linked to increased incidence of asthma attacks, eye and lung irritations in humans, as well as indirect effects such as causing crop damage [21].

In the stratosphere, the principal source of ozone is the termolecular recombination of O_2 with an oxygen atom generated by photodissociation of molecular oxygen, as outlined by reactions (1.1) and (1.2) in Section (1.3.1). In the troposphere, as photons with sufficient energy to photolyse O_2 ($\lambda < 242$ nm) do not penetrate through the stratosphere, the oxygen atom necessary to ozone formation *via* reaction (1.2) is typically produced by photolysis of nitrogen dioxide:

$$NO_2 + h\nu\ (\lambda < 400\ \text{nm}) \rightarrow \quad NO + O \qquad (1.22)$$

$$O + O_2 + M \quad \rightarrow \quad O_3 + M \qquad (1.2)$$

Other sources of ozone in the troposphere include downward transport from the stratosphere and dissociation of molecular oxygen in electrical storms. [2]

Tropospheric ozone acts as the precursor of key oxidising species in the lower atmosphere. Formation of these species is initiated by the photolysis of ozone. The electronic state of the oxygen atom released by the photolysis of ozone is crucially dependent on the wavelength of the incident radiation: generally, ground state atomic oxygen, $O(^3P)$ is formed upon photolysis of O_3 at $\lambda > 320$ nm, whereas the quantum yield for an electronically excited oxygen atom, $O(^1D)$, becomes dominant at $\lambda < 320$ nm. [10] In most cases, in the troposphere, the fate of the excited oxygen atom $O(^1D)$ is to be collisionally quenched to its ground state:

$$O(^1D) + M \quad \rightarrow \quad O(^3P) + M \qquad (1.23)$$

However, given the elevated abundances of water vapour commonly found in the troposphere, the excited oxygen atom may react, in competition, with H_2O to generate the hydroxyl radical, OH:

$$O(^1D) + H_2O \quad \rightarrow \quad 2\ OH \qquad (1.24)$$

Reaction (1.24) would not compete efficiently with reaction (1.23) in the stratosphere due to the low concentration of water vapour in that region of the atmosphere. In the

absence of NO_x species typical of the unpolluted atmosphere, the OH radical reacts with carbon monoxide releasing a hydrogen atom which undergoes rapid association with O_2 in air to generate the hydroperoxy radical, HO_2:

$$OH + CO \rightarrow H + CO_2 \quad (1.25)$$

$$H + O_2 + M \rightarrow HO_2 + M \quad (1.26)$$

The hydroxyl radical is then regenerated upon reaction of HO_2 with ozone:

$$HO_2 + O_3 \rightarrow OH + 2O_2 \quad (1.27)$$

$$\text{Net: } CO + O_3 \rightarrow CO_2 + O_2$$

The overall sequence of reactions (1.25)-(1.27) results in ozone removal. The interconversion between OH and HO_2 is rapid and the two species are commonly referred to as the "odd-hydrogen" family, HO_x, where $[HO_x] = [OH] + [HO_2]$. HO_x compounds are key species in atmospheric oxidation: the OH radical initiates the oxidation of many trace gases, including methane and alkenes. [2]

However, in the polluted atmosphere, characterised by elevated concentrations of NO_x species (NO and NO_2), reaction of the hydroperoxy radical with NO competes with reaction (1.27):

$$HO_2 + NO \rightarrow OH + NO_2 \quad (1.28)$$

Nitrogen dioxide produced by reaction (1.28) is readily photolysed by solar radiation, ultimately leading to ozone *production via* reaction (1.2). The presence of NO_x therefore perturbs the balance of atmospheric oxidation processes: in the unpolluted troposphere, atmospheric oxidation results in ozone removal, whereas ozone is *produced* in the presence of NO_x.

The rate of tropospheric ozone production is mitigated to an extent by reaction of O_3

with NO:

$$O_3 + NO \rightarrow O_2 + NO_2 \qquad (1.29)$$

Thus, a photostationary state is established between O_3, NO and NO_2 *via* reactions (1.22), (1.2) and (1.29). The $[NO]/[O_3]$ ratio is critical in establishing the balance between ozone production and ozone loss as a result of the competition between reactions (1.27) and (1.28). Simple kinetic calculations show that net ozone production occurs when the $[NO]/[O_3]$ ratio exceeds *ca.* 2×10^{-4}, as it is the case in many urban and industrialised regions. [26] Emissions of NO_2 and hydrocarbons from vehicle exhaust and industrial processes therefore contribute to the production of tropospheric ozone in industrialised areas *via* the oxidation processes outlined above. Under particular meteorological conditions, this chemistry leads to *photochemical smog*, a mixture of enhanced concentrations of ozone, NO_2, hydrocarbons and their breakdown products, associated with an adverse effect on human health and the environment.

Whilst ozone production has been observed in the troposphere, severe ozone depletion has also been reported, notably in the Arctic marine boundary layer (MBL) during polar springtime [27, 28] and at mid-latitudes, for instance in the MBL above the Dead Sea [29] and over the Atlantic Ocean. [30] As with the stratosphere, these events have been associated with enhanced abundances of halogen oxides, particularly BrO (Figure 1.13), originating from the photolysis of short-lived species emitted by marine micro-

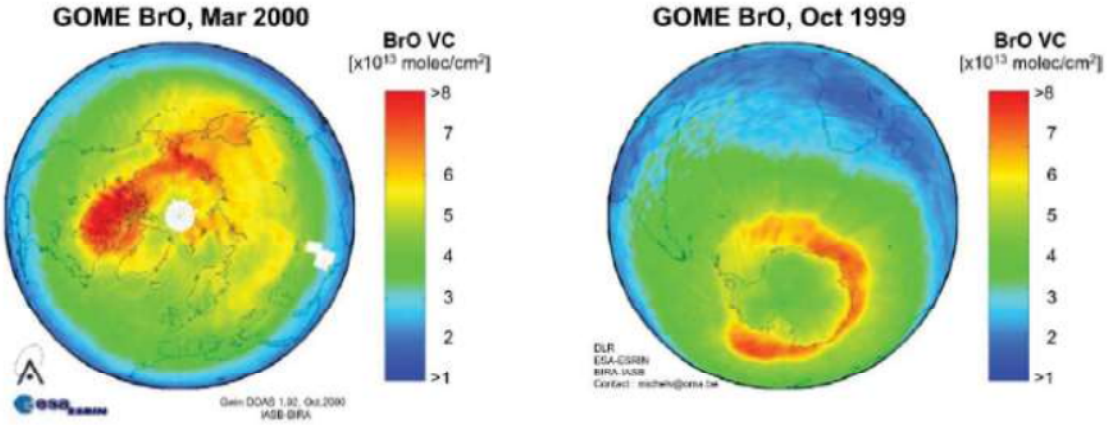

Figure 1.13 : Satellite measurements showing elevated BrO concentrations in the Polar marine boundary layer during springtime. From reference 31, reproduced by permission of the Royal Society of Chemistry.

organisms and also from the oxidation of sea salt halides (Cl^-, Br^-) on aerosol particles, [32, 33] and IO. [34, 35, 36] Halogen oxides are formed upon reaction of a halogen atom with ozone. Regeneration of the halogen atoms from halogen oxide radicals leads to catalytic ozone destruction in a fashion similar to that described in Section 1.3.1. It is also notable that chlorine-catalysed ozone loss reactions are less efficient in the troposphere than their bromine and iodine counterparts. This can be directly attributed to the ready formation and stability of chlorine-containing reservoir species through reactions such as (1.10) and (1.11). Irrespective of the name of the halogen, when the concentration of reactive halogens is sufficiently high, halogen oxide self- and cross-reactions can provide an efficient pathway to the regeneration of the halogen atom. At low concentrations of reactive halogen species, synergistic interactions between halogen oxides (XO) and other radical families, such as the HO_x family, can initiate another catalytic cycle: [31, 32]

	$XO + HO_2$	→	$HOX + O_2$	(1.30)
	$HOX + h\nu$	→	$X + OH$	(1.31)
	$X + O_3$	→	$XO + O_2$	(1.6)
	$OH + CO$	→	$CO_2 + H$	(1.25)
	$H + O_2 + M$	→	$HO_2 + M$	(1.26)
Net:	$O_3 + CO$	→	$O_2 + CO_2$	

In both cases ozone is removed, with significant implications on the oxidising capacity of the troposphere and the removal of pollutants.

1.4 Sources of Atmospheric Halogens

The halogen content of the atmosphere is the result of both natural and anthropogenic emissions. The principal sources of stratospheric chlorine and bromine are summarised in Figure 1.14. The principal natural source of stratospheric chlorine is methyl chloride, CH_3Cl, with a typical mixing ratio at the tropopause of about 0.55 ppb. [2] The remaining chlorine found in the stratosphere (up to 3 ppb) originates from compounds emitted as a

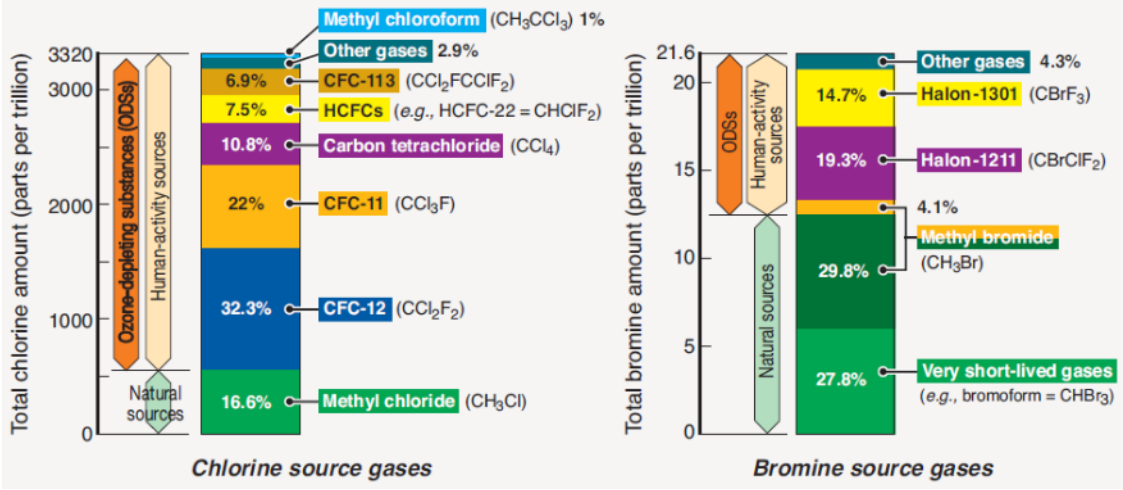

Figure 1.14 : Primary sources of chlorine (left) and bromine (right) transported into the stratosphere in 2008, as reported in reference 21. It is important to notice the different vertical scales of the two graphs and the difference partitioning natural and anthropogenic sources for chlorine and bromine.

result of human activities, mainly chlorofluorocarbons (CFCs), methyl chloroform (CH_3CCl_3) and carbon tetrachloride (CCl_4). CFCs were developed in the 1930s as replacements for toxic and flammable refrigerants. Their chemical inertness led to numerous industrial applications: CFCs were also employed as aerosol propellants, blowing agents for plastic-foam production and as solvents. Ultimately, the fate of CFCs was to leak into the atmosphere. In the 1970s, James Lovelock [37] first observed the presence of man-made halocarbons in the troposphere, showing that these compounds accumulated in the atmosphere due to their chemical inertness: CFCs were not only photostable in the troposphere, but they were also immune to atmospheric oxidation, giving rise to very long atmospheric lifetimes, as illustrated in Table 1.2. As CFCs can reside in the atmosphere for 50 years or longer, Molina and Rowland [14] postulated that they would eventually be transported into the stratosphere. The photochemical environment found in that region, considerably harsher than that found in the troposphere, would then be expected to lead to the photolysis of the chlorinated species and the release of chlorine atoms, initiating ozone depletion. This mechanism is confirmed by field measurements, as shown in the vertical profile of $CFCl_3$ in Fig 1.14: mixing ratios of this compound are effectively constant in the troposphere but they decrease significantly in the stratosphere as a result of photochemical loss.

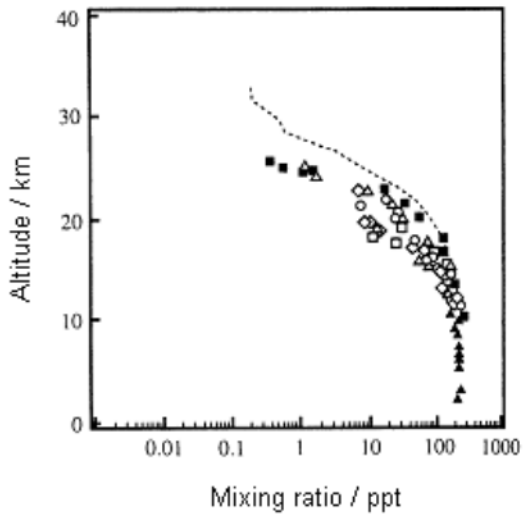

Figure 1.15 : Vertical distribution of $CFCl_3$ (CFC-11) in the Northern Hemisphere. The different symbols identify particular measurements performed over the period 1987-1990, whilst the dashed line represents the modelled profile. From reference 38.

Halocarbon	**Atmospheric lifetime / yr**	**Ozone-depletion potential**
$CFCl_3$ (CFC-11)	45	1*
CF_2Cl_2 (CFC-12)	100	0.82
$CF_2ClCFCl_2$ (CFC-113)	85	0.85
CHF_2Cl (HCFC-22)	11.8	0.04
CF_3Br (halon-1301)	65	15.9
CF_2BrCl (halon-1211)	16	7.9
CH_3CCl_3	5	0.16
CCl_4	26	0.82
CH_3Br	0.8	0.66

*by definition

Table 1.2 : Lifetime and ozone-depleting potentials of selected halocarbons as reported in reference 21. The ozone-depleting potential of a species is defined as the ability of said species to deplete stratospheric ozone relative to the depletion caused by the same mass of $CFCl_3$.

Emissions of bromine-containing substances also have a profound impact on atmospheric ozone. Methyl bromide, CH_3Br, and halons are the main sources of atmospheric bromine. Methyl bromide is produced naturally by marine algae but it is also emitted following human activities such as fumigation of soils and biomass

burning. Halons are the bromine analogues of CFCs and were used as fire extinguishing agents and fire retardants in the 20th century. Analogously to chlorine-containing compounds, the long lifetimes of these species allow transport into the stratosphere and release of the bromine atom following solar photolysis.

Natural emissions of bromine, besides methyl bromide, include a number of species such as CH_2Br_2, $CHBr_3$, CH_2ClBr. The emission rate of these compounds is thought to be comparable to that of methyl bromide and the halons combined but their short tropospheric lifetimes ensure that only a fraction of these species reaches the stratosphere. In this case, bromine released by solar photolysis can affect the tropospheric ozone budget.

1.4.1 CFC Control Measures

The seminal work of Molina and Rowland in 1974 [14] first identified the threat that emissions of halocarbons represented to the Earth's ozone layer. In the years following their study, a number of countries including the United States, Canada and Sweden passed legislation to reduce the use of CFCs and replace them with less harmful HCFCs. These compounds were designed as CFCs in which one or more of the chlorine atoms were replaced by hydrogen. HCFCs are preferable to CFCs as they have shorter atmospheric lifetimes than their hydrogen-free counterparts (Table 1.2). This is because HCFCs are subject to hydrogen abstraction by the OH radical in the troposphere, so they are degraded before they reach the stratosphere. However, the unexpected discovery of severe ozone depletion over Antarctica by Farman *et al*. [20] in 1985 called for harsher restrictions on halocarbons. The Montreal Protocol, signed in 1987, and its successive amendments (London 1990, Copenhagen 1992, Vienna 1995, Montreal 1997, Beijing 1999) aimed to enforce rapid and wide-ranging phase-out of halogen containing species initially by freezing emissions of CFCs and halons and then by reducing them according to an agreed timetable. This has been achieved by replacing CFCs with HCFCs; however HCFCs are still considered a transitional replacement as they still contribute to the presence of chlorine in the stratosphere, albeit to a considerably smaller extent than CFCs, and are, incidentally, powerful greenhouse gases. The Montreal Protocol (1987) and its successive amendments have been ratified

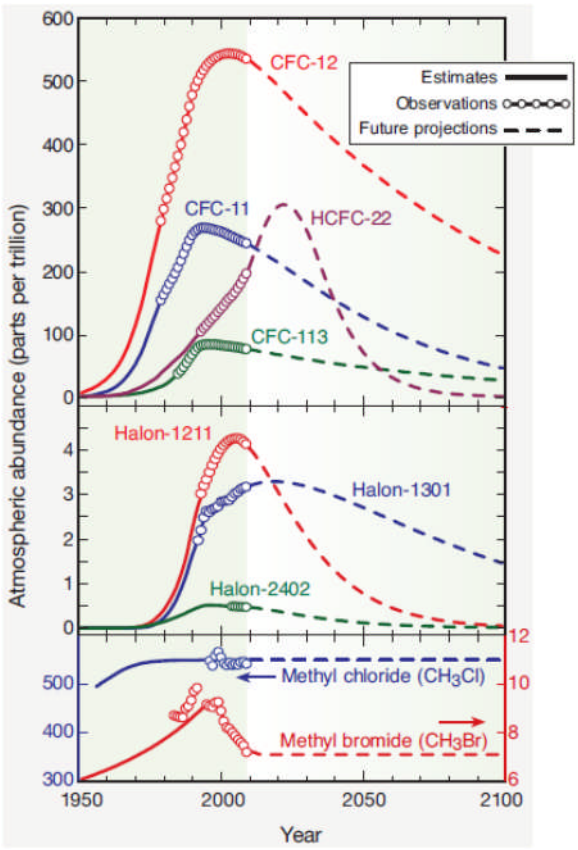

Figure 1.16 : Mixing ratios of ozone-depleting compounds at the Earth's surface shown as a combination of direct measurements, estimates of historical abundance and future projections. From reference 21.

by many, but not all, of the producing countries.

The efficacy of these regulatory policies is reflected by the trends in the atmospheric abundance of some ozone-depleting species, including CFCs and halons, shown in Figure 1.16 along with future projections. Mixing ratios of HCFCs are expected to rise up until 2040, a date by which they will be phased out. The two panels of Figure 1.17 show projections of the effects of the Montreal protocol and some of its amendments on the chlorine content of the stratosphere (left hand side panel) and on skin cancer rates (on the right hand side). It should be noted, however, that even with the latest restrictions on CFC/HCFC production and use, the effective stratospheric chlorine levels are not expected to return to 1980 levels for several decades, meaning that halogen-mediated ozone loss is an ongoing environmental issue. Another as yet unresolved problem is the potential effect of global warming on ozone loss processes.

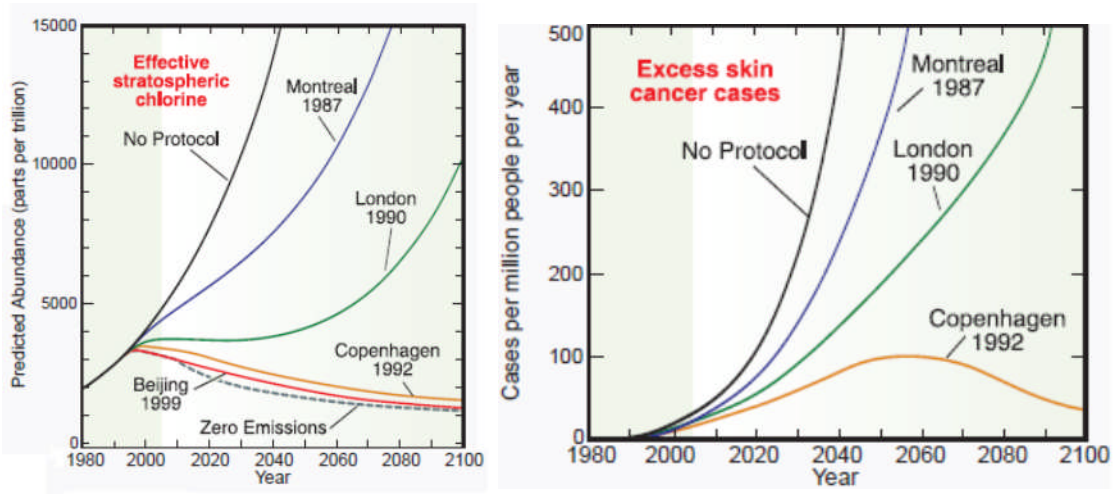

Figure 1.17 : Effects of the Montreal Protocol and successive amendments on effective stratospheric chlorine (left) and excess skin cancer cases (right). From reference 21.

1.5 Summary and Concluding Remarks

A thorough understanding of the composition of the Earth's atmosphere is only possible when the dynamic equilibrium between the sources of atmospheric gases and their sinks is fully characterised. In a world in which human activities have an increasingly greater impact on the atmosphere, as the history of stratospheric ozone depletion shows, an accurate account of the chemistry of atmospheric trace components is of paramount importance.

Our knowledge of the composition of the atmosphere and understanding of its chemistry relies on the joint effort of field measurements, atmospheric modelling and laboratory studies. Any attempt to replicate field observations by means of modelling requires accurate characterisation of the kinetics and photochemistry of processes affecting the composition of the atmosphere.

The ozone chemistry discussed in this chapter is a suitable example of the complexity of atmospheric processes: a full understanding of the mechanisms affecting ozone abundances is only possible by taking into account many reactive species as well as physical and meteorological processes. Recent studies, [39, 40] discussed in specific terms in subsequent chapters, have reported discrepancies in the current understanding of ozone chemistry by highlighting the disagreement between field observations and

atmospheric models. The present work aimed to address these uncertainties by characterising key reactions of halogen oxides free radicals involved in ozone depletion.

Specifically, the kinetics and thermochemistry of halogen oxide self- and cross-reactions have been studied using laser flash photolysis coupled with UV absorption spectroscopy with charge-coupled device (CCD) detection, discussed extensively in Chapter 3. Some of the theoretical principles of kinetics and photochemistry, fundamental to the experiments performed in the current work, are discussed in the following chapter.

1.6 References

1. D.C. Lindberg, *The Beginnings of Western Science*, 2nd edition, **2007**, University of Chicago Press, Chicago, United States
2. R.P. Wayne, *Chemistry of Atmospheres*, 3rd edition, **2002**, Oxford University Press, Oxford, United Kingdom
3. G. Brasseur, J. Orlando, G. Tyndall, *Atmospheric Chemistry and Global Change*, **1999**, Oxford University Press, Oxford, United Kingdom
4. *Geostationary Earth Radiation Budget (GERB) mission: planned research*, Imperial college, London, www3.imperial.ac.uk/spat/research/missions/atmos_missions/gerb/research
5. S. Solomon, D. Qin, M. Manning, Z. Chen, M. Marquis, K.B. Averyt, M. Tignor, H.L. Miller, *Contribution of Working Group I to the Fourth Assessment Report of the Intergovernmental Panel on Climate Change (IPCC)*, **2007**, Cambridge University Press, Cambridge, United Kingdom
6. Kyoto Protocol, *United Nations Framework Convention on Climate Change*, **2009**, www.unfccc.int
7. G. Brasseur, S. Solomon, *Aeronomy of the Middle Atmosphere*, 3rd edition, **2005**, Springer, Dordrecht, The Netherlands
8. W. Hartley, *J. Chem. Soc.*, **1881**, 39, 111
9. S. Chapman, *Phil. Mag.*, **1930**, 10, 369

10. S.P. Sander, J. Abbatt, J. R. Barker, J.B. Burkholder, R.R. Friedl, D.M. Golden, R.E. Huie, C.E. Kolb, M.J. Kurylo, G.K. Moortgat, V.L. Orkin, P.H. Wine, *Chemical Kinetics and Photochemical Data for Use in Atmospheric Studies*, Evaluation No. 17, **2011**, JPL Publication 10-6, Jet Propulsion Laboratory, Pasadena, United States, http://jpldataeval.jpl.nasa.gov
11. D.R. Bates, M. Nicolet, *Publ. Astron. Soc. Pac.*, **1950**, 62, 106
12. J. Hampson, *Photochemical Behaviour of the Ozone Layer*, **1964**, Canadian Armament Research and Development Establishment, Technical Note 1627
13. P.J. Crutzen, *Quart. J. R. Met. Soc.*, **1970**, 96, 320
14. M.J. Molina, F.S. Rowland, *Nature*, **1974**, 249, 810
15. R. S. Stolarski, R. J. Cicerone, *Can. J. Chem*, **1974**, 52, 1610
16. S.C. Wofsy, M.B. McElroy, Y.L. Yung, *Geophys. Res Lett.*, **1975**, 2, 215
17. W.L. Chameides, D.D. Davis, *J. Geophys. Res.*, **1980**, 85, 7383
18. S. Solomon, R.R. Garcia, A.R. Ravishankara, *J. Geophys. Res.*, **1994**, 99, 20491
19. D.R. Bates, M. Nicolet, *J. Geophys. Res.*, **1950**, 55, 301
20. J.C. Farman, B.G. Gardiner, J.D. Shanklin, *Nature*, **1985**, 315, 207
21. WMO (World Meteorological Organization), *Scientific Assessment of Ozone Depletion: 2010, Global Ozone Research and Monitoring Project*, Report No. 52, **2011**, Geneva, Switzerland
22. J.G. Anderson, W.H. Brune, M.H. Proffitt, *J. Geophys. Res.*, **1989**, 94, 11465
23. L. Molina, M. Molina, *J. Phys. Chem.*, **1987**, 91, 433
24. K. Frieler, M. Rex, R.J. Salawitch, T. Canty, M. Streibel, R.M. Stimpfle, K. Pfeilsticker, M. Dorf, D.K. Weisenstein, S. Godin-Beekmann, *Geophys. Res. Lett.*, **2006**, 33, L10812
25. G.L. Manney, M.L. Santee, M. Rex, N.J. Livesey, M.C. Pitts, P.Veefkind, E.R. Nash, I. Wohltmann, R. Lehmann, L. Froidevaux, L.R. Poole, M.R. Schoeberl, D.P. Haffner, J. Davies, V. Dorokhov, H. Gernandt, B. Johnson, R. Kivi, E. Kyrö, N. Larsen, P.F. Levelt, A. Makshtas, C.T. McElroy, H. Nakajima, M.C. Parrondo, D.W. Tarasick, P. von der Gathen, K.A.Walker, N.S. Zinoviev, *Nature*, **2011**, 478, 469

26. P.J. Crutzen, *Topics in Atmospheric and Interstellar Physics and Chemistry*, **1994**, Les Editions de Physique, Les Ulis
27. M. Hausmann, U. Platt, *J. Geophys. Res.*, **1994**, 99, 25399.
28. L.A. Barrie, J.W. Bottenheim, W.R. Hart, *J. Geophys. Res.*, **1994**, 99, 25313
29. V. Matveev, M. Peleg, D. Rosen, D.S. Tov-Alper, K. Hebestreit, J. Stutz, U. Platt, D. Blake, M. Luria, *J. Geophys. Res.*, **2001**, 106, 10375
30. A. Saiz-Lopez, J.M.C. Plane, J.A. Shillito, *Geophys. Res. Lett.*, **2004**, 31, L03111
31. P.S. Monks, *Chem. Soc. Rev.*, **2005**, *34*, 376 http://dx.doi.org/10.1039/B307982C
32. U. Platt, G. Hönninger, *Chemosphere*, **2003**, *52*, 325
33. R. Vogt, P.J. Crutzen, R. Sander, *Nature*, **1996**, 383, 327
34. B. Alicke, K. Hebestreit, J. Stutz, U. Platt, *Nature*, **1999**, 397, 572
35. B.J. Allan, G. McFiggans, J.M.C. Plane, H. Coe, *J. Geophys. Res.*, **2000**, 105, 14,363
36. A.S. Mahajan, M. Shaw, H. Oetjen, K.E. Hornsby, L.J. Carpenter, L. Kaleschke, X. Tian-Kunze, J.D. Lee, S.J. Moller, P. Edwards, R. Commane, T. Ingham, D.E. Heard, J.M.C., *J. Geophys. Res.*, **2010**, 115, D20303
37. J.E. Lovelock, R.J. Maggs, R.J. Wade, *Nature*, **1973**, 241, 194
38. WMO (World Meteorological Organization), *Scientific Assessment of Ozone Depletion: 1994, Global Ozone Research and Monitoring Project*, Report No. 37, **1995**, Geneva, Switzerland
39. M. von Hobe, R.J. Salawitch, T. Canty, H. Keller-Rudek, G.K. Moortgat, J.-U. Grooß, R. Müller, F. Stroh, *Atmos.Chem. Phys.*, **2007**, 7, 3055
40. T. Canty, E.D. Rivière, R.J. Salawitch, G. Berthet, J.-B. Renard, K. Pfeilsticker, M. Dorf, A. Butz, H. Bösch, R.M. Stimpfle, D.M. Wilmouth, E.C. Richard, D.W. Fahey, P.J. Popp, M.R. Schoeberl, L.R. Lait, T.P Bui, *J. Geophys. Chem.* **2005**, 110, D01301

Chapter 2
Gas Kinetics, Thermochemistry and Photochemistry

A thorough understanding of the chemistry of the atmosphere requires an accurate characterisation of the lifetime and fate of atmospheric trace species. The rates at which these species are formed and destroyed depend crucially on their reaction kinetics, thermochemistry and photochemistry. A summary of the fundamental principles of these disciplines is presented in this chapter.

2.1 Gas-Phase Kinetics

2.1.1 Fundamentals of Gas-Phase Kinetics

The change in extent of reaction, $\delta\xi$, defined for any species Q in a gas phase chemical reaction, is given by:

$$\delta\xi = \frac{\delta n_{\mathrm{Q}}}{\nu_{\mathrm{Q}}} \qquad (2.\mathrm{i})$$

where δn_{Q} is the change in the number of moles of species Q brought about by the chemical reaction and ν_{Q} is the stoichiometric coefficient of Q in the reaction. Thus, considering the general reaction between species A and B to products C and D:

$$\mathrm{aA} + \mathrm{bB} \quad = \quad \mathrm{cC} + \mathrm{dD} \qquad (2.1)$$

where a, b, c, and d are the stoichiometric coefficients of species A, B, C and D respectively, equation (2.i) can be written as:

$$\delta\xi = \frac{\delta n_{\mathrm{A}}}{-\mathrm{a}} = \frac{\delta n_{\mathrm{B}}}{-\mathrm{b}} = \frac{\delta n_{\mathrm{C}}}{\mathrm{c}} = \frac{\delta n_{\mathrm{D}}}{\mathrm{d}} \qquad (2.\mathrm{ii})$$

where the stoichiometric coefficients are, by definition, negative for the reagents and positive for the products. The rate of reaction, $\hat{r}$, is then defined as the rate of change of the extent of reaction with time:

$$\hat{r} = \frac{d\xi}{dt} = \frac{1}{\nu_{\mathrm{Q}}}\frac{dn_{\mathrm{Q}}}{dt} \tag{2.iii}$$

Hence, for reaction (2.1),

$$\hat{r}_{2.1} = -\frac{1}{\mathrm{a}}\frac{dn_{\mathrm{A}}}{dt} = -\frac{1}{\mathrm{b}}\frac{dn_{\mathrm{B}}}{dt} = \frac{1}{\mathrm{c}}\frac{dn_{\mathrm{C}}}{dt} = \frac{1}{\mathrm{d}}\frac{dn_{\mathrm{D}}}{dt} \tag{2.iv}$$

Equation (2.iii) illustrates the *extensive* definition of reaction rate. However, if the volume of the system in which the reaction occurs remains constant, then the more transferrable *intensive* definition of reaction rate can be used:

$$r = \frac{1}{\nu_{\mathrm{Q}}}\frac{d\left(n_{\mathrm{Q}}/V\right)}{dt} = \frac{1}{\nu_{\mathrm{Q}}}\frac{d[\mathrm{Q}]}{dt} \tag{2.v}$$

where [Q] indicates the concentration of any species Q in the usual notation. Hence, for reaction (2.1):

$$r = -\frac{1}{\mathrm{a}}\frac{d[\mathrm{A}]}{dt} = -\frac{1}{\mathrm{b}}\frac{d[\mathrm{B}]}{dt} = \frac{1}{\mathrm{c}}\frac{d[\mathrm{C}]}{dt} = \frac{1}{\mathrm{d}}\frac{d[\mathrm{D}]}{dt} \tag{2.vi}$$

which allows for a definition of reaction rate irrespective of which species is monitored. In the current work, the expression “reaction rate” is used to always indicate the intensive reaction rate, as defined in this way.

Kinetic experiments show that the rate of a reaction can often be expressed in the form of a product between some constant and the concentration of, typically, the reactants elevated to a power:

$$r = k_{obs}[A]^{\alpha}[B]^{\beta} \qquad (2.vii)$$

where k_{obs} is the observed rate constant or rate coefficient. The exponents α and β are determined experimentally and cannot be predicted from the overall reaction; they are defined as the orders of the reaction with respect to reagents A and B respectively. The overall order of the reaction is given by the sum of α and β.

However, when a reaction proceeds in a single step, *i.e.* without intermediates (an *elementary reaction*), the reaction order with respect to each of the reagents corresponds to the stoichiometric number for that species. Therefore the overall reaction order of an elementary reaction, called the molecularity, is simply given by the total number of reagent molecules participating in the reaction. Elementary reactions involving a single reagent molecule are called unimolecular and are therefore first-order reactions; elementary reactions involving the collision between two species are bimolecular and are second-order reactions; elementary reactions involving the collision between three particles are referred to as termolecular and are third-order reactions.

If the elementary steps constituting an overall reaction are known, then the overall rate equation can be predicted. For example, if reaction (2.1) were known to proceed by the following elementary steps:

$$A + B \rightarrow AB \qquad (2.2)$$

$$AB \rightarrow C + D \qquad (2.3)$$

$$\text{Net: } A + B \rightarrow C + D \qquad (2.1)$$

then the following rate equations can be established:

$$-\frac{d[\mathrm{A}]}{dt} = -\frac{d[\mathrm{B}]}{dt} = k_{2.2}[\mathrm{A}][\mathrm{B}] \qquad \text{(2.viii)}$$

$$\frac{d[\mathrm{AB}]}{dt} = k_{2.2}[\mathrm{A}][\mathrm{B}] - k_{2.3}[\mathrm{AB}] \qquad \text{(2.ix)}$$

$$\frac{d[\mathrm{C}]}{dt} = \frac{d[\mathrm{D}]}{dt} = k_{2.3}[\mathrm{AB}] \qquad \text{(2.x)}$$

Reaction rates (2.vii)-(2.x) are expressed in the form of differential equations; if these equations are soluble, they can be used to express the overall rate constant of the reaction in terms of the rate constants for the elementary steps in the mechanism.

In complex reaction systems a solution to the differential rate equation is often not available. However, in some of these cases, the presence of a reactive intermediate allows the derivation of an overall rate equation through approximation. If the rate of removal of an intermediate species far exceeds the rate at which it is produced, then the concentration of this species remains small and largely invariant after an initial induction period. If these requirements are met, then the steady state approximation (SSA), stating that the rate of change of the concentration of the reactive intermediate approximates to zero, can be applied after the intermediate concentration maximises.

Adopting the example for reaction (2.1) above, if species AB in the reaction sequence (2.2)-(2.3) is a reactive intermediate, then the steady state approximation can be applied to rate equation (2.ix):

$$\frac{d[\mathrm{AB}]}{dt} = k_{2.2}[\mathrm{A}][\mathrm{B}] - k_{2.3}[\mathrm{AB}] \overset{\text{SSA}}{\approx} 0 \qquad \text{(2.xi)}$$

It follows that :

$$k_{2.3}[\mathrm{AB}] = k_{2.2}[\mathrm{A}][\mathrm{B}] \qquad \text{(2.xii)}$$

Therefore the rate of product formation, equation (2.x), can be expressed in terms of the reagent concentrations:

$$\frac{d[\mathrm{C}]}{dt} = \frac{d[\mathrm{D}]}{dt} = k_{2.3}[\mathrm{AB}] = k_{2.2}[\mathrm{A}][\mathrm{B}] \qquad \text{(2.xiii)}$$

In this case, since the intermediate AB is removed far more rapidly than it is formed, the rate of product formation is controlled solely by the rate of A + B association, reaction (2.2). This is known as the rate determining step.

In more complex reaction systems, an exact solution to the rate equations is often not available even when the steady state approximation is invoked. In such cases, numerical 'integration' is used to simulate species concentration from the differential equations. This method effectively approximates that, for any species X over suitably short time steps, Δt:

$$\frac{d[\mathrm{X}]}{dt} \approx \frac{\Delta[\mathrm{X}]}{\Delta t} \qquad \text{(2.xiv)}$$

Δ[X] can then be calculated from the rate equation, either simplistically from equation (2.xiv) or using more elegant mathematical procedures, using Δt, and the time profile of [X] can be built up iteratively, albeit requiring a very large number of calculation steps. Rate constants are then obtained from fitting the simulated to the observed temporal concentration profiles *via* least-squares optimisation, as discussed below in Chapter 3.

2.1.2 Temperature Dependence of Reaction Rates

In 1889, Svante Arrhenius [1] derived empirically an expression for the temperature dependence of bimolecular rate constants, now referred to as the Arrhenius equation:

$$k = A\exp\left(\frac{-E_{\mathrm{a}}}{RT}\right) \qquad \text{(2.xv)}$$

where A is the pre-exponential factor, E_a the activation energy for the reaction, R the gas constant and T the absolute temperature. The pre-exponential factor and the activation energy are commonly referred to as the Arrhenius parameters, and are used to parameterise the temperature dependence of k.

A number of theories have been developed to explain the temperature dependence of gas phase bimolecular reactions. A brief summary of some of these theories is given in the following sections.

2.1.3 Bimolecular Rate Theories

Simple Collision Theory (SCT) provides a useful initial conceptual framework to understand bimolecular reactions in the gas phase. In this approach, reactants are described using kinetic theory, *i.e.* as hard spheres undergoing only elastic collisions. No intermolecular forces are taken into account and reactions only occur upon collision provided that the collision energy exceeds a certain threshold value. The rate of a general elementary bimolecular reaction:

$$\mathrm{A} + \mathrm{B} \rightarrow \text{products} \qquad (2.4)$$

is then equated to the product of the collision frequency of reagent species A and B, Z_{AB}, and the fraction of colliding species, F, possessing sufficient energy to overcome the threshold or activation barrier to the reaction. Therefore the theoretical rate of reaction (2.4) can be written as:

$$r_{2.4} = Z_{AB} \times F \qquad (2.xvi)$$

An expression for the collision frequency, Z_{AB}, is readily obtained from the kinetic theory of gases:

$$Z_{AB} = V_{coll} L^2 [A][B] \qquad (2.xvii)$$

where V_{coll} is the 'collision volume' and L is Avogadro's number. The collision volume is that volume notionally swept out by one moving molecule, travelling at the *mean relative speed*, $\bar{c}_{rel}$, surrounded by a gas of effectively stationary molecules. This volume represents the space in which any other molecule must be to undergo collision in a given time period, Δt, with the molecule of interest. The collision volume is therefore expressed as the product of the mean relative speed $\bar{c}_{rel}$, the time interval Δt and the collision cross-section of reaction (2.4), $\sigma_{AB:}$

$$V_{coll} = \sigma_{AB} \bar{c}_{rel} \Delta t \qquad \text{(2.xviii)}$$

The collision cross-section is readily obtained from the effective radii of particles A and B, r_A and r_B respectively:

$$\sigma_{AB} = \pi (r_A + r_B)^2 \qquad \text{(2.xvix)}$$

The mean relative speed is given by:

$$\bar{c}_{rel} = \left(\frac{8 k_B T}{\pi \mu} \right)^{1/2} \qquad \text{(2.xx)}$$

where k_B is the Boltzmann constant and μ is the reduced mass of the two reacting species. The total A-B collision frequency, per unit time, therefore becomes:

$$Z_{AB} = \sigma_{AB} \left(\frac{8 k_B T}{\pi \mu} \right)^{1/2} L^2 [A][B] \qquad \text{(2.xxi)}$$

As discussed above, Simple Collision Theory states that species A and B will undergo reaction upon collision only if they posses sufficient energy. The fraction of particles with kinetic energy above a specific threshold ε is obtained from the normalised Boltzmann distribution function for energies, $f(E)$:

$$f(E) = \frac{1}{k_B T} \exp\left(\frac{-E}{k_B T}\right) \qquad \text{(2.xxii)}$$

Integrating the Boltzmann distribution function between the energy threshold ε and infinity results in the fraction, F, of molecules with kinetic energy above the threshold or activation barrier:

$$F = f(E > \varepsilon) = \frac{1}{k_B T} \int_{\varepsilon}^{\infty} \exp\left(\frac{-E}{k_B T}\right) dE = \exp\left(\frac{-\varepsilon}{k_B T}\right) \qquad \text{(2.xxiii)}$$

Combining the expressions for Z_{AB} and F, the reaction rate for an elementary bimolecular reaction (2.4) as predicted from Simple Collision Theory is therefore expressed as:

$$r_{2.4} = \sigma_{AB} \left(\frac{8k_B T}{\pi\mu}\right)^{1/2} L^2 [\mathrm{A}][\mathrm{B}] \exp\left(\frac{-\varepsilon}{k_B T}\right) \qquad \text{(2.xxiv)}$$

which is in the form of equation (2.vii) for an elementary process, $r = k[\mathrm{A}][\mathrm{B}]$. It therefore follows that the rate coefficient predicted by SCT is given by:

$$k = \sigma_{AB} \left(\frac{8k_B T}{\pi\mu}\right)^{1/2} L^2 \exp\left(\frac{-\varepsilon}{k_B T}\right) \qquad \text{(2.xxv)}$$

which is comparable in form to the empirical Arrhenius equation (2.xv).

Simple Collision Theory provides a reasonable qualitative description of the principal features of elementary bimolecular reactions and, notably, predicts the experimentally-observed exponential temperature dependence of rate constants, along with an account of the physical significance of the Arrhenius parameters. However, the comparison of experimental data against SCT theoretical calculations of reaction rates from equation (2.xxiv) shows that SCT usually tends to overestimate rate constants.[2] The discrepancies between experimental and theoretical results stem principally from the

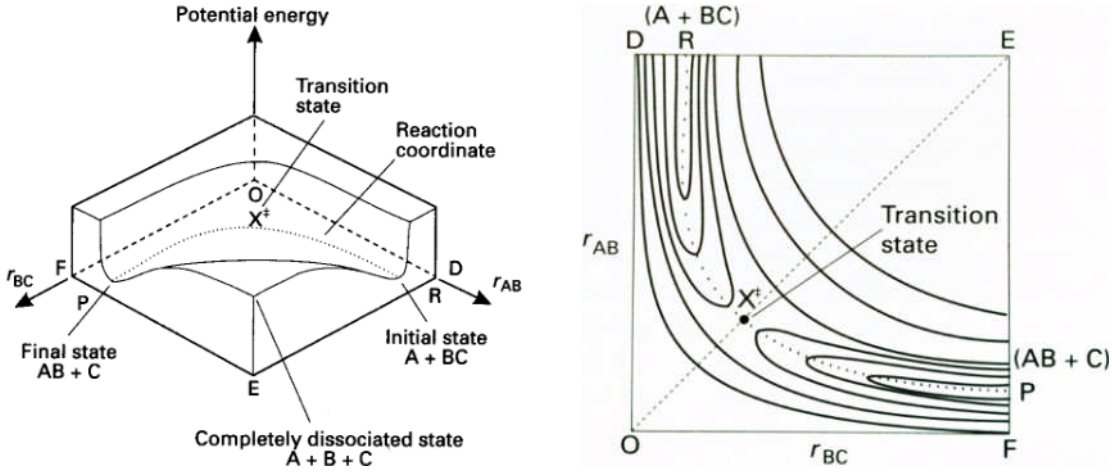

Figure 2.1 : Potential energy surface for the collinear reaction A + BC → AB + C shown in three dimensions (*left*) and as a contour plot (*right*). Taken from reference 2.

assumptions made in SCT. SCT treats particles as rigid spheres, ignores intermolecular forces and assumes that all particles with sufficient kinetic energy undergo reaction instantaneously upon collision. In most cases, however, the hard-sphere model is a poor approximation and neglects directional and steric requirements necessary for a collision to be reactive: as a result, only collisions with a certain orientation lead to reaction. Moreover, particles interact with one another over distances greater than the sum of their radii thanks to intermolecular forces. Finally, the changes in structure and electronic distribution brought about by the reaction are not instantaneous but actually take place over a finite period of time. [2]

Transition State Theory (TST), often also referred to as Activated Complex Theory (ACT), tries to address some of the limitations of SCT by modelling the events that take place during the reaction more realistically. To illustrate the fundamentals of this theory it is useful to refer to the collinear bimolecular reaction:

$$A + BC \rightarrow AB + C \qquad (2.5)$$

TST describes the reaction coordinate as a trajectory across the potential energy surface (PES) of the reaction, as shown in Figure 2.1. The PES is a function of both the A-B and the B-C co-ordinates. As A approaches BC, the potential energy of the system rises to a maximum at the saddle point of the PES: this point on the energy surface is called

the *transition state* and the configuration of the reactant/product entity at this point is referred to as the *activated complex*, $ABC^{‡}$. TST assumes that the activated complex exists in equilibrium with the reactants and that the transition state, once passed, cannot lead to the regeneration of the reagents but must proceed to form the products. Furthermore, TST treats the motion of the activated complex over the energy barrier as a classical process in which a single vibration of the activated complex, considered separable from all the other vibrational modes, is responsible for the bond fission equivalent to the motion over the barrier.

As TST postulates the existence of an equilibrium between reactants and activated complex, the overall reaction (2.5) can be written in terms of elementary steps as:

$$A + BC \quad \leftrightarrows \quad ABC^{‡} \qquad (2.6, -2.6)$$

$$ABC^{‡} \quad \rightarrow \quad AB + C \qquad (2.7)$$

It follows that the rate of product formation, reaction (2.7), is determined by the concentration of the activated complex and its decomposition rate. $[ABC]^{‡}$ can be obtained from the equilibrium constant for reactions (2.6, −2.6):

$$K^{‡} = \frac{[ABC]^{‡}}{[A][BC]} \qquad (2.xxvi)$$

The rate of product formation can therefore be expressed as:

$$\frac{d[AB]}{dt} = \frac{d[C]}{dt} = k^{‡}[ABC]^{‡} \qquad (2.xxvii)$$

where $k^{‡}$ is the rate constant for reaction (2.7). Substituting an expression for $[ABC]^{‡}$ obtained from equation (2.xxvi) into equation (2.xxvii) gives an expression for the rate of product formation in terms of $k^{‡}$, $K^{‡}$ and the reactant concentrations:

$$\frac{d[\mathrm{AB}]}{dt} = \frac{d[\mathrm{C}]}{dt} = k^{\ddagger}K^{\ddagger}[\mathrm{A}][\mathrm{BC}] \qquad \text{(2.xxviii)}$$

Determination of the bimolecular rate of reaction is therefore reduced to evaluating $k^{\ddagger}$ and $K^{\ddagger}$. The equilibrium constant $K^{\ddagger}$ can be expressed in terms of the total partition functions for species A, B and $ABC^{\ddagger}$ from statistical mechanics:

$$K^{\ddagger} = \left(\frac{Q^{\ddagger}_{\mathrm{ABC}}}{Q_{\mathrm{A}}Q_{\mathrm{BC}}}\right)\exp\left(-\frac{\Delta\varepsilon_0}{k_{\mathrm{B}}T}\right) \qquad \text{(2.xxix)}$$

where Q_i indicates the total partition function of species i and $\Delta\varepsilon_0$ is the energy difference between the ground states of the reagents and that of the activated complex. The total partition function Q is the product of the individual translational, rotational, vibrational and electronic partition functions calculated from statistical mechanics and spectroscopic data.

The total partition function for the activated complex can be separated into two components: one is the partition function for the reactive 'vibration', q, that takes the activated complex over the transition state, and the other is the partition function of the activated complex excluding the reactive vibration, $Q^{\ddagger}_{\mathrm{ABC}}{}'$:

$$Q^{\ddagger}_{\mathrm{ABC}} = qQ^{\ddagger}_{\mathrm{ABC}}{}' \qquad \text{(2.xxx)}$$

The partition function for the reactive vibration can be approximated to

$$q = \frac{k_{\mathrm{B}}T}{h\nu} \qquad \text{(2.xxxi)}$$

where ν is the vibrational frequency of the bond that is breaking. The expression for the equilibrium constant $K^{\ddagger}$, equation (2.xxix) therefore becomes:

$$K^{\ddagger} = \frac{k_{\mathrm{B}}T}{h\nu}\frac{Q^{\ddagger}_{\mathrm{ABC}}{}'}{Q_{\mathrm{A}}Q_{\mathrm{BC}}}\exp\left(-\frac{\Delta\varepsilon_0}{k_{\mathrm{B}}T}\right) \qquad \text{(2.xxxii)}$$

The rate constant for the decomposition of the activated complex into products, $k^{\ddagger}$, is identified as the frequency of the critical bond-breaking vibration, ν, leading to product formation:

$$k^{\ddagger} = \kappa\nu \qquad \text{(2.xxxiii)}$$

where κ is a transmission coefficient accounting for the fraction of critical vibrations that lead to product formation. The transmission coefficient can therefore have values between 0 and 1. Substituting expressions for $k^{\ddagger}$ and $K^{\ddagger}$ into equation (2.xxviii) returns an expression for the rate of reaction (2.5):

$$\frac{d[\mathrm{AB}]}{dt} = \frac{d[\mathrm{C}]}{dt} = \kappa \frac{k_{\mathrm{B}}T}{h} \frac{Q^{\ddagger}_{\mathrm{ABC}}{}'}{Q_{\mathrm{A}}Q_{\mathrm{BC}}} \exp\left(-\frac{\Delta\varepsilon_0}{k_{\mathrm{B}}T}\right)[\mathrm{A}][\mathrm{BC}] \qquad \text{(2.xxxiv)}$$

which, since reaction (2.5) is also an elementary process, is also in the form of rate = k[A][B]. Therefore the overall rate constant of reaction (2.5) is expressed as:

$$k_{2.5} = \kappa \frac{k_{\mathrm{B}}T}{h} \frac{Q^{\ddagger}_{\mathrm{ABC}}{}'}{Q_{\mathrm{A}}Q_{\mathrm{BC}}} \exp\left(-\frac{\Delta\varepsilon_0}{k_{\mathrm{B}}T}\right) \qquad \text{(2.xxxv)}$$

which compares qualitatively well with the Arrhenius equation. TST provides an effective way to calculate rate constants given that spectroscopic data on the species involved are available. However, spectroscopic data for activated complexes are usually scarce, as these are by definition transient species. Hence further assumptions have to be made to evaluate $Q^{\ddagger}_{\mathrm{ABC}}{}'$.

2.1.4 Unimolecular and Termolecular Rate Theories

Whilst pure bimolecular reactions exhibit no significant pressure dependence, both unimolecular and termolecular reactions are usually pressure dependent and their mechanisms involve an additional species, commonly denoted M.

Unimolecular reactions, such as isomerisation and dissociation processes, typically exhibit second order kinetics at low pressures (low [M]) and first order kinetics at high pressures (high [M]). A mechanism attempting to rationalise the observed kinetics of unimolecular reactions was first described by Lindemann.[3] The proposed kinetic scheme suggests that a general unimolecular reaction from the reagent A to products P:

$$A \quad = \quad P \qquad (2.8)$$

is not an elementary reaction but involves at least three steps. Initially, reagent A undergoes collision with any other molecule M to form an energised molecule, A*:

$$A + M \quad \rightarrow \quad A^* + M \qquad (2.9)$$

The fate of the energised molecule A* is either to be deactivated by an additional collision with M, or to undergo reaction and form the products:

$$A^* + M \quad \rightarrow \quad A + M \qquad (2.10)$$

$$A^* \quad \rightarrow \quad P \qquad (2.11)$$

The rate of product formation from this mechanism is given by:

$$\frac{d[\mathrm{P}]}{dt} = k_{2.11}[\mathrm{A}^*] \qquad (2.xxxvi)$$

Since A* is considered a reactive intermediate, the steady state approximation can be applied to the expression for the rate of formation and removal of A*:

$$\frac{d[\mathrm{A}^*]}{dt} = k_{2.9}[\mathrm{A}][\mathrm{M}] - k_{2.10}[\mathrm{A}^*][\mathrm{M}] - k_{2.11}[\mathrm{A}^*] \overset{SSA}{\approx} 0 \qquad (2.xxxvii)$$

Hence:

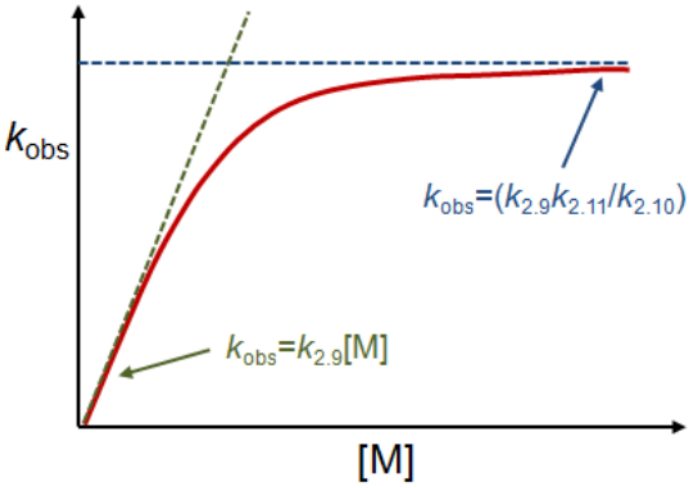

Figure 2.2 : Schematic diagram of the apparent first order rate coefficient, *k*, as a function of [M], for a unimolecular reaction A = P (reaction 2.8). The observed rate is second order at low pressures and tends to a limiting first order value at high pressures.

$$[A^*] = \frac{k_{2.9}[A][M]}{k_{2.10}[M] + k_{2.11}} \qquad (2.xxxviii)$$

Substituting the above expression for [A*] into equation (2.xxxvi) gives the following expression for the rate of product formation:

$$\frac{d[P]}{dt} = \frac{k_{2.9}k_{2.11}[A][M]}{k_{2.10}[M] + k_{2.11}} \qquad (2.xxxix)$$

At high pressures, and therefore high [M], the rate of deactivation of A* is much faster than product formation, *i.e.* $k_{2.10}[M] >> k_{2.11}$, so equation (2.xxxix) is approximated to:

$$\frac{d[P]}{dt} = \frac{k_{2.9}k_{2.11}}{k_{2.10}}[A] \qquad (2.xl)$$

which is first-order in A, as observed experimentally at high pressures. On the other hand, at low pressures, product formation dominates over deactivation of the energised molecule, hence $k_{2.10}[M] << k_{2.11}$. Under these conditions, equation (2.xxxix) approximates to:

$$\frac{d[\mathrm{P}]}{dt} = k_{2.9}[\mathrm{A}][\mathrm{M}] \qquad (2.\mathrm{xli})$$

which is evidently overall second order. The deviation of the rate of unimolecular reactions from first order kinetics is illustrated in Figure 2.2.

The Lindemann mechanism therefore gives a good qualitative account of the principal features of unimolecular reactions and agrees with experimental kinetic data at low pressure. However, the mechanism often fails to reproduce the rate constants measured experimentally at high pressures. The explanation for this lies in the 'realism' of the theory. Similarly to the limitations of Simple Collision Theory for bimolecular reactions, the Lindemann mechanism assumes that *all* energised molecules A*, if not deactivated, will undergo reaction. In reality, whilst the energised species has enough energy to react, this energy must be distributed appropriately within A* for the reaction to occur.

Rice Ramsperger [4] Kassel [5] Marcus [6] (RRKM) theory addresses this issue in an analogous fashion to how Transition State Theory improved on the limitations of Simple Collision Theory, as discussed above in Section 2.1.3. In this approach, the energised molecule A* is distinguished from the activated complex $A^{\ddagger}$ which represents the molecule 'poised for reaction', *i.e.* the molecule with sufficient energy localised in the required mode for the reaction to occur. [2] RRKM theory requires a rigorous analysis of the population of the rotational and vibrational states of A* and $A^{\ddagger}$ by means of statistical mechanics. The rate constants obtained *via* this method are often in good agreement with experimental data. The main limitation of RRKM theory lies in the fact that reliable thermodynamic data, necessary for the statistical mechanics calculations, are not available for a number of transient species; hence this method cannot be used unfailingly to predict the rate of reactions involving these species.

As with unimolecular reactions, the order of termolecular processes varies with pressure: experiments show that termolecular reactions are commonly second order at high pressure and third order at low pressure. This behaviour arises from the competition between the activation/deactivation and the dissociation of the energised

complex, [2] analogously to the mechanism outlined by Lindemann for unimolecular reactions.

The majority of termolecular processes are association reactions in which an excited adduct is initially formed. The extra energy from adduct formation either leads to the dissociation of the adduct back into the reagents or is collisionally transferred onto a third body, M. A reaction scheme similar to the Lindemann theory of unimolecular reactions can be then adopted:

$$A + B \rightarrow AB^* \quad (2.12)$$

$$AB^* \rightarrow A + B \quad (2.13)$$

$$AB^* + M \rightarrow AB + M \quad (2.14)$$

The rate of product formation is given by:

$$\frac{d[AB]}{dt} = k_{2.14}[AB^*][M] \quad (2.xlii)$$

The energised AB* adduct can be treated as a reactive intermediate using the steady state approximation. Hence the rate of AB* formation and removal is given by:

$$\frac{d[AB^*]}{dt} = k_{2.12}[A][B] - k_{2.13}[AB^*] - k_{2.14}[AB^*][M] \overset{SSA}{\approx} 0 \quad (2.xliii)$$

The concentration of AB* can be expressed rearranging the expression above:

$$[AB^*] = \frac{k_{2.12}[A][B]}{k_{2.13} + k_{2.14}[M]} \quad (2.xliv)$$

Substituting this expression for [AB*] into equation (2.xlii) gives an expression for the rate of product formation:

$$\frac{d[\mathrm{AB}]}{dt} = \frac{k_{2.12}k_{2.14}[\mathrm{A}][\mathrm{B}][\mathrm{M}]}{k_{2.13} + k_{2.14}[\mathrm{M}]} \qquad (2.\mathrm{xlv})$$

As with unimolecular reactions, the overall order is determined by the relative importance of the terms in the denominator of equation (2.xlv). At high pressures, $k_{2.14}[\mathrm{M}] >> k_{2.13}$, hence the equation (2.xlv) becomes:

$$\frac{d[\mathrm{AB}]}{dt} = k_{2.12}[\mathrm{A}][\mathrm{B}] \qquad (2.\mathrm{xlvi})$$

which is second order overall. Commonly, in the high pressure limit, $k_{2.12}$ is referred to as k_∞. On the other hand, in the limit of low pressures, $k_{2.13} >> k_{2.14}[\mathrm{M}]$, hence the rate of product formation can be simplified to:

$$\frac{d[\mathrm{AB}]}{dt} = \frac{k_{2.12}k_{2.14}}{k_{2.13}}[\mathrm{A}][\mathrm{B}][\mathrm{M}] \qquad (2.\mathrm{xlvii})$$

which is third order overall. The effective rate constant here, $(k_{2.12}k_{2.14})/k_{2.13}$, is often referred to as k_0 in the low pressure limit. The overall termolecular rate constant in equation (2.xlv) can then be re-written in terms of k_0, k_∞ and [M] as:

$$k_{\text{termolecular}} = \frac{k_0[\mathrm{M}]k_\infty}{k_0[\mathrm{M}] + k_\infty} \qquad (2.\mathrm{xlviii})$$

RRKM theory can be adapted to calculate termolecular rate constants. However, due to the paucity of thermodynamic data on the intermediates involved, the application of RRKM encounters many limitations. To overcome this issue, Troe [7] showed that multiplying equation (2.xlviii) by a "broadening factor" F can adequately parameterise termolecular rate coefficients from experimental studies over pressure regimes typical of the atmosphere:

$$k_{\text{Troe}} = \frac{k_0[\mathrm{M}]k_\infty}{k_0[\mathrm{M}] + k_\infty} \times F \qquad (2.\mathrm{il})$$

The broadening factor F is itself a function a function of k_0, k_∞ and [M]:

$$F = F_c \left\{ 1 + \left[\log_{10} \left(\frac{k_0[\mathrm{M}]}{k_\infty} \right) \right]^2 \right\}^{-1} \qquad (2.l)$$

The value of F_c is specific to each individual reaction; however, a value of $F_c = 0.6$ provides an adequate description of most atmospherically relevant termolecular reactions. [8]

2.1.5 Deviations from the Arrhenius Behaviour

Whilst the theories outlined in the preceding sections adequately account for the main features of bimolecular, unimolecular and termolecular gas phase reactions, anomalous behaviour is sometimes observed in reactions (especially) involving free radicals. These processes, for example, often proceed faster as the temperature is lowered: this negative temperature dependence of their rate constants is in stark contrast with the positive temperature dependence predicted by the Arrhenius equation (2.xv). Such behaviour is often attributed to the reversible formation of a reactive intermediate with a subsequent energetic barrier to the products that lies lower in energy than the energy of the reagent entrance channel, giving rise to an apparent "negative" activation energy. A number of atmospherically important reactions exhibit negative temperature dependence of reaction rates, making these reactions more efficient at the low temperatures encountered in the atmosphere. A more in-depth account of the negative temperature dependence arising from the specific features of the potential energy landscape is given in Section 2.3 with specific regard to halogen monoxide self- and cross-reactions.

The temperature dependence of the rate constant of a reaction is often presented as a plot of the natural logarithm of the rate constant, ln k, against reciprocal temperature, a so-called Arrhenius plot. It is clear, by simply taking the natural logarithm of both sides of equation (2.xv), that an Arrhenius plot obeying the Arrhenius equation should result in a straight line of gradient $-E_a/R$ and intercept ln A. Whilst this behaviour is observed

for the majority of bimolecular reactions, *curved* Arrhenius plots have also been reported. [9, 10, 11] In these anomalous cases, the Arrhenius plot is typically linear across a broad range of temperatures but curvature is observed at either the high-temperature end or the low-temperature end of the data set. Deviation from linearity at low temperatures in Arrhenius plots often arises from quantum tunnelling. It is known from quantum mechanics that a particle can appear on, *i.e.* tunnel through to, the other side of a potential energy barrier. The tunnelling rate becomes comparable to the reaction rate only at low temperatures, meaning that at such temperatures the reaction may proceed faster than expected and resulting in a positive curvature in the Arrhenius plot. [2] As the probability of tunnelling depends exponentially on the mass of the particle, this non-Arrhenius behaviour has been principally observed in reactions involving light species such as hydrogen atoms. [12, 13]

In other reactions, deviation from linear Arrhenius plots is observed at high temperatures. In these cases, non-Arrhenius behaviour can be explained in terms of the temperature dependence of the pre-exponential factor A. Both SCT and TST predict a temperature dependent pre-exponential factor. It is clear from the results of TST, as shown in equation (2.xxxv), that the variation of the partition functions of the reagents and the activated complex with temperature will also affect the pre-exponential factor. For instance, it can be envisaged that, at high temperatures, the vibrational partition function may become appreciable and could significantly alter the magnitude of the pre-exponential factor. Nonetheless, in most cases the temperature dependence of A is usually weak and dominated by that of the exponential term over the temperature ranges typically used in laboratory studies. [2] However, when A exhibits a strong temperature dependence and/or when long extrapolations of parameterised k are necessary, the Arrhenius equation can be modified by expressing the pre-exponential factor in terms of a power n of T:

$$k = A' T^{n} \exp\left(-\frac{E_{\mathrm{a}}}{RT} \right) \qquad (2.\mathrm{li})$$

2.2 Thermochemistry

2.2.1 Equilibration

In principle all chemical reactions are reversible; however in most cases the equilibrium concentration of the reactants is vanishingly small compared to that of the products and the reaction is said to "go to completion". In some cases however the equilibrium concentrations of reactants and products are both finite and measurable. In the case of a general reversible reaction, in elementary steps:

$$\mathrm{A} + \mathrm{B} \quad \leftrightarrows \quad \mathrm{C} \qquad (2.15, -2.15)$$

the rate of formation and removal of both reagents and products is expressed as:

$$-\frac{d[\mathrm{A}]}{dt} = -\frac{d[\mathrm{B}]}{dt} = k_{2.15}[\mathrm{A}][\mathrm{B}] - k_{-2.15}[\mathrm{C}] \qquad (2.\mathrm{lii})$$

$$\frac{d[\mathrm{C}]}{dt} = k_{2.15}[\mathrm{A}][\mathrm{B}] - k_{-2.15}[\mathrm{C}] \qquad (2.\mathrm{liii})$$

At equilibrium, the concentrations of A, B and C are by definition constant, therefore the rate of species formation and removal is equal to zero. Defining $[\mathrm{A}]_{eq}$, $[\mathrm{B}]_{eq}$ and $[\mathrm{C}]_{eq}$ as the equilibrium concentrations of A, B and C respectively, equations (2.lii) and (2.liii) can be re-written as:

$$-\frac{d[\mathrm{A}]_{eq}}{dt} = -\frac{d[\mathrm{B}]_{eq}}{dt} = k_{2.15}[\mathrm{A}]_{eq}[\mathrm{B}]_{eq} - k_{-2.15}[\mathrm{C}]_{eq} = 0 \qquad (2.\mathrm{liv})$$

$$\frac{d[\mathrm{C}]_{eq}}{dt} = k_{2.15}[\mathrm{A}]_{eq}[\mathrm{B}]_{eq} - k_{-2.15}[\mathrm{C}]_{eq} = 0 \qquad (2.\mathrm{lv})$$

By re-arranging either of the equations above, an expression for the equilibrium constant K_{eq} is obtained:

$$\frac{k_{2.15}}{k_{-2.15}} = \frac{[\mathrm{C}]_{\mathrm{eq}}}{[\mathrm{A}]_{\mathrm{eq}}[\mathrm{B}]_{\mathrm{eq}}} = K_{\mathrm{eq}} \qquad (2.\mathrm{lvi})$$

An example of how K_{eq} can be obtained from the kinetic analysis of temporal concentration profiles is illustrated in Section 4.2.4, with specific regard to the ClO dimerisation.

Equilibrium constants obtained from equation (2.lvi), for an equilibration such as that discussed above, are expressed in units of reciprocal concentration (K_c/cm^3 molecule^{-1}). For the purpose of this thermodynamic analysis, it is necessary to convert them into units of reciprocal pressure (K_p/atm^{-1}) according to the relationship:

$$K_{\mathrm{p}}/\mathrm{atm}^{-1} = 101325/\mathrm{Pa}\cdot 10^{-6}\cdot(K_{\mathrm{c}}/\mathrm{cm}^3\ \mathrm{molecule}^{-1})(k_{\mathrm{B}}T)^{\Delta n} \qquad (2.\mathrm{lvii})$$

where Δn is the mole change of the reaction; for the prototypical reactions (2.15, −2.15), $\Delta n = -1$. Equation (2.lvii) is obtained by relating the pressure to the concentration *via* the Ideal Gas Law. [14]

Equation (2.lvi) is extremely important as it relates a thermodynamic quantity (K_{eq}) to kinetic parameters (the forward and reverse rate constants). K_p (in units of reciprocal pressure) is also related to the standard Gibbs free energy change of reaction, $\Delta_r G°$, *via*:

$$\ln K_{\mathrm{p}} = -\frac{\Delta_{\mathrm{r}} G°}{RT} \qquad (2.\mathrm{lviii})$$

$\Delta_r G°$ is in turn linked to the standard enthalpy change of reaction $\Delta_r H°$ *via* the Gibbs-Helmholtz equation, in the form:

$$\frac{d\left(\Delta_{\mathrm{r}} G°/T\right)}{dT} = -\frac{\Delta_{\mathrm{r}} H°}{T^2} \qquad (2.\mathrm{lix})$$

Differentiation of $\ln K_p$ in equation (2.lviii) with respect to temperature gives:

$$\frac{d\left(\ln K_{\mathrm{p}}\right)}{dT} = -\frac{1}{R}\frac{d\left(\Delta_{\mathrm{r}}G^{\circ}/T\right)}{dT} \tag{2.lx}$$

Substituting the Gibbs-Helmholtz equation (2.lix) into equation (2.lx) and integrating results in the van't Hoff equation, which relates the equilibrium constant to the change in enthalpy of reaction:

$$\frac{d\left(\ln K_{\mathrm{p}}\right)}{dT} = \frac{\Delta_{\mathrm{r}}H^{\circ}}{RT^{2}} \tag{2.lxi}$$

The van't Hoff equation can similarly be derived from the definition of the standard change in Gibbs free energy:

$$\Delta_{\mathrm{r}}G^{\circ} = \Delta_{\mathrm{r}}H^{\circ} - T\Delta_{\mathrm{r}}S^{\circ} \tag{2.lxii}$$

where $\Delta_{\mathrm{r}}S^{\circ}$ is the standard entropy change of reaction. Combination of equations (2.lviii) and (2.lxii) results in another expression for the van't Hoff equation:

$$\ln K_{\mathrm{p}} = -\frac{\Delta_{\mathrm{r}}H^{\circ}}{R}\frac{1}{T} + \frac{\Delta_{\mathrm{r}}S^{\circ}}{R} \tag{2.lxiii}$$

It is important to note how equation (2.lxi) can be obtained simply by differentiating equation (2.lxiii) with respect to temperature, assuming that $\Delta_{\mathrm{r}}H^{\circ}$ and $\Delta_{\mathrm{r}}S^{\circ}$ are independent of temperature. Thanks to the van't Hoff equation the study of equilibrium constants as a function of temperature allows probing of the energetics and therefore of the potential energy surface of a number of equilibration reactions, as discussed in the following section.

2.2.2 Second Law and Third Law Analyses

The characterisation of equilibrium constants as a function of temperature constitutes a valuable method to investigate the energetics of equilibration. It is clear from equation (2.lxiii) that a plot of $\ln K_{\mathrm{p}}$ against reciprocal temperature, a so-called van't Hoff plot,

should result in a straight line of gradient $-\Delta_r H°/R$ and intercept $\Delta_r S°/R$, assuming that $\Delta_r H°$ and $\Delta_r S°$ are temperature-independent. Extraction of the thermochemical parameters from a linear fit to the van't Hoff plot is known as a *Second Law* analysis.

On the other hand, a so-called Third Law analysis relies on constraining the entropic term in equation (2.lxiii) from calculations of the standard entropies of reagents and products of the equilibration. In this way $\Delta_r H°$ can be calculated by simply rearranging the van't Hoff equation:

$$\Delta_r H°(T) = -RT \ln K_p(T) + T\Delta_r S°(T) \qquad (2.lxiv)$$

The Third Law analysis is typically more rigorous since it accounts for the temperature dependence of $\Delta_r H°$ and $\Delta_r S°$. Since K_p and the calculated $\Delta_r S°$ are both temperature dependent, the resulting $\Delta_r H°$ is also temperature dependent. $\Delta_r S°$ is calculated from standard entropies using the Third Law of thermodynamics:

$$\Delta_r S° = \sum_Q \nu_Q S°(Q) \qquad (2.lxv)$$

where ν_Q is the stoichiometric number of chemical species Q (negative for reagents, positive for products) and $S°(Q)$ is the standard entropy of any species Q calculated from statistical mechanics. The standard reaction entropy $\Delta_r S°$ is therefore defined as the difference between the entropies of the pure separated products and those of the pure separated reactants. [15] Hence, for reactions (2.15, −2.15):

$$\Delta_r S° = S°(C) - \{S°(A) + S°(B)\} \qquad (2.lxvi)$$

$S°(A)$, $S°(B)$ and $S°(C)$ are calculated from the sum of the contributions to the total molecular standard entropy from the translational, rotational, vibrational and electronic partition functions. These entropy calculations require a number of physical parameters of the molecules (*e.g.* molecular moments of inertia, rotational constants, vibrational constants, energies of electronic states) to be known.

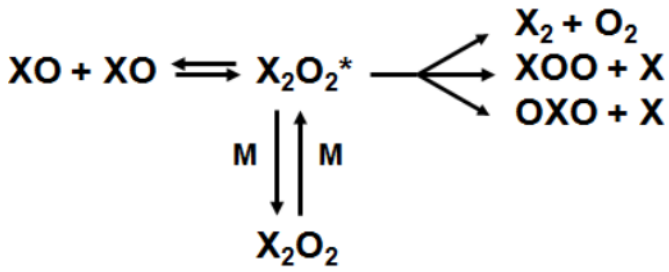

Figure 2.3 : Diagram illustrating the intermediates and *known* multiple product channels of a general XO + XO reaction.

2.3 Halogen oxide self- and cross-reactions: a mechanistic approach

Halogen monoxide self- and cross-reactions possess many of the kinetic features described in this chapter as they are complex multichannel processes, with both bimolecular and termolecular components contributing to the overall reaction. Halogen monoxide self- cross-reactions can be represented as:

$$XO + XO \rightarrow \text{products} \qquad (2.16)$$

$$XO + YO \rightarrow \text{products} \qquad (2.17)$$

where X and Y represent halogen atoms and X ≠ Y. As shown diagrammatically in Figure 2.3, a typical XO + XO self-reaction proceeds through the formation of an excited intermediate X_2O_2* (XYO_2* in the case of the cross-reactions) that can either dissociate to re-form the reactants or proceed to generate the products. Formation of the excited intermediate X_2O_2* from the two XO free radicals is typically a barrierless process and gives rise to an energy well in the potential energy surface (PES) of the reaction as shown in Figure 2.4. Collision with a third body M may then lead to formation of a stable adduct; the energy difference between the reagents and the stabilised adduct is the change in enthalpy (ΔH) for this product formation. Alternatively, the excited intermediate may overcome an energy barrier arising from structural and energetic rearrangement leading to the products of the 'bimolecular' (pressure independent) channels. The height of this energy barrier with respect to the energy of the entrance channel of reaction is the activation energy (E_a) to the

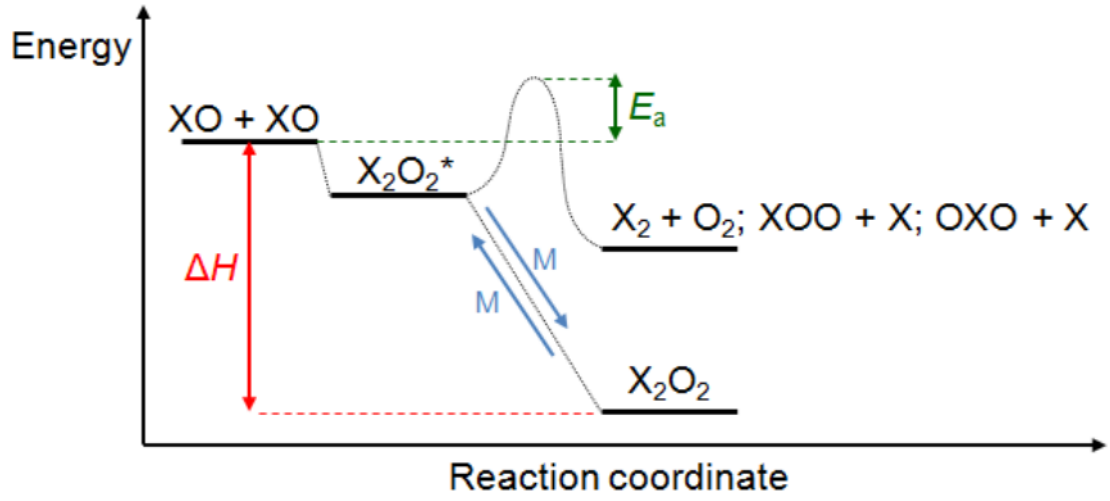

Figure 2.4 : Schematic representation of the potential energy surface of an XO + XO self-reaction. ΔH indicates the change in enthalpy of adduct (X_2O_2) formation and E_a the activation energy barrier to the bimolecular products (see text).

bimolecular channels and this barrier may actually exist at a lower energy than that of the entrance channel, leading to a negative temperature dependence of the rate constants as a result of a negative effective E_a as discussed in Section 2.1.5 above. Moreover, as halogen monoxide self- and cross-reactions possess multiple bimolecular channels, each of them has its own activation energy barrier. For clarity, only one energy barrier is shown in Figure 2.4. The partitioning between the termolecular stabilisation of the adduct and the formation of the bimolecular products depends profoundly on the PES of a specific halogen oxide self- or cross-reaction; more specifically, it is also controlled by the energetics of the formation of a stable X_2O_2 species (ΔH) and the size of the energy barrier leading to the bimolecular products relative to the entrance channel (E_a).

Termolecular association of XO + XO (or YO) into X_2O_2 (or XYO_2) commonly exhibits a negative temperature dependence. This behaviour arises from the interaction between collisional stabilisation of the excited intermediate and the lifetime of the intermediate itself. The lifetime of the intermediate depends critically on its internal energy, which is in turn dictated by the kinetic energy of the reagents: at high temperatures the reagents possess high kinetic energy and the lifetime of the intermediate is short so that it is more likely to dissociate back into the reagents before stabilisation. [2]

The temperature dependence of the bimolecular channels is somewhat more complex and depends critically on the magnitude of the activation energy barrier relative to the entrance channel. When the activation barrier to the bimolecular products lies higher in energy than the entrance channel, as shown in Figure 2.4, E_a is positive and the reaction exhibits a positive temperature dependence, as illustrated previously in Section 2.1.2. On the other hand, if the activation barrier to the bimolecular products lies lower in energy than the entrance channel, E_a is effectively negative and the rate of reaction is dictated by the lifetime (hence stability) of the excited intermediate, as discussed for the termolecular channels above and in Section 2.1.5, giving rise to a negative temperature dependence.

2.4 Computational Methods

The preceding discussion outlined the theories and mechanistic interpretation of gas phase kinetic data from an experimental point of view. However, with greater computational power available, theoretical methods have become increasingly adopted to calculate rate constants from first principles and to gain valuable mechanistic insight on specific reactions. These methods typically complement experimental work, and are sometimes used to investigate reactions that are particularly difficult to study in the laboratory. A detailed description of these techniques is beyond the scope of this thesis, however a brief summary is given in this section.

The starting point of all computational calculations of reaction rate constants is the characterisation of the potential energy surface (PES) for the reaction system of interest.[2, 16] As shown previously in Figure 2.1, a reaction can be described as a trajectory across the potential energy surface specific to that process. PESs are typically calculated using either *semi-empirical* or *ab initio* methods. In the former, an empirical function describing the reaction PES is fitted to existing experimental data, such as the activation energy of reaction, by optimising some adjustable parameters. In the latter, the Schrödinger equation is solved numerically from *first principles* of quantum mechanics: *ab initio* methods therefore provide information on the reaction of interest effectively *independently* of experiments (hence the name). An exact solution to the Schrödinger equation is however only available for the simplest molecular systems; for more

complex systems, several methods have been developed to approximate to a solution to the Schrödinger equation. The majority of these methods rely upon approximating the electronic structure of the system of interest to a linear combination of mathematical functions (the *basis set*). As the basis set and the corrections for effects not accounted for by the basis set (*e.g.* electron correlation) become more complex and sophisticated, the quality and computing cost of these calculations increase markedly for realistic systems.

Once the PES has been calculated, transition state theory (TST) can be used to calculate rate constants. As discussed previously at the end of Section 2.1.3, one of the major limitations of TST is the lack of knowledge of molecular parameters for the activated complex necessary to calculate its partition function and, consequently, the rate constant *via* equation (2.xxxv). These parameters are extremely difficult to measure experimentally on account of the transience of the activated complex but can be obtained readily from *ab initio* methods. Following calculation of the desired PES, the geometry of the activated complex is obtained by locating the saddle point on the PES. Furthermore, the shape of the PES at the saddle point allows determination of the vibrational frequencies of the activated complex. [2]

Alternatively, quasi-classical trajectory methods can also be used to determine the rate constants. After characterisation of the PES, collisions are simulated by computationally solving classical equations for the relative motions of nuclei for particular starting conditions.

2.5 Photochemistry

The interaction of radiation with matter is of fundamental interest in the physical and natural sciences. More specifically, with respect to the Earth's atmosphere, absorption of solar radiation can bring about significant chemical change as the energies of the photons emitted by the sun, principally in the visible and UV domains of the spectrum, as described in Chapter 1, are similar in magnitude to molecular bond strengths. Ultimately solar radiation initiates most of the chemistry occurring in the Earth's atmosphere. Furthermore, absorption of photons also provides the basis for a number of

powerful analytical methods, including the detection technique employed in the present work (UV absorption spectroscopy). The principles governing the absorption of photons and the fate of the resulting excited species are therefore discussed in this section.

2.5.1 Absorption

The infinitesimal attenuation of intensity, *dI*, occurring when light passes through a sample of infinitesimal thickness *dl* containing an absorbing species at a concentration *c* is equal to:

$$dI = -I \cdot \sigma \cdot c \cdot dl \tag{2.lxvii}$$

where σ is the absorption cross-section of the absorbing species. Separating the variables gives:

$$\frac{dI}{I} = -\sigma \cdot c \cdot dl \tag{2.lxviii}$$

Thus the intensity I_t that emerges from a sample of thickness l when the intensity of the incident light is I_0 is obtained by integrating equation (2.lxviii):

$$\int_{I_0}^{I_t} \frac{dI}{I} = -\sigma \int_0^l c \cdot dl \tag{2.lxix}$$

If the concentration of the absorber is uniform, c is independent of pathlength and equation (2.lxix) integrates to:

$$\ln\left(\frac{I_0}{I_t}\right) = \sigma \cdot c \cdot l \tag{2.lxx}$$

Equation (2.lxx) is an expression for the Beer-Lambert Law, which can be used to define the extent of absorption of a sample, quantified by the absorbance A_λ, at wavelength λ, as follows:

$$A_\lambda = \ln\left(\frac{I_{0,\lambda}}{I_{t,\lambda}}\right) \qquad \text{(2.lxxi)}$$

where $I_{0,\lambda}$ is the intensity of the incident light at wavelength λ and $I_{t,\lambda}$ the light intensity at wavelength λ transmitted through a sample of the species of interest. In many cases more than one absorber is present in the sample; as absorbance is additive, the Beer-Lambert Law can be then conveniently written as:

$$A_\lambda = \sum_i \sigma_{i,\lambda} \cdot l \cdot [i]_t \qquad \text{(2.lxxii)}$$

where i labels each of the absorbers present in the sample. The Beer-Lambert Law governs the attenuation of incoming solar radiation by atmospheric species and it is also fundamental to experimental absorption spectroscopy. In atmospheric science, the Beer-Lambert Law is used in both laboratory studies and field measurements alike to quantify the concentrations of atmospherically important gases, provided that the absorption cross-sections of these species are known.

Absorption cross-sections are critically wavelength-dependent and determine the extent of absorption by a species at a particular wavelength. Absorption occurs when the energy of the incident photon corresponds to the energy difference between electronic, vibrational or rotational levels (or all three) within a molecule. Consequently, depending upon the wavelength of the incident radiation, the absorption of photons may result in the electronic, vibrational or rotational excitation of species. Wavelengths in the ultraviolet and visible regions of the spectrum, typical of incoming solar radiation and of the emission of analysis lamps commonly used in absorption spectroscopy, give rise to electronic transitions in molecules. The shape and the magnitude of absorption cross-sections in the UV/visible region of the spectrum can be rationalised by invoking the Franck-Condon principle, as discussed below.

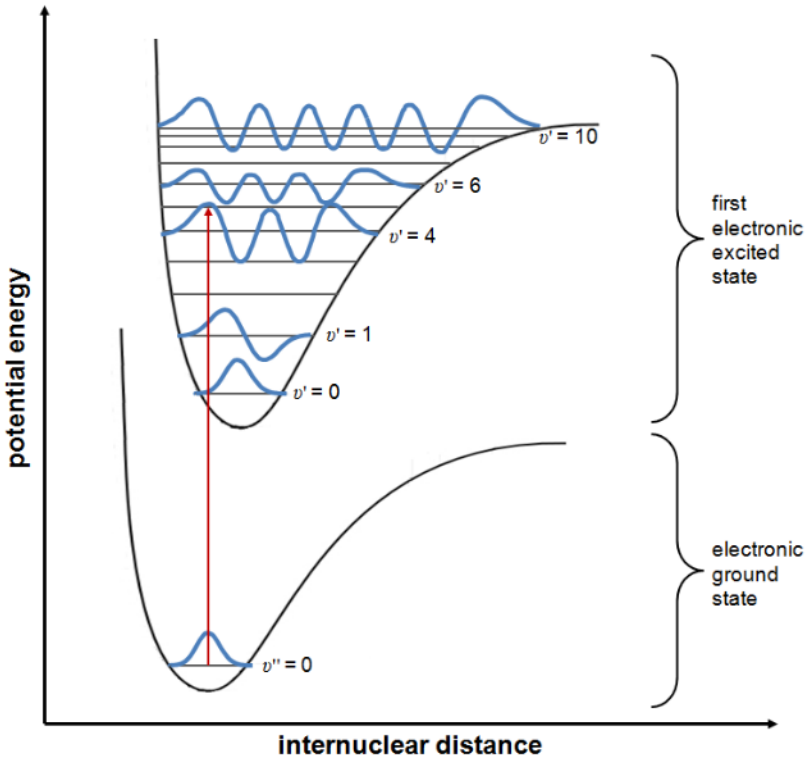

Figure 2.5 : Diagram illustrating the quantum mechanical version of the Franck-Condon principle for an electronic transition in a diatomic molecule. The most intense transition is the one to an upper vibrational level ($\upsilon' = 4$ in this case), the wavefunction of which has the greatest overlap integral with that of the ground state ($\upsilon'' = 0$).

According to the Franck[17]-Condon[18] principle, electronic excitation of molecules on photon absorption occurs on a much faster timescale than molecular vibration and, throughout the electronic transition, the nuclei can be considered stationary. As a result, the electronic transition from the electronic ground state to the electronic excited state can be represented as a vertical line in a plot of potential energy against internuclear distance, as shown in Figure 2.5 for a diatomic molecule. Furthermore, if the upper state is bound, a number of vibrational levels can be populated upon electronic excitation. The Franck-Condon principle states, in classical terms, that the most favoured transition is the one from the vibrational ground state of the electronic ground state (typically $\upsilon'' = 0$ at ambient temperature) to the vibrational level vertically above it in the first electronic excited state that most resembles the geometry of the ground state, as the transition occurs without change in the nuclear geometry. In quantum mechanical terms, the molecule is most likely to be excited to the upper vibrational level that most closely resembles the vibrational wavefunction of the vibrational ground state of the

electronic ground state, *i.e.* to an upper level with a wavefunction with the greatest "overlap integral" to that of the ground state, [15] as illustrated in Figure 2.5. However, the favoured excited vibrational state is not the only accessible level in the upper electronic state, as many other vibrational levels have appreciable overlap integrals of their wavefunctions with that of the ground state (*i.e.* similar geometry to the ground state). Therefore transitions occur to a number of vibrational levels and a *vibronic progression* is observed in the resulting spectrum, with the most favoured transition being the most intense.

The absorption cross-sections of many atmospherically important species, including many halogen oxides, exhibit vibronic bands. The spectrum of the chlorine monoxide radical, ClO, illustrated in Figure 2.6, shows distinctive vibronic features as well as a continuum absorption at $\lambda < 265$ nm. The observed vibronic progression can be accounted for by referring to the potential energy diagram shown in Figure 2.7. On the other hand, the unstructured part of the ClO spectrum arises from excitation above the dissociation threshold of the upper electronic state. This smooth, continuum absorption is also observed when the electronic transition occurs from the ground state to an unbound (dissociative or repulsive) upper state. In this case the molecule dissociates

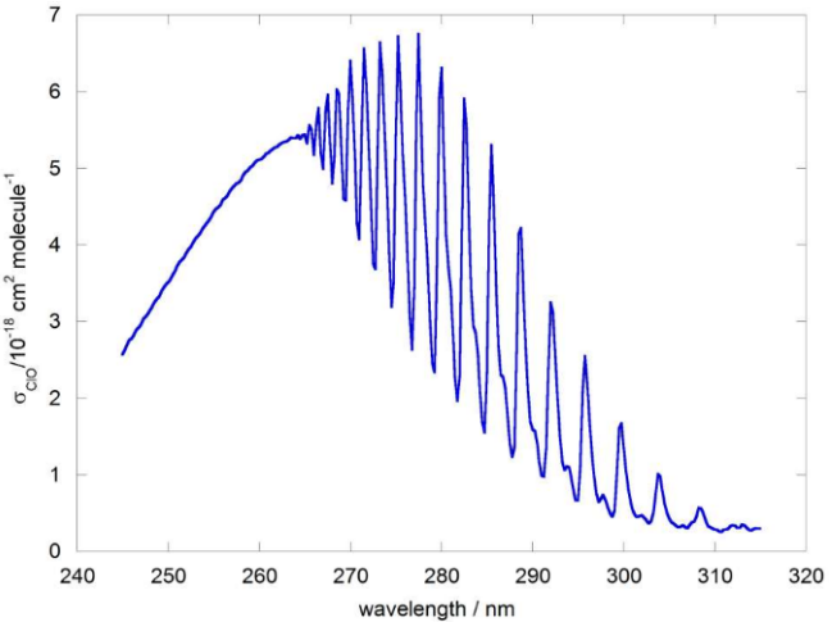

Figure 2.6 : Absorption cross-section of the ClO radical, measured at $T = 298$ K and at a spectral resolution of 0.1 nm (FWHM). From reference 19.

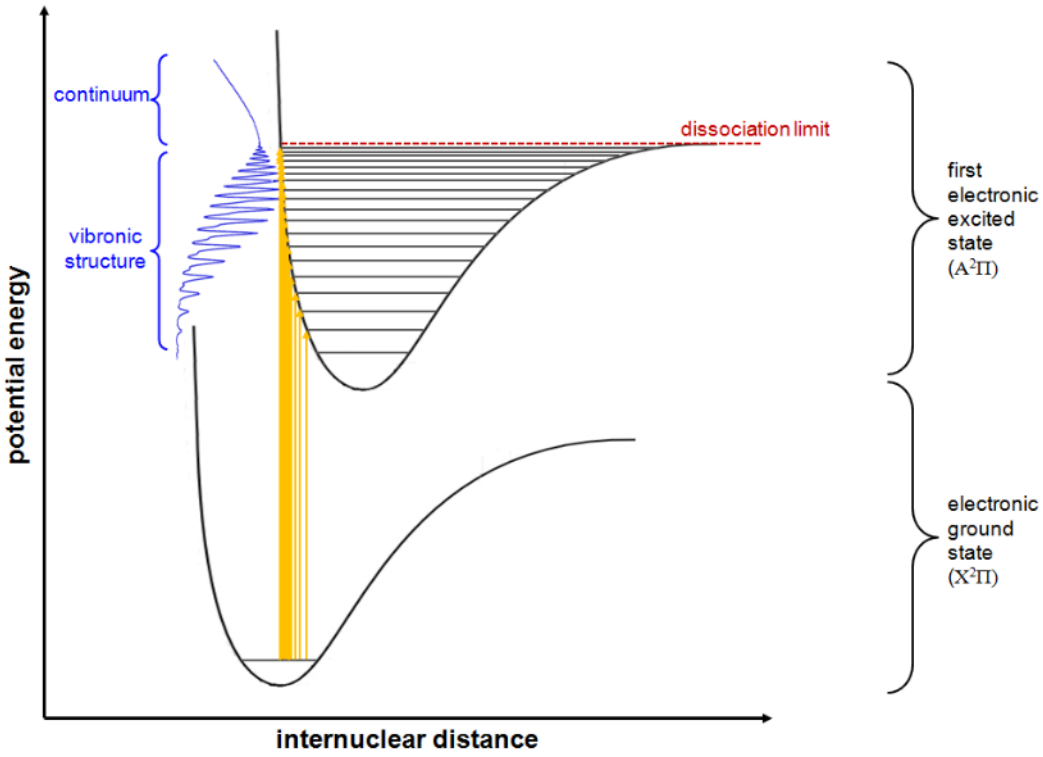

Figure 2.7 : Schematic potential energy diagram for the electronic excitation of ClO from the electronic ground state ($X^2\Pi$) to the first electronic excited state ($A^2\Pi$) showing the transitions giving rise to the observed vibronic progression.

upon absorption and the cross-section is a broad, continuous band devoid of structured features at all wavelengths as the excited state is ultimately represented by the unquantised translational motion of the fragments [15] and the shape of the spectrum largely reflects that of the wavefunction of the ground state.

2.5.2 Fate of Excited Species

Following absorption, an electronically excited species can undergo a number of processes: it can re-emit radiation *via* luminescence (*fluorescence* or *phosphorescence*), redistribute its energy internally *via* non-radiative transitions or transfer its newly acquired energy to another molecule *via* collision (*quenching*).

Electronically excited species often exhibit different chemical reactivity from the ground state species: for instance, reactions of electronically excited species can

proceed at faster rates than those involving ground state counterparts. In some cases, reactions that do not occur for ground state species become accessible to electronically excited species; for instance, the electronically excited oxygen atom, $O(^1D)$, is known to react with many atmospheric species unlike ground-state oxygen atoms, $O(^3P)$, as discussed in Chapter 1.

In molecules, electronic excitation following absorption of a photon can also lead to fragmentation. The resulting photodissociation is of particular interest in atmospheric science as it leads to the formation of free radicals and atomic species that are typically highly reactive and play crucial roles in the atmosphere. Dissociation can occur when a molecule is excited to a repulsive (non-bonding) upper electronic state, or when it is excited above the highest vibrational level (dissociation threshold) of an upper bound state, as discussed in Section 2.5.1. An alternative mechanism for photodissociation, called predissociation, arises when absorption to an upper bound state is followed by an internal conversion (IC) or inter-system crossing (ISC) to a repulsive state leading to molecular fragmentation. [20]

The rate coefficient for solar photodissociation for a given species x, J_x, is defined as:

$$J_x = \int_0^\infty I_\lambda \sigma_{x,\lambda} \Phi_{x,\lambda} d\lambda \qquad \text{(2.lxxiii)}$$

where I_λ is the intensity of the incident solar radiation at wavelength λ, $\sigma_{x,\lambda}$ is the absorption cross-section of species x at wavelength λ and $\Phi_{x,\lambda}$ is the quantum yield for photodissociation of species x at wavelength λ. The quantum yield for photodissociation is defined as the number of molecules decomposed for each quantum of radiation absorbed and can therefore assume values between 0 and 1. [20] Equation (2.lxxiii) allows calculation of the photolysis rate of atmospherically relevant species given that I_λ, $\sigma_{x,\lambda}$ and $\Phi_{x,\lambda}$ may be measured. Absorption cross-sections and quantum yields are measured in laboratory studies, whereas the wavelength-resolved intensity of solar radiation can be obtained from computer models that include processes such as absorption of solar radiation by other species in the atmosphere (principally O_2 and O_3), light scattering and surface albedo, or measured in the field using radiometers.

2.5 Concluding Remarks

Theories of gas-phase kinetics, thermochemistry and photochemistry provide valuable insights into the mechanism and therefore role of atmospheric physical and chemical processes. In order to test these theories against experiments, techniques capable of monitoring the concentrations of species as a function of time are necessary. Principles of such experiments used to study gas phase reaction kinetics and photochemistry are discussed in the following chapter.

2.6 References

1. S. Arrhenius, *Z. Physik. Chem.*, **1889**, 4, 226
2. M.J. Pilling, P.W. Seakins, *Reaction Kinetics*, **1995**, Oxford University Press, Oxford, United Kingdom
3. F.A. Lindemann, *Trans. Farad. Soc.*, **1921**, 17, 598
4. O.K. Rice, H.C. Ramsperger, *J. Am. Chem. Soc.*, **1927**, 49, 1617
5. L.S. Kassel, *J. Phys. Chem.*, **1928**, 32, 255
6. R.A. Marcus, *J. Chem. Phys.*, **1952**, 20, 359
7. J. Troe, *J. Chem. Phys.*, **1977**, 66, 4745
8. S.P. Sander, J. Abbatt, J. R. Barker, J.B. Burkholder, R.R. Friedl, D.M. Golden, R.E. Huie, C.E. Kolb, M.J. Kurylo, G.K. Moortgat, V.L. Orkin, P.H. Wine, *Chemical Kinetics and Photochemical Data for Use in Atmospheric Studies*, Evaluation No. 17, **2011**, JPL Publication 10-6, Jet Propulsion Laboratory, Pasadena, United States, http://jpldataeval.jpl.nasa.gov
9. R. Zellner, W. Steinert, *Int. J. Chem. Kin*, **1976**, 8, 397
10. R.R. Baldwin, R.W. Walker, *J. Chem. Soc. Farady. Trans.*, **1979**, 75, 140
11. J. Braun, R. Schwesinger, P.G. Williams, H. Morimoto, D.E. Wemmer, H.H. Limbach, *J. Am. Chem. Soc.*, **1996**, 118, 11101
12. V.I. Goldanskii, *Ann. Rev. Phys. Chem.*, **1976**, 27, 85
13. V.I. Goldanskii, *Nature*, **1979**, 279, 109
14. S.W. Benson, *Thermochemical Kinetics*, **1968**, Wiley and Sons, New York, United States

15. P. Atkins, J. De Paula, Atkins' Physical Chemistry, 7th Edition, 2002, Oxford University Press, Oxford, United Kingdom
16. M.J. Pilling, I.W.M. Smith, *Modern Gas Kinetics: Theory, Experiment and Application*, **1987**, Blackwell Scientific Publications, Oxford, United Kingdom
17. J. Franck, *Trans. Faraday Soc.*, **1926**, 21, 536
18. E.U. Condon, *Physic. Rev.*, **1928**, 32, 858
19. Sander, S. P.; Friedl, R. R. *J. Phys. Chem.* **1989**, 93, 4764-4771
20. R.P. Wayne, Chemistry of Atmospheres, 3rd Edition, **2000**, Oxford University Press, Oxford, United Kingdom

Chapter 3
Laser Flash Photolysis with UV/visible Absorption Spectroscopy

Reactions involving free radicals are commonplace in atmospheric chemistry. As these highly reactive species have notoriously short lifetimes, studies of radical reaction kinetics in the laboratory must satisfy a number of requirements. First, the start of the reaction must be well-defined in time, and secondly, a monitoring technique able to respond quickly to changes in concentration of the species involved must be employed. The reaction of interest also needs to be studied under suitable atmospheric conditions of, notably, temperature and pressure.

The flash photolysis technique, coupled with UV/visible absorption spectroscopy, satisfies a number of these requirements. The experiments on halogen monoxide self- and cross-reactions described in this thesis were performed using a laser flash photolysis/UV absorption system incorporating, uniquely, charge-coupled device (CCD) detection. In this chapter, the principles and the historical development of this technique are presented, followed by a description of the experimental apparatus and the analytical procedure used to extract kinetic information from the data recorded.

3.1 Flash Photolysis/UV Absorption Spectroscopy

3.1.1 Principles

The technique of flash photolysis relies on the rapid generation (relative to the timescale of their subsequent reactions) of reactive species (radicals and/or atoms) and on monitoring their concentration as a function of time. An intense, short-lived pulse of light (the "flash") initiates the desired reaction within a pre-mixed gas mixture containing the precursor gases carried in an unreactive, usually inert carrier flow. The radicals of interest are formed *in situ* either from the direct photolysis of a precursor species or from chemical reactions initiated by the photolysis of precursor gases and subsequent reaction of these photolysis products with another reagent. The concentrations of reactants and/or products as a function of time are monitored in real time using UV/visible absorption spectroscopy. Analysis of the decay or build-up

concentration profiles of the species monitored provides information on the kinetics of the reaction studied.

One of the essential requirements for a flash photolysis experiment is that the radical generation step must occur on a much smaller timescale than the subsequent chemistry so that the two events are entirely temporally decoupled and radical generation does not interfere with the kinetics of the subsequent reaction of interest. This is achieved by using intense light pulses operating on very rapid timescales and by careful design of experimental conditions. High-voltage flashlamps (with microsecond output) or lasers (with nanosecond output) are generally employed to provide the photolytic pulse; the differences between the two photolysis sources are discussed further below in Section 3.3.2.

Another crucial requirement to study radical reactions is for the detection technique to be not only sufficiently fast in order to respond to rapidly changing concentrations, but also to be sensitive enough to monitor changes in trace species abundances. A number of optical methods satisfy these criteria, including absorption and fluorescence spectroscopy. UV/visible absorption spectroscopy is particularly advantageous: as the electronic transitions of many gas-phase radicals occur in the UV/visible region of the electromagnetic spectrum, species of interest exhibit distinct spectra and absorption spectroscopy therefore also ensures unequivocal identification of species in the reaction mixture.

Flash photolysis also overcomes many of the problems associated with other techniques often used in the study of radical reactions, notably flow methods, typically associated with mass spectrometry detection. Such methods rely on the separate generation of reactive species in fast gas flows, on their mixing and their detection after an elapsed interaction time. To achieve sufficiently fast linear flow velocities these techniques usually require low pressures (generally $p < 10$ Torr) within the flow tube. By contrast, in the flash photolysis experiment, pre-mixing of the gas mixture ensures that the precursor species are uniformly mixed *before* the reaction is initiated and therefore data can be collected over a wide range of pressures (typically $p > 50$ Torr), more characteristic of the lower atmosphere. Furthermore, such higher pressures minimise

heterogeneous loss of reactive species to the cell walls, which is on the contrary frequent at the low pressures typical of flow methods.

The principal limitations of the flash photolysis with UV absorption technique arise from the need for the rapidity and sensitivity of the detectors employed and their wavelength coverage. The historical development of this technique reflects the attempts made at addressing these issues, as described in the following section.

Figure 3.1 : Time-resolved transmission spectra recorded on photographic plates showing the characteristic absorption features of the ClO radical. Reproduced from reference 1.

3.1.2 History of Flash Photolysis

The flash photolysis technique was first developed by Norrish, Porter and co-workers in Cambridge in the late 1940s and early 1950s. [2, 3] In these experiments, photolytic pulses emitted by rare-gas flashlamps initiated the reaction of interest; after a certain delay, a second lamp provided a probe light pulse which was passed through the reaction vessel. Light transmitted through the reaction mixture was focused into a spectrograph, giving rise to wavelength resolved signals recorded on photographic plates situated in the dispersive plane of the spectrograph. These were converted manually into absorptions by measuring the degree of darkening across the photographic plates compared to an

exposure collected without a photolytic pulse. A temporal absorption profile was therefore obtained by repeating experiments with different time intervals between the photolytic and the probe pulses. An example of recorded photolysis spectra is given in Figure 3.1. These early studies provided the first evidence for the existence of many free radical species, including the ClO radical, and the Nobel Prize for Chemistry was awarded to Norrish and Porter in 1967 for their ground-breaking work on flash photolysis.

The advent of electronic detectors such as photomultiplier tubes (PMTs) in the 1960s enabled continuous, rapid real-time monitoring of the light transmitted through a reaction vessel for the first time so that an entire concentration profile could be generated in a single flash photolysis experiment. As a result, the probe pulse used in the early flash photolysis experiments was replaced with the output from continuous analysis lamps. However, due to the inability of PMTs to discriminate between photons arriving at different positions on the detector window coupled with the physical size of the detector window relative to the dispersion plane of available spectrographs, wavelength discrimination was lost. This limitation compromised the ability to discern between multiple species with overlapping absorptions in the reaction mixture and was partially overcome by either correcting the measured absorbance to account for the presence of other known or modelled absorbers or by repeating experiments at different wavelengths to build a time-resolved absorption spectrum of the reacting mixture.

The development of photodiode arrays in more recent years has enabled the electronic monitoring of transmitted light intensity as a function of both time and wavelength. These detectors consist of a row of small, light-sensitive elements (pixels), which can be aligned along the dispersive axis of a spectrograph. The wide wavelength coverage allows the monitoring of entire absorption bands rather than single wavelengths, resulting in an unequivocal and therefore more accurate determination of species concentrations and improved signal-to-noise ratio. However the temporal resolution of a photodiode array is dictated by the readout time of the device: with a single output amplifier, pixels are read out sequentially. This is typically on a timescale of milliseconds, therefore limiting the effectiveness of photodiode array detection for reactions occurring on a faster timescale. One solution to this issue consists of coupling

the array with fast electronic time gating, allowing the recording of a spectrum at a certain delay time after photolysis. Analogously to the procedure used with photographic plates, repeated experiments with different delay times are then necessary to build up the variation of wavelength-resolved absorption as a function of time.

The inclusion of charge-couple device (CCD) detectors in flash photolysis experiments, pioneered by Rowley and co-workers in Cambridge in the mid-1990s, [4] combined the advantages of PMTs (rapid temporal resolution) and photodiode arrays (spectral resolution) and overcame the limitations associated with previous detectors. CCDs, similarly to photodiode arrays, consist of light sensitive pixels that convert incident light into photocharge. However, unlike photodiode arrays, CCDs are *two*-dimensional arrays of pixels in which the recorded photocharge may be rapidly and efficiently transferred across the device to a storage region, allowing continuous, rapid acquisition of spectral data throughout the experiment. Full readout of the device only occurs when the entire device has been filled with signal and real-time data acquisition has stopped, so that the readout process can take place on a slower timescale than the photolytically initiated reaction of interest. The temporal resolution of the experiment is therefore dictated by the rate of charge transfer, typically on the scale of microseconds. As the data recorded *via* CCD detection are both spectrally *and* temporally resolved, the quality and the amount of information obtained in each photolysis experiment are maximised.

All flash photolysis experiments reported in this thesis were conducted using CCD detection, hence a more detailed description of the principles of this is given in the following section.

3.2 CCD detection in Flash Photolysis

3.2.1 Charge-coupled devices

Charge-coupled devices (CCDs) consist of a two-dimensional grid of metal oxide semiconductor elements (pixels) embedded in a silicon substrate. The pixels are photosensitive and convert incident light into photocharge; the light-to-charge

conversion efficiency (quantum efficiency, QE) of the CCD typically peaks at approximately λ = 700 nm, with a value of about 60%. A fine coating of fluorescing phosphor is applied on the pixels to enhance the QE at wavelengths λ < 400 nm, where most atmospherically relevant species absorb: the phosphor coating emits visible light when UV light is incident upon it, effectively increasing the QE to approximately 20% over the range λ = 180-400 nm. The fluorescence lifetime of the phosphor, typically of the order of nanoseconds, does not distort the temporal resolution of CCD detection. Furthermore, the phosphor coating is thin (0.3 μm) relative to pixel size (22.5 μm square) so that the extent of cross-talk between pixels is negligible.

The photocharge on the CCD is stored in a potential well within the pixels and may be rapidly transferred across the device along one axis of the array. This is achieved by applying a suitably phased voltage to a series of parallel electrodes mounted across the surface of the device in a direction perpendicular to that of the charge transfer, as shown in Figure 3.2. The efficiency of charge transfer is very high, typically of the order of 99.9999% per transfer, and charge transfer frequencies of 1 MHz (one transfer per microsecond) are readily attainable. [4]

Given these properties of the CCD, by imaging spectrally resolved light across the top rows of the device perpendicular to the charge transfer axis, time resolved signal (charge) can be shifted and transferred to a storage region which is only read out when the photocharge from the first row of pixels has traversed the whole device, as illustrated in Figure 3.2. In this way spectra are recorded as a function of time, on fast (up to MHz) timescales.

The principal source of noise arising from CCD detectors is ‘dark current’, originating from the thermal excitation of charge carriers within the device. Dark current can be reduced by Peltier cooling the CCD and enclosing it in a vacuum for thermal insulation. As dark current is produced by the device regardless of its exposure to light, it ideally must be recorded for each pixel prior to exposure and this signal subtracted from the measured light intensity. The effect of dark current on the recorded light intensities and the detailed ways to account for it in the analytical procedures are described in Section 3.4.1. Photonic noise, inherent to the light incident on the device, is also a major source

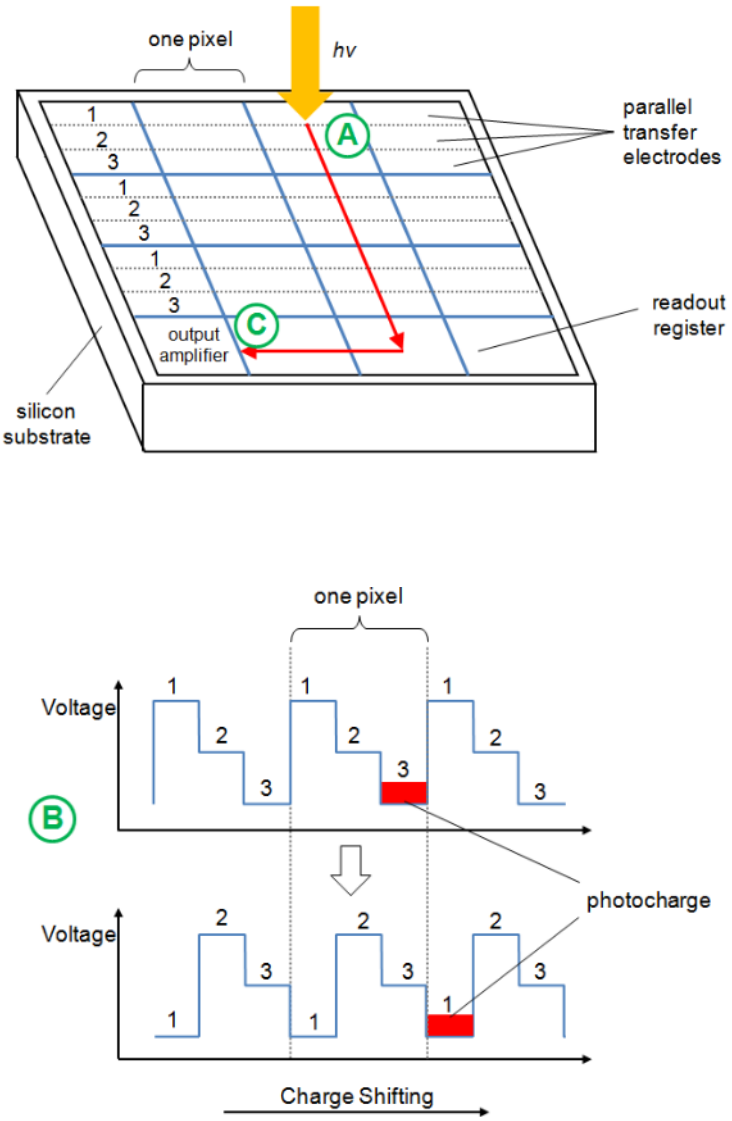

Figure 3.2 : Diagram of the principles of CCD operation; incoming light is converted into photocharge (A); three sets of parallel transfer electrodes (1, 2, 3) are charged cyclically to maintain a potential gradient across the device, pushing the charge towards the storage region (B). Once the charge has crossed the entire device, the charge is readout *via* the output amplifier (C) (adapted from reference 4).

of noise. As the photon flux exhibits a Poisson distribution, the photonic noise is typically equivalent to the square root of the number of photons detected at each pixel of the CCD. Thus, for a typical full pixel capacity of 2×10^6 photoelectrons, the associated photonic noise is about ±0.07%. The effective noise can, of course, be reduced through co-addition of experiments as described below.

3.2.2 Application of the CCD to Flash Photolysis

A CCD detector consisting of an array of 1152 rows by 298 columns of light sensitive pixels was incorporated into the laser flash photolysis system used in the present work. The CCD was aligned in the dispersive plane of the spectrograph so that spectrally resolved transmitted light illuminated the top 31 rows of the device, whilst the other rows remained optically masked. Each row therefore represented a wavelength-resolved spectrum of the transmitted light intensity. As charge transfer was effected in a direction perpendicular to the dispersive plane of the spectrograph, rows of photocharge were moved out of the illuminated region of the device and sequential spectra of the reaction mixture were recorded, as shown schematically in Figure 3.3. Once the first row of signal had reached the end of the device, the recorded signal was readout from the device to a computer as described above.

The time between each charge transfer event dictates the temporal resolution of the flash photolysis experiments. This time interval is called *shift time* and is selected prior to the experiment.

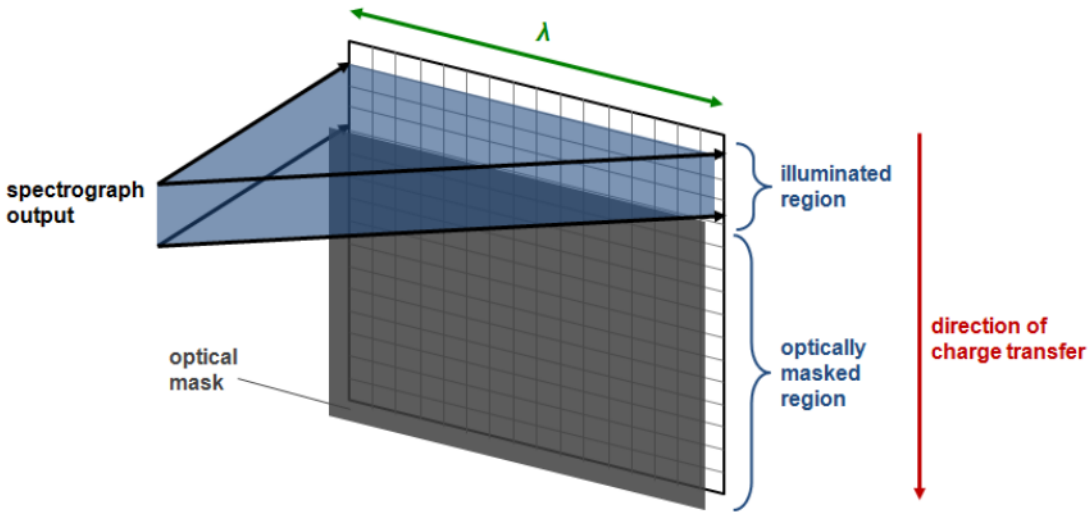

Figure 3.3: Schematic representation of the principles of CCD operation: wavelength resolved light illuminates the top of the detector, generating photocharge that is rapidly transferred down the CCD.

Thus, in the application of CCD detection to UV absorption spectroscopy in flash photolysis, the charge transfer starts, the photolysis event is initiated after some predetermined time and, once a full signal has been recorded, readout occurs. In this way, CCD detection allows continuous *broadband* monitoring of the light transmitted through the reaction mixture before, during and after photolysis in a single experiment. The experiment is described in detail in the following section.

3.3 Description of the Laser Flash Photolysis Apparatus

3.3.1 Gas Handling

Precursor gases were mixed with a carrier gas flow in a Pyrex mixing line prior to their arrival in the reaction cell. The mixing line consisted of a cylindrical vessel punctuated with gas injectors equipped with Teflon taps (Young and Co.); the injectors were oriented against the carrier gas flow to promote efficient mixing. Gases were introduced directly to the mixing line from pure or diluted mixtures as provided. For condensed-phase reagents, their vapours were taken up by a known flow of an inert gas passed through appropriate bubblers or traps containing the reagent.

Gases were delivered to the mixing line *via* Teflon tubing and their flow rates, in the case of non-corrosive gases, were set using mass flow controllers (MKS). The flow rate of corrosive gases was controlled using Teflon needle valves and measured using calibrated glass ball meters (rotameters). All mass flow controllers and ball meters were regularly calibrated as described in Appendix 1.

After mixing with the carrier flow (typically N_2, O_2 or synthetic air) inside the mixing line, precursor gases flowed into the reaction cell *via* Teflon tubing. The reaction cell consisted of a double-jacketed spectrosil quartz vessel of 98.2 cm in length and 1.48 cm in diameter. This gave a reaction cell volume of 169 cm^3, and a typical total gas flow rate of 900 SCCM (standard cm^3 per minute) was employed to ensure a fresh gas fill approximately 10 seconds. The inner jacket of the reaction vessel was connected to a thermostat unit (Huber CC 180) which recycled perfluorinated fluid (Galden HT110) to allow regulation of the cell temperature over the range T = 206-373 K with an accuracy

of ±0.5 K. This was checked by carrying out offline experiments using an inert gas flow and a Pt-100 resistance thermometer. The outer jacket was evacuated to improve thermal insulation and prevent any build up of condensation when operating at low temperatures. Similarly, the double windowed end-pieces of the reaction cell were evacuated to prevent condensation on the optical surfaces. The pressure inside the cell could be regulated by connecting the cell exit to a rotary pump and was monitored using a capacitance manometer (MKS Baratron).

During experiments, precursor gases were flowed continuously through the reaction vessel so that a fresh gas mixture was available for each photolysis experiment. On the timescale of kinetic experiments, however, the flow out of gas was negligible and was in any case accounted for in the analysis of data.

3.3.2 Laser Photolysis: radical generation

The radicals of interest were generated *via* chemical reactions following laser photolysis of precursor gases. An excimer laser (Lambda Physik COMPex 201) operating at λ = 351 nm with a Xe/F_2/Ne gas fill was used, with pulse energy of typically 110 mJ/pulse delivered within 10 ns. The laser was operated from the control computer *via* a fibre optic cable connected to a trigger module (EG&G, TM11A). The beam exiting the laser was expanded in order to exceed the cross sectional area of the reaction cell using a pair of fused silica cylindrical lenses (Exitech Ltd.). The expanded beam was then collimated to match the cross sectional area of the reaction cell through an iris and directed along the length of the reaction cell counter to a UV-visible analysing beam using a dichroic reflector (Elliot Scientific). The alignment of the laser and optics was routinely tested and optimised using a co-propagated He-Ne laser beam.

The use of a laser in the place of (the pre-existing) flashlamp presented a number of advantages. Whilst both photolysis sources induce photodissociation on a much smaller timescale than the subsequent chemistry, they differ in their spectral output: flashlamps produce broadband spectral output, whereas lasers are monochromatic. Therefore the laser can selectively photolyse components in a gas mixture by operating at a wavelength that maximises the yield of the radical of interest, keeping any unwanted

secondary chemistry to a minimum. Furthermore, the quality of kinetic traces obtained from laser photolysis is usually superior to those obtained with a flashlamp due to the reduced radio frequency noise typically associated with the laser compared to the flashlamp. In addition, the laser offers a higher pulse repetition rate, which leads to further noise reduction in the traces *via* addition of many traces on the same overall experimental timescale.

A potentially complicating consequence of the longitudinal pathway of the laser beam through the reaction cell is the possibility of a non-uniform concentration profile of photolysis products within the reaction cell. If the precursor mixture absorbs strongly at the laser wavelength, then most of the laser photons would be absorbed in the initial portion of the reaction cell where the beam enters, leading to a high concentration of photolysis products in that part of the reaction vessel. Conversely, at the opposite end of the reaction cell, the abundance of photolytically-generated species would be low due to the attenuation of the laser beam. This leads to the generation of a longitudinal concentration gradient of photolysis products. As this gradient is non-linear along the cell, it may then give rise to spuriously enhanced apparent reaction rates. To investigate this, simulations of the optical depth of each precursor mixture employed in this work were devised and the distortion on apparent kinetic parameters was assessed, as described in Appendix 2. In all cases, experiments were designed so that the optical density of the precursor mixture at the laser wavelength was suitably low that a significant longitudinal concentration gradient within the reaction cell was avoided.

3.3.3 UV/visible spectroscopy: species monitoring

Species in the reaction mixture were monitored before, during and after photolysis *via* UV/visible absorption spectroscopy. A 70 W continuous xenon arc lamp (Hamamatsu L2174) was employed as the source of ultraviolet radiation. Light from the xenon lamp was collimated through the reactant gas mixture using a Spectrosil quartz lens (Comar Ltd.), passed through the cell and then was focused by a further lens onto the entrance slit of a 0.25 m Czerny-Turner spectrograph (Chromex 250IS).

The spectrograph was fitted with three interchangeable diffraction gratings, ruled with 150, 300 and 600 grooves mm^{-1}. Each of these gratings gave rise to a different dispersion at the CCD (of *ca*. 0.45, 0.22, 0.11 nm $pixel^{-1}$ respectively), resulting in wavelength coverages across the CCD device of approximately 120, 60 and 30 nm respectively. The resolution of the spectrograph was also determined as the full-width half maximum (FWHM) of an isolated emission line from a mercury 'pen-ray' lamp for each diffraction grating over a range of entrance slit widths, from 20-100 μm, as discussed in Appendix 3. The spectrograph was also wavelength calibrated for each experiment using the known wavelengths of spectral lines from the same mercury lamp as described in Appendix 1.

Wavelength-resolved light from the spectrograph was imaged onto the CCD detector (EEV CCD05-10-0-202, Wright Instruments). The principles of operation of the CCD have been illustrated above in Section 3.2.2. The CCD was mounted in a camera head which was evacuated and Peltier cooled to $T \approx 200$ K to minimise dark current. An optical shutter was installed within the optical line to prevent accumulation of photocharge between experiments. An optical filter absorbing at the laser wavelength was also placed over the spectrograph entrance slit to protect the detector from possible back-scattered laser beam.

3.3.4 Operating Procedure

A schematic representation of the laser photolysis/UV absorption spectroscopy apparatus used in the present work is shown in Figure 3.4. The laser and the CCD detector were controlled from a personal computer. To improve the signal-to-noise ratio, each experiment consisted of the co-addition of data from typically 10-100 photolysis runs, all conducted under identical conditions. The repetition rate of photolysis events was dictated by the residence time of the gaseous mixture in the reaction cell; this was arranged so that a fresh precursor gas mixture was available for each photolysis event. After each experiment, the temporally and spectrally resolved light intensities recorded were transferred to a separate PC for analysis.

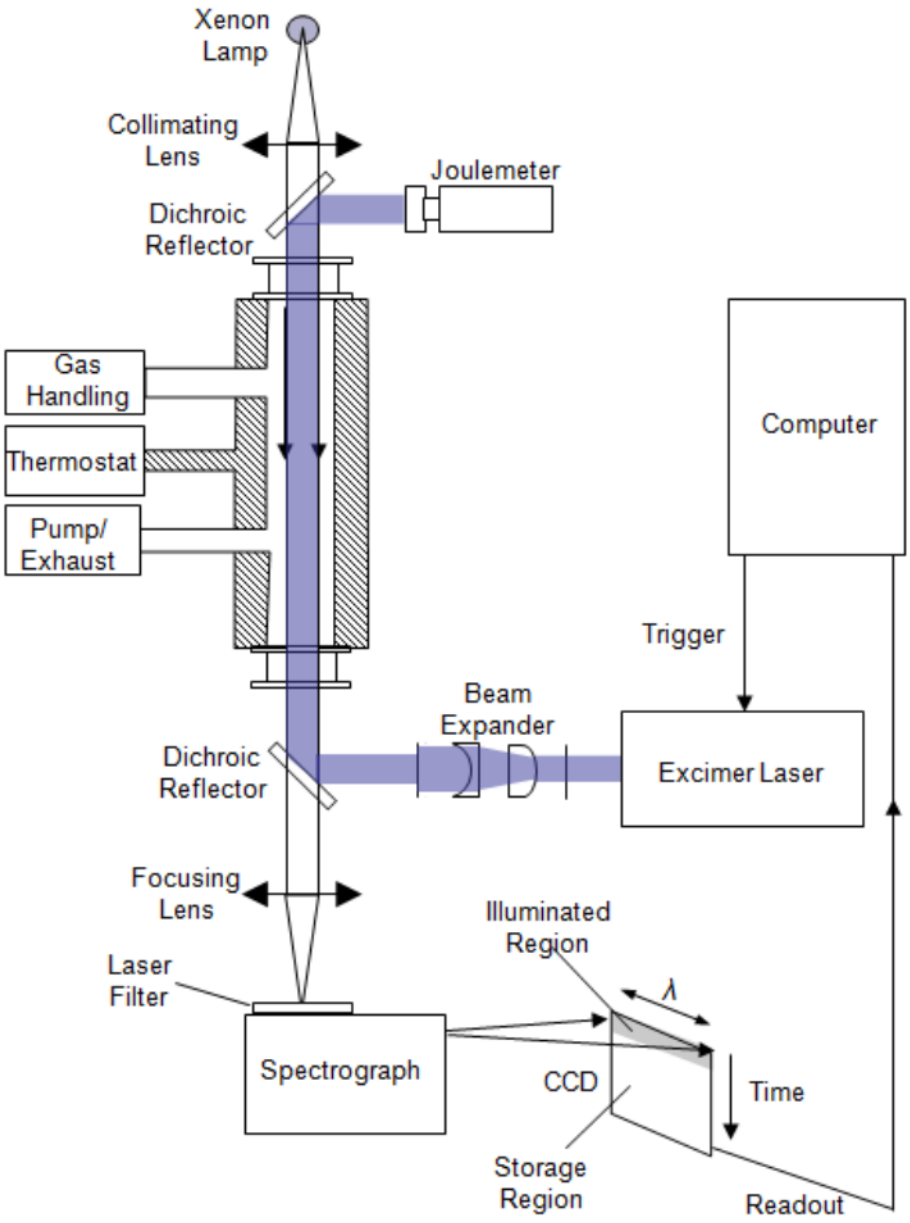

Figure 3.4 : Schematic representation of the apparatus used.

3.4 Analysis Procedures

3.4.1 Determination of absorbances

The transmitted light intensities recorded by the detector were arranged in 1152 × 298 matrices: each of the 1152 rows of data represented a wavelength resolved spectrum of transmitted analysing light intensity at a particular time point, whereas each of the 298 columns showed temporally resolved light intensities at a particular wavelength.

The light intensities recorded on each pixel of the CCD detector were converted into time and wavelength resolved absorbances, $A_{t,\lambda}$, of the reaction mixture using Beer's law:

$$A_{t,\lambda} = \ln\left(\frac{\langle I_{0,\lambda} \rangle}{I_{t,\lambda}}\right) \qquad (3.i)$$

where $\langle I_{0,\lambda} \rangle$ is the 'pre-flash' average intensity at wavelength λ, *i.e.* the average intensity of the light transmitted through the reactive mixture *before* the laser pulse is fired, whereas $I_{t,\lambda}$ is the intensity at any wavelength λ and time t. The resulting absorption spectra therefore represented the total *change* in absorbance of the reactive mixture brought about by the photolytically initiated chemistry.

A small correction to equation (3.i) was necessary to account for a complication inherent to the charge transfer routine. As a row of photocharge is shifted down the CCD device into the non-illuminated region, it acquires a small amount of extra charge upon each transfer, referred to as 'dark current' (see Section 3.2.1). As this effect is cumulative and since early rows travel a longer physical distance down the CCD array, the signal recorded on the first rows accumulates more of this additional charge than the later ones. As a result all recorded charges consist of the principal charge generated by the light transmitted through the spectrograph plus a small amount of additional charge that effectively decreases as a function of time. The overall result of this decreasing

trend in time resolved intensities is to produce an apparent increase in the absorbance calculated using equation (3.i) as a function of time.

To account for the additional charge, each photolysis experiment was accompanied by a "non-flashed" experiment, namely an experiment performed in the absence of a laser pulse but under otherwise identical experimental conditions. Since dark current affects the intensities recorded in the non-flashed runs in the same way as those recorded in the flashed ones, it was possible to remove the contribution of the dark current to the total absorbance of the mixture by subtracting the absorbance of the non-flashed experiment from that of the "flashed" run:

$$A_{t,\lambda} = A_{t,\lambda\,\mathrm{FLASHED}} - A_{t,\lambda\,\mathrm{NON\text{-}FLASHED}} =$$

$$= \ln\left(\frac{\langle I_{0,\lambda}\rangle}{I_{t,\lambda}}\right)_{\mathrm{FLASHED}} - \ln\left(\frac{\langle I_{0,\lambda}\rangle}{I_{t,\lambda}}\right)_{\mathrm{NON-FLASHED}} \qquad \text{(3.ii)}$$

This correction was typically very small and would not exceed approximately 2% of the total absorbance. Furthermore, experiments in the present work were usually run in groups of three for a given set of experimental conditions: a flashed run followed by a non-flashed run followed by a second flashed run. Hence, for each group of three experiments, two sets of time resolved absorption spectra were produced. As spectra obtained from equation (3.ii) are both spectrally and temporally resolved, they can be represented in three dimensions as shown for example in Figure 3.5 for the ClO radical.

3.4.2 Determination of Species Concentrations

The total absorbance of a gaseous mixture at wavelength λ and time t, $A_{t,\lambda}$, is related to the concentration of the absorbing species *via* the Beer-Lambert law:

$$A_{t,\lambda} = \sum_i \sigma_{i,\lambda} \cdot l \cdot [i]_t \qquad \text{(3.iii)}$$

where $\sigma_{i,\lambda}$ is the absorption cross section of any species i at wavelength λ, l is the optical

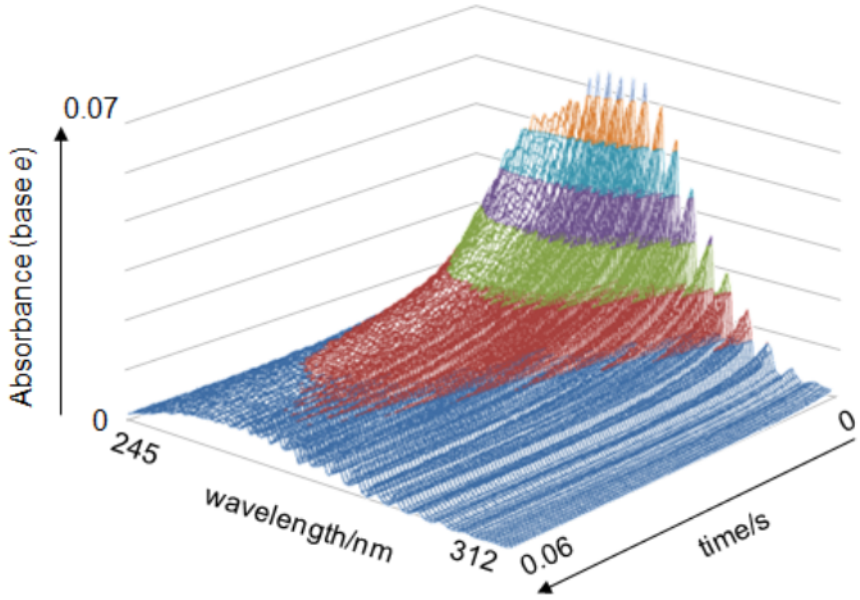

Figure 3.5 : Recorded absorbance as a function of time and wavelength for the post-photolysis decay of ClO radicals (photolysis at $t = 0$), demonstrating the nature of data acquired by the CCD detector.

pathlength of light through the gas mixture and $[i]_t$ is the concentration of species i at time t. As the absorbance spectra obtained from equation (3.ii) represent the *change* in absorbance brought about by photolysis, absorbers formed upon photolysis or by the subsequent chemistry make a positive contribution to the total absorbance, whereas those species removed by photolysis and/or by the photolytically induced chemistry make a negative contribution to the total recorded absorbance. Temporally resolved concentration profiles of absorbing species were obtained by fitting a linear combination of the scaled absorption cross sections to the recorded absorbance spectra at each time point *via* a least-squares routine, discussed in greater detail below.

In theory, the broadband coverage afforded by CCD detection allows the possibility of monitoring multiple absorbers. However this is, in most cases, compromised by similarities and overlaps in the cross-sections of absorbers in the gas mixture over the chosen spectral range. This limitation can be overcome however when absorbers possess characteristic spectral structured features (*e.g.* vibronic absorption bands), as is the case with halogen monoxide radicals. In this case *differential* fitting routines can be used to quantify the concentrations of the absorbers accurately and unequivocally and to achieve an optimal signal-to-noise ratio of the temporal traces. The principles of this

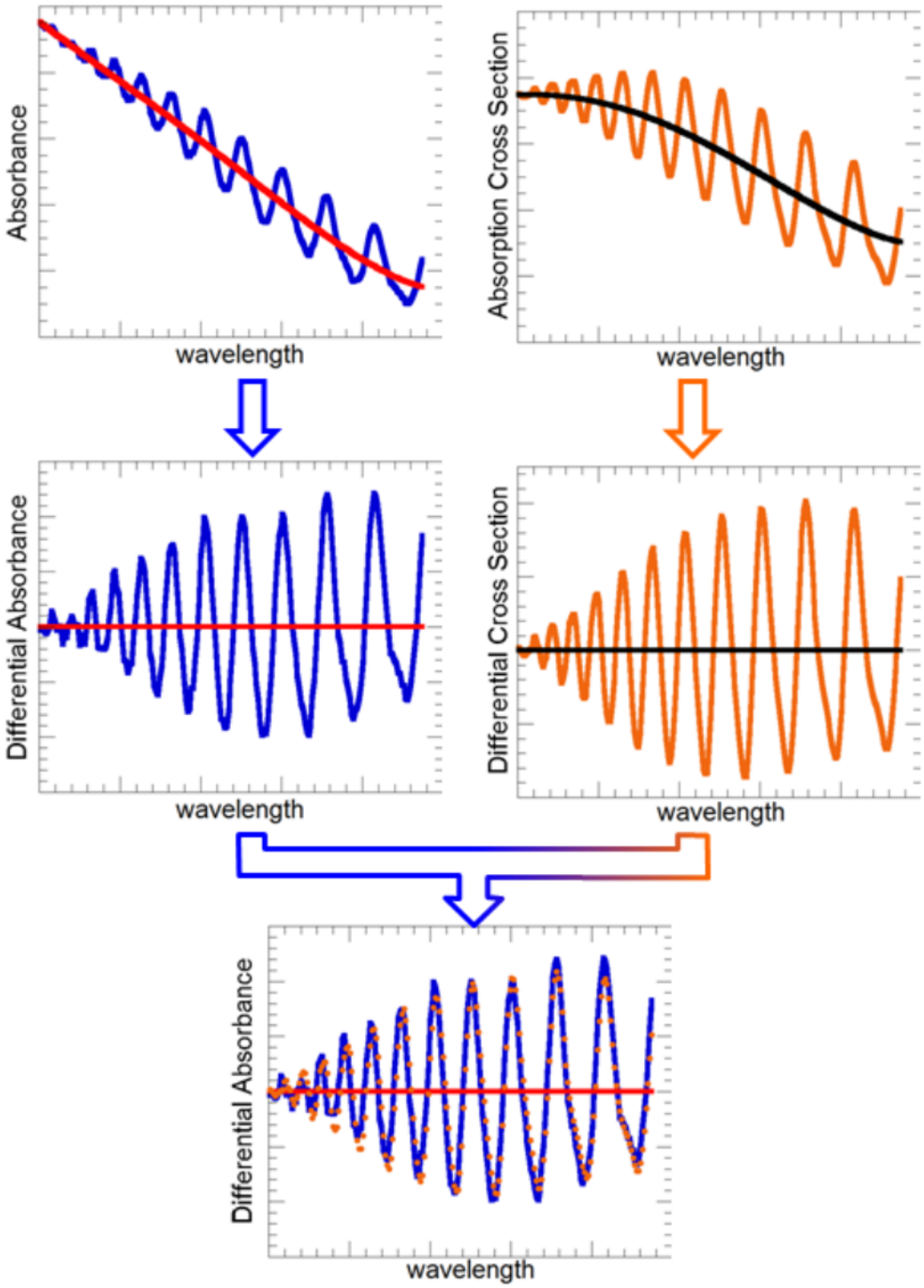

Figure 3.6 : Principles of differential fitting: the composite recorded absorbance is high-pass filtered (top left); the reference cross-section is also high-pass filtered (top right) so that the differential cross-section is fitted to the differential absorbance (bottom panel), determining species concentration *via* the Beer-Lambert law.

technique are illustrated in Figure 3.6: a high pass filter consisting of a smooth function, *i.e.* a function that does not replicate the structured features of the spectrum, is fitted to and subtracted from the recorded absorbance spectrum to give a differential absorbance spectrum. The analogous procedure is then performed for the reference cross-section and the resulting differential (*i.e.* filtered) cross-section is fitted to the differential absorbance *via* a least-squares routine, *i.e.* minimising the square of the difference between each point in the spectrum. In this way the concentration of *only* the structured absorber is determined *via* fitting to equation (3.iii). This method allows *unequivocal* identification and *accurate* quantification of structured absorbers regardless of the presence of overlapping absorbers. Furthermore, spectral subtraction of the "differentially-quantified" structured absorber and further fitting potentially facilitates spectral deconvolution and quantification of underlying absorbers.

Different types of smooth functions can be used as a high-pass filter in differential fitting routines. Typically, low-order polynomials are used. In the work presented in this thesis, a high-pass filter consisting of a 31-point triangular average was employed.

Since structured spectral features such as vibronic bands are strong functions of the instrumental spectral resolution, the resolution of the reference cross-sections must also match that of the experimental spectra. When reference cross-sections were available at higher resolutions than those employed in the current work, they were smoothed to ensure that their resolution matched that of the experimental spectra. This is explained on a case-by-case basis in the subsequent Chapters. The principles of the "spectral convolution" routine employed are described extensively in Appendix 3.

3.4.3 Precursor Concentration Measurements *via* Absorption Spectroscopy

Absorption spectroscopy was also used to quantify gas concentrations in the precursor mixture. These measurements were performed by flowing gas mixtures in the reaction cell in the absence of the photolytic laser pulse. Absorbance of the gas mixture was calculated using Beer's law (equation 3.i), in which, in this case, I_t and I_0 are respectively the light intensities transmitted through the cell in the presence and in the absence of a particular absorber. As the concentration of said absorber is not changing

with time due to the absence of photolysis, the Beer-Lambert law is applied to a temporally averaged absorbance spectrum to quantify the concentration of the reagent of interest, and arbitrarily long acquisition times may be used to optimise the signal-to-noise ratio.

Spectroscopic quantification of reagents was crucial in many experiments which required a particular reactant to be present in excess or at a well-defined concentration. This method was also used, for example, to calibrate ozone production from an ozoniser and the efficiency of a mercuric (II) oxide trap used to convert Cl_2 into Cl_2O, as described in Appendix 1.

3.4.4 Kinetic Analysis: extraction of kinetic parameters

Following automation of the spectral fitting procedure described above, experimental kinetic traces (concentrations as a function of time) were fitted to classical kinetic solutions wherever possible. In the case of insoluble differential equations, the commercial numerical integration package FACSIMILE [5] was used to fit simulated concentrations to the experimental traces to extract kinetic parameters. FACSIMILE models were built for each reaction system studied: they included all known reactions occurring in the cell as well as physical processes such as gas flow-out. The FACSIMILE model was also used to conduct sensitivity studies for experimental design in advance of kinetic experiments. In the fitting procedure, concentrations calculated from the classical solutions or the FACSIMILE model were fitted to the observed concentrations *via* a least squares routine by varying the rate constants of the reactions of interest and typically the initial concentration of the species monitored.

An unavoidable consequence of the continuous flow set up of the flash photolysis experiment was the small flow of precursors and reactants in/out of the reaction vessel during the timescale of a kinetic experiment. Gas flow-out was accounted for as a zeroth-order decay superimposed to the temporal behaviour of the species monitored resulting from their chemistry.

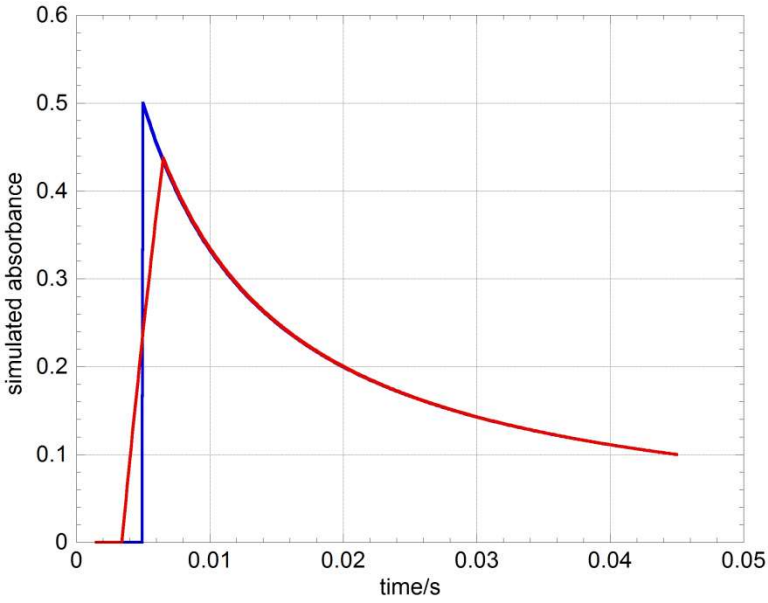

Figure 3.7 : Effect of the simultaneous illumination of the top 31 rows of the CCD detector. A simulated absorbance trace as a function of time is shown in blue along with a curve showing the distortion imparted by temporal averaging arising from the simultaneous illumination (in red).

One final correction was incorporated in both kinetic analysis schemes. Since the illuminated region of the CCD comprised 31 rows of pixels, each row of data read out actually recorded transmitted light intensity for 31 times the shift time (*i.e.* the time of charge transfer). Hence an absorption spectrum resulting from a single output row on the CCD is, in reality, an average of the true absorption spectrum over a period of time equal to the duration of the exposure of that row of signal to the light. The simultaneous illumination of 31 rows therefore results in a small distortion of the experimental kinetic traces obtained from the Beer-Lambert law which is possible to account for by applying a 31-point sliding averaging function to the concentrations simulated as a function of time prior to the fitting procedure. The effects of this correction are illustrated in Figure 3.7.

Sensitivity analyses were also carried out *following* each kinetic study to assess the effects of the secondary chemistry on the derived kinetic parameters. This method typically involved the re-analysis of a representative experimental trace using a model in which the rate coefficients of secondary reactions were sequentially perturbed (in both directions) by a factor of two. Another form of sensitivity analysis assessed the

effect of the uncertainties in concentration of precursor species on the extracted kinetic parameters. Details of the sensitivity analyses carried out are given in the appropriate results chapters.

3.5 Concluding Remarks

The flash photolysis/time resolved UV absorption technique provides a powerful method to investigate the kinetics of short-lived, highly reactive species such as free radicals which are found in the atmosphere. The inclusion of a CCD detector in the experimental apparatus allows a more accurate determination of kinetic parameters and mechanistic information than had been possible previously, thanks to the spectral and temporal coverage provided.

3.6 References

1. N. Basco, S.K. Dogra, *Proc. R. Soc. London, Ser. A*, **1971**, 323, 29
2. R.G.W. Norrish, G. Porter, *Nature*, **1949**, 164, 658
3. G. Porter, *Proc. R. Soc.*, **1950**, 200, 284
4. D.M. Rowley, M.H. Harwood, R.A. Freshwater, R.L. Jones, *J. Phys. Chem.*, **1996**, 100, 3020
5. A.R. Curtis, W.P. Sweetenhan, FACSIMILE, **1987**, AERE Harwell Publication, Oxford

Chapter 4
Kinetic and Thermochemical Studies of ClO Dimerisation

4.1 Introduction

Under the perturbed conditions encountered in the polar stratosphere at the onset of spring, described in detail in Section 1.3.2, abundances of chlorine monoxide, ClO, radicals are sufficiently elevated that the formation of the ClO dimer, Cl_2O_2, *via* termolecular association of two ClO radicals becomes rapid and efficient. This subsequently initiates one of the most effective ozone-destroying catalytic cycles operating in the atmosphere: [1]

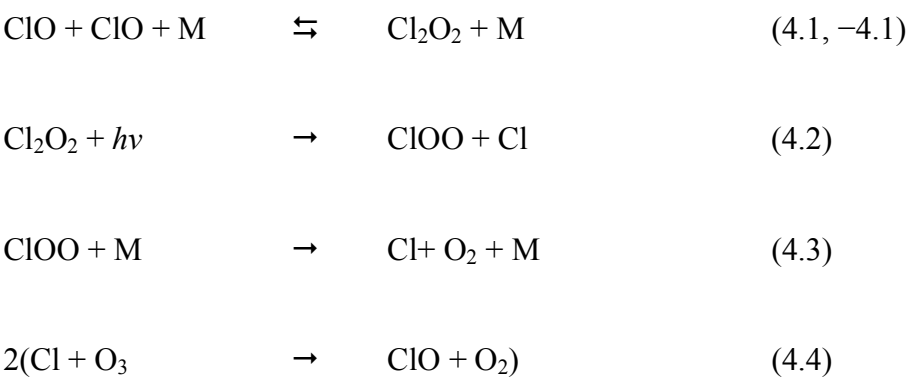

	$ClO + ClO + M$	$\leftrightarrows$	$Cl_2O_2 + M$	(4.1, −4.1)
	$Cl_2O_2 + h\nu$	$\rightarrow$	$ClOO + Cl$	(4.2)
	$ClOO + M$	$\rightarrow$	$Cl + O_2 + M$	(4.3)
	$2(Cl + O_3$	$\rightarrow$	$ClO + O_2)$	(4.4)
Net:	$2O_3 + h\nu$	$\rightarrow$	$3O_2$	

In the absence of solar radiation, photolysis of the ClO dimer (process (4.4)) evidently cannot occur and a thermal equilibrium between ClO and Cl_2O_2 is established, with the equilibrium constant K_{eq} defined as:

$$K_{eq} = \frac{[Cl_2O_2]_{eq}}{[ClO]_{eq}^2} = \frac{k_{4.1}}{k_{-4.1}} \qquad (4.i)$$

where $[Cl_2O_2]_{eq}$ and $[ClO]_{eq}$ are the equilibrium concentrations of the ClO dimer and ClO respectively, $k_{4.1}$ is the rate constant of ClO recombination (forward reaction (4.1)) and $k_{-4.1}$ is the rate constant of the Cl_2O_2 thermal dissociation (reverse reaction (–4.1)).

In sunlight, reactions (4.1) and (4.2) are the rate determining steps in this "ClO dimer" cycle, hence $k_{4.1}$ and $J_{4.2}$, the photolysis frequency of Cl_2O_2, are crucial parameters required to establish the amount of ozone destroyed by this process. Many laboratory studies have focused on characterising $k_{4.1}$ [2, 3, 4] or K_{eq}, [5, 6, 7] or both. [8, 9, 10] The photolysis frequency of the dimer, $J_{4.2}$, requires an accurate characterisation of the absorption cross-section of the dimer, $\sigma_{Cl_2O_2}$, as described in Section 2.5.2. Therefore several studies have also focused on $\sigma_{Cl_2O_2}$. [11, 12, 13] Again, laboratory studies of such processes are to an extent reliant on the knowledge of the ClO/ Cl_2O_2 partitioning, defined by K_{eq}.

In a paper published in 2007, von Hobe *et al*. [14] highlighted significant inconsistencies in the understanding of the ClO dimer cycle at the time, as evidenced by a disparity between models and atmospheric measurements. These authors argued that the values of $k_{4.1}$ and $\sigma_{Cl_2O_2}$ that best reproduced the observed ozone depletion in atmospheric models were not consistent with the then current JPL-NASA recommendations [15] and were therefore not regarded as the most reliable experimental values. Von Hobe *et al*. also noted that the values of $k_{4.1}$ from Boakes *et al*. [4] and $\sigma_{Cl_2O_2}$ from Pope *et al*. [13], the most recent studies at the time, fell outside the uncertainty limits of all previously published data with $k_{4.1}$ from Boakes *et al*. being the largest value of $k_{4.1}$ to date and $\sigma_{Cl_2O_2}$ from Pope *et al*. leading to the lowest photolysis rate, $J_{4.2}$, to date. Moreover, the inclusion of $k_{4.1}$ and $\sigma_{Cl_2O_2}$ from these studies in atmospheric models led to a significant underestimate of ozone loss rates compared to observations. Von Hobe *et al*. argued that these observations could only be explained by either inaccuracies in the experimental work or in the field measurements, or in terms of an unknown process affecting the ClO/Cl_2O_2 partitioning. The lack of agreement between field observations and atmospheric models based on laboratory studies highlighted by von Hobe *et al*. is summarised graphically in Figure 4.1.

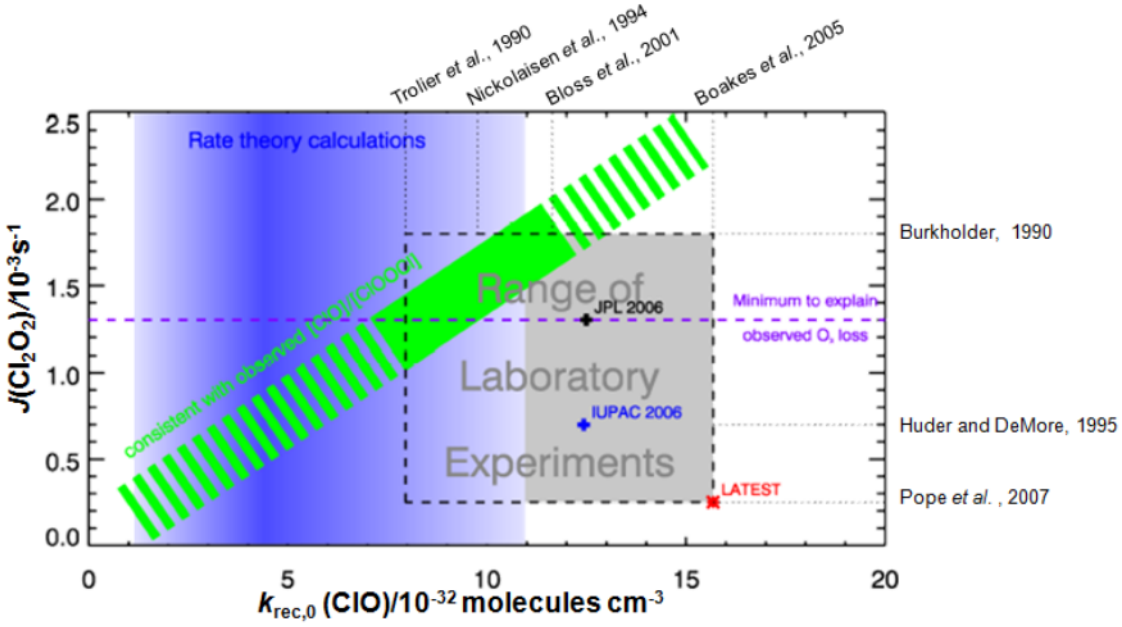

Figure 4.1 : Graphical representation of the discrepancies between laboratory experiments, theoretical calculations and field observations concerning the photolysis frequency of the ClO dimer, $J(Cl_2O_2)$, and the rate of recombination of two ClO radicals in the low pressure limit, $k_{rec,0}(ClO)$ as reported by von Hobe and co-workers. [14] Areas in the diagram are colour-coded as follows: in grey, the range of kinetic parameters encompassed by laboratory studies published prior to the paper by von Hobe *et al.*; in green, the range of $k_{rec,0}(ClO)$ and $J(Cl_2O_2)$ deduced from atmospheric observations; in blue the range of $k_{rec,0}(ClO)$ values consistent with unimolecular rate theory calculations. The diagram is plotted for T = 190 K and solar zenith angle (SZA) = 80°, but it does not vary significantly over the temperature range observed in polar vortices and for SZA < 93°. This plot is taken from reference 14.

Since the publication of the paper by von Hobe *et al*. a number of studies [16, 17, 18, 19] have focussed on determining $\sigma_{Cl_2O_2}$. These works all used different techniques to measure the cross-section of the ClO dimer and their results generally disagree with the findings of Pope *et al*. Typically a greater $\sigma_{Cl_2O_2}$ was measured at λ > 300 nm leading to an increased value for the photolysis rate $J_{4.2}$ which also better reproduces the observed ozone loss. In addition, some of these studies [16, 17, 18] also attempted to rationalise the results obtained by Pope *et al.* in terms of an overcorrection for Cl_2 impurities in the reaction system.

Whilst several studies of $\sigma_{Cl_2O_2}$ have been recently reported, the rate of ClO recombination $k_{4.1}$ along with the equilibrium constant K_{eq} have received comparatively little attention and have therefore remained the object of studies and debate.

4.1.1 Previous studies

The ClO self-reaction is a complex process comprising multiple reaction channels. In addition to the termolecular dimer formation, reactions (4.1, −4.1), three pressure-independent, often referred to as 'bimolecular' channels, (4.1b)-(4.1d), are also known:

$$ClO + ClO \rightarrow Cl_2 + O_2 \quad (4.1b)$$

$$\rightarrow ClOO + Cl \quad (4.1c)$$

$$\rightarrow OClO + Cl \quad (4.1d)$$

Early studies on the ClO self-reaction in the 1950s and 1960s ignored the very existence of the dimerisation channel, and therefore assumed that the bimolecular channels were the only reaction pathways for the ClO self-reaction. Dimerisation was only first reported in the late 1960s, [20] when termolecular kinetics were observed in experiments at high pressures, in stark contrast with the behaviour observed at low pressures. The first accurate characterisation of the equilibrium constant for ClO dimerisation, K_{eq}, as a function of temperature was reported by Cox and Hayman [5] in 1988. An extensive account of the early studies on the ClO self-reaction, prior to the work of Cox and Hayman, is given in Chapter 5. The following paragraphs therefore focus exclusively on the studies of Cox and Hayman on K_{eq} and those that followed.

The results of previous laboratory studies that measured the equilibrium constant of ClO dimerisation as a function of temperature are summarised in Table 4.1. Cox and Hayman [5] employed modulated photolysis with UV absorption spectroscopy to monitor ClO radicals and determined K_{eq} over the range T = 233-300 K. Nickolaisen *et al.* [9] used flash photolysis with UV absorption spectroscopy to obtain values of the equilibrium constant over a narrower temperature range (T = 260-310 K). Plenge *et al.*[6]

measured the bond strength of the ClO dimer, hence the enthalpy change of ClO dimerisation, by photoionisation mass spectrometry and based their parameterisation of $K_{eq}(T)$ on the value of $\Delta_r H°$ from their own study and Third Law entropies $\Delta_r S°$ derived from statistical mechanics. Bröske and Zabel [7] monitored Cl_2O_2 decomposition by means of IR and UV spectroscopy to determine $k_{-4.1}$ over the range T = 243-261 K; they then calculated K_{eq} employing the JPL-NASA recommended values of $k_{4.1}$ available at the time. [21] On the other hand, both Avallone and Toohey [22] and von Hobe *et al.*[23] inferred K_{eq} from nighttime measurements of stratospheric ClO and Cl_2O_2 abundances. Both studies measured ClO concentrations by titrating air samples with NO and measuring the resulting Cl atom abundance by means of resonance fluorescence spectroscopy. Avallone and Toohey [22] then inferred the concentration of Cl_2O_2 from the total concentration of inorganic chlorine (Cl_y) and that of the measured ClO radical, assuming complete conversion of chlorine reservoir compounds (*e.g.* HCl, $ClONO_2$) into active species (*e.g.* Cl, ClO). On the other hand, von Hobe *et al.* [23] measured the abundance of Cl_2O_2 by heating the air samples up to T = 370 K, thus promoting the thermal dissociation of the ClO dimer; the ClO radicals resulting from the dissociation, along with the background ClO radicals, were then converted into Cl atoms *via* injection of NO and quantified by resonance fluorescence.

Reference	***A*/cm^3 molecule^{-1}**	***B*/K**
Cox and Hayman [5]	$(2.9 \pm 0.4) \times 10^{-27}$	8446 ± 266
Nickolaisen *et al.* [9] (2nd Law analysis)	$(8.1 \pm 0.5) \times 10^{-29}$	9569 ± 352
Nickolaisen *et al.* [9] (3rd Law analysis)	$(1.24 \pm 0.18) \times 10^{-27}$	8820 ± 440
Plenge *et al.* [6]	1.92×10^{-27}	8430
Bröske and Zabel [7]	3.0×10^{-27}	8433
Avallone and Toohey [22]	1.44×10^{-27}	8588
von Hobe *et al.* [23]	3.61×10^{-27}	8167
JPL-NASA 2011 [24]	1.72×10^{-27}	8649 ± 200
this work (2nd Law analysis)	$(1.05 \pm 0.8) \times 10^{-28}$	9564 ± 133
this work (3rd Law analysis)	$(1.95 \pm 0.7) \times 10^{-27}$	8696 ± 375

Table 4.1: $K_{eq}(T)$ in the form $A \exp(B/T)$

Thermochemical analyses from these studies result in a range of values for the enthalpy ($\Delta_r H°$) and entropy ($\Delta_r S°$) changes of ClO dimerisation, as discussed in detail below. Given the crucial importance of K_{eq} in determining the ClO/Cl_2O_2 partitioning and considering the current uncertainties in all the reported thermochemical data on reactions (4.1, −4.1), this work aimed to determine $K_{eq}(T)$ by measuring $k_{4.1}$ and $k_{-4.1}$ using broadband CCD monitoring of ClO radicals, in order to also obtain the enthalpy and entropy changes of reaction (4.1) *via* both Second Law and Third Law analytical methods.

4.2 Experimental

The kinetics and thermochemistry of ClO dimerisation were studied using the laser flash photolysis/UV absorption spectroscopy apparatus described in Chapter 3. Two different radical precursor mixtures were employed. In both cases, ClO radicals were generated following laser photolysis of precursor species and the characteristic vibronic bands of the ClO spectrum were monitored by means of differential UV absorption spectroscopy. The time-resolved concentration of ClO radicals was quantified using the differential absorption cross-section calibrated using the (12, 0) vibronic band of ClO.

4.2.1 Radical Generation

In both reaction schemes used to generate ClO, exploratory experiments and numerical integration simulations were employed to establish the optimum concentration of precursor species that maximised prompt ClO formation upon photolysis and also minimised unwanted secondary chemistry, without compromising the quality of the signal.

In the first reaction scheme, a gaseous mixture of Cl_2/Cl_2O in a variety of carrier flows (N_2, O_2, synthetic air) was used. The principal source of ClO radicals resulted from the photolysis of Cl_2 at λ = 351 nm followed by reaction of Cl atoms with excess Cl_2O to generate ClO:

$$Cl_2 + h\nu \rightarrow 2Cl \qquad (4.5)$$

$$Cl + Cl_2O \rightarrow Cl_2 + ClO \quad (4.6)$$

Direct photolysis of Cl_2O represented an additional but minor source of ClO, given the relatively small absorption cross-section of Cl_2O at λ = 351 nm (σ_{Cl_2O}= 7.0 × 10^{-21} cm^2 $molecule^{-1}$) compared to that of Cl_2 (σ_{Cl_2} = 1.8 × 10^{-19} cm^2 $molecule^{-1}$) at the same wavelength. [24] It has been shown that only one of the several possible channels resulting from Cl_2O photolysis operates at λ = 351 nm, the one yielding Cl atoms and ClO [25]:

$$Cl_2O + h\nu \rightarrow Cl + ClO \quad (4.7)$$

All precursor gases were delivered *via* Teflon tubing to the gas mixing line where they mixed with the carrier flow. Experiments were carried out employing N_2 (BOC, > 99.98%), O_2 (BOC, > 99.98%) and synthetic air (BOC, > 99.98%) carrier flows. The flow rate of the carrier flow was set using calibrated mass flow controllers (MKS), whereas that of Cl_2 (BOC, supplied as 5% by volume in N_2; purity > 99%) was controlled using needle valves and measured by means of a calibrated glass ball meter. This calibration procedure is described in Appendix 1. Cl_2O was produced *in situ* using the method originally described by Hinshelwood and Pritchard: [26] a known flow of the diluted Cl_2 gas was passed through a trap containing solid dried yellow mercuric (II) oxide (HgO, Sigma-Aldrich, > 99%):

$$2Cl_2(g) + HgO(s) \rightarrow Cl_2O(g) + HgCl_2(s) \quad (4.8)$$

To ensure that the solid HgO was not too closely packed and that the gas would flow easily through the trap, the mercuric oxide was mixed with glass beads (5 mm diameter, Sigma Aldrich). The presence of Cl_2O in excess over photolytically generated chlorine atoms was crucial to ensure the prompt formation of ClO radicals. The amount of Cl_2O delivered to the mixing line was quantified *via* UV absorption spectroscopy as discussed in Section 3.4.3. However, it was observed that the efficiency of the conversion of Cl_2 into Cl_2O obtained with fresh HgO was very high (> 90%), thus leaving very little Cl_2 available for direct photolysis and therefore leading to low initial

concentrations of ClO in the immediate post-photolysis spectra. To obtain more control on the conversion of molecular chlorine into Cl_2O, a T-junction was placed upstream of the trap containing HgO so that part of the Cl_2 flow was sent through a side arm leading directly into the mixing line. The side arm was equipped with a needle valve, so that the amount of chlorine *not* going through the HgO trap, and therefore *not* being converted into Cl_2O, could be regulated by opening or closing the needle valve. The conversion efficiency of this set-up was calibrated for different settings of the needle valve by quantifying Cl_2O spectroscopically as described in Appendix 1.

Typical optimised pre-photolysis concentrations of precursor gases in the reaction cell were $[Cl_2] = (1\text{-}2) \times 10^{16}$ molecule cm^{-3}, as determined from measured gas flow rates; $[Cl_2O] = (4\text{-}5) \times 10^{15}$ molecule cm^{-3} as determined by UV spectroscopy, with the carrier gas to balance to $p = 1$ atm. Under these conditions, photolytically generated Cl atoms were always rapidly and stoichiometrically converted to ClO. Initial Cl atom and therefore ClO radical concentrations immediately after photolysis were typically 1.5-2.5 $\times 10^{14}$ molecule cm^{-3}, as obtained from fitting to the temporal [ClO] traces, as discussed in Section 4.2.4.

A second reaction scheme employing a different precursor mixture was also employed. This consisted of a $Cl_2/O_3/O_2$ gaseous mixture in a synthetic air carrier flow. ClO radicals were formed following reaction of the photolytically-generated chlorine atoms with excess ozone:

$$Cl_2 + h\nu \rightarrow 2Cl \qquad (4.5)$$

$$Cl + O_3 \rightarrow ClO + O_2 \qquad (4.4)$$

The mercuric oxide trap was in this case temporarily removed from the experimental set-up as the presence of Cl_2O was not necessary in these experiments, and the diluted Cl_2 was delivered directly into the mixing line. Ozone was produced by flowing a known amount of oxygen through an industrial ozoniser (Ozonia Triogen 213). Ozone concentrations in the precursor mixture were measured *via* UV spectroscopy, in a similar fashion to the method used to quantify $[Cl_2O]$. The conversion efficiency of the

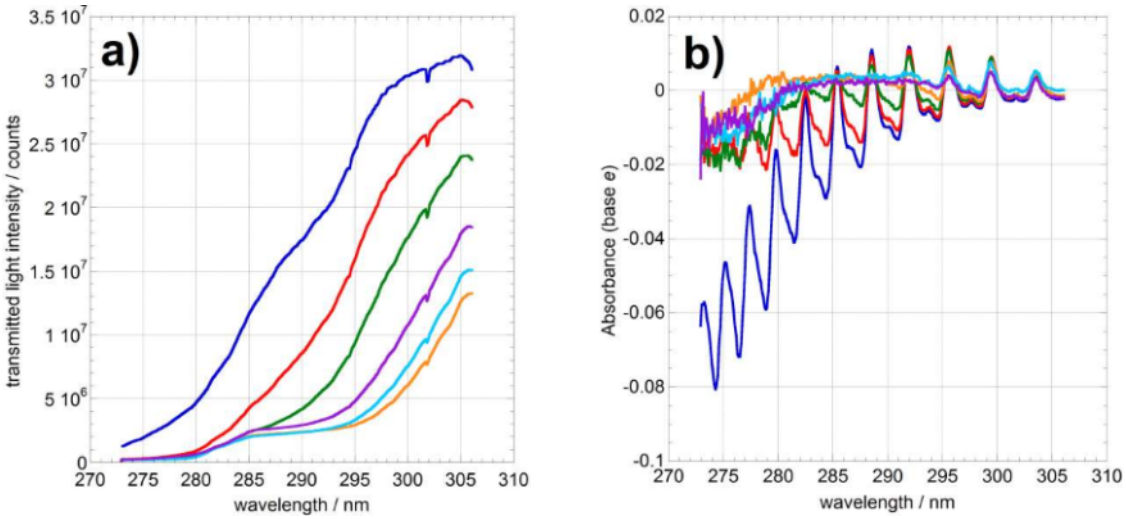

Figure 4.2 : a) Attenuation of transmitted light intensity and b) its effects on the absorbance spectra as a function of $[O_3]$ in the precursor mixture. Data are colour-coded as follows: $[O_3] = 5\times10^{15}$ molecule cm^{-3} (blue); 1.1×10^{16} molecule cm^{-3} (red); 2.4×10^{16} molecule cm^{-3} (green); 3.8×10^{16} molecule cm^{-3} (purple); 5×10^{16} molecule cm^{-3} (light blue); 6.6×10^{16} molecule cm^{-3} (orange).

ozoniser was investigated for a range of O_2 flows, as discussed in detail in Appendix 1, and was found to be approximately 6-7% for most oxygen flows.

As ozone absorbs strongly at $\lambda < 290$ nm, its presence in the precursor mixture led to a significant attenuation of the transmitted light over the critical spectral range necessary to monitor ClO radicals (typically λ = 265-300 nm, as discussed in Section 4.2.2). Exploratory experiments in which the ozone concentration was varied (and indeed simple calculations using the Beer-Lambert law) showed a significant decrease in the transmitted light at $\lambda < 280$ nm for $[O_3] > 5\times10^{15}$ molecule cm^{-3}, as illustrated in Figure 4.2a. This compromised the capacity to monitor the signal at the (12, 0) vibronic band (λ = 275.2 nm) necessary to convert ClO differential absorbance into concentration (Section 4.2.3), as shown in the absorbance spectra in Figure 4.2b. Ozone concentrations of approximately $2\text{-}3\times10^{15}$ molecule cm^{-3} were employed in the present study: at these concentrations enough light was transmitted through the cell to ensure a sufficient signal-to-noise ratio for radical monitoring, while at the same time $[O_3]$ was sufficiently high to ensure prompt ClO formation *via* reaction (4.4).

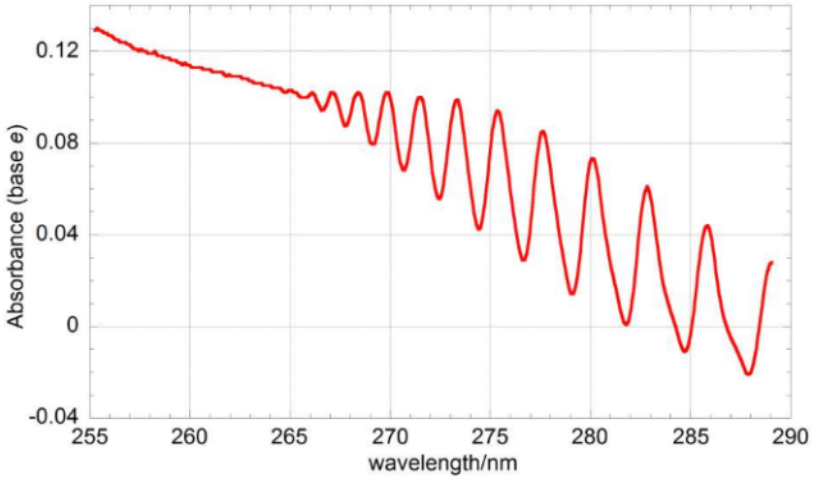

Figure 4.3 : Typical post-photolysis absorption spectrum recorded at a resolution of 0.8 nm (FWHM) and averaged over 3.5-53.5 ms after photolysis following photolysis of a $Cl_2/Cl_2O/N_2$ gas mixture.

4.2.2 Species Monitoring

Species in the reaction cell were monitored using UV absorption spectroscopy *via* charge coupled device (CCD) detection as discussed in Chapter 3. A spectrograph diffraction grating of 600 grooves mm^{-1} was employed, giving rise to a wavelength coverage of approximately 34 nm. In experiments using the Cl_2O/Cl_2 reaction mixture,

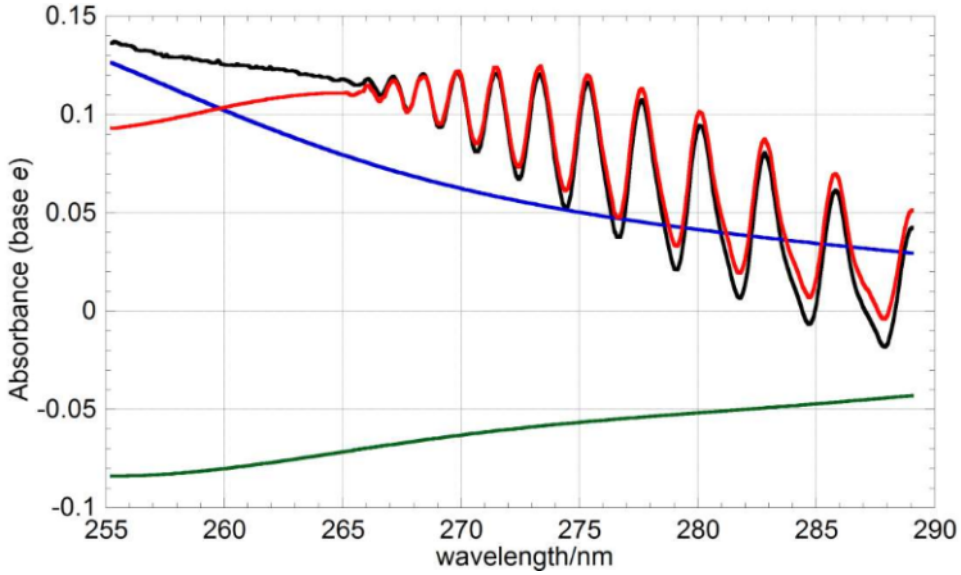

Figure 4.4 : Typical average post-photolysis absorption spectrum (in black) with the contribution of the absorbing species present in the mixture: ClO (red), Cl_2O_2 (blue) and Cl_2O (green). The absorbance of individual species was calculated using literature cross-sections and the concentrations were obtained from a numerical integration model of the reaction scheme used.

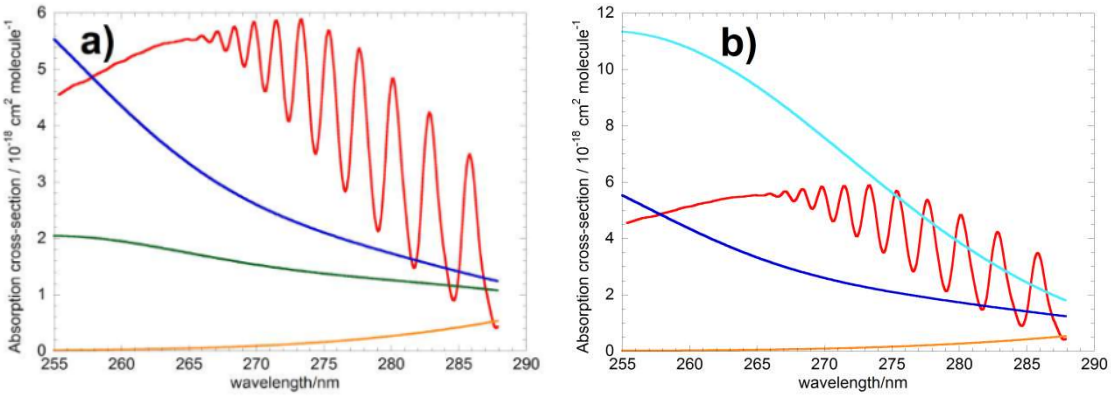

Figure 4.5 : Cross-sections of the absorbing species in a) Cl_2O/Cl_2 and b) Cl_2/O_3 reaction systems. Cross-sections are colour-coded as follows: ClO (red), Cl_2O_2 (blue), Cl_2O (green), Cl_2 (magnified ×10, orange) and O_3 (light blue).

the wavelength range λ = 265-299 nm was typically monitored, whereas in those involving the Cl_2/O_3 precursors the spectral window λ = 270-304 nm was adopted. In all experiments, the CCD charge-shift time was typically set to 100 μs. The spectrograph entrance slit width was set to 112 μm resulting in a resolution (FWHM) of 0.8 nm, as determined by recording emission spectra from a mercury 'pen-ray' lamp using the procedure described in Appendix 3.

Absorbance spectra were obtained as described in detail in Section 3.4.1. A typical absorption spectrum recorded following photolysis of a $Cl_2/Cl_2O/N_2$ gaseous mixture is shown in Figure 4.3. As such spectra represent the change in absorbance brought about by photolysis, these are composed of a positive contribution to the total absorbance arising from the species generated by photolysis and/or by the photolytically-initiated chemistry as well as a negative contribution from species removed from the reaction mixture upon photolysis and/or by the subsequent chemistry, as illustrated in Figure 4.4.

In principle, both ClO and its dimer could be monitored using UV spectroscopy. However Cl_2O_2 exhibits a smooth, unstructured cross-section similar in shape to those of both Cl_2O and O_3 over the same wavelength range, as shown in Figures 4.5a and 4.5b. The absence of a distinctive spectral signature in the Cl_2O_2 cross-section and the presence of overlapping absorbers therefore made the deconvolution of the signal from the ClO dimer extremely inaccurate. Therefore ClO alone was monitored, with the spectral windows reported above focused on the structured part of the ClO spectrum,

allowing an accurate quantification of ClO concentration *via* differential fitting routines, as described below.

4.2.3 Determination of ClO concentrations

Quantification of the concentration of ClO radicals *via* the Beer-Lambert Law required the knowledge of the ClO absorption cross-section, σ_{ClO}, as discussed in Section 3.4.2. The vibronic bands of σ_{ClO} and indeed of any absorber showing spectral structure depend strongly on both temperature and instrumental resolution: it was therefore crucial to determine σ_{ClO} accurately under the experimental conditions used in the present work.

In this study each ClO spectrum was calibrated following the procedure developed by Boakes *et al*. [4] in this same laboratory and using the same apparatus. This technique relied on the determination of the differential absorption cross-section of the (12, 0) vibronic band of ClO, corresponding to the cross-section at the peak at λ = 275.2 nm minus that at the trough at λ = 276.4 nm, recorded at a spectral resolution of 0.8 nm (FWHM) and scaling an uncalibrated absorbance spectrum accordingly.

However, Boakes *et al*. operated under slightly different experimental conditions from the current work: as these authors used a flashlamp as the photolysis source, they incorporated Br_2 in the precursor gas mixture to enhance initial ClO concentrations *via* reaction of photolytically generated Br atoms with Cl_2O. The use of laser photolysis at λ = 351 nm in the present work made the inclusion of Br_2 in the precursor mixture unnecessary, as the cross-section of Cl_2 at the laser wavelength exceeds that of Br_2 ($\sigma_{Cl_2} = 1.84\times10^{-19}$ cm^2 molecule^{-1} *cf.* $\sigma_{Br_2} = 4.10\times10^{-20}$ cm^2 molecule^{-1} [24]). Therefore, to verify the validity of the parameterisation of the ClO differential absorption cross-section reported by Boakes *et al*. under different experimental conditions, the same calibration procedure was carried out over the range T = 280-310 K using $Cl_2O/Cl_2/N_2$ gas mixtures.

The procedure developed by Boakes *et al*. to measure the differential absorption cross-section of ClO, $\sigma_{ClO\ diff}$, essentially relied on the use of the temperature and resolution

independent part of the recorded spectrum, the *continuum* region, to calibrate the vibronic structure. Thus, following the procedure by Boakes *et al.*, spectra were recorded over the range λ = 255-289 nm using a 600 grooves mm^{-1} diffraction grating; the width of the entrance slit to the spectrograph was set to 112 μm, giving rise to a resolution of 0.8 nm (FWHM), identical to that used by Boakes *et al*. A typical time-averaged absorbance spectrum recorded in this study (averaged over 5 ms immediately post-photolysis) is shown in Figure 4.3: it consists of a spectrally unstructured part at λ < 265 nm (the continuum region) and a structured component at higher wavelengths attributed to absorption corresponding to the ($A\,^2\Pi \leftarrow X\,^2\Pi$) vibronic transition of ClO. On the other hand, Cl_2O_2 and Cl_2O, which also absorb in the spectral window monitored, have smooth, unstructured cross-sections which depend very weakly upon resolution and temperature, as shown in Figure 4.5a. The cross-sections of Cl_2O_2 and Cl_2O were parameterised by least-squares fitting of a set of Gaussian functions to those recommended by JPL-NASA, [24] as illustrated in Appendix 4.

The Beer-Lambert Law for a $Cl_2O/Cl_2/N_2$ precursor mixture can be written as:

$$A_{t,\lambda} = \left(\sigma_{Cl_2O,\lambda}\Delta[Cl_2O]_t + \sigma_{ClO,\lambda}[ClO]_t + \sigma_{Cl_2O_2,\lambda}[Cl_2O_2]_t\right)\cdot l \qquad (4.ii)$$

where, aside from the positive contributions to the absorbance from ClO and Cl_2O_2, $\Delta[Cl_2O]_t$ is the *change* in $[Cl_2O]$ at time t following photolysis, which, since Cl_2O is removed upon photolysis and subsequent chemistry, is negative. Cl_2 was also present in the reaction mixture and is known to absorb light over the wavelength range adopted. However, its absorption cross-section at such wavelengths is so small, as illustrated in Figure 4.5a, that this species does not significantly affect the recorded absorbance and its inclusion in our analysis did not affect the final results.

Immediately following photolysis, at a time defined as t = 0, ClO radicals are promptly formed whereas the dimer has not been formed yet ($[Cl_2O_2]$ = 0), hence equation (4.ii) can be simplified to:

$$A_{0,\lambda} = l\left(\sigma_{Cl_2O,\lambda}\Delta[Cl_2O]_0 + \sigma_{ClO,\lambda}[ClO]_0\right) \qquad (4.iii)$$

Moreover, at $t = 0$, $\Delta[Cl_2O]_0 = -[ClO]_0$ by stoichiometry, regardless of how ClO is produced, as discussed in Section 4.2.1. Hence the expression for $A_{0,\lambda}$ can be simplified further to:

$$A_{0,\lambda} = l[\mathrm{ClO}]_0 \left(\sigma_{\mathrm{ClO},\lambda} - \sigma_{\mathrm{Cl_2O},\lambda}\right) \tag{4.iv}$$

Rearranging (4.iv), an expression for $[ClO]_0$ in terms of the immediate post-photolysis absorbance, $A_{\lambda,0}$, and of the continuum, and hence reference, cross-sections of ClO and Cl_2O, $\sigma_{\mathrm{ClO},\lambda}$ and $\sigma_{\mathrm{Cl_2O},\lambda}$, is obtained:

$$[\mathrm{ClO}]_0 = \frac{A_{0,\lambda}}{l\left(\sigma_{\mathrm{ClO},\lambda} - \sigma_{\mathrm{Cl_2O},\lambda}\right)} \tag{4.v}$$

where λ refers to any wavelength in the continuum region of the absorption spectrum (λ < 265 nm). At longer wavelengths, where the vibronic features of ClO appear, the *differential* (high-pass filtered) absorbance at time $t = 0$, $A_{\mathrm{diff}\ 0,\lambda}$, arises solely from ClO as contributions from any smooth absorbers have been filtered out, hence:

$$A_{\mathrm{diff}\ 0,\lambda} = \sigma_{\mathrm{ClO\ diff},\lambda}[\mathrm{ClO}]_0 l \tag{4.vi}$$

where here $\sigma_{\mathrm{ClO\ diff},\lambda}$ is the differential ClO cross section. Substituting (4.v) into (4.vi) gives:

$$A_{\mathrm{diff}\ 0,\lambda} = \frac{\sigma_{\mathrm{ClO\ diff},\lambda}}{\left(\sigma_{\mathrm{ClO},\lambda} - \sigma_{\mathrm{Cl_2O},\lambda}\right)} A_{0,\lambda} \tag{4.vii}$$

Equation (4.vii) shows that a plot of $A_{\mathrm{diff}\ 0,\lambda}$ against $A_{0,\lambda}$ from experiments with different initial ClO absorbances (*i.e.* different $[ClO]_0$) should result in a straight line passing through the origin and with gradient $\frac{\sigma_{\mathrm{ClO\ diff},\lambda}}{\left(\sigma_{\mathrm{ClO},\lambda} - \sigma_{\mathrm{Cl_2O},\lambda}\right)}$. Determination of such gradient hence allows calculation of $\sigma_{\mathrm{ClO\ diff},\lambda}$ since $\sigma_{\mathrm{ClO},\lambda}$ at continuum wavelengths and

$\sigma_{Cl_2O,\lambda}$ are well characterised in the literature and, crucially, do not show any temperature or resolution dependence. [27]

The calibrating wavelength chosen for the continuum absorbance was λ = 260 nm and the (12, 0) vibronic band was chosen for determining $A_{\text{diff } 0,\lambda}$, consistent with the work of Boakes *et al.* [4] and Bloss *et al.* [3]

Thanks to the unique properties of CCD detection, plots of absorbance at the continuum calibration wavelength as a function of time could be readily obtained from columns of transmission data. These traces were fitted to a kinetic model of ClO dimerisation, described in Section 4.2.4, with arbitrary kinetic parameters to allow back extrapolation to the true t = 0 necessary due to the inherent temporal averaging imparted on the data by the CCD system, described in Section 3.4.4. This fitting routine optimised values of $[ClO]_0$, $k_{4.1}$ and $k_{-4.1}$ *via* a least squares routine, although these arbitrary values were not used in any subsequent analysis as the sole purpose of fitting to the continuum trace was to carry out the short back extrapolation of absorbance to obtain $A_{0,\lambda}$. A typical plot of $A_{\lambda=260\text{nm}}$ as a function of time with back extrapolation to t = 0 is shown in Fig. 4.6.

By contrast, $A_{\text{diff } 0,\lambda}$ was obtained by generating a time averaged absorption spectrum

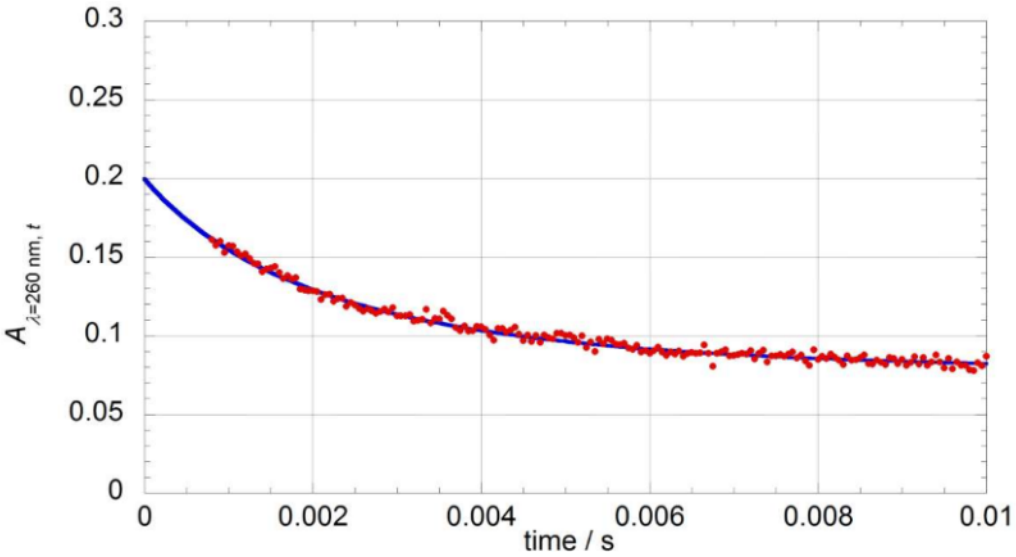

Figure 4.6 : Least squares fit of modelled A_λ (blue line) at λ = 260 nm, to time resolved data (red points), back extrapolated to t_0 in the absence of time averaging. Data points at t < 0.8 ms are not shown as they were not used in the fitting procedure.

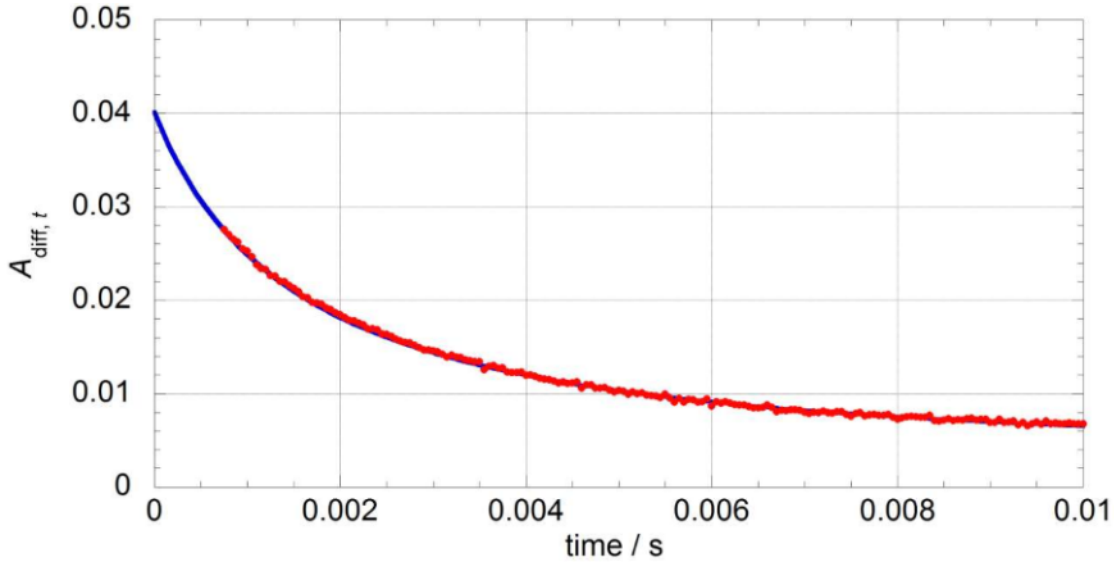

Figure 4.7 : Least squares fit of modelled A_{diff} (blue line) to time resolved data (red points), back extrapolated to $t = 0$ in the absence of time averaging. Data points at $t < 0.8$ ms are not shown as they were not used in the fitting procedure.

and fitting it *differentially* to each individual sequential spectrum for the same data set. This resulted in a temporal trace proportional to [ClO] which was least squares fitted to a kinetic model of ClO dimerisation to allow back extrapolation to $t = 0$. The value of the trace at $t = 0$ was then multiplied by the peak-to-trough difference for the (12, 0) band from the reference spectrum employed to generate the temporal trace, to obtain the true value of $A_{\text{diff } 0,\lambda}$. A plot of $A_{\text{diff } t,\lambda}$ and the corresponding back extrapolation is shown in Figure 4.7.

As discussed above, provided a range of initial absorbances in both spectral regions is available, equation (4.vii) may be corroborated and the ClO differential cross-section obtained. This range was achieved by undertaking experiments at different concentrations of Cl_2 in the precursor mixture so that variation in the absorbance at $t = 0$ resulted from changing the initial concentration of [ClO] radicals.

Calibration of $\sigma_{\text{ClO diff}}$ was carried out at five temperatures over the range $T = 280$-310 K. The measured values of $A_{\text{diff } 0,\lambda}$ and $A_{0,\lambda}$ are given in Table 4.2 and the resulting calibration plots of $A_{\text{diff } 0,\lambda}$ against $A_{0,\lambda}$ are shown in Figures 4.8 and 4.9 for $T = 298$ K and all other temperatures respectively. These plots show excellent linearity and near-zero intercepts, as predicted by equation (4.vii), at all temperatures.

T / K	$[Cl_2]_{initial}$ / 10^{16} molecule cm^{-3}	$A_{0,\lambda}$	$A_{\text{diff } 0,\lambda}$
280	1.37	0.0662 ± 0.0007	0.0642 ± 0.0007
	2.06	0.1205 ± 0.0012	0.1287 ± 0.0024
	2.75	0.1697 ± 0.0012	0.1811 ± 0.0018
	3.43	0.2059 ± 0.0019	0.2297 ± 0.0015
	4.12	0.2486 ± 0.0015	0.2790 ± 0.0022
288	1.33	0.0529 ± 0.0013	0.0640 ± 0.0007
	2.00	0.1101 ± 0.0012	0.1258 ± 0.0047
	2.67	0.1570 ± 0.0016	0.1829 ± 0.0016
	3.34	0.1998 ± 0.0020	0.2324 ± 0.0007
	4.00	0.2288 ± 0.0021	0.2793 ± 0.0020
298	1.29	0.0605 ± 0.0017	0.0626 ± 0.0013
	1.93	0.1069 ± 0.0023	0.1177 ± 0.0011
	2.58	0.1540 ± 0.0030	0.1682 ± 0.0008
	3.27	0.1927 ± 0.0041	0.2176 ± 0.0011
	3.87	0.2240 ± 0.0044	0.2584 ± 0.0016
303	1.27	0.0558 ± 0.0013	0.0539 ± 0.0006
	1.90	0.1086 ± 0.0020	0.1035 ± 0.0004
	2.54	0.1533 ± 0.0019	0.1477 ± 0.0004
	3.17	0.1955 ± 0.0007	0.1873 ± 0.0007
	3.81	0.2262 ± 0.0019	0.2235 ± 0.0019
310	1.24	0.0540 ± 0.0012	0.0561 ± 0.0011
	1.86	0.1018 ± 0.0015	0.1025 ± 0.0010
	2.48	0.1509 ± 0.0012	0.1446 ± 0.0009
	3.10	0.1835 ± 0.0009	0.1844 ± 0.0009
	3.72	0.2328 ± 0.0034	0.2203 ± 0.0030

Table 4.2 : Experimentally determined values of $A_{0,\lambda}$ and $A_{\text{diff } 0,\lambda}$ Errors are 2σ, statistical only, from typically five repeated experiments.

As the gradient of these plots corresponds to $\frac{\sigma_{\text{ClO diff (12,0)}}}{\left(\sigma_{\text{ClO,260 nm}} - \sigma_{\text{Cl}_2\text{O,260 nm}}\right)}$, determination of $\sigma_{\text{ClO diff}}$ at the (12, 0) band required knowledge of the absorption cross-sections of ClO and Cl_2O at the continuum wavelength (λ = 260 nm), which are well-defined in the literature. As the temperature dependence of these cross-sections is negligible, all

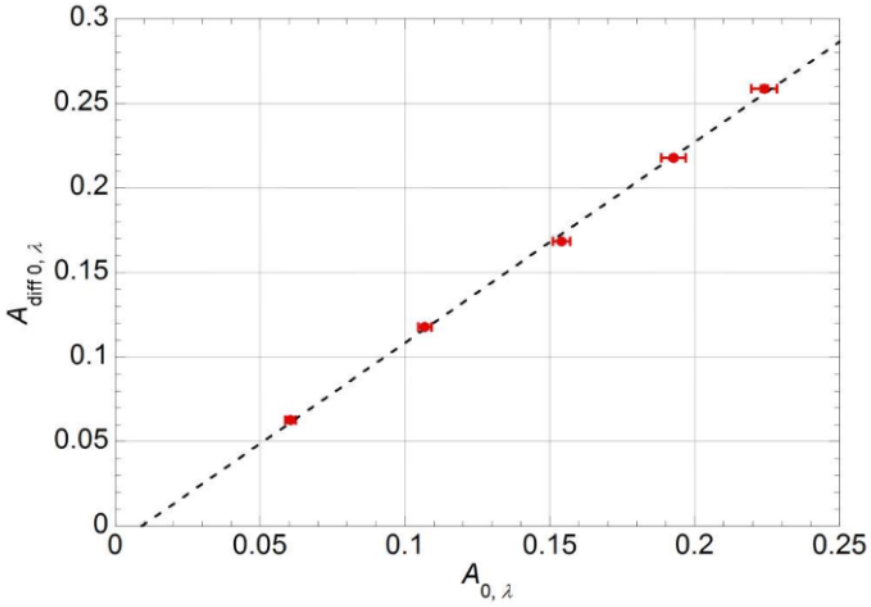

Figure 4.8 : Calibration plot of $A_{\text{diff } 0,\lambda}$ versus $A_{0,\lambda}$ obtained from photolysis of $Cl_2O/Cl_2/N_2$ gas mixtures at $T = 298$ K.

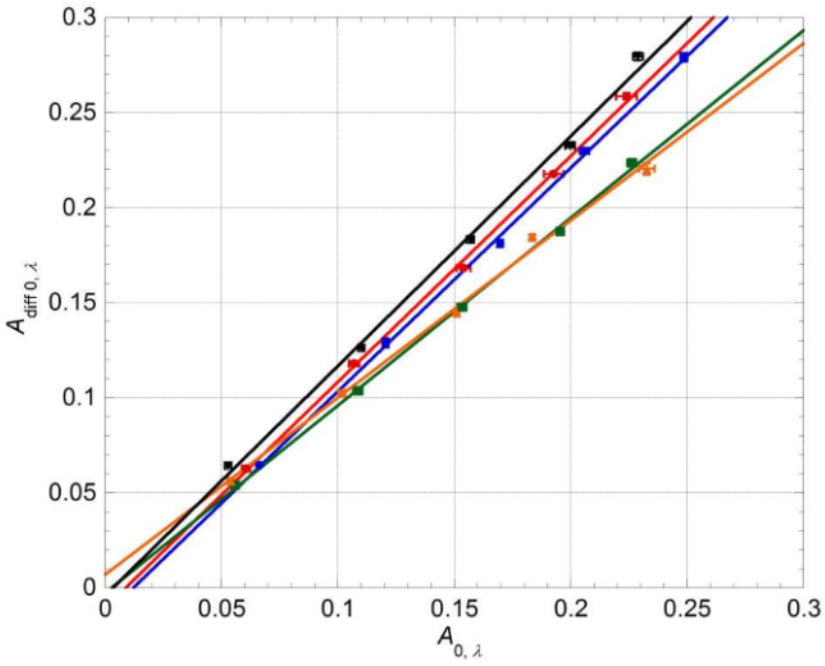

Figure 4.9 : Calibration plots of $A_{\text{diff } 0,\lambda}$ versus $A_{0,\lambda}$, obtained from photolysis of $Cl_2O/Cl_2/N_2$ gas mixtures, at different temperatures: $T = 310$ K (in orange), $T = 303$ K (in green), $T = 298$ K (in red), $T = 288$ K (in black), $T = 280$ K (in blue).

T/K	$\sigma_{ClO\ diff}$ /10^{-18} cm^{2}molecule^{-1}
280	3.75 ± 0.06
288	3.85 ± 0.13
298	3.79 ± 0.08
303	3.14 ± 0.06
310	2.97 ± 0.10

Table 4.3 : Results for the temperature dependence of $\sigma_{ClO\ diff}$. Errors are ±2σ, statistical only.

determinations of $\sigma_{ClO\ diff}$ over the range T = 280-310 K used the values of $\sigma_{ClO\ 260\ nm}$ and $\sigma_{Cl_2O\ 260\ nm}$ reported at T = 298 K.

Five values of $\sigma_{ClO\ diff}$ were obtained at each temperature; averages of these values are shown in Table 4.3 and plotted in Figure 4.10 along with the parameterisation of $\sigma_{ClO\ diff}$ from Boakes *et al.* [4]

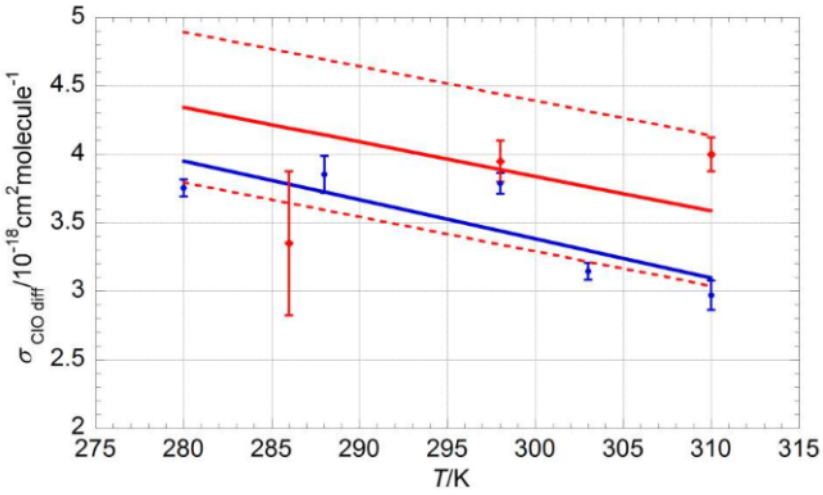

Figure 4.10 : Temperature dependence of $\sigma_{ClO\ diff}$ for the (12, 0) vibronic absorption band of ClO at 0.8 nm (FWHM) spectral resolution. Data from the present work are shown as blue circles along with the resulting parameterisation (blue line). Also shown are the data points from Boakes *et al.* [4] (red diamonds) along with the resulting parameterisation (solid red line) and its associated errors (dashed red lines).

An unweighted linear fit to the measured $\sigma_{\mathrm{ClO\ diff}}$ returned the following parameterisation:

$$\sigma_{\mathrm{ClO\ diff}}/\mathrm{cm}^2\ \mathrm{molecule}^{-1} = (1.07 \pm 0.33) \times 10^{-17} - \{(2.46 \pm 1.1) \times 10^{-20}\ T\} \qquad (4.\mathrm{viii})$$

which is in excellent agreement with that determined by Boakes *et al*. for the same vibronic band at the same experimental resolution:

$$\sigma_{\mathrm{ClO\ diff}}/\mathrm{cm}^2\ \mathrm{molecule}^{-1} = (1.14 \pm 0.11) \times 10^{-17} - \{(2.52 \pm 0.45) \times 10^{-20}\ T\} \qquad (4.\mathrm{ix})$$

Equation (4.viii) was employed to calibrate the entire structured wavelength region of each spectrum using the expression:

$$\sigma_{\mathrm{ClO}} = A_{\lambda} \times \frac{\sigma_{\mathrm{ClO\,diff\,(12,0)}}}{A_{\mathrm{diff\,(12,0)}}} \qquad (4.\mathrm{x})$$

Equation (4.x) allowed the generation of a calibrated ClO cross-section from every experimental spectrum at every experimental temperature. These cross-sections were subsequently fitted *differentially* to every time-resolved spectrum in each kinetic run according to the Beer-Lambert law to generate time resolved [ClO] traces. These experimental traces were used in the kinetic and thermochemical analyses described in the following sections.

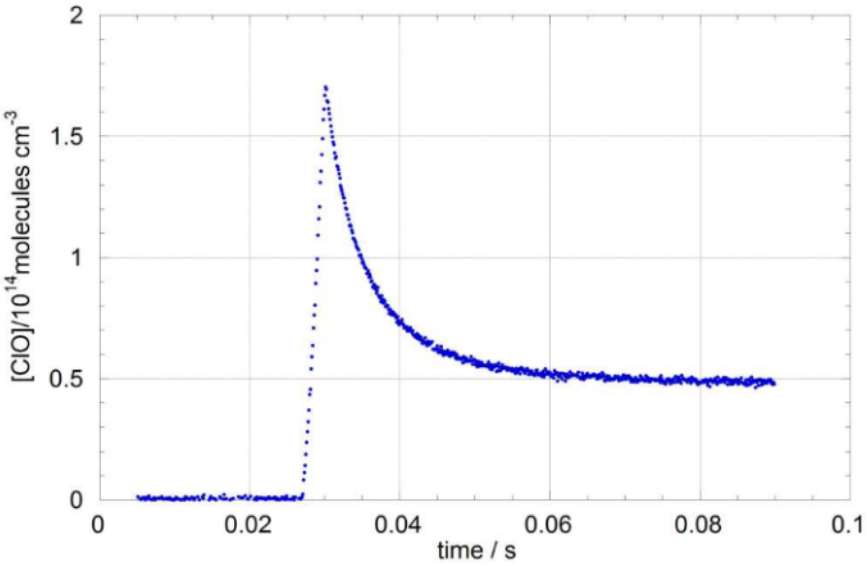

Figure 4.11 : Typical $[ClO]_t$ trace recorded at T = 285.8 K using a Cl_2O/Cl_2/air precursor mixture with photolysis initiated at t = 0.027 s.

4.2.4 Kinetic analysis

The $[ClO]_t$ temporal traces recorded in this work confirmed rapid radical generation compared to decay, as designed and described in Section 4.2.1. As shown in the example trace in Figure 4.11, following rapid radical formation, [ClO] decayed to an equilibrium concentration attributed to the reversible ClO dimerisation:

$$ClO + ClO + M \quad \leftrightarrows \quad Cl_2O_2 + M \qquad (4.1, -4.1)$$

By describing ClO dimerisation as the combination of two elementary steps, reactions (4.1) and reaction (−4.1), the rate of reaction can be written as:

$$-\frac{1}{2}\frac{d[ClO]}{dt} = \frac{d[Cl_2O_2]}{dt} = k_{4.1}[ClO]^2 - k_{-4.1}[Cl_2O_2] \qquad (4.xi)$$

The exact solution to this differential equation is complex but can be obtained by making the following substitution:

$$[ClO] = [ClO]_{eq} + 2x \qquad (4.xii)$$

where $2x$ is the concentration of ClO radicals in excess of the equilibrium concentration of ClO, $[ClO]_{eq}$. It follows that, by stoichiometry:

$$[Cl_2O_2] = [Cl_2O_2]_{eq} - x \tag{4.xiii}$$

where $[Cl_2O_2]_{eq}$ is the concentration of the ClO dimer at equilibrium. By differentiating equation (4.xiii), and noting that $[Cl_2O_2]_{eq}$ is a constant, an expression for the rate of formation of the ClO dimer is obtained:

$$\frac{d[Cl_2O_2]}{dt} = -\frac{dx}{dt} \tag{4.xiv}$$

Combining equations (4.xi), (4.xii) and (4.xiii) gives:

$$-\frac{dx}{dt} = k_{4.1}\left([ClO]_{eq} + 2x\right)^2 - k_{-4.1}\left([Cl_2O_2]_{eq} - x\right) \tag{4.xv}$$

The equilibrium constant is defined as:

$$K_{eq} = \frac{[Cl_2O_2]_{eq}}{[ClO]_{eq}^2} = \frac{k_{4.1}}{k_{-4.1}} \tag{4.i}$$

which can be conveniently rearranged to give:

$$k_{4.1}[ClO]_{eq}^2 = k_{-4.1}[Cl_2O_2]_{eq} \tag{4.xvi}$$

Substituting equation (4.xvi) into equation (4.xv) and expanding the quadratic term in equation (4.xv) returns the following expression:

$$-\frac{dx}{dt} = 4k_{4.1}[ClO]_{eq}x + 4k_{4.1}x^2 + k_{-4.1}x \tag{4.xvii}$$

Equation (4.xvii) can be rearranged as follows:

$$\frac{dx}{x\left(4k_{4.1}[\mathrm{ClO}]_{\mathrm{eq}} + 4k_{4.1}x + k_{-4.1}\right)} = -dt \qquad \text{(4.xviii)}$$

Equation (4.xviii) is a differential equation of the form:

$$\frac{dx}{x(a+bx)} = -dt$$

where $a = (4k_{4.1}[\mathrm{ClO}]_{\mathrm{eq}} + k_{-4.1})$ and $b = 4k_{4.1}$. This expression can be integrated between limits of t and 0 (defined here as immediately post-photolysis):

$$\int_{x_0}^{x_t} \frac{dx}{x(a+bx)} = -\int_0^t dt \qquad \text{(4.xix)}$$

Integrating gives:

$$-\frac{1}{a}\ln\left(\frac{a+bx_t}{x_t}\right) + \frac{1}{a}\ln\left(\frac{a+bx_0}{x_0}\right) = -t$$

$$\ln\left(\frac{a+bx_0}{x_0} \cdot \frac{x_t}{a+bx_t}\right) = -at$$

Thus,

$$x_t = \frac{ax_0\exp(-at)}{a + bx_0 - bx_0\exp(-at)} \qquad \text{(4.xx)}$$

Therefore equation (4.xii), combined with equation (4.xx), can be used to describe the temporal decay of ClO radicals following photolysis, given that:

$$[\mathrm{ClO}]_t = [\mathrm{ClO}]_{\mathrm{eq}} + 2x_t \qquad \text{(4.xii)}$$

It can be shown that the variables a, b, x_0, as well as $[\mathrm{ClO}]_{\mathrm{eq}}$, necessary to produce the simulated $[\mathrm{ClO}]_t$ trace, can all be obtained from the initial ClO concentration, $[\mathrm{ClO}]_0$, $k_{4.1}$ and $k_{-4.1}$. The concentration of the ClO dimer at equilibrium corresponds to the amount of ClO radicals produced directly after photolysis minus the equilibrium concentration halved; therefore the expression for the equilibrium constant, equation (4.1), can be rewritten as:

$$K_{\mathrm{eq}} = \frac{\left([\mathrm{ClO}]_0 - [\mathrm{ClO}]_{\mathrm{eq}}\right)/2}{[\mathrm{ClO}]_{\mathrm{eq}}^2} = \frac{k_{4.1}}{k_{-4.1}} \qquad \text{(4.xxi)}$$

This expression can be readily rearranged into a quadratic function in $[\mathrm{ClO}]_{\mathrm{eq}}$. Of the two roots, only one is positive and therefore $[\mathrm{ClO}]_{\mathrm{eq}}$ can be expressed in terms of $[\mathrm{ClO}]_0$ and K_{eq} (*i.e.* $k_{4.1}/k_{-4.1}$) as follows:

$$[\mathrm{ClO}]_{\mathrm{eq}} = \frac{-1 + \sqrt{1 + 8[\mathrm{ClO}]_0 K_{\mathrm{eq}}}}{4K_{\mathrm{eq}}} \qquad \text{(4.xxii)}$$

This definition of $[\mathrm{ClO}]_{\mathrm{eq}}$ is used in the determining variable a, whereas variable b is calculated using the input value of $k_{4.1}$. x_0 is then obtained by simply rearranging equation (4.xii) using $t = 0$:

$$x_0 = \frac{[\mathrm{ClO}]_{\mathrm{eq}} + [\mathrm{ClO}]_0}{2} \qquad \text{(4.xxiii)}$$

Simulated $[\mathrm{ClO}]_t$ using equation (4.xii), combined with equation (4.xx), was fitted to experimental ClO decay traces by varying $[\mathrm{ClO}]_0$, $k_{4.1}$ and $k_{-4.1}$ *via* a least-squares routine. K_{eq} was determined as the ratio of the rate constants of the forward and reverse reactions (4.1, −4.1). A typical plot of the $[\mathrm{ClO}]_t$ decay obtained by fitting equation (4.xii) to an experimental ClO decay trace is shown in Figure 4.12.

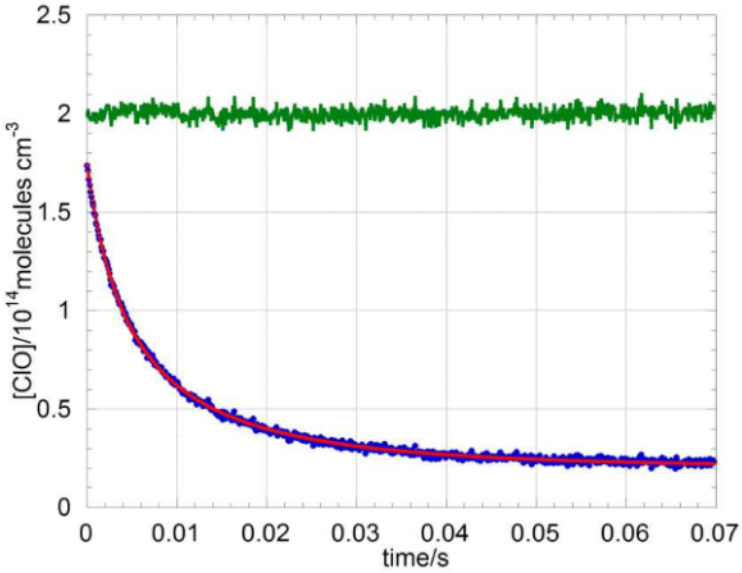

Figure 4.12 : Classical model fit (red line) to an experimental $[ClO]_t$ decay trace (blue points) recorded at T = 270.4 K from the photolysis of a $Cl_2O/Cl_2/N_2$ precursor mixture. The magnified (×5) residuals (in green) have been offset by $+2\times10^{14}$ molecules cm^{-3} for clarity.

The excellent quality of the fit of a kinetic model based on the solution of the differential equations for a two-reaction system describing ClO dimerisation (with a small correction for gas flowout) lent further confidence to the extraction of a 'pure' $[ClO]_t$ signal from the differential spectral fitting procedure.

To further confirm the validity of the exact kinetic solution to the pure dimerisation model, the commercial numerical integration package FACSIMILE [28] was used to build a reaction model comprising all the known reactions occurring in the cell as well as physical processes such as gas flow-out. A list of the reactions included in the FACSIMILE model and their rate constants is given in Table 4.4 for both the Cl_2O/Cl_2/carrier gas and the Cl_2/O_3/air systems. The output of the FACSIMILE model was also fitted to the experimental $[ClO]_t$ decay traces by optimising the values of $[ClO]_0$, $k_{4.1}$ and $k_{-4.1}$ *via* least-squares routines, therefore allowing determination of K_{eq}. The FACSIMILE model was also used to carry out sensitivity studies which are described in Section 4.2.4 below. The results obtained from the FACSIMILE model at ambient and sub-ambient temperatures were in excellent agreement with those obtained from the classical kinetic model, with the returned values of K_{eq} from the two different analyses within < 1% at most temperatures.

Reaction	k/cm^{3}molecule^{-1}s^{-1}	*reference*
Cl_2O/Cl_2/carrier system		
$Cl + Cl_2O \rightarrow Cl_2 + ClO$	$6.2 \times 10^{-11}\exp(130/T)$	24
$ClO + ClO \rightarrow Cl_2 + O_2$	$1 \times 10^{-12}\exp(-1590/T)$	24
$ClO + ClO \rightarrow OClO + Cl$	$3.5 \times 10^{-13}\exp(-1370/T)$	24
$ClO + ClO \rightarrow Cl + ClOO$	$3.0 \times 10^{-11}\exp(-2450/T)$	24
$ClO + ClO \rightarrow Cl_2O_2$	$k_{4.1}$ [c]	*this work*
$Cl_2O_2 \rightarrow ClO + ClO$	$k_{-4.1}$ [a, c]	*this work*
$ClOO + Cl \rightarrow Cl_2 + O_2$	2.3×10^{-10} [b]	24
$ClOO + Cl \rightarrow ClO + ClO$	1.2×10^{-11} [b]	24
$Cl_2O + ClO \rightarrow Cl_2 + O_2 + Cl$	1.08×10^{-15} [b]	29
$ClO + OClO \rightarrow Cl_2O_3$	$1.9 \times 10^{-14}\exp(1250/T)$ [c]	24
$Cl_2O_3 \rightarrow ClO + OClO$	$1.2 \times 10^{13}\exp(-5905/T)$ [a, c]	24
$Cl + Cl_2O_2 \rightarrow Cl_2 + ClOO$	1.0×10^{-10} [b]	24
$Cl + OClO \rightarrow ClO + ClO$	$3.4 \times 10^{-11}\exp(160/T)$	24
$Cl + O_2 \rightarrow ClOO$	$1.25 \times 10^{-15}\exp(1129/T)$ [c]	24
$ClOO \rightarrow Cl + O_2$	$1.89 \times 10^{9}\exp(-1372/T)$ [a, c]	24
Cl_2/O_3/air system		
$Cl + O_3 \rightarrow ClO + O_2$	$2.3 \times 10^{-11}\exp(-200/T)$	24
$ClO + ClO \rightarrow Cl_2 + O_2$	$1 \times 10^{-12}\exp(-1590/T)$	24
$ClO + ClO \rightarrow OClO + Cl$	$3.5 \times 10^{-13}\exp(-1370/T)$	24
$ClO + ClO \rightarrow Cl + ClOO$	$3.0 \times 10^{-11}\exp(-2450/T)$	24
$ClO + ClO \rightarrow Cl_2O_2$	$k_{4.1}$ [c]	*this work*
$Cl_2O_2 \rightarrow ClO + ClO$	$k_{-4.1}$ [a, c]	*this work*
$ClOO + Cl \rightarrow Cl_2 + O_2$	2.3×10^{-10} [b]	24
$ClOO + Cl \rightarrow ClO + ClO$	1.2×10^{-11} [b]	24
$ClO + OClO \rightarrow Cl_2O_3$	$1.9 \times 10^{-14}\exp(1250/T)$ [c]	29
$Cl_2O_3 \rightarrow ClO + OClO$	$1.2 \times 10^{13}\exp(-5905/T)$ [a, c]	24
$Cl + Cl_2O_2 \rightarrow Cl_2 + ClOO$	1.0×10^{-10} [b]	24
$Cl + OClO \rightarrow ClO + ClO$	$3.4 \times 10^{-11}\exp(160/T)$	24
$Cl + O_2 \rightarrow ClOO$	$1.25 \times 10^{-15}\exp(1129/T)$ [c]	24
$ClOO \rightarrow Cl + O_2$	$1.89 \times 10^{9}\exp(-1372/T)$ [a, c]	24

Notes [a]: units s^{-1}

[b]: k at $T = 298$ K

[c]: k at $p = 760$ Torr

Table 4.4 : Reactions used for the FACSIMILE model of ClO dimerisation and their rate constants expressed in the Arrhenius form, $k = A\exp(-E_a/RT)$ where possible.

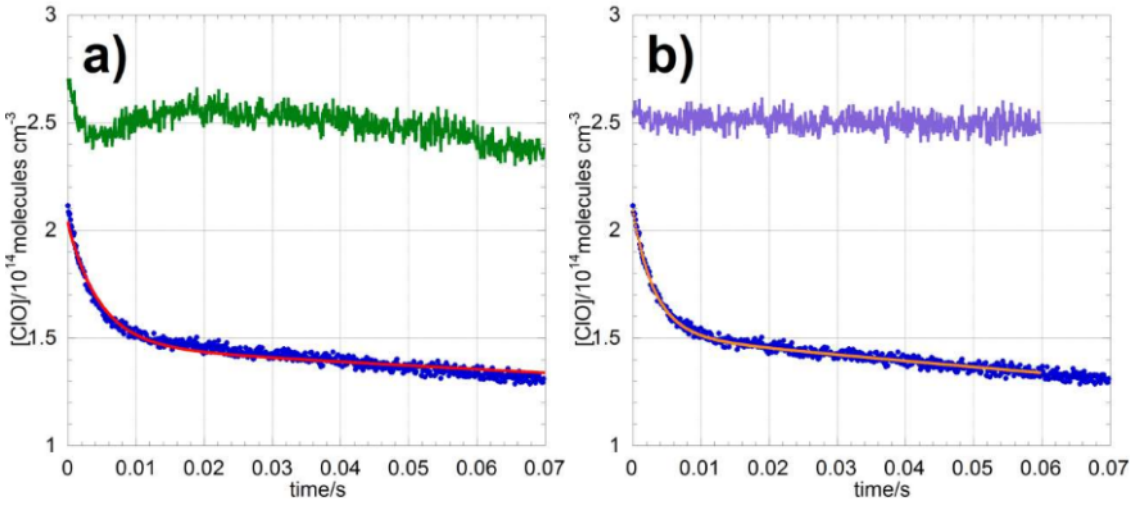

Figure 4.13 : Typical [ClO] decay trace recorded at T = 312.6 K and p = 760 Torr (blue data points) from the photolysis of $Cl_2O/Cl_2/N_2$ mixtures. Least squares fits to the experimental trace (solid line) from a) the analytical solution to the ClO rate equation and b) from FACSIMILE are also shown. In both figures the magnified (×5) residuals from the fits have been offset by +2.5 × 10^{14} molecule cm^{-3} for clarity.

However, above ambient temperature (T > 298 K), the classical kinetic model fits to the experimental data were found to be somewhat poorer than the corresponding FACSIMILE fits. For example, at T = 312.6 K, the average residuals of the classical kinetic model fit were found to be 45% greater than those of the FACSIMILE fit. This is shown graphically in Figure 4.13. This discrepancy arose from the fact that dimerisation is not the only fate of two ClO radicals reacting together: as described in Section 4.1.1, three pressure-independent so-called "bimolecular" channels are also known:

ClO + ClO	→	$Cl_2 + O_2$	(4.1b)
	→	Cl + ClOO	(4.1c)
	→	OClO + Cl	(4.1d)

At ambient temperature, these reactions constitute minor channels of the ClO self-reaction ($k_{4.1b} + k_{4.1c} + k_{4.1d} \approx 0.068\ k_{4.1}$, at T = 298 K, p = 760 Torr). [24] Furthermore, under the experimental conditions of excess $[Cl_2O]$ (and $[O_3]$) adopted in this work, the rapid reconversion of Cl to ClO implied that some of these bimolecular channels effectively did not operate. In channel (4.1c), the ClOO product is known to be

unstable and rapidly dissociates to Cl + O_2 (k (ClOO → Cl + O_2) = 1.89 × 10^7 s^{-1} at T = 298 K and p = 760 Torr). [24] Thus two chlorine atoms are effectively produced in (4.1c) and this channel would not contribute to the observed decay of ClO in excess [Cl_2O] as ClO is instantly regenerated. Similarly in (4.1d) a single Cl atom is formed and the effective rate constant for ClO loss through channel (4.1d) would be halved. However, as the rate constants for all of the bimolecular channels have positive temperature dependence, these reactions did distort the ClO decay away from pure dimerisation kinetics as the temperature was increased. This interference was accounted for in the numerical integration modelling to extract $k_{4.1}$, $k_{-4.1}$ and K_{eq} , and was also used to define the upper limit of temperature for these studies, as discussed below.

4.2.5 Sensitivity analysis and temperature limits

As the temperature was lowered below T = 298 K, the observed rate constant for the forward reaction $k_{4.1}$ for ClO dimerisation increased, as reported in previous studies [2, 3, 4, 9] whereas that of the reverse reaction (–4.1) markedly decreased, which is unsurprising given that reaction (–4.1) is the thermal decomposition of the ClO dimer. Furthermore, in the initial series of experiments, those carried out using $Cl_2O/Cl_2/N_2$ precursor mixtures, it was found that, at T = 250.1 K, neither the kinetic model nor the FACSIMILE model would readily converge to a stable value for $k_{-4.1}$. In addition, the value of K_{eq} obtained at this temperature was inconsistent with the trend exhibited by the other temperature data, as shown in Section 4.3 below. Procedures were therefore devised to test and show the sensitivity of the observed ClO decay traces to $k_{-4.1}$, and therefore K_{eq}, at low temperatures. To this purpose, it is useful to consider a simple second-order reaction:

$$A + A \rightarrow \text{products} \qquad (4.9)$$

From classical kinetics, the rate of decay of reagent [A] can be expressed as:

$$-\frac{d[A]}{dt} = 2k_{4.9}[A]^2 \qquad (4.xxiv)$$

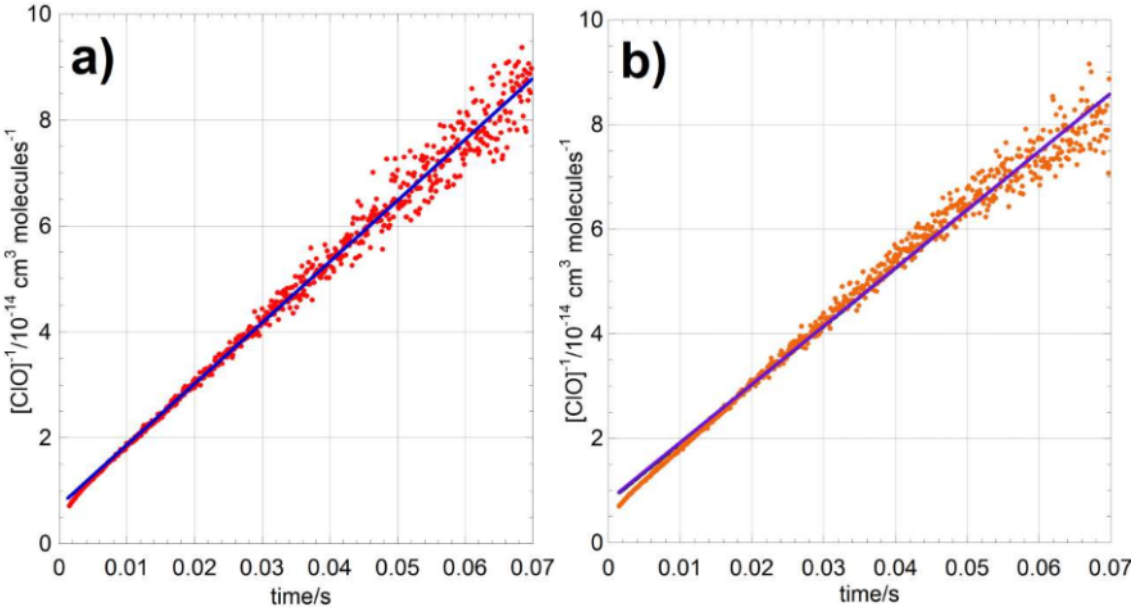

Figure 4.14 : Second order plots ($1/[ClO]_t$ *vs* time) for [ClO] traces recorded a) at T = 250.1 K and b) T = 256.5 K at p = 760 Torr (data points). Also shown are the linear fits to both datasets (solid lines).

Separating the variables and integrating between time $t = 0$ and t gives an expression for the decay of [A] as a function of time:

$$\frac{1}{[A]_t} = 2k_{4.9}t + \frac{1}{[A]_0} \qquad (4.xxv)$$

Therefore, for such an irreversible second-order reaction, a plot of the reciprocal of the concentration of the reactants should be linearly proportional to time. A plot of $1/[ClO]_t$ against time for a ClO trace recorded at T = 250.1 K from $Cl_2O/Cl_2/N_2$ showed linearity, as illustrated in Figure 4.14(a), implying *irreversible* loss of the ClO radicals. By contrast, the analogous plot from data recorded at T = 256.5 K, Figure 4.14(b), did exhibit an appreciable degree of non-linearity, implying deviation from irreversible second-order loss of ClO radicals and hence in principle sensitivity to Cl_2O_2 decomposition. As an illustration of this, these low temperature traces were fitted to both a model of irreversible second-order loss of ClO (including secondary chemistry) and to a model including reversible dimerisation of ClO, and (whilst not physically meaningful) the mean residuals of these fits were compared. Figure 4.15 shows that, at T = 250.1 K, the ratio of the residuals for these two fits did not differ significantly from

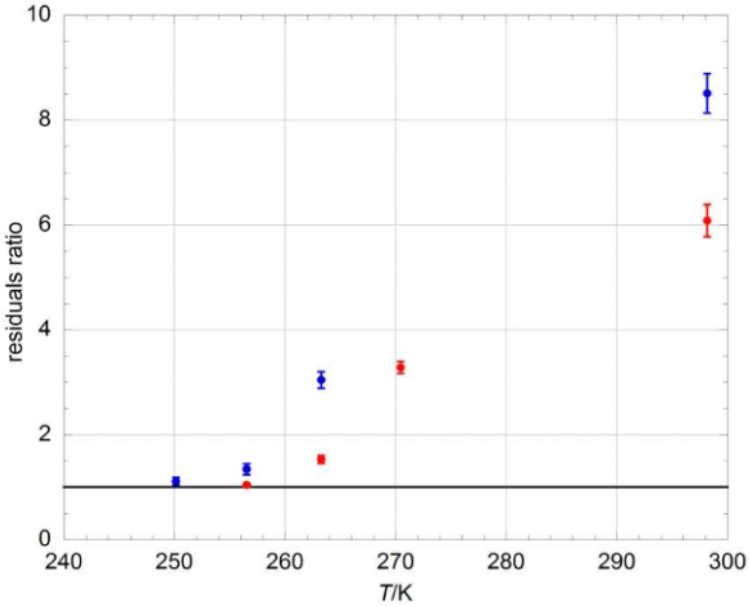

Figure 4.15 : Reversion to second order kinetics for ClO dimerisation at low temperatures for Cl_2O/Cl_2/air (blue points) and Cl_2/O_3/air (red points) precursor mixtures. Both a kinetic model of ClO equilibration and one of irreversible ClO second order decay were fitted to experimental traces: the ratio of the average residuals from each fit are shown as a function of temperature. When the ratio between residuals tends to one (solid line), the model does not distinguish between irreversible second order kinetics and reversible equilibration.

unity, indicating a loss of sensitivity to the reverse reaction (–4.1). T = 256. 5 K was therefore taken as the lowest temperature to determine K_{eq} in the experiments employing Cl_2O/Cl_2/carrier precursor mixtures.

An analogous sensitivity analysis was performed for traces obtained as a function of temperature from the photolysis of Cl_2/O_3/air precursor mixtures. In this case, traces measured at T = 256.5 K showed loss of sensitivity to the reverse reaction, as also illustrated in Figure 4.15. The loss of sensitivity to the reverse reaction at a higher temperature than that found for the Cl_2O/Cl_2/carrier system could be readily rationalised in terms of the initial concentration of ClO, $[ClO]_0$. Under otherwise identical conditions, $[ClO]_0$ from Cl_2/O_3/air mixtures was typically lower than that obtained from Cl_2O/Cl_2/carrier mixtures by 30-40 %. This arose from the absence of an additional source of ClO radicals in the Cl_2/O_3/air system (*i.e.* direct Cl_2O photolysis). Also contributory was the slower kinetics of ClO formation in the ozone containing system, which were in turn the result of the smaller rate constants of the reaction generating ClO ($k_{4.6} \approx 8 \times k_{4.9}$ at T = 298 K [24]), and also of the smaller concentration of ozone employed

relative to that of Cl_2O ($[O_3]$ could not be increased for the reasons elucidated in Section 4.2.1). It follows from equation (4.xxii) that, as the initial concentration of ClO radical is lowered, the equilibrium concentration of ClO radicals following the initial decay is also smaller and, when $[ClO]_{eq}$ falls below the noise threshold limit, sensitivity to the reverse reaction (−4.1) is effectively lost. T = 263.2 K was therefore the lowest temperature in the experiments using Cl_2/O_3/air precursor mixtures.

A sensitivity study was also carried out to investigate how uncertainties in the kinetic parameters for other reactions in the model used for numerical integration (shown in Table 4.4) propagated into potential uncertainty into $k_{4.1}$, $k_{-4.1}$ and hence K_{eq}. At each temperature, a representative $[ClO]_t$ decay trace was reanalysed using a model with one of the kinetic parameters perturbed upwards or downwards by a factor of two (*i.e.* doubled or halved). Results from this analysis showed that uncertainty in the reactions included in the FACSIMILE model had a minimal (much less than 1%) effect on the dimerisation equilibrium constant at most temperatures. This lack of interference was expected, on the basis of a two reaction (4.1, –4.1) model providing an excellent fit to the $[ClO]_t$ temporal traces as discussed above. However, at the highest temperatures used, uncertainty on the rate coefficients for the bimolecular channels of the ClO self-reaction did start to propagate into uncertainty in K_{eq}. At the highest temperature used in this study, T = 312.6 K, it was found that the perturbed value of K_{eq} differed from the original value by +2.08% when the rate coefficient for reaction (4.1b) (the bimolecular channel of ClO + ClO yielding Cl_2 + O_2) was halved. This alteration of $k_{4.1b}$ exceeds the reported recommended uncertainty on $k_{4.1b}$ at this temperature [24] but, taking an approximate 2% change as a limit to the potential perturbation of K_{eq}, T = 312.6 K was therefore taken as the highest temperature in this study. Thus, whilst the temperature span of this study appears narrow (~ 56 K), both the upper and (especially) lower limits of temperature taken were clearly defined by sensitivity analyses. Furthermore, as shown below, the equilibrium constant for ClO dimerisation varies by a factor of nearly a thousand over this temperature range, due to the profound temperature dependence of reaction (−4.1).

A further sensitivity study was conducted to investigate the effects of uncertainty in the absorption cross-sections of the ClO radical on the derived values of K_{eq}. Data at each

temperature were re-analysed with the $\sigma_{ClO\ diff}$ placed at both the upper and lower bounds of uncertainty, as indicated in the parameterisation in equation (4.viii). As expected, an increase in the (differential) cross-section of ClO led to a proportional increase in the forward reaction rate constant $k_{4.1}$ and consequently an increase in K_{eq}. Given the relatively large (~15%) errors obtained from the parameterisation of the ClO absorption cross-sections shown in equation (4.viii), the effect on the absolute value of the equilibrium constants of perturbing $\sigma_{ClO\ diff}$ to these limits was significant, up to a factor of two at the extremes of temperature. However, the difference in the effect of perturbing $\sigma_{ClO\ diff}$ on the temperature dependence of the equilibrium constants was somewhat smaller, as reflected in the thermochemical parameters (notably $\Delta_r H$) discussed below.

All experiments were performed under ambient (atmospheric) pressure. The pressure in the laboratory fluctuated over the range p = 760 ± 20 Torr. As reactions (4.1, −4.1) exhibit pressure-dependence, fluctuations in ambient pressure could potentially affect the extracted kinetic parameters. Simulations run using the Troe formalism, described in Section 2.1.4, showed that the effect of pressure fluctuations of this magnitude on $k_{4.1}$ and $k_{-4.1}$ were minimal (< 2%) and the effect on K_{eq} even smaller.

4.3 Results

ClO dimerisation was studied at ten temperatures, with at least six experiments at each temperature, over the temperature range T = 250.1-312.6 K and at p = 760 Torr, using each of the $Cl_2O/Cl_2/N_2$, $Cl_2O/Cl_2/O_2$, Cl_2O/Cl_2/air and Cl_2/O_3/air precursor gas mixtures. Each experiment typically involved 25-50 photolysis events. As discussed above, the data recorded at T = 250.1 K with Cl_2O/Cl_2/carrier precursor mixtures showed no sensitivity to the reverse reaction (–4.1) and were not used in subsequent analysis. Similarly, the data obtained from Cl_2/O_3/air precursor mixtures at T = 256.5 K showed irreversible second-order kinetics and were not used in the subsequent analysis. All recorded values for $k_{4.1}$, $k_{-4.1}$ and K_{eq} are however given in Tables 4.5, 4.6 and 4.7.

$k_{4.1}/10^{-13}$ cm^3 molecule^{-1} s^{-1}				
***T*/K**	**$Cl_2O/Cl_2/N_2$**	**$Cl_2O/Cl_2/O_2$**	**Cl_2O/Cl_2/air**	**Cl_2/O_3/air**
250.1	6.9 ± 0.4*			
256.5	6.49 ± 0.12		6.4 ± 0.12	6.45 ± 0.2*
263.2	6.21 ± 0.21		6.10 ± 0.09	6.17 ± 0.28
270.4	5.96 ± 0.14	5.35 ± 0.13	6.15 ± 0.13	5.95 ± 0.24
277.9	5.52 ± 0.24		5.40 ± 0.09	5.23 ± 0.18
285.8	4.73 ± 0.05		4.74 ± 0.08	4.66 ± 0.22
294.2	4.16 ± 0.08		3.59 ± 0.06	3.90 ± 0.08
298	3.84 ± 0.08	3.47 ± 0.08	3.77 ± 0.04	3.46 ± 0.14
303.1	3.5 ± 0.12		3.10 ± 0.08	3.06 ± 0.08
312.6	2.84 ± 0.12	2.67 ± 0.1	2.01 ± 0.09	2.52 ± 0.08

Table 4.5 : Values of $k_{4.1}$ for ClO dimerisation obtained from FACSIMILE fitting. Errors are ±2σ, statistical only. Systematic errors are discussed in Section 4.4.1. The asterisk denotes data for which irreversible second-order kinetics was observed, which were not used in subsequent analysis.

$k_{-4.1}$ / s^{-1}				
***T*/K**	**$Cl_2O/Cl_2/N_2$**	**$Cl_2O/Cl_2/O_2$**	**Cl_2O/Cl_2/air**	**Cl_2/O_3/air**
250.1	0.58 ± 0.06*			
256.5	0.41 ± 0.06		0.45 ± 0.08	0.13 ± 0.03*
263.2	0.95 ± 0.02		0.92 ± 0.08	0.56 ± 0.04
270.4	2.48 ± 0.05	2.33 ± 0.05	2.4 ± 0.05	1.84 ± 0.04
277.9	5.97 ± 0.10		5.7 ± 0.07	4.77 ± 0.21
285.8	14.5 ± 0.3		13.4 ± 1.04	11.3 ± 0.31
294.2	31.2 ± 0.5		28.9 ± 0.17	22.4 ± 0.94
298	43.5 ± 0.6	40.90 ± 2.88	41.7 ± 1.22	34.58 ± 1.16
303.1	69.3 ± 1.1		50.3 ± 3.06	46.61 ± 1.07
312.6	135.6 ± 3.1	134.2 ± 1.7	95.7 ± 4.8	95.76 ± 3.47

Table 4.6 : Values of $k_{-4.1}$ for Cl_2O_2 dissociation obtained from FACSIMILE fitting. Errors are ±2σ, statistical only. Systematic errors are discussed in Section 4.4.1. The asterisk denotes data for which irreversible second-order kinetics was observed, which were not used in subsequent analysis.

	$K_{eq}/10^{-14}$ cm^3 molecule^{-1}			
***T*/K**	**$Cl_2O/Cl_2/N_2$**	**$Cl_2O/Cl_2/O_2$**	**Cl_2O/Cl_2/air**	**Cl_2/O_3/air**
250.1	109.4 ± 14.5*			
256.5	157.5 ± 25.3		140.8 ± 23	481 ± 89*
263.2	64.88 ± 3.01		66.1 ± 5.9	110.2 ± 8.5
270.4	24.05 ± 0.72	22.96 ± 0.58	25.8 ± 1.0	32.3 ± 1.5
277.9	9.24 ± 0.34		9.43 ± 0.26	10.9 ± 0.3
285.8	3.26 ± 0.07		3.52 ± 0.26	4.12 ± 0.2
294.2	1.33 ± 0.01		1.24 ± 0.02	1.74 ± 0.07
298	0.88 ± 0.01	0.85 ± 0.05	0.904 ± 0.024	1.0 ± 0.02
303.1	0.50 ± 0.01		0.616 ± 0.022	0.66 ±0.01
312.6	0.21 ± 0.01	0.198 ± 0.005	0.210 ± 0.005	0.26 ±0.02

Table 4.7 : Values of K_{eq} for ClO dimerisation obtained from FACSIMILE fitting. Errors are ±2σ, statistical only. Systematic errors are discussed in Section 4.4.1. The asterisk denotes data for which irreversible second-order kinetics was observed, which were not used in subsequent analysis.

4.3.1 Second Law analysis

The energetics of ClO dimerisation were studied *via* Second Law analysis. The van't Hoff equation, derived in Section 2.2, relates the temperature-dependent equilibrium constants to the standard enthalpy change of reaction, $\Delta_r H°$, and the standard entropy change of reaction $\Delta_r S°$:

$$\ln K_p = -\frac{\Delta_r H°}{R}\frac{1}{T} + \frac{\Delta_r S°}{R} \qquad \text{(4.xxvi)}$$

The van't Hoff equation thus predicts that a plot of $\ln K_p$ against reciprocal temperature (a so-called van't Hoff plot) would result in a straight line of gradient $-\Delta_r H°/R$ and intercept $\Delta_r S°/R$. The Second Law method relies on the direct fitting of the measured values of the equilibrium constant to the van't Hoff equation to extract the thermochemical parameters $\Delta_r H°$ and $\Delta_r S°$. Before being fitted to the van't Hoff equation, equilibrium constants obtained as the ratio $k_{4.1}/k_{-4.1}$ and hence expressed in reciprocal concentration units (K_{eq} or alternatively K_c/cm^3 molecule^{-1}) were converted into thermodynamic (reciprocal pressure) units (K_p/atm^{-1}) according to the following

	$\ln(K_p/\text{atm}^{-1})$			
***T*/K**	**$Cl_2O/Cl_2/N_2$**	**$Cl_2O/Cl_2/O_2$**	**Cl_2O/Cl_2/air**	**Cl_2/O_3/air**
250.1	17.37 ± 0.37*			
256.5	17.63 ± 0.18		17.51 ± 0.17	18.74 ± 0.2*
263.2	16.72 ± 0.05		16.73 ± 0.09	17.24 ± 0.07
270.4	15.69 ± 0.03	15.64 ± 0.02	15.76 ± 0.04	15.98 ± 0.04
277.9	14.70 ± 0.04		14.73 ± 0.03	14.87 ± 0.03
285.8	13.63 ± 0.02		13.71 ± 0.07	13.87 ± 0.06
294.2	12.71 ± 0.01		12.64 ± 0.02	12.98 ± 0.04
298	12.29 ± 0.01	12.24 ± 0.05	12.31 ± 0.03	12.41 ± 0.02
303.1	11.71 ± 0.02		11.91 ± 0.04	11.97 ± 0.02
312.6	10.80 ± 0.05	10.75 ± 0.03	10.80 ± 0.03	11.03 ± 0.06

Table 4.8 : Values of $\ln K_p$ for ClO dimerisation obtained from FACSIMILE fitting. Errors are ±2σ, statistical only. The asterisk denotes data for which irreversible second-order kinetics was observed, which were not used in subsequent analysis.

relationship:

$$K_p/\text{atm}^{-1} = 101325/\text{Pa}\cdot 10^{-6}\cdot(K_c/\text{cm}^3\ \text{molecule}^{-1})(k_B T)^{\Delta n} \qquad \text{(4.xxvii)}$$

where Δn is the mole change of the reaction; for the dimerisation reaction $\Delta n = -1$. The values of $\ln K_p$ are given in Table 4.8

The van't Hoff plot resulting from the data in Table 4.8 is shown in Figure 4.16 and the results of the Second Law analysis (carried out excluding the data points at temperatures where irreversible second-order kinetics were observed) are shown in Table 4.9.

Precursor mixture used	$-\Delta_r H°/\text{kJ mol}^{-1}$	$-\Delta_r S°/\text{J K}^{-1}\text{ mol}^{-1}$
$Cl_2O/Cl_2/N_2$	82.0 ± 1.0	172.9 ± 3.6
$Cl_2O/Cl_2/O_2$	81.63 ± 1.0	171.8 ± 3.4
Cl_2O/Cl_2/air	80.8 ± 2.1	168.4 ± 7.6
Cl_2/O_3/air	85.2 ± 3.6	181.9 ± 12.7

Table 4.9 : Thermochemical parameters of ClO dimerisation obtained in this work from Second Law analysis. Errors are ±2σ, statistical only from the linear regression.

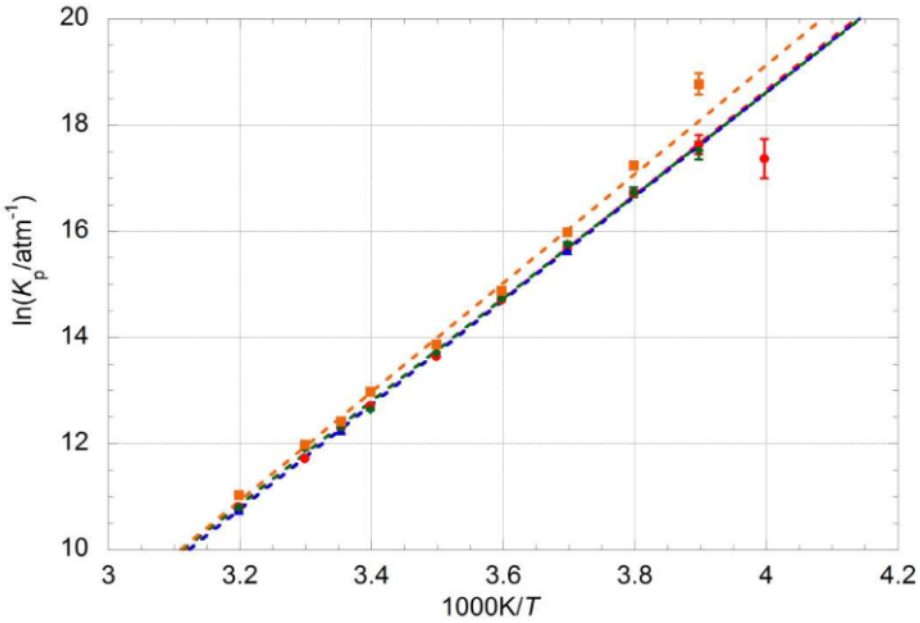

Figure 4.16 : van't Hoff plot showing the temperature dependence of $\ln K_p$ determined in this work from laser flash photolysis of $Cl_2O/Cl_2/N_2$ (red circles), $Cl_2O/Cl_2/O_2$ (blue triangles), Cl_2O/Cl_2/air (green diamonds) and Cl_2/O_3/air (orange squares) gas mixtures. The errors bars shown are ±2σ, statistical only. The parameterisations (dashed lines) ignore data recorded at $T = 250.1$ K (1000/ $T = 4$ K^{-1}) for the $Cl_2O/Cl_2/N_2$ dataset and at $T = 256.5$ K (1000/ $T = 3.5$ K^{-1}) for the Cl_2/O_3/air dataset for the reasons discussed in Section 4.2.5.

The thermochemical parameters obtained from the Second Law analysis of data from different reaction mixtures exhibit very good agreement, with the values of $\Delta_r H°$ and $\Delta_r S°$ all within 2σ of one another.

4.3.2 Third Law analysis

The Third Law method was introduced in Section 2.2.2. This analysis relies effectively on constraining the entropic term in the van't Hoff equation by calculating $\Delta_r S°$ of the equilibration reaction from first principles. As $K_{eq}(T)$ gives $\Delta_r G°$, $\Delta_r H°$ is then calculated from simple thermodynamics. The first step in the Third Law analysis is thus to calculate the absolute entropies of ClO and Cl_2O_2: $S°_{ClO}$ and $S°_{dimer}$ respectively. At this stage an assumption therefore has to be made on the structure on the ClO dimer, as the partition functions used in the calculation of $S°_{dimer}$ are isomer-specific. Of all the possible structures of the ClO dimer, only one, the symmetrical chlorine peroxide ClOOCl, has been observed experimentally by means of its rotational spectrum. [30] It

was therefore assumed that the ClO dimer was present solely as ClOOCl. $S°_{ClO}$ and $S°_{ClOOCl}$ were calculated as the sum of the contributions to the total molecular standard entropy from the translational, rotational, vibrational and electronic partition functions. The entropic partition functions used are shown in Table 4.10; all the definitions of $S°$ were taken from the literature, [31, 32, 33, 34, 35] All the data necessary to calculate $S°_{ClO}$ and $S°_{ClOOCl}$ (*e.g.* molecular moments of inertia, vibrational constants, energies of electronic states) were those reported by Chase. [31] The vibrational frequencies of ClOOCl and their uncertainties were those reported by von Hobe *et al*. [14] and Chase. [31]

The rotational and vibrational constants for ClO reported by Chase only refer, however, to the $^{35}Cl^{16}O$ isotope of chlorine monoxide. [31] Given that the natural isotopic abundance of ^{37}Cl is not negligible (24.6%), these spectroscopic constants were converted using the procedure illustrated by Herzberg to account for the naturally occurring isotopic abundances. [36] This is briefly summarised in this section. Considering a classical harmonic oscillator, the vibrational frequency ω is given by:

$$\omega = \frac{1}{2\pi}\sqrt{\frac{k}{\mu}} \qquad \text{(4.xxviii)}$$

where k is the force constant and μ the reduced mass of the molecule. For molecules containing different isotopes, k is largely unchanged as it is solely determined by the electronic motion, [36] whereas μ is, evidently, different. We can therefore define a parameter ρ expressing the relationship between the vibrational frequencies of two isotopic molecules as follows:

$$\rho = \frac{\omega^i}{\omega} = \sqrt{\frac{\mu}{\mu^i}} \qquad \text{(4.xxix)}$$

where the superscript i indicates a molecule containing a different isotope from the original molecule. The value of ρ for the $^{35}Cl^{16}O$,$^{37}Cl^{16}O$ pair was 0.98304. The

	ClO	ClOOCl
$S°_{\text{translation}}/R$	$\ln\left[\left(\frac{2\pi M_R k_B T}{N_A h^2}\right)^{3/2}\frac{k_B T}{p°}\right]+\frac{5}{2}$	
$S°_{\text{rotation}}/R$	$1-\ln\left(\frac{hcB\sigma}{k_B T}\right)$	$\frac{3}{2}\ln T+\frac{1}{2}\ln I_A I_B I_C-\ln\sigma+\ln\frac{8\pi^2(2\pi k)^{3/2}}{h^3}+\frac{3}{2}$
$S°_{\text{vibration}}/R$	$\frac{\theta_\upsilon/T}{e^{\theta_\upsilon/T}-1}-\ln\left(1-e^{-\theta_\upsilon/T}\right)$	
$S°_{\text{electronic}}/R$	$\frac{T}{Q}\frac{dQ}{dT}+\ln Q$	

Notes:

M_R = molar mass

k_B = Boltzmann constant

N_A = Avogadro's number

h = Planck's constant

c = speed of light *in vacuo*

$p°$ = standard atmospheric pressure (10^5 Pa)

σ = molecular symmetry number

$B = \frac{h}{8\pi^2 cI}$

I = moment of inertia of a diatomic molecule

I_A, I_B, I_C = principal moments of inertia of a polyatomic molecule

$\theta_v = \frac{hc}{k_B}\left(\omega_e - 2\omega_e x_e\right)$ for ClO

ω_e = vibrational wavenumber

x_e = anharmonicity constant

$\theta_v = \frac{hc\,\omega}{k}$ for ClOOCl for 3N – 6 vibrational modes (N = number of atoms in the molecule)

$Q = \sum_i g_i \exp\left(-\frac{hc\,\varepsilon_i}{k_B T}\right)$

$\frac{dQ}{dT} = \sum_i \frac{hc\varepsilon_i}{k_B T^2} g_i \exp\left(-\frac{hc\varepsilon_i}{k_B T}\right)$

g_i = degeneracy of state i ($2\Omega+1$)

ε_i = energy of state i

Table 4.10 : Contributions to the total standard entropy of ClO and ClOOCl from translational, rotational, vibrational and electronic partition functions.

vibrational constants for the isotope-containing molecule are then calculated as follows:

$$\omega_e^i = \rho\omega_e \tag{4.xxx}$$

$$\omega_e^i x_e^i = \rho^2 \omega_e x_e \tag{4.xxxi}$$

Similarly, the different reduced mass of two molecules containing different isotopes of the same element affects the rotational constant, B, defined as:

$$B = \frac{h}{8\pi^2 c\mu r^2} \tag{4.xxxii}$$

As the internuclear distance, r, is entirely determined by the electronic structure, and therefore identical in two isotopic molecules (analogously to the force constant k), [36] the relationship between the rotational constants of two different isotopic molecules can be expressed as:

$$\frac{B^i}{B} = \frac{\mu}{\mu^i} = \rho^2 \tag{4.xxxiii}$$

The isotopic correction was therefore calculated for ClO and had, ultimately, a small effect on the calculated $S°_{ClO}$ (~ 0.09% at T = 298 K).

The value of the symmetry number, σ, of the ClO dimer used in the calculations of $S°_{ClOOCl}$ was 1, as recommended by Golden, [37] and not 2, as the rotational symmetry of the molecule might initially suggest. The reason for this lies in the fact that gaseous ClOOCl actually exists as a racemic mixture of two optical isomers, as illustrated graphically in Figure 4.17. Therefore the entropy of mixing of these two isomers, ΔS_{mixing}, must be included in the calculation of the total $S°_{ClOOCl}$ to account for the presence of two isomers. In the case of ClOOCl, ΔS_{mixing} is defined as: [38]

$$\Delta S_{mixing} = R \ln 2 \tag{4.xxxiv}$$

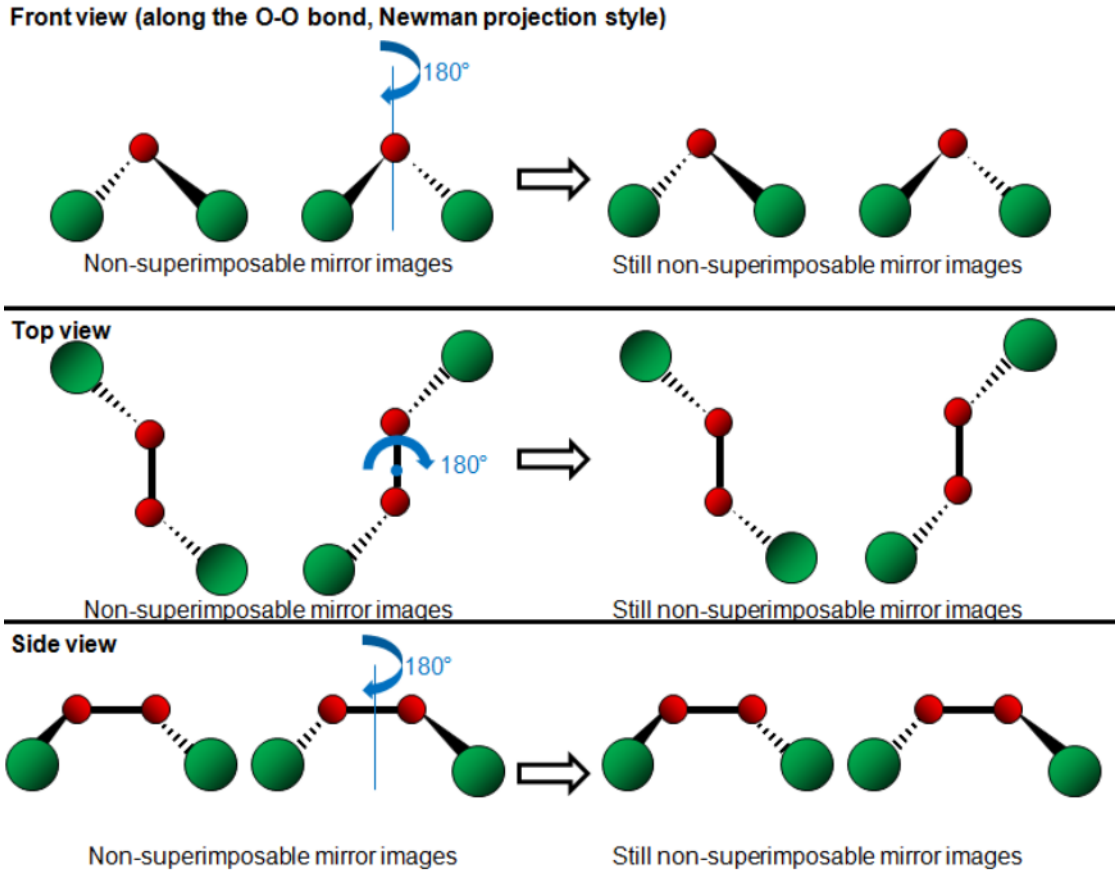

Figure 4.17 : Two optical isomers of ClOOCl (left hand side). Regardless of the symmetry operation performed (*e.g.*, rotation of 180° along one of the main axes of one of the isomers, as shown above), the two molecules remain non-superimposable mirror images of one another.

The value of $S°_{ClOOCl}$ obtained using $\sigma = 2$ and including the isomeric correction factor is equivalent to simply using $\sigma = 1$ with no isomeric correction.

Table 4.11 illustrates how the standard entropies calculated in this work compare to those reported in the literature. The results of Third Law fits to the data recorded in this work are also shown along with the findings of previous studies. The values of $\Delta_r H°$ and $\Delta_r S°$ obtained from Third Law analysis differ slightly from the outcome of Second Law analysis, giving a higher (less negative) $\Delta_r H°$ and $\Delta_r S°$ than those reported in Section 4.3.1. An overall excellent agreement was observed between the present work and previous studies for the calculated standard entropies, for $\Delta_r H°$ and for $\Delta_r S°$. The discrepancies between the values of $\Delta_r H°$ and $\Delta_r S°$ from the Third Law method and those obtained *via* the Second Law analysis are discussed in the following section.

Reference	$S°_{ClO}$ /J K^{-1} mol^{-1}	$S°_{ClOOCl}$ /J K^{-1} mol^{-1}	$-\Delta_r S°$ /J K^{-1} mol^{-1}	$-\Delta_r H°$ /kJ mol^{-1}
Chase [31]	225.07 ± 0.5	300.983 ± 5	149.16 ± 6	
Von Hobe *et al.* [14]	225.07 ± 0.5	$302.08^{+1.11}_{-0.42}$	148.06 ± 2.1	
Plenge *et al.* [6]			147.96 ± 6[a]	72.39 ± 2.8
Nickolaisen *et al.* [9]	227.54 ± 2	$302.08^{+4.94}_{-3.42}$	153.4 ± 2.8	75.7 ± 0.8
Barker [39, 40]	224.96 ± 0.1	302.33 ± 0.1	147.59 ± 0.1	73.88 ± 0.1
this work (Cl_2O/Cl_2/air)	225.04 ± 0.5	$302.08^{+1.11}_{-0.42}$	148.00 ± 0.7	74.65 ± 0.4

Note: [a]: Calculated from reported $\Delta_r H°(T = 298\ K)$ and K_{eq} parameterisation.

Table 4.11 : Standard entropies at $T = 298.15$ K and $p = 10^5$ Pa of ClO and ClOOCl along with $\Delta_r H°(T = 298.15\ K)$ and $\Delta_r S°(T = 298.15\ K)$ obtained from Third Law analysis from this work and previous studies.

4.4 Discussion

Table 4.12 shows how the thermochemical parameters for the ClO dimerisation determined in this work from Second Law analysis compare to those from previous

Reference	*T* /K	technique	$-\Delta_r H°$/kJ mol^{-1}	$-\Delta_r S°$/J K^{-1} mol^{-1}
Cox and Hayman [5] (Second Law)	233-303	MM/UV	72.5 ± 3	144.0 ± 11
Nickolaisen *et al.* [9] (Second Law)	260-310	FP/UV	81.6 ± 2.9	173.2 ± 10.0
Plenge *et al.* [6]		PI/MS	72.4 ± 2.8	
Bröske and Zabel [7]	243-261	FP/UV	78.3 ± 6.7	
JPL-NASA [24]			75.7 ± 2.5	153.8 ± 10
this work (Cl_2O/Cl_2/air, Second Law)	256-312	LP/UV	80.8 ± 2.1	168.4 ± 7.6

Notes: MM/UV = molecular modulation with UV absorption spectroscopy
FP/UV = flash photolysis with UV absorption spectroscopy
PI/MS = photoionisation with mass spectrometry
LP/UV = laser photolysis with UV absorption spectroscopy

Table 4.12 : Comparison between the thermochemical parameters of ClO dimerisation available in the literature and those determined in this work from Second Law analysis.

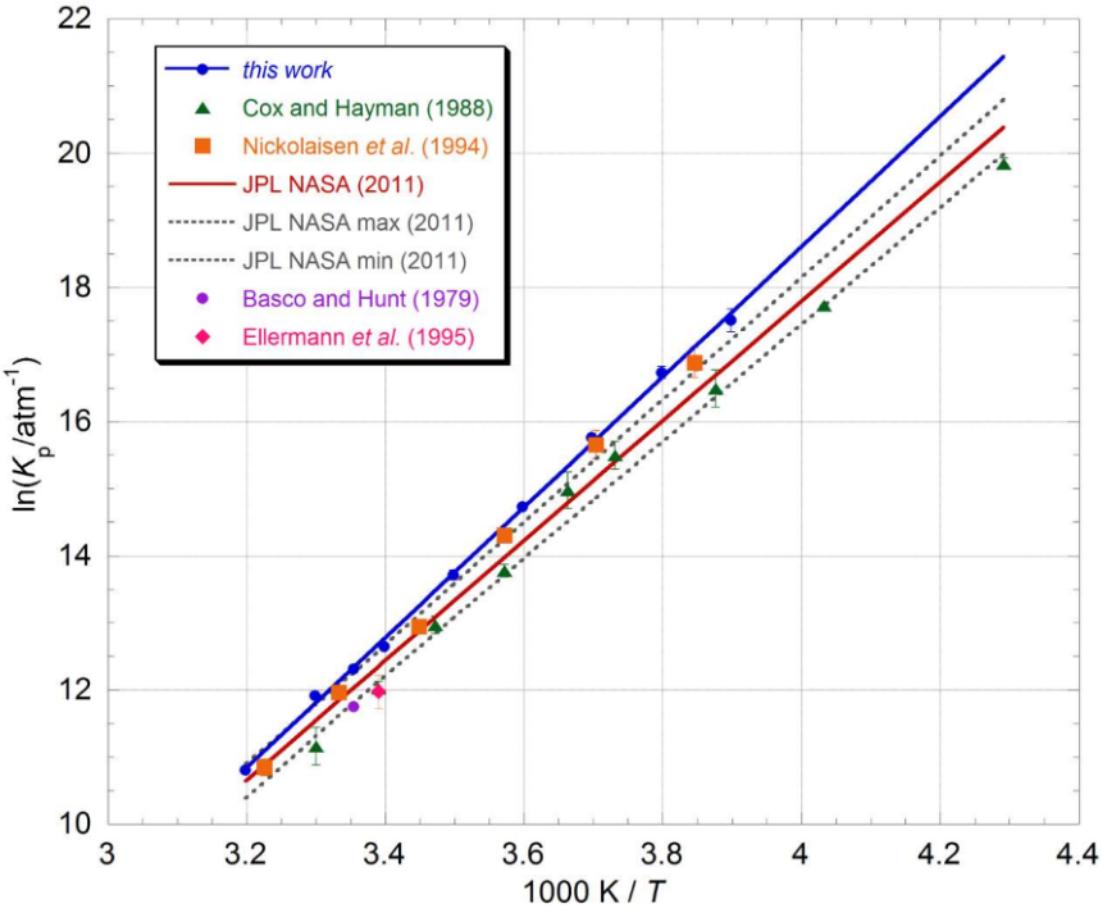

Figure 4.18 : van't Hoff plot showing the temperature dependence of K_{eq} for ClO dimerisation. Data from this work (using Cl_2O/Cl_2/air precursor mixtures) are plotted as blue circles and the resulting Second Law parameterisation is shown as a solid blue line. Also shown are the recommended values from JPL-NASA [24] (solid red line) with their upper and lower limits (grey dashed lines), data from Cox and Hayman [5] (green triangles) and from Nickolaisen *et al.* [9] (orange squares). Also shown are the determinations of K_{eq} at fixed T from Basco and Hunt [8] (purple circle) and from Ellermann *et al.* [10] (pink diamond).

analogous studies. A van't Hoff plot including data from this study together with the current JPL-NASA recommended values [24] and data from Cox and Hayman [5] and from Nickolaisen *et al.* [9] is shown in Figure 4.18.

The values of K_{eq} measured in this work are greater than the current JPL-NASA recommendation, [24] which is based on the work of Cox and Hayman and that of Nickolaisen *et al.* As shown in the van't Hoff plot in Figure 4.18, data from this study lie close to the upper limit of the JPL-NASA recommended uncertainty range at room

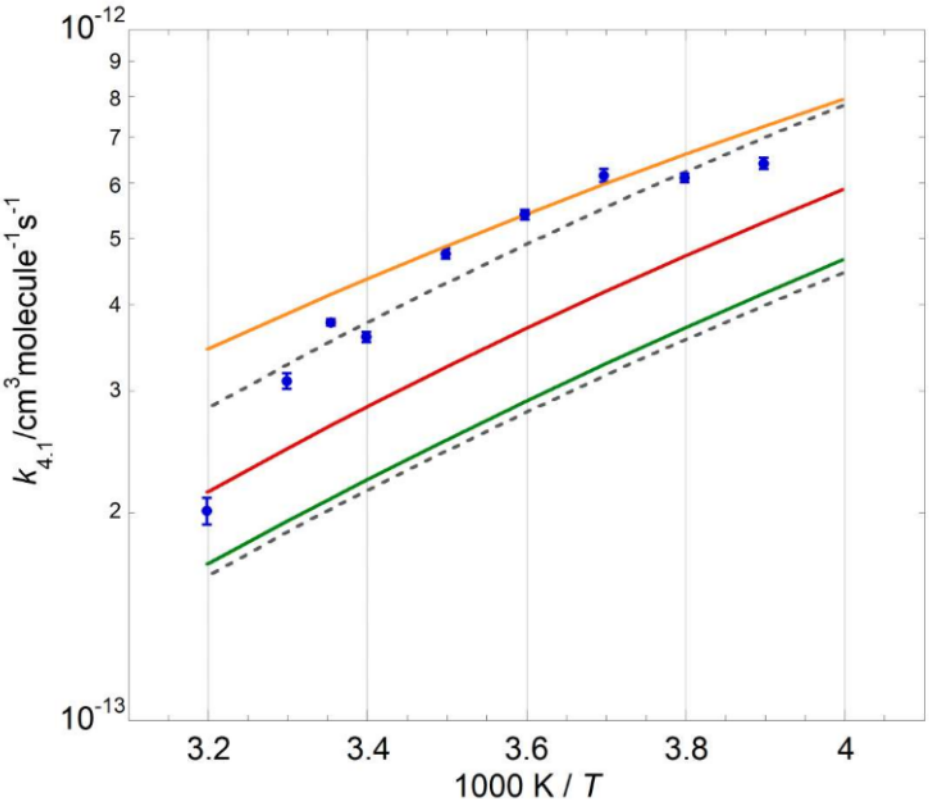

Figure 4.19 : Arrhenius plot for $k_{4.1}$. Data from this work (Cl_2O/Cl_2/air data set) are plotted as filled circles. Also shown are the parameterisation from Boakes *et al.* [4] (orange line), the JPL-NASA [24] recommended values (red line) with their upper and lower limits (dashed lines) and the parameterisation from Bloss *et al.* [3] (green line).

temperature but diverge from it slightly at lower temperatures. The origin of this discrepancy lies in the rate of the recombination reaction (4.1) which is greater than that taken from the JPL-NASA recommendation. This is shown in Figure 4.19 in the form of an Arrhenius plot for $k_{4.1}$ at p = 760 Torr. Also shown in Figure 4.19 are values of $k_{4.1}$ taken from the parameterisations from Boakes *et al.* [4] and Bloss *et al.* [3] The values of $k_{4.1}$ recorded in this work lie between the findings of Boakes *et al.* (the largest $k_{4.1}$ measured to date) and the current JPL-NASA recommended values.

As discussed in Section 4.2.5 above, the forward reaction rate constant, $k_{4.1}$, and hence the equilibrium constant K_{eq} for the ClO dimerisation, as determined *via* absorption spectroscopy, are directly proportional to the absorption cross-sections for ClO adopted. However, given that the ClO absorption cross-sections are dependent upon instrumental resolution as well as temperature, it is often inappropriate to compare directly results

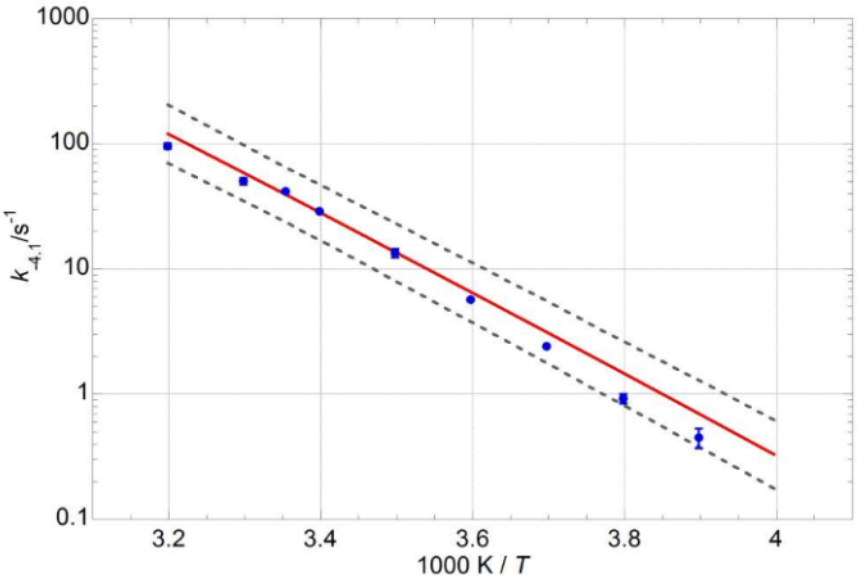

Figure 4.20 : Arrhenius plot for $k_{-4.1}$. Data from this work are plotted as filled blue circles. Also shown are the calculated JPL-NASA [24] recommended values (red line) with their upper and lower limits of uncertainty (dashed lines).

from different studies with different instrumental resolution. The present study obtained a parameterisation of the differential ClO cross-section at the (12, 0) band which was in good agreement with that determined by Boakes *et al.*; hence, somewhat unsurprisingly, $k_{4.1}$ from this work is in reasonably good agreement with that measured by Boakes *et al*. As discussed by Boakes *et al.*, extrapolation of resolution-dependent cross-sections to the instrumental resolution adopted by Bloss *et al.* actually gives a higher $\sigma_{\mathrm{ClO\ diff}}$ than that determined by Bloss *et al.* and the absolute magnitude of the recombination rate constant $k_{4.1}$ recorded by Boakes *et al.* is also higher than that of Bloss *et al*. partly in consequence of this.

$k_{-4.1}$, on the other hand, was found to be in excellent agreement with the current JPL-NASA recommendations, as shown in the Arrhenius plot in Figure 4.20.

The thermochemical parameters derived from the equilibrium constant measurements reported in this work for the Cl_2O/Cl_2/air reaction system, giving $\Delta_r H° = -80.8 \pm 2.1$ kJ mol^{-1}; $\Delta_r S° = -168.4 \pm 7.6$ J K^{-1} mol^{-1} from Second Law analysis and $\Delta_r H° = -74.65 \pm 0.4$ kJ mol^{-1}; $\Delta_r S° = -148.00 \pm 0.7$ J K^{-1} mol^{-1} from Third Law

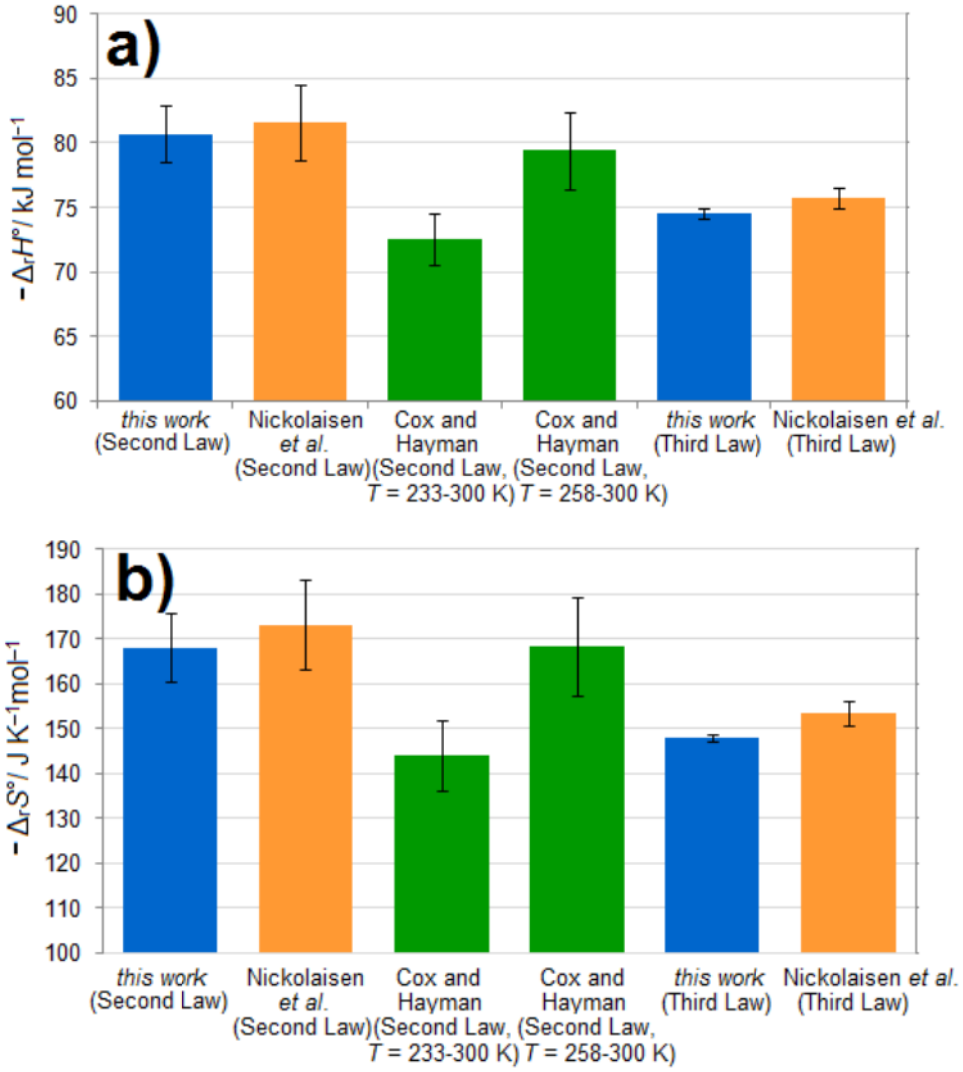

Figure 4.21 : Comparison of the values of a) $\Delta_r H°$ and b) $\Delta_r S°$ obtained from Second and Third law methods in the current study (in blue) and from Nickolaisen *et al.* [9] (in orange). Also shown are the values obtained from Second Law analysis of the data reported by Cox and Hayman [5] over the ranges T = 233-300 K and T = 258-300 K, as discussed in Section 4.4.2.

analysis, are not in agreement with one another within error. This is illustrated in the histograms in Figure 4.21, along with values from previous studies. This disparity is almost identical in magnitude and sign as that reported between the same thermochemical parameters by Nickolaisen *et al.,* [9] and comparable in magnitude to the typical uncertainties obtained from such analyses. [38] Furthermore, in the Second Law analysis, it is assumed that $\Delta_r H°$ is independent of temperature over the, albeit limited, temperature range of these studies, and $\Delta_r S°$ is obtained from a very long extrapolation to the y-axis. The parameters derived from the Third Law analysis are therefore

preferred, although results from both methods are compared in detail to previous work below.

4.4.1 Sensitivity Analysis

As with the equilibrium constants K_{eq}, a sensitivity analysis was performed to investigate the effects of potential uncertainties in the kinetic model rate coefficients on the eventual thermochemical parameters derived from this study. In this case, individual kinetic parameters in the model used for numerical integration were in turn perturbed by a factor of two, representative kinetic traces at all experimental temperatures were reanalysed using the perturbed kinetics and the equilibrium constants fitted, using a Second Law analysis, to quantify the effects on $\Delta_r H°$ and $\Delta_r S°$. Results showed that uncertainties in the secondary chemistry reaction rate constants used in the kinetic model had a near negligible effect on $\Delta_r H°$ and $\Delta_r S°$. The maximum perturbation of $\Delta_r H°$ obtained from this analysis was 0.64%. The greatest effect on $\Delta_r S°$ observed was 1.09%, and all others were below 1%. Thus we conclude that uncertainties in the parameters in the kinetic model have a negligible effect on the thermochemical parameters reported here. A similar study was conducted to assess the effect of uncertainties in the absorption cross-sections for ClO, $\sigma_{ClO\ diff}$, used to obtain radical concentrations, kinetic traces and hence equilibrium constants. In this case, the temperature dependent ClO temporal traces were each scaled according to the errors reported in the parameterisation of the ClO absorption cross-section given in expression (4.viii) above. These traces were then reanalysed, and the temperature dependent equilibrium constants re-fitted, in this case using both the Second Law and Third Law methods, to obtain perturbed values of $\Delta_r H°$ and (for Second Law analysis only) $\Delta_r S°$.

	$\sigma_{ClO\ diff}$ **maximum**	$\sigma_{ClO\ diff}$ **minimum**
− $\Delta_r H°$ **(Second Law)**/ kJ mol^{-1}	78.9	84.8
− $\Delta_r S°$ **(Second Law)**/ J K^{-1}mol^{-1}	158.5	187.9
− $\Delta_r H°$ **(Third Law)**/ kJ mol^{-1}	73.25	75.82

Table 4.13 : Sensitivity of $\Delta_r H°$ and $\Delta_r S°$ from Cl_2O/Cl_2/air data set to ClO absorption cross-sections: standard enthalpy and entropy changes for equilibrium (4.1) recalculated using ClO absorption cross-sections at the upper and lower limits of uncertainty as given in equation (4.viii).

Results from this analysis are summarised in Table 4.13, and show that for the Second Law analysis, putting the ClO absorption cross-sections to the upper of their error bounds increases $\Delta_r H°$ (*i.e.* makes $\Delta_r H°$ less negative) by 2.2 %; whereas for ClO cross-sections at the lower end of their uncertainty limit, $\Delta_r H°$ is reduced by 5.1%. From the Third Law analysis the corresponding perturbations in $\Delta_r H°$ were +2.1% ($\sigma_{\mathrm{ClO\ diff}}$ increased) and −1.3% ($\sigma_{\mathrm{ClO\ diff}}$ reduced). Considering the entropy change for reactions (4.1, −4.1), the sensitivity to changes in $\sigma_{\mathrm{ClO\ diff}}$ was somewhat greater. Increasing the ClO absorption cross-sections to their maximum values gave an increase in $\Delta_r S°$ of +5.7%, conversely reducing the cross-sections reduced $\Delta_r S°$ by 11.8%, using a Second Law analysis. This is as expected, since changing the ClO cross-sections changes the absolute magnitude of K_{eq}, as discussed in Section 4.2.5 above, and therefore affects the *y*-axis intercept of the van't Hoff plot. Evidently, given that, for the Third Law method, the entropy change was *calculated* from statistical mechanics, without recourse to experimental data for K_{eq}, $\Delta_r S°$ for this analysis is unaffected by $\sigma_{\mathrm{ClO\ diff}}$. It was therefore concluded that, despite the errors on the differential absorption cross-sections for ClO being quite considerable, the effects of these errors on the enthalpy change for reactions (4.1, −4.1) are small. By contrast, the effects on the entropy change obtained from the Second Law analysis are significant, reflecting the direct effect of a perturbed K_{eq} on the intercept of the van't Hoff plot.

Also the effect of using $\sigma_{\mathrm{ClO\ diff}}$ from Boakes *et al.*, given by equation (4.ix), on $\Delta_r H°$ and $\Delta_r S°$, as opposed to the expression for $\sigma_{\mathrm{ClO\ diff}}(T)$ derived in this work, was investigated. Values of $\Delta_r H° = -79.4 \pm 1.8$ kJ mol^{-1} and $\Delta_r S° = -162.1 \pm 6.5$ J mol^{-1} K^{-1} were obtained from the Second Law method, respectively 1.7% and 3.7% less negative than the values of $\Delta_r H°$ and $\Delta_r S°$ obtained using the ClO differential cross-section parameterised in the current work.

4.4.2 Comparison with Previous Studies

The values of $\Delta_r H°$ and $\Delta_r S°$ obtained from this work (using both Second and Third Law analyses) are greater in absolute magnitude (more negative) than those reported by Cox and Hayman [5] using a Second Law method, as given in Table 4.12. Cox and Hayman employed long-timescale modulated photolysis of a static gas mixture to

generate ClO radicals and their dimerisation products, and deconvolved UV spectra of the evolving gas mixture to obtain ClO radical and Cl_2O_2 concentrations and therefore K_{eq}. Thus, whilst the Cox and Hayman study monitors ClO and Cl_2O_2 always, in principle, in equilibrium, the presence of other reactive chlorine species (*e.g.* higher oxides of chlorine such as Cl_2O_3 from ClO + OClO) and their photolysis products (given the long photolysis times) will affect the UV absorption (interpreted as ClO/Cl_2O_2) profoundly and might be expected to perturb the extracted ClO and Cl_2O_2 concentrations and, therefore, K_{eq}. This can be shown, for example, by taking raw data from Figure 4.2 of the Cox and Hayman paper and attempting to extract K_{eq} from instantaneous (approximate) post photolysis concentrations. Whilst this reanalysis cannot replicate the individual values for K_{eq} reported by Cox and Hayman from a single data set, as would be expected given that multiple data sets would have been averaged and reported in the Cox and Hayman study, the variation of the ratio of $\{[Cl_2O_2]/[ClO]^2\}$ is large (a range of a factor of two) during the post photolysis period perhaps indicative of secondary chemistry, which the authors themselves acknowledge. Closer consideration of the Cox and Hayman study also suggests that the disparity between the analysis of the Cox and Hayman data and of those reported here, and elsewhere, may not be so great. Cox and Hayman report K_{eq} down to a temperature of T = 233 K. However, in the present study, as discussed in Section 4.2.5 above, sensitivity to $k_{-4.1}$ and hence K_{eq} is lost below $T \approx 256$ K. Evidently, this sensitivity loss is also dependent upon the concentrations of radicals employed, but simple calculations show that at higher total concentrations of ClO/Cl_2O_2 the ratio of [ClO] at equilibrium to the total reactive chlorine present is actually reduced. Indeed, Cox and Hayman employ radical concentrations in the range (1-10) $\times 10^{15}$ molecule cm^{-3}, somewhat higher than in the present study. The Cox and Hayman equilibrium constant data recorded as a function of temperature also seem to reflect a subtle change in gradient of the van't Hoff plot as temperature is reduced as shown in Figure 4.22. Reanalysis of the Cox and Hayman K_{eq} dataset omitting the lowest temperature point (at T = 233 K) results in $\Delta_r H° = -75.4 \pm 3$ kJ mol^{-1} and $\Delta_r S° = -154.5 \pm 10$ J K^{-1} mol^{-1}. Repeating this reanalysis of the Cox and Hayman data omitting the two lowest temperature points at T = 233 K and at T = 248 K results in $\Delta_r H° = -79.4 \pm 3$ kJ mol^{-1} and $\Delta_r S° = -168.4 \pm 11$ J K^{-1} mol^{-1}. These thermochemical parameters, reanalysed from a very similar temperature range dataset to those employed in this work, are in excellent agreement with those reported

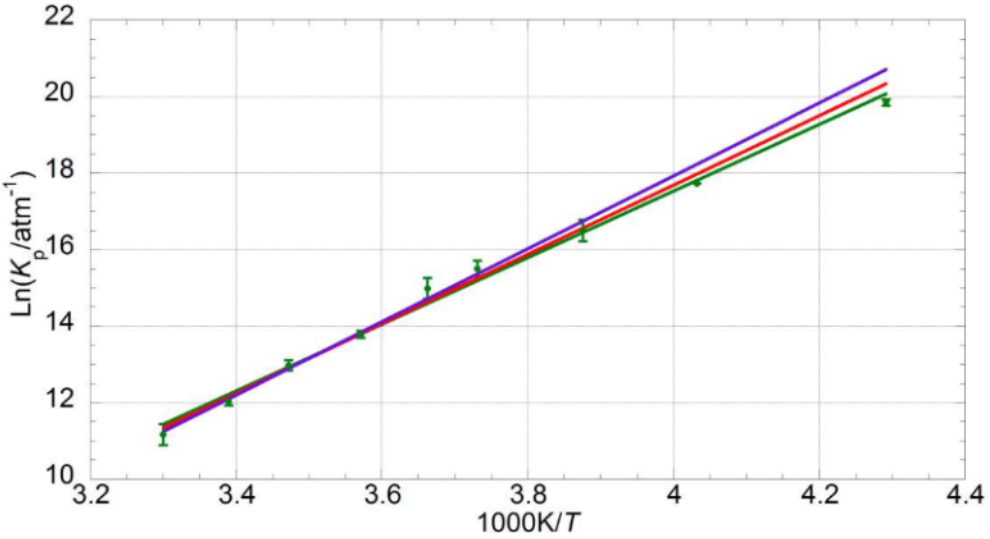

Figure 4.22 : van't Hoff plot for the data from Cox and Hayman [5] (green data point). Also shown are the linear fits to the data over the ranges T = 233-300 K (green line), T = 248-300 K (in red) and T = 258-300 K (in purple).

here and from Nickolaisen *et al.* from a Second Law analysis, as illustrated in Figure 4.21. Furthermore, the temperature range adopted in the present work is similar to that used by Nickolaisen *et al.*, [9] who studied K_{eq} (using comparable initial concentrations of ClO to those in the present work) down to a minimum temperature of T = 260 K. This temperature limitation is also in implicit accord with the work of Bloss *et al.*, [3] who studied $k_{4.1}$ as a function of temperature - again using comparable initial concentrations to those used in this work - assuming *irreversible* second order loss of ClO radicals up to a *maximum* temperature of T = 245 K. The thermochemical parameters reported in this work are in excellent agreement with those reported by Nickolaisen *et al.* using an analogous technique, as shown in Figure 4.21. Values for $\Delta_r H°$ from the present study lie within 1.2% of those reported by Nickolaisen *et al.* using the Second Law method and within 1.4% using the Third Law method. Similarly, values for $\Delta_r S°$ lie within 3% of the Nickolaisen *et al.* values using the Second Law. From the Third Law analysis, the $\Delta_r S°$ obtained in this work differs from that of Nickolaisen *et al.* by *ca.* 3.5%, the origin of which lies in the calculated entropy for ClO. However, as shown in Table 4.11, the absolute entropy of ClO calculated at T = 298.15 K reported in this work was nearly identical (well within 0.1%) to that calculated using the method of Chase *et al.*, [31] and those at reported by von Hobe *et al.* [14] and Barker *et al.* [39, 40] The combined UV/IR spectroscopic study of Bröske and Zabel [7] also reports an enthalpy change for ClO dimerisation (from Second Law analysis) in agreement with that reported in this work.

There thus appears to be a degree of consensus between the thermochemical parameters for ClO dimerisation as investigated using optical monitoring of ClO and/or Cl_2O_2. Taking the Cox and Hayman data, reanalysed excluding the two lowest temperature points as discussed above, along with $\Delta_r H°$ reported by Bröske and Zabel (both from Second Law analysis), along with the (preferred) Third Law analyses from Nickolaisen *et al.* and the present work results in an average $\Delta_r H°$ for reaction (4.1) of −77.0 ± 2.2 kJ mol^{-1} (error 1σ from the unweighted average). By contrast, the work of Plenge *et al.* [6], who employed an entirely different technique to deduce the enthalpy change for reactions (4.1, −4.1), reports a value for $\Delta_r H°$ of −72.4 ± 2.8 kJ mol^{-1}. Plenge *et al.* employed photoionisation mass spectrometry to investigate the ionisation energy of ClO, from a room temperature sample of the radicals, along with the appearance energy for ClO^+ from a sample of ClOOCl, generated by cooling the ClO source to T = 170 K. After thermal corrections, and using the heat of formation of ClO, [41] the bond dissociation energy for ClOOCl was calculated. Plenge *et al.* do report a slightly lower ionisation threshold for production of ClO^+ from that of Thorn *et al*. [42], and attribute this difference to the method of extraction of the threshold energy. Plenge *et al.* adopted the method described by Traeger and McLoughlin [43] wherein a linear extrapolation of the post threshold ion intensity is used to establish the threshold ion appearance energy. This method appears reliable and, in any case adopting the higher ionisation threshold for ClO reported by Thorn *et al.* cannot reconcile the differences in the ClO–OCl bond strength reported by Plenge *et al*. and other studies, including this work, discussed above.

Naturally all Third Law analyses rely on the critical assumption that all Cl_2O_2 exists as the symmetrical ClOOCl isomer. If this assumption were false, Third Law calculations would be flawed and this could potentially account for the consistent disparity between Second Law and Third Law methods. Recent uncertainties on the structure of the dimer are discussed briefly in Chapter 8.

4.4.3 Atmospheric Implications

The parameterisation of K_p obtained from the Third Law analysis of the present study is compared to previous work in Figure 4.23. The K_p parameterisation has been

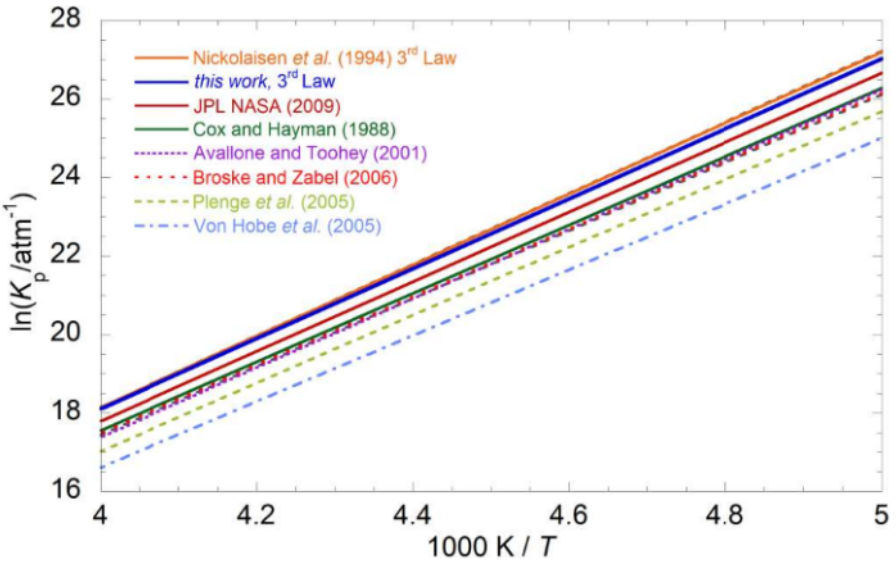

Figure 4.23 : van't Hoff plot showing extrapolation of K_{eq} to stratospheric temperatures.

extrapolated to 1000K/T = 5; *i.e.* to a typical polar stratospheric temperature of T = 200 K. Such extrapolation is necessary as laboratory studies (which use higher radical concentrations than those found in the stratosphere) lose sensitivity to K_{eq} at $T \leq 250$ K, as discussed above. As with the van't Hoff plot shown in Figure 4.18, the data from the present work lie close to the upper limit of uncertainty of the most recent JPL-NASA recommendation [24]. However, in this case, as the preferred Third Law parameterisation is shown, the data from this work do not deviate away from this upper limit as temperature is reduced (as they do for the Second Law analysis shown in Figure 4.18). As evident from the thermochemical parameters derived in this work, the Third Law parameterisation of K_p obtained here is in excellent agreement with that of Nickolaisen *et al.* [9] at all temperatures. Conversely, data from Cox and Hayman [5] and Bröske and Zabel [7] give K_p lying at the lower limit of the JPL-NASA uncertainty, which are also consistent with data from Avallone and Toohey obtained from atmospheric measurements. [22] The parameterisation of K_p derived from the Plenge *et al.* photoionisation study [6], and that obtained from von Hobe *et al.* [16] both lie below the lower limits of the current JPL-NASA uncertainty. To illustrate the effects of K_p recorded in the present work on the partitioning of active stratospheric chlorine, simple calculations were performed to examine the ratio of the equilibrium ClO concentration to that of the ClO dimer as a function of total ClO_x defined as $[ClO_x] = [ClO] + (2 \times [Cl_2O_2])$. This ratio, calculated at three typical Polar stratospheric temperatures of T = 190, 200 and 210 K, for $[ClO_x]$ ranging from 0.5-10 ppbv, is shown in Figure 4.24 and

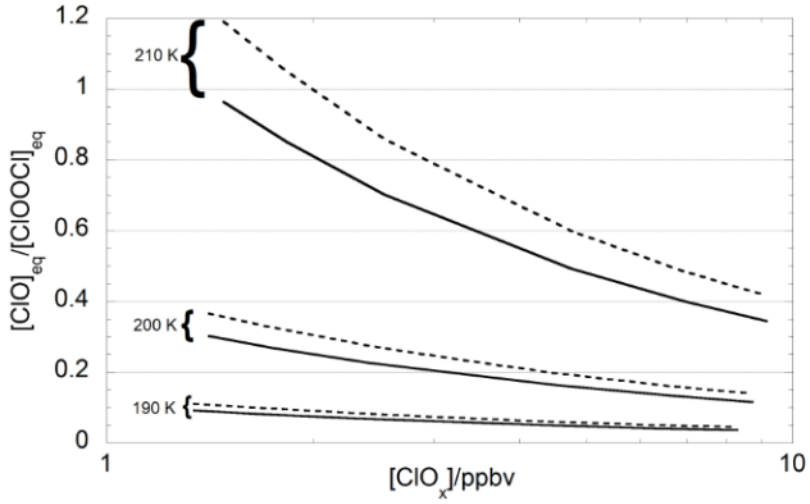

Figure 4.24 : Ratio of the equilibrium concentrations of [ClO] to [ClOOCl] against total [ClO_x] (defined as [ClO_x] = $[ClO]_{eq}$ + 2× $[ClOOCl]_{eq}$) calculated for an altitude of z = 20 km, from both the JPL-NASA [24] recommendation for K_{eq} (dashed line) and from the results of Third Law analysis performed in this work (solid line).

shows a near uniform reduction in the ratio of ClO to its dimer of approximately 17%. Thus, this not only affects the partitioning of the active Cl in the stratosphere, it would also, in the absence of sunlight, reduce the concentration of ClO radicals available for potential participation in other stratospheric cycles.

4.5 Conclusions

The equilibrium constant for the ClO dimerisation reaction has been studied using laser photolysis of a variety of gas mixtures along with broadband spectral monitoring over the temperature range T = 256.5-312.6 K, a range which was constrained by sensitivity analyses. The resulting equilibrium constants were found to be at the upper limit of uncertainty of the current JPL-NASA recommendations but in agreement with other optical studies of these parameters once sensitivity issues are taken into account. The resulting thermochemical parameters, $\Delta_r H°$ and $\Delta_r S°$ were found to be lower (more negative) than the current JPL-NASA recommendations, implying a shift in partitioning of ClO towards the ClO dimer at Polar stratospheric temperatures.

4.6 References

1. L.T. Molina, M.J. Molina, *J. Phys. Chem.*, **1987**, 91, 433
2. M. Trolier, R.L. Mauldin III, A.R. Ravishankara, J. Phys. Chem., **1990**, 94, 4896
3. W.J. Bloss, S.L. Nickolaisen, R.J. Salawitch, R.R. Friedl, S.P. Sander, *J. Phys. Chem. A*, **2001**, 105, 11226
4. G. Boakes, W.H. Hindi Mok, D.M. Rowley, *Phys. Chem. Chem. Phys.*, **2005**, 7, 4102
5. R.A. Cox, G.D. Hayman, *Nature*, **1988**, 332, 796
6. J. Plenge, S. Kuhl, B. Vogel, R. Muller, F. Stroh, R. Flesch, E. Ruhl, *J. Phys. Chem. A*, **2005**, 109, 6730
7. R. Bröske, F. Zabel, *J. Phys. Chem. A*, **2006**, 110, 3280
8. N. Basco and J.E. Hunt, *Int. J. Chem. Kinet.*, **1979**, 11, 649
9. S.L. Nickolaisen, R.R. Friedl, S.P. Sander, *J. Phys. Chem.*, **1994**, 98, 155
10. T. Ellermann, K. Johnsonn, A. Lund, P. Pagsberg, *Acta Chem Scand.*, **1995**, 48, 28
11. J.B. Burkholder, J.J. Orlando, C.J. Howard, *J. Phys. Chem.*, **1990**, 94, 687
12. K.J. Huder, W.B. DeMore, *J. Phys. Chem.*, **1995**, 99, 3905
13. F.D. Pope, J.C. Hansen, K.D. Bayes, R.R. Friedl, S.P. Sander, *J. Phys. Chem. A*, **2007**, 111, 4322
14. M. von Hobe, R.J. Salawitch, T. Canty, H. Keller-Rudek, G.K. Moortgat, J.-U. Grooß, R. Müller, F. Stroh, *Atmos. Chem. Phys.*, **2007**, **7**, 3055
15. S.P. Sander, B.J. Finlayson-Pitts, R.R. Friedl, D.M. Golden, R.E. Huie, H. Keller-Rudek, C.E. Kolb, M.J. Kurylo, M.J. Molina, G.K. Moortgat, V.L. Orkin, A.R. Ravishankara and P.H. Wine: *Chemical Kinetics and Photochemical Data for Use in Atmospheric Studies*, Evaluation No. 15, **2006**, JPL Publication 06-2, Jet Propulsion Laboratory, Pasadena, United States, http://jpldataeval.jpl.nasa.gov
16. M. von Hobe, F. Stroh, H. Beckers, T. Benter, H. Willner, *Phys. Chem. Chem. Phys.*, **2009**, 11, 1571
17. H.-Y. Chen, C.-Y. Lien, W.-Y. Lin, Y.T. Lee and J.J. Lin, *Science*, 2009, 324, 781

18. D.K. Papanastasiou, V.C. Papadimitriou, D.W. Fahey, J.B. Burkholder, *J. Phys. Chem. A*, 2009, 133, 13711
19. D.M. Wilmouth, T.F. Franco, R.M. Stimpfle, J.G. Anderson, *J. Phys. Chem. A*, 2009, 133, 14099
20. M.A.A. Clyne, J.A. Coxon, *Proc. R. Soc. Lond. Ser. A*, **1968**, 303, 207
21. S.P. Sander, B.J. Finlayson-Pitts, R.R. Friedl, D.M. Golden, R.E. Huie, C.E. Kolb, M.J. Kurylo, M.J. Molina, G.K. Moortgat, V.L. Orkin and A.R. Ravishankara: *Chemical Kinetics and Photochemical Data for Use in Atmospheric Studies*, Evaluation No. 14, **2003**, JPL Publication 02-25, Jet Propulsion Laboratory, Pasadena, United States
22. L.M. Avallone, D.W. Toohey, *J. Geophys. Res.*, **2001**, 106, 10411
23. M. von Hobe, J.-U. Grooβ, R. Müller, S. Hrechanyy, U. Winkler, F. Stroh, *Atmos. Chem. Phys.*, **2005**, 5, 693
24. S.P. Sander, J. Abbatt, J.R. Barker, J.B. Burkholder, R.R. Friedl, D.M. Golden, R.E. Huie, C.E. Kolb, M.J. Kurylo, G.K. Moortgat, V.L. Orkin, P.H. Wine, *Chemical Kinetics and Photochemical Data for Use in Atmospheric Studies*, Evaluation No. 17, **2011**, JPL Publication 10-6, Jet Propulsion Laboratory, Pasadena, United States
25. G.D. Smith, F,M.G. Tablas, L.T. Molina and M.J. Molina, *J. Phys. Chem. A.*, **2001**, 105, 8658
26. C. N. Hinshelwood, C. R. Prichard, *J. Chem. Soc.*, **1923**, 123, 2730
27. V. Ferracci, D.M. Rowley, *Phys. Chem. Chem. Phys.*, **2010**, 12, 11596
28. A. R. Curtis, W. P. Sweetenhan, *FACSIMILE*, **1987**, AERE Harwell Publication, Oxford
29. N. Basco, S.K. Dogra, *Proc. Roy. Soc. London Ser A.*, **1971**, 323, 401
30. M. Birk, R.R. Friedl, E.A. Cohen, H.M. Pickett, S.P. Sander, *J. Chem. Phys.*, **1989**, 91, 6588
31. M.W. Chase, *NIST-JANAF Thermochemical Tables, J. Phys. Chem. Ref. Data Monograph*, 9 (complete issue) **1998**
32. P.A. Rock, *Chemical Thermodynamics*, **1983**, Oxford University Press
33. J.B. Ott, J. Boerio-Goates, *Chemical Thermodynamics: Principles and Applications*, **2000**, Academic Press, London

34. D.A. Mc Quarrie, J.D. Simon, *Molecular Thermodynamics*, **1999**, University Science Book, Sausalito, California, United States
35. B. Widom, *Statistical Mechanics*, **2002**, Cambridge University Press, Cambridge
36. G. Herzberg, in *Molecular Spectra and Molecular Structure I. Spectra of Diatomic Molecules*, 2nd edition, **1950**, Van Nostrand Reinhold Company
37. D.M. Golden, *Int. J. Chem. Kinet.*, **2003**, 35, 206
38. S.W. Benson, *Thermochemical Kinetics*, 2nd Edition, 1976, John Wiley & Sons
39. MultiWell-2010 Software, **2010**, designed and maintained by John R. Barker with contributors Nicholas F. Ortiz, Jack M. Preses, Lawrence L. Lohr, Andrea Maranzana, Philip J. Stimac, T. Lam Nguyen, and T. J. Dhilip Kumar; University of Michigan, Ann Arbor, MI; http://aoss.engin.umich.edu/multiwell
40. J. R. Barker, *Int. J. Chem. Kinetics*, **2001**, 33, 232
41. S. Abramowitz, M.W. Chase Jr., *Pure Appl. Chem.*, 1991, 63, 1449
42. R.P. Thorn Jr., L.J. Stief, S.-C.Kuo, R.B. Klemm, *J. Phys. Chem.*, 1996, 100, 14178
43. J.C. Traeger, R.G. McLoughlin, *J. Am. Chem. Soc.*, 1981, 103, 3647

Chapter 5
Kinetic Studies of the Bimolecular Channels of the ClO Self-Reaction

5.1 Introduction

The ClO self-reaction is a very complex multichannel process. In addition to the termolecular dimer formation, extensively described in Chapter 4,

$$ClO + ClO + M \quad \leftrightarrows \quad Cl_2O_2 + M \qquad (5.1a, -5.1a)$$

three "bimolecular" (pressure-independent) channels are known:

$$ClO + ClO \quad \rightarrow \quad Cl_2 + O_2 \qquad (5.1b)$$

$$\rightarrow \quad ClOO + Cl \qquad (5.1c)$$

$$\rightarrow \quad OClO + Cl \qquad (5.1d)$$

Unlike the forward reaction (5.1a), channels (5.1b-5.1d) have a positive temperature dependence: they are therefore negligible under polar stratospheric conditions but become relevant above ambient temperature. According to the current JPL-NASA recommended kinetic data,[1] the sum of the bimolecular rate constants contributes only to 0.06% of the total rate constant for the ClO self-reaction, $k_{5.1}$ (defined as $k_{5.1} = k_{5.1a}[M] + k_{5.1b} + k_{5.1c} + k_{5.1d}$) at $T = 200$ K and $p = 760$ Torr, but their contribution rises to approximately 6% at $T = 298$ K and $p = 760$ Torr. Figure 5.1 illustrates the variation with temperature of the percentage contribution of the bimolecular channels to the total loss rate coefficient for ClO $k_{5.1}$ at $p = 760$ Torr and at $p = 50$ Torr. At both pressures, the combined rate constants of channels (5.1b-5.1c) only represent < 1% of the total $k_{5.1}$ at temperatures typical of Polar vortices (T = 180-200 K). However, a number of laboratory studies, [2, 3, 4, 5, 6] including material presented in this thesis, have investigated the ClO dimerisation and other ClO reactions at temperatures $T \geq 298$ K where the effect of the bimolecular channels on the observed ClO decay is not negligible. An accurate characterisation of these channels is therefore required in order to improve the

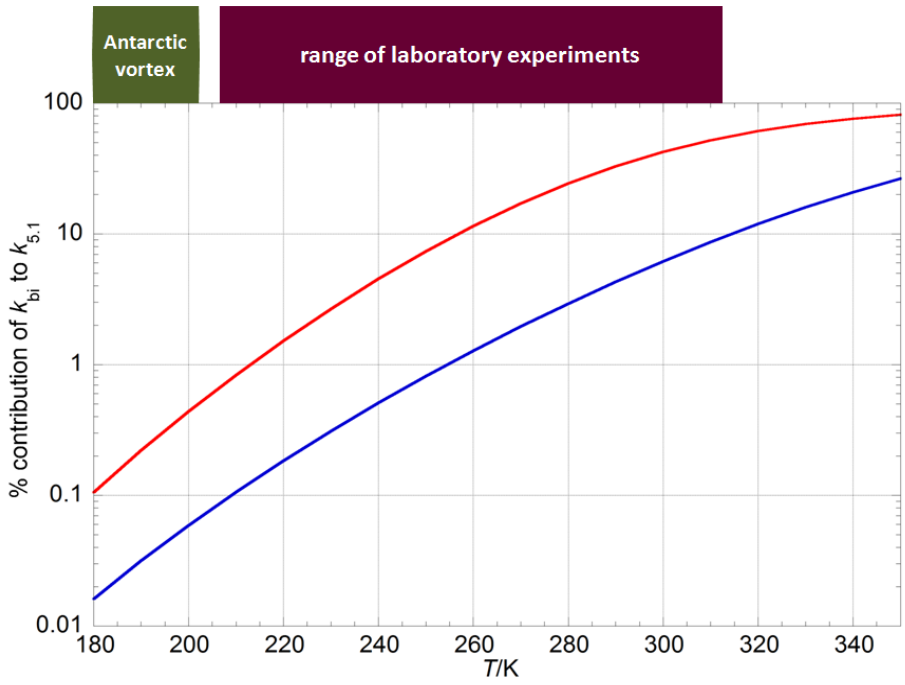

Figure 5.1 : Percentage contribution of the sum of the bimolecular rate constants, k_{bi} (k_{bi} = $k_{5.1b}$ + $k_{5.1c}$ + $k_{5.1d}$) to the total $k_{5.1}$ ($k_{5.1}$ = $k_{5.1a}$[M] + k_{bi}) at p = 760 Torr (blue line) and at p = 50 Torr (red line) as a function of temperature. Also shown is the temperature range typical of the Antarctic Stratospheric vortex (T = 180-200 K) and that of laboratory experiments on ClO dimerisation [2, 3, 4, 5, 6] (T = 206-312 K).

reliability of, for example, the dimerisation kinetics of ClO at such temperatures and also to gain valuable insight on the energetics of the potential energy surface of the ClO self-reaction, as discussed in Section 2.3.

5.1.1 Previous Studies

Previous work on the bimolecular channels of the ClO self-reaction, summarised below, has reported conflicting results on both the absolute rate constants and on the branching of reactions (5.1b)-(5.1d).

Early studies [7, 8, 9, 10, 11, 12, 13] of the ClO self-reaction date back to the 1950s and reflect the uncertainties as to the very existence of the multiple channels. Initially, channel (5.1b) was thought to be the only reaction pathway of the ClO self-reaction: flash photolysis studies by Porter and Wright [7] and Edgecombe *et al.* [8] observed second-order [ClO] decay and suggested that the reaction proceeded through a short-lived Cl_2O_2

intermediate, existing in equilibrium with ClO and decaying slowly to form the molecular products Cl_2 and O_2.

Benson and Buss [9] invoked an alternative mechanism involving regeneration of Cl atoms to account for the observed chain decomposition of Cl_2O and OClO. In their work, channel (5.1b) still represented the overall reaction but these authors proposed that ClOO was initially formed *via* (5.1c) which then reacted with Cl atoms to yield Cl_2 and O_2. However, due to its rapid thermal dissociation, no direct evidence for the production of the ClOO radical was obtained until the study by Johnston *et al*., [10] the first to detect this transient species by means of its electronic and vibrational absorption spectra using molecular modulation kinetic spectroscopy.

The studies of Clyne and co-workers [11, 12, 13] were crucial in identifying some of the product channels of the ClO self-reaction. Initially, kinetic evidence for the production of Cl atoms was obtained by Clyne and Coxon [11] using discharge flow coupled with UV absorption spectroscopy: Cl atom-scavenging species such as OClO and O_3 were introduced to the reaction mixture and their removal was monitored. This result was interpreted as an indication of reaction (5.1c) operating, hence supporting the mechanism originally proposed by Benson and Buss. In the same study, Clyne and Coxon also observed third-order ClO kinetics at high pressures and postulated the existence of a termolecular branch leading to ClO dimerisation at higher pressures, whereas the bimolecular decay described by Benson and Buss would dominate at lower pressures. Following on from these conclusions, Clyne and White [12] carried out a study in the low pressure regime to characterise the bimolecular mechanism using discharge flow with UV absorption spectroscopy. Channel (5.1d) was first identified by Clyne *et al*. [13] in one of the first experiments to monitor the species involved, in this case OClO, in the ClO self-reaction using mass spectrometry in the place of UV absorption spectroscopy.

A modulated photolysis study by Cox and Derwent [14] also identified OClO as one of the products of the ClO self-reaction. In their study the temporal behaviour of ClO, OClO and O_3 was monitored using UV absorption spectroscopy and found to be consistent with a mechanism consisting of a termolecular component (reactions (5.1a),(−5.1a)) and

three bimolecular reactions (channels (5.1b)–(5.1d)). Cox and Derwent determined the rate constants of the individual channels at T = 298 K and p = 1 atm and also calculated the branching ratios as (5.1b) = 0.49, (5.1c) = 0.34, (5.1d) =0.17. A coeval study of the chlorine photosensitised decomposition of ozone by Wongdontri-Stuper *et al.* [15] agreed with the mechanism identified by Cox and Derwent but obtained somewhat different branching ratios (5.1b) = 0.34, (5.1c) = 0.63, (5.1d) = 0.032 at T = 296 K .

In a brief communication, Hayman *et al.* [16] stressed the importance of the termolecular component of the ClO self-reaction in light of the ozone depletion events which were first observed in the mid-1980s. Studying the temperature dependence of both the ClO dimerisation and the bimolecular channels of ClO + ClO by means of molecular modulation spectroscopy over the range T = 268-338 K, Hayman *et al*. concluded that the ClO dimerisation was the dominant process for ClO loss at stratospheric temperatures. The value obtained in the Hayman *et al*. study for the overall bimolecular rate constant, k_{bi} (defined as $k_{bi} = k_{5.1b} + k_{5.1c} + k_{5.1d}$) at T = 298 K, $k_{bi} = 5.5\times10^{-15}$ cm^3 molecule^{-1} s^{-1}, is the smallest reported to date.

Simon *et al*. [17] also employed modulated photolysis to study the ClO self-reaction and determined the absolute rate constants of the three bimolecular channels, hence their branching ratios, at T = 300 K. Their findings indicate nearly equal contributions from all three channels to the overall bimolecular rate constant, with individual rate constants higher than those measured by Cox and Derwent by up to a factor of two. The overall bimolecular rate constant measured in their study ($k_{bi} = 2.18\times10^{-14}$ cm^3 molecule^{-1} s^{-1}) is the largest reported to date.

Horowitz and co-workers measured the branching ratios of the bimolecular channels of ClO + ClO by monitoring the chlorine-sensitised continuous photolysis of ozone coupled with time resolved diode array spectroscopy, first at T = 298 K,[18] then at ten temperatures over the range T = 285–331 K. [19] Their findings identify reaction (5.1d) as a minor channel, in good agreement with the results of Cox and Derwent but in contrast with those of Simon *et al*. However, unlike Cox and Derwent and Wongdontri-Stuper *et al*., Horowitz and co-workers observed an almost equal contribution of channels (5.1b) and (5.1c) to the overall bimolecular decay of ClO.

By far the most comprehensive study on the bimolecular channels of the ClO self-reaction is the work of Nickolaisen *et al.*, [2] who studied reactions (5.1b)-(5.1d) at eight temperatures over the range T = 300-390 K using flash photolysis with UV absorption spectroscopy using an optical multichannel analyser. These authors determined an overall rate constant of $k_{bi} = 1.65\times10^{-14}$ cm^3 molecule^{-1} s^{-1} and branching ratios of (5.1b) = 0.29, (5.1c) = 0.49, (5.1d) = 0.22 at T = 298 K. Results from previous studies of the ClO + ClO bimolecular channels are summarised in Table 5.1. The current JPL-NASA [1] recommended values for the rate constants of the bimolecular channels have remained unchanged since 1997 and are based exclusively on the work by Nickolaisen *et al.* [2]

In the light of the paucity and conflicting results of previous studies, a thorough characterisation of the ClO + ClO bimolecular channels was proposed. A more accurate knowledge of the temperature dependence of $k_{5.1b}$, $k_{5.1c}$ and $k_{5.1d}$ would reduce some of the uncertainties affecting laboratory studies of the ClO dimerisation and other reactions of ClO especially above ambient temperature.

5.2 Experimental

This work aimed at studying the kinetics of the ClO + ClO bimolecular reaction channels by means of laser flash photolysis coupled with UV absorption spectroscopy. The incorporation of charge-coupled device (CCD) detection allowed broadband monitoring of multiple absorbing species, ClO and OClO, in the same experiment.

5.2.1 Radical Generation

The reaction scheme of ClO radical generation for the study of the bimolecular channels was identical to one of the methods used in the study of ClO dimerisation described in Section 4.2.1 and consisted of laser photolysis at λ = 351 nm of $Cl_2O/Cl_2/N_2$ precursor mixtures. Photolysis of Cl_2, followed by reaction of Cl atoms with excess Cl_2O, was the principal source of ClO radicals:

$$Cl_2 + h\nu \rightarrow 2Cl \qquad (5.2)$$

Reference	Technique[a]	T/K	$k_{5.1b}$	$k_{5.1c}$	$k_{5.1d}$	k_{bi}[b]	$k_{5.1b}/k_{bi}$	$k_{5.1c}/k_{bi}$	$k_{5.1d}/k_{bi}$
			/10^{-15} cm^3 molecule^{-1} s^{-1}						
Cox and Derwent (1978)[14]	MM/UV	298	4.5 ± 1	3.1 ± 0.8	1.5 ± 0.4	9.1 ± 1.3	0.49 ± 0.1	0.34 ± 0.1	0.17 ± 0.1
Wongdontri-Stuper *et al.* (1979) [15]	PD						0.34[c]	0.63[c]	0.032[c]
Burrows and Cox (1981)[20]	MM/UV	298	8.2 ± 2	7.2[d]	8.0[d]	23.4	0.35	0.31	0.34
Hayman *et al.* (1986) [16]	MM/UV	268-338				$5.5^{+15.2}_{-4}$			
Simon *et al.* (1990) [17]	MM/UV	300	7.3 ± 1.8[e]	7.2 ± 1.6[e]	7.3 ± 2.6[e]	21.8 ± 3.5[e]	0.33 ± 0.1[e]	0.33 ± 0.1[e]	0.33 ± 0.1[e]
Horowitz *et al.* (1993) [18]	PD	298					0.40 ± 0.08	0.42 ± 0.08	0.18 ± 0.02
Nickolaisen *et al.* (1994) [2]	FP/UV	300-380	4.88 ± 0.6	8.0 ± 1.8	3.5 ± 0.3	16.5 ± 2.7	0.29 ± 0.06	0.49 ± 0.13	0.22 ± 0.04
Horowitz *et al.* (1994) [19]	PD	285-331					0.39 ± 0.06	0.41 ± 0.06	0.20 ± 0.03
This work	LP/UV	298-323	11.6 ± 0.3		4.08 ± 0.07				

Notes

[a]: MM/UV = molecular modulation / UV absorption spectroscopy; PD = photosensitised decomposition; FP/UV = flashlamp photolysis / UV absorption spectroscopy; LP/UV = Laser photolysis / UV absorption spectroscopy

[b]: defined as $k_{bi} = k_{5.1b}+k_{5.1c}+k_{5.1d}$

[c]: at $T = 296$ K

[d]: errors not reported

[e] : at $T = 300$ K

Table 5.1 : Summary of the results of previous studies on the ClO + ClO bimolecular channels. All rate constants and branching ratios reported are at T = 298 K except where noted.

$$Cl + Cl_2O \rightarrow Cl_2 + ClO \qquad (5.3)$$

Direct photolysis of Cl_2O represented a minor source of ClO, as a result of the small absorption cross-section of Cl_2O at λ = 351 nm (σ_{Cl_2O} = 7.0 × 10^{-21} cm^2 molecule^{-1}), compared to that of Cl_2 (σ_{Cl_2} = 1.8 × 10^{-19} cm^2 molecule^{-1}) [1].

All precursor gases were delivered *via* Teflon tubing to a Pyrex mixing line where they mixed with a nitrogen (BOC, > 99.98%) carrier flow. The nitrogen flow rate was set using mass flow controllers (MKS), whereas that of Cl_2 (BOC, supplied as 5% by volume in N_2; purity > 99%) was controlled using needle valves and measured using a calibrated glass ball meter (rotameter). Cl_2O was produced *in situ* by passing a known flow of the diluted Cl_2 gas through a trap containing solid dried yellow mercuric (II) oxide (HgO, Sigma-Aldrich, > 99%), as originally described by Hinshelwood and Pritchard [21] and as discussed in Section 4.2.1.

Pre-photolysis concentrations of precursor gases in the reaction cell were typically [Cl_2] = (7-13) × 10^{15} molecule cm^{-3}, as determined from measured gas flow rates; [Cl_2O] = (7-10) × 10^{15} molecule cm^{-3} as determined by UV spectroscopy (Section 5.2.4), with the N_2 carrier gas to balance to p = 1 atm. Under these conditions, photolytically generated Cl atoms were rapidly and stoichiometrically converted to ClO *via* reaction (5.3). Initial Cl atom and therefore ClO radical concentrations immediately after photolysis were typically (1-2) × 10^{14} molecule cm^{-3}.

5.2.2 Species Monitoring

Species in the reaction cell were monitored using UV absorption spectroscopy *via* charge coupled device (CCD) detection. The width of the spectral window arising from the use of a 600 grooves mm^{-1} diffraction grating, used in the experiments on ClO dimerisation, of approximately 30 nm was, however, somewhat insufficient to encompass the region where *both* ClO and OClO absorb, as illustrated in Figure 5.2. Therefore a diffraction grating of 300 grooves mm^{-1} was employed, giving rise to a

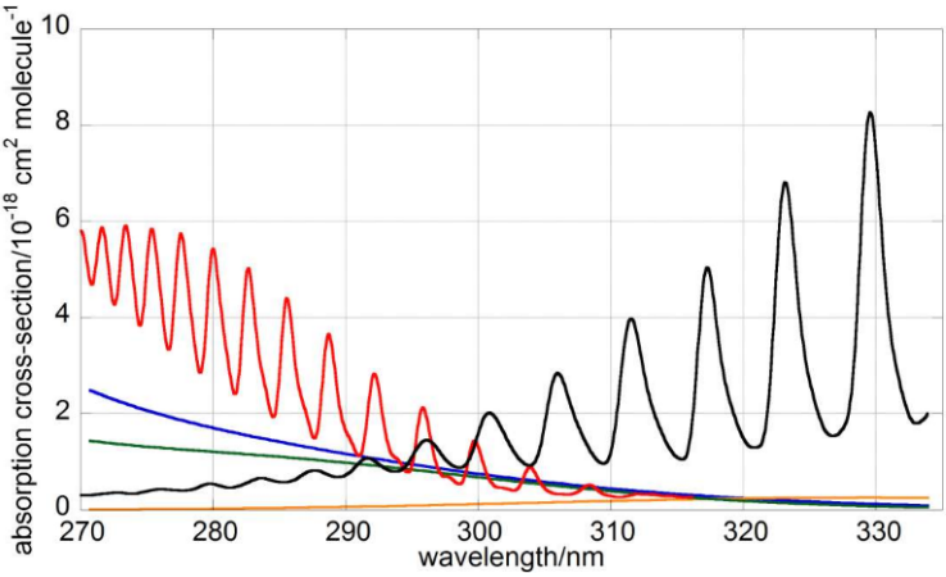

Figure 5.2 : Cross-sections of the absorbing species involved in the photolysis experiments of $Cl_2O/Cl_2/N_2$ precursor mixtures. Cross-sections are colour-coded as follows: ClO (red), Cl_2O_2 (blue), Cl_2O (green), Cl_2 (orange) and OClO (black).

wavelength coverage across the CCD device of approximately 60 nm. A spectral range of λ = 270-330 nm was typically monitored in these experiments. The spectrograph entrance slit width was set to 75 μm resulting in a spectral resolution (FWHM) of 1.1 nm, as determined by recording the emission spectrum of a mercury 'pen-ray' lamp.

The temporal resolution of the experiment was dictated by the time between each charge transfer event (*shift time*) of the CCD, as extensively described in Section 3.2.2. As the kinetics of the ClO + ClO bimolecular channels are somewhat slower than those of ClO dimerisation, a shift time greater than that used in the dimerisation experiments (100 μs) had to be employed for the observed [ClO] temporal trace to show decay *via* channels (5.1b)-(5.1d), as illustrated in Figure 5.3. However, as the shift time was increased, the exposure time of the detector to the transmitted light also increased and, at values of the shift time above 1 ms, and for the spectral window adopted, the detector became saturated. It was therefore necessary to insert a neutral density filter along the path of the analysis light beam to reduce transmission of the output of the xenon lamp over the chosen wavelength range. After the inclusion of this neutral density filter, shift times greater than 1 ms were readily attainable without saturating the detector. In the experiments on the ClO bimolecular channels, the shift time was typically set to 2-3 ms/row, giving a total exposure time of 2-3 s.

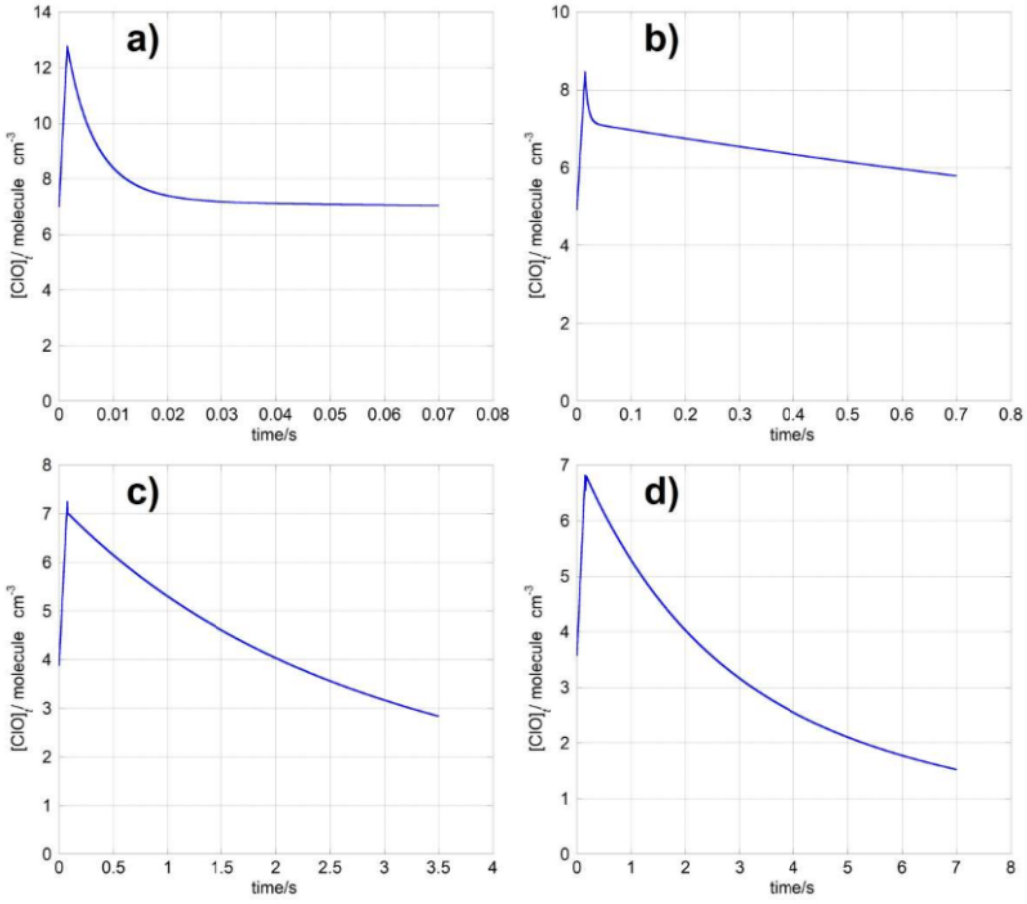

Figure 5.3 : Simulations of [ClO] decay at T = 298 K following photolysis at different timescales: a) shift time = 100 μs, b) shift time = 1 ms, c) shift time = 5 ms, d) shift time = 10 ms.

Absorbance spectra were calculated relative to the pre-photolysis light intensity as described in Section 3.4.1. These spectra therefore represented the change in absorbance brought about by photolysis and by the photolytically initiated chemistry. An "early" spectrum (recorded in the immediate post-photolysis) and a "late" spectrum (recorded at longer timescales after photolysis) are illustrated in Figure 5.4 and show the successful detection of two characteristic absorbing species. ClO vibronic peaks (λ = 270-305 nm) are very pronounced in the "early" spectrum due to the initial rapid formation of ClO *via* reaction (5.3); however the ClO signal is much weaker in the "late" spectrum following bimolecular decay of ClO. On the other hand, OClO vibronic features arising from the A ($^2A_2$) ← X ($^2B_1$) transition (λ = 305–330 nm) are very weak in the "early" spectrum but become stronger at longer timescales following OClO build-up *via* reaction (5.1d).

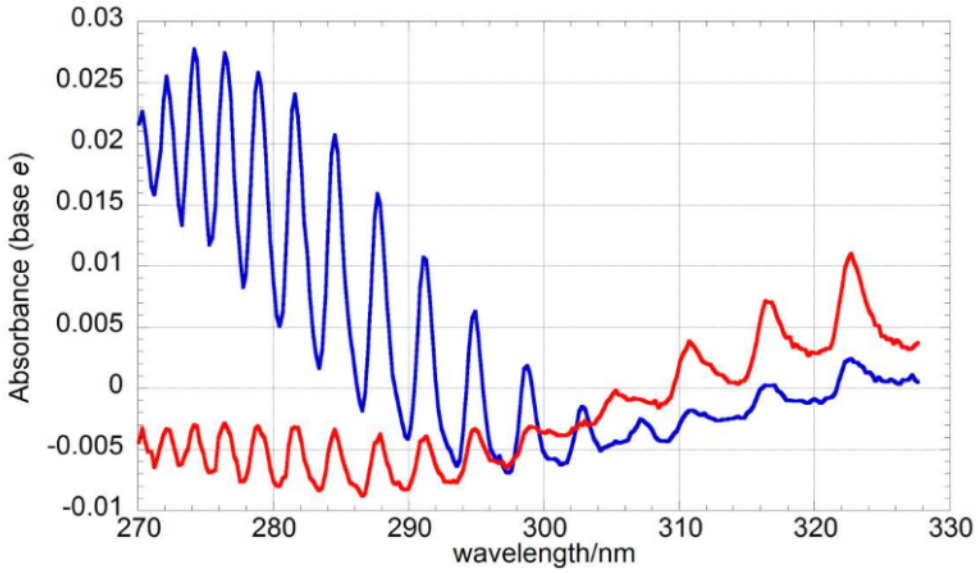

Figure 5.4 : Typical absorbance spectra recorded at T = 323 K at different times after photolysis. The 'early' spectrum in blue (averaged between t = 0.09-0.2 s after photolysis) shows the distinctive bands of the ClO spectrum at shorter wavelengths and a weak signal from OClO at the high wavelength end of the spectrum. The 'late' spectrum in red (averaged between t = 1.21-1.34 s after photolysis) shows a decreased ClO signal following decay of the radical but stronger OClO peaks originating from OClO build-up over longer timescales.

5.2.3 Determination of Species Concentrations

Quantification of ClO and OClO concentrations *via* the Beer-Lambert law required an accurate determination of the cross-section of both species, as discussed in Section 3.4.2. As elucidated in detail in Section 4.2.3, a parameterisation of the temperature dependence of the ClO differential cross-section, $\sigma_{\mathrm{ClO\ diff}}$, at the (12, 0) peak ($\lambda$ = 275.2 nm) was available from the study of Boakes *et al.* [5] and from the experiments on the ClO dimerisation presented in Chapter 4. [6] Both parameterisations were obtained in this laboratory under very similar conditions to the experiments on the bimolecular channels. However, the parameterised $\sigma_{\mathrm{ClO\ diff}}$ available were reported at a higher resolution (0.8 nm FWHM) than that employed in the study of the bimolecular channels (1.1 nm FWHM) arising principally from the use of a different diffraction grating to facilitate wavelength coverage, as described above. Since structured spectral features such as the ClO vibronic bands are a strong function of the instrumental resolution, the high-resolution parameterisations from previous studies could not be used to scale directly the low-resolution ClO spectrum from the current work on the ClO bimolecular

channels. Therefore a series of experiments was undertaken to calibrate $\sigma_{ClO\ diff}$ at the lower resolution employed here. Experiments involving the photolysis of $Cl_2O/Cl_2/N_2$ mixtures, each consisting of 20 co-added photolysis events, were performed at each experimental temperature. Eight experiments were carried out back to back, with the odd ones recorded at the higher resolution of 0.8 nm FWHM whilst the even ones at the lower resolution used in the present study (1.1 nm FWHM); conditions were otherwise identical. The parameterisation of $\sigma_{ClO\ diff}(T)$ from this study on ClO dimerisation, reported in Section 4.2.3, was then used to quantify time-resolved ClO concentrations from the high-resolution experiments. These concentrations were then used to calibrate cross-sections from the interleaving low resolution experiments, described below. The returned values for $[ClO]_t$ from different high-resolution experiments at each temperature agreed within 2%, as illustrated in Figure 5.5. This indicated that no significant change to ClO concentrations and kinetic decay had occurred between the experiments and lent confidence to the assumption that the chemistry within the reaction cell was unchanged during the back-to-back experiments at different resolutions.

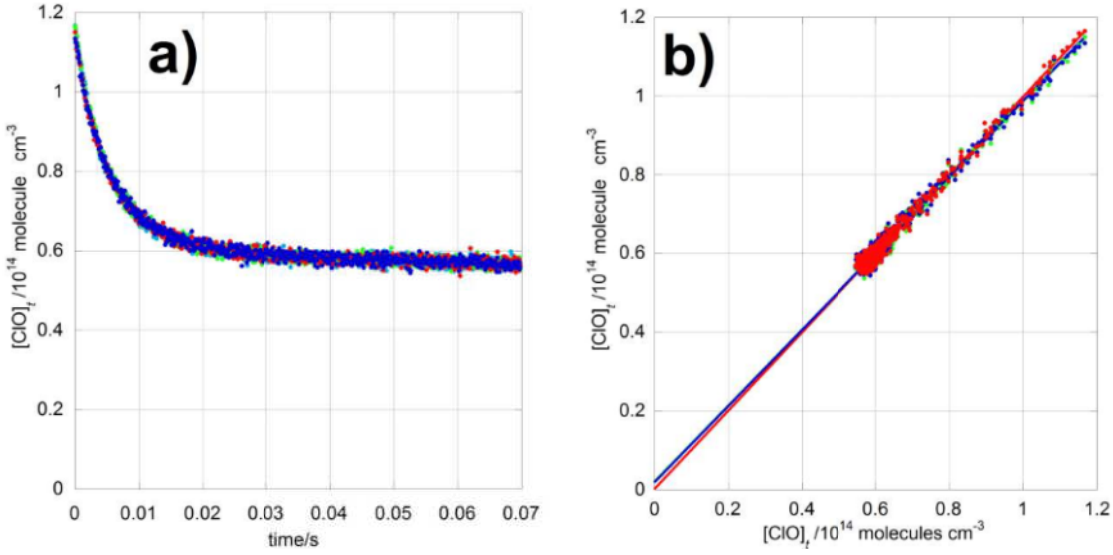

Figure 5.5 : Reproducibility in the [ClO] temporal traces obtained from high-resolution experiments at $T = 298$ K: a) the four traces show excellent agreement with minimal (< 2%) deviation from one another; b) this can be shown by plotting three of the ClO concentrations from traces against those from the first one recorded (data points): the result is a straight line of the form $y = x$, with gradient approaching unity and a near-zero intercept, as shown by the linear fits (solid lines).

σ_{ClO} at the lower resolution was obtained by rearranging the Beer-Lambert law:

$$\sigma_{ClO,\lambda} = \frac{A_{ClO,\lambda}}{[ClO]\,l} \qquad (5.i)$$

where $\sigma_{ClO,\lambda}$ is the low resolution cross-section of ClO at wavelength λ, $A_{ClO,\lambda}$ is the ClO absorbance at wavelength λ from the low resolution experiments, [ClO] is the concentration of ClO quantified from the high resolution experiments and l is the optical pathlength of the reaction cell.

This procedure was repeated at each experimental temperature. Validation of this method was also provided by direct comparison of the differential low-resolution ClO cross-section at the (12, 0) vibronic peak of ClO with the results of previous studies. This is illustrated in Figure 5.6: for every temperature at which the low-resolution ClO

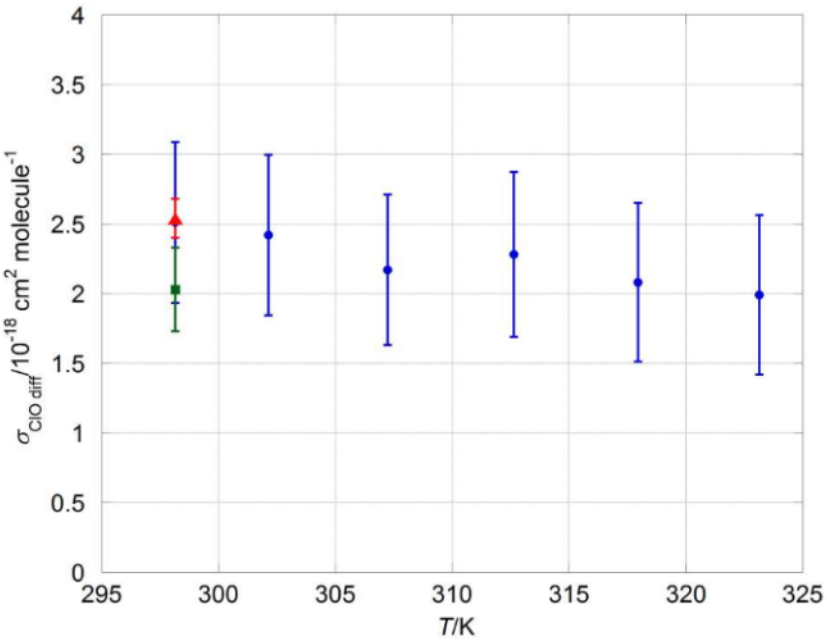

Figure 5.6 : ClO differential cross-section at the (12, 0) band (λ = 275.2 nm) to the trough at higher wavelength (λ = 276.4 nm) at a spectral resolution of 1.1 nm (FWHM) as a function of temperature. Values of $\sigma_{ClO\ diff}$ from back-to-back experiments performed in this work are shown as blue circles. The error bars shown result from the error analysis discussed in Section 5.4.1. Also shown are the values of $\sigma_{ClO\ diff}$ at T = 298 K from Boakes *et al.* [5] (red triangle) and from this work using the same method as Boakes *et al.* (green square), with error bars corresponding to 1σ, statistical only.

cross-section was calibrated using the method described above, the cross-section difference between the peak of the (12, 0) vibronic band at λ = 275.2 nm and the trough lying at higher wavelengths (λ = 276.4 nm) was measured to give a plot of low-resolution $\sigma_{\text{ClO diff}}$ as a function of temperature. Boakes *et al*. [5] investigated the effect of spectral resolution on $\sigma_{\text{ClO diff}}$; their method, described in detail in Section 4.2.3, relied on calibrating the structured part of the ClO spectrum using the *continuum* (unstructured) absorbance at λ < 265 nm. The value of $\sigma_{\text{ClO diff}}$ reported for the same vibronic band at T = 298 K and at a resolution of 1.1 nm (FWHM) in their work is in excellent agreement with the one obtained from the back-to-back experiments carried out in this work as shown in Figure 5.6. A calibration of $\sigma_{\text{ClO diff}}$ analogous to the procedure used by Boakes *et al*. was also carried out in the present study at T = 298 K and returned a value of $\sigma_{\text{ClO diff}}$ in overall excellent agreement with the back-to-back experiments method, as also shown in Figure 5.6.

The OClO cross-section measured by Wahner *et al*. [22] was used to generate the reference OClO spectrum for analysis in this work. This reference spectrum was reported at a higher resolution (0.25 nm FWHM) than the one employed in the current study (1.1 nm FWHM), hence it was degraded to the lower resolution using a 29-point Gaussian averaging kernel, as described in Appendix 3. The high-resolution spectrum from Wahner *et al*. [22] and the lower resolution one obtained from the spectral smoothing procedure are both shown in Figure 5.7. The residuals obtained by spectral subtraction of the scaled (differential) reference spectrum from the (differential) experimental spectra reported here (Figure 5.8) did not show any systematic features, thus adding confidence to this spectral smoothing procedure.

As the OClO vibronic bands are also a function of temperature, reference OClO cross-sections were interpolated to each experimental temperature using the spectra recorded by Wahner et *al*. at T = 204 K and T = 296 K, assuming that σ_{OClO} changed linearly with temperature over the range T = 204-323 K.

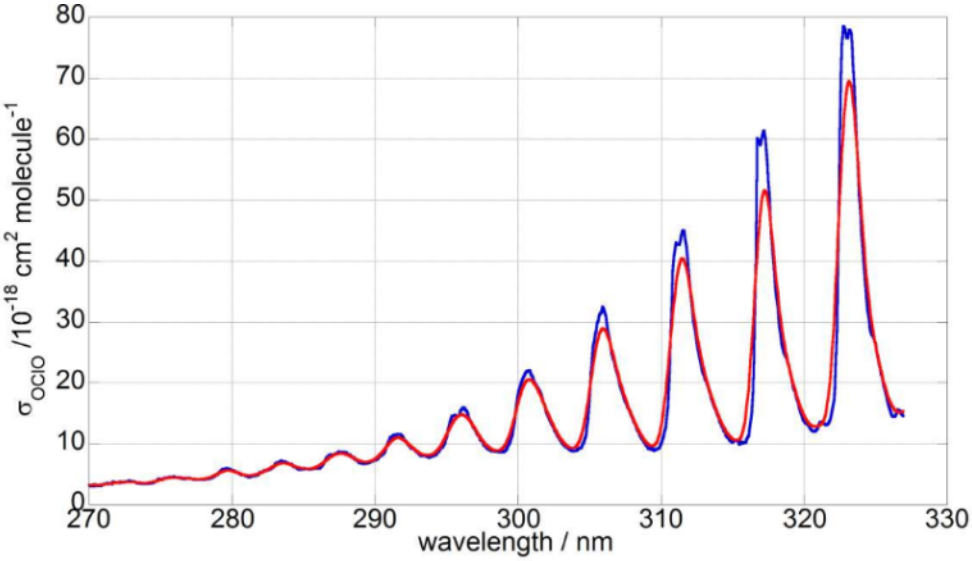

Figure 5.7 : The high-resolution OClO cross-section from Wahner *et al*. [22] (in blue) and the one at lower resolution obtained from spectral smoothing routine described in Appendix 3 (in red).

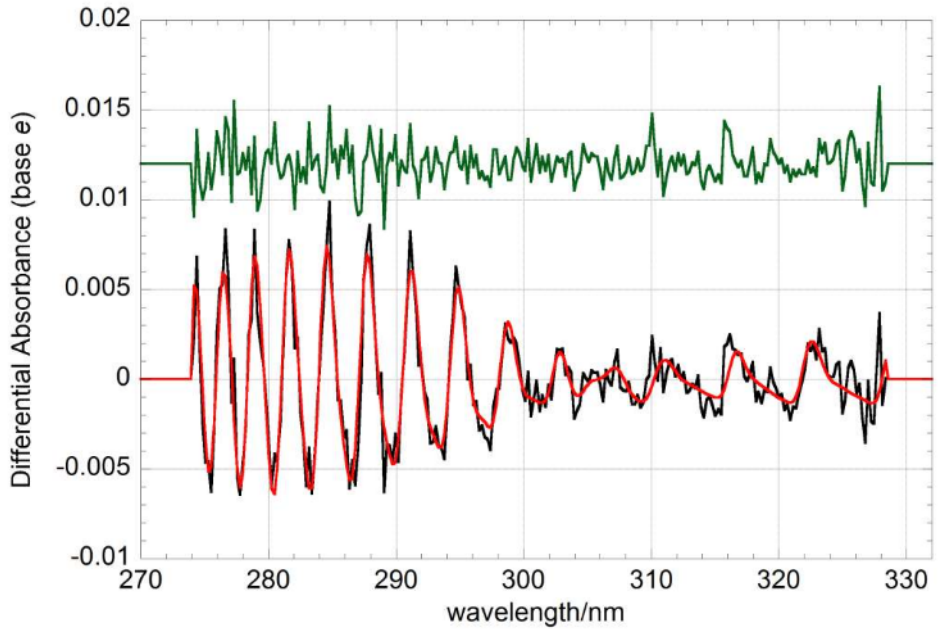

Figure 5.8 : Typical differential fit to a ClO and OClO spectrum reported here. The differential experimental spectrum is shown in black, the sum of the scaled differential cross-sections of both ClO and OClO is shown in red. Residuals, in green, have been offset by +0.012 differential absorbance units for clarity.

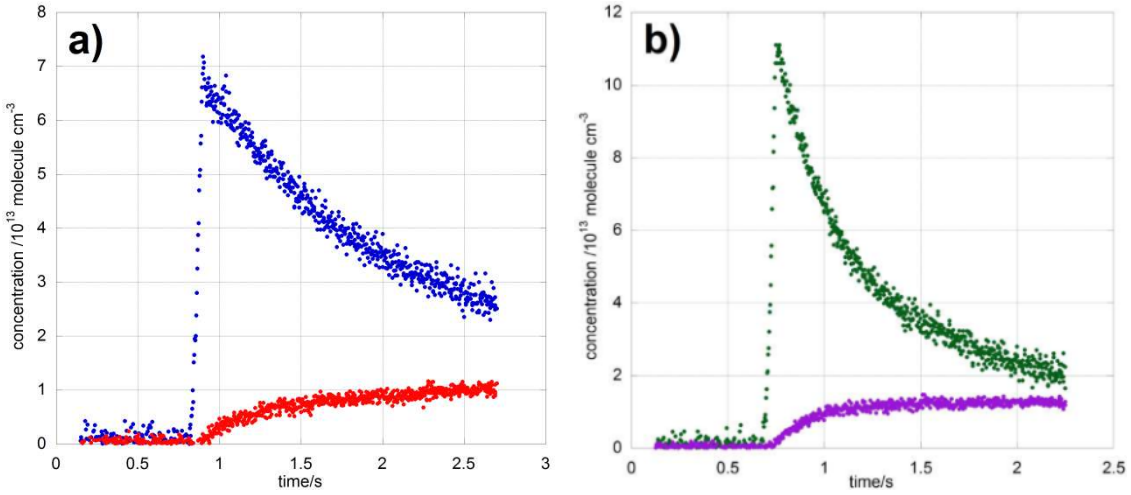

Figure 5.9 : Typical traces recorded at a) $T = 298$ K ($[ClO]_t$ in blue, $[OClO]_t$ in red) and b) $T = 323$ K ($[ClO]_t$ in green, $[OClO]_t$ in purple).

The cross-sections of ClO and OClO were fitted *simultaneously* and *differentially* to each sequential absorption spectrum to quantify $[ClO]_t$ and $[OClO]_t$ using a least squares minimisation routine. A typical differential fit to a recorded spectrum is shown in Figure 5.8. Typical $[ClO]_t$ and $[OClO]_t$ traces obtained at the two extremes of the temperature range studied, $T = 298$ K and $T = 323$ K, are shown in Figure 5.9.

5.2.4 Kinetic Analysis

Following production of the temporal concentration traces of ClO and OClO, kinetic analysis was carried out. Under the experimental conditions employed, the observed [ClO] decay showed no sensitivity to channel (5.1c). This results as chlorine peroxy radicals, ClOO, produced by reaction (5.1c) rapidly undergo thermal dissociation:

$$ClOO + M \rightarrow Cl + O_2 + M \qquad (5.4)$$

and channel (5.1c) can be considered as producing effectively two Cl atoms and molecular oxygen. Subsequently, reaction of these Cl atoms with excess Cl_2O present under the reaction conditions used promptly regenerated ClO radicals *via* reaction (5.3). This chemistry ensured that channel (5.1c) was effectively masked as verified by kinetic (steady state) derivations and numerical modelling. In analogous fashion, as a single

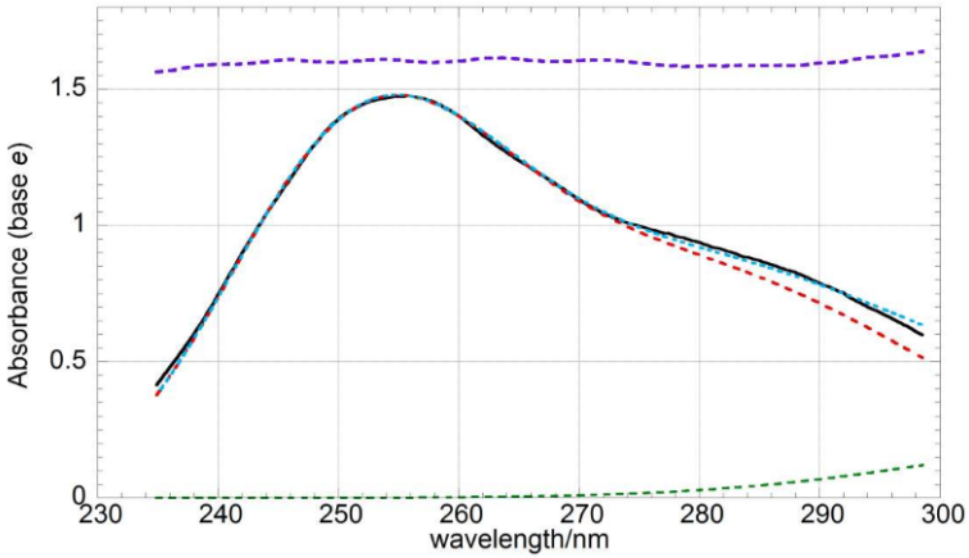

Figure 5.10 : Typical spectrum used to quantify [Cl_2O] in the precursor mixture showing the recorded absorbance (solid black line), the contribution of Cl_2O (dashed red line) and Cl_2 (dashed green line) to the total calculated absorbance (thinly dashed light blue line). Residuals (dashed purple line) were offset by +1.6 absorbance units for clarity. The spectrum shown corresponds to a mixture of [Cl_2O] = 8×10^{15} molecule cm^{-3} and [Cl_2] = 1.1×10^{16} molecule cm^{-3}.

chlorine atom is also produced by channel (5.1d), the effective rate constant for ClO loss *via* channel (5.1d) is halved.

To ensure that ClO radicals were promptly generated from any chlorine atom produced, Cl_2O concentrations were quantified accurately *via* UV spectroscopy before each photolysis experiment by recording absorbance spectra in the range λ = 235-298 nm, where the Cl_2O absorption is strongest. Cl_2O and Cl_2 cross-sections, parameterised by least-squares fitting of a set of Gaussian functions to the values recommended by JPL-NASA [1] as illustrated in Appendix 4, were fitted to the recorded absorbance (without photolysis) over the wavelength range used *via* the least squares method by optimising the value of [Cl_2O]. [Cl_2] was then calculated from the optimised [Cl_2O] as this value was also constrained by the overall number of chlorine molecules flowed into the HgO trap (known from calibration of the ball meter) and by the (2:1) stoichiometry of the Cl_2–Cl_2O conversion using HgO. Typical values of [Cl_2O] were $(7\text{-}10)\times10^{15}$ molecule cm^{-3} with residual [Cl_2] varying between $(7\text{-}13)\times10^{15}$ molecule cm^{-3}. A typical

absorbance spectrum recorded to quantify [Cl_2O] is shown in Figure 5.10 along with the contributions of both Cl_2O and Cl_2 to the recorded absorbance.

Regardless of the complete masking of channel (5.1c) and the partial (half) masking of channel (5.1d) under the experimental conditions used, the observed ClO decay is in principle described by the rate equation:

$$-\frac{1}{2}\frac{d[\mathrm{ClO}]}{dt} = \left(k_{5.1a}[\mathrm{M}] + k_{5.1b} + k_{5.1c} + k_{5.1d}\right)[\mathrm{ClO}]^2 - k_{-5.1a}[\mathrm{M}][\mathrm{Cl_2O_2}] \qquad (5.ii)$$

Taking into account the masking of channel (5.1c) and the partial ClO regeneration following channel (5.1d), *i.e.* putting Cl atoms into steady state, equation (5.ii) can be rewritten as:

$$-\frac{1}{2}\frac{d[\mathrm{ClO}]}{dt} = \left(k_{5.1a}[\mathrm{M}] + k_{5.1b} + \frac{1}{2}k_{5.1d}\right)[\mathrm{ClO}]^2 - k_{-5.1a}[\mathrm{M}][\mathrm{Cl_2O_2}] \qquad (5.iii)$$

To test the effective masking of channel (5.1c) and the halving of ClO decay *via* channel (5.1d), a simple numerical integration model was built in which ClO decay was calculated using equation (5.iii), thus ignoring channel (5.1c) and any other secondary chemistry. The simulated [ClO] temporal trace obtained from this simple model was compared to that generated using a FACSIMILE [23] model containing all of the known reactions of the species contained in the reaction cell, listed in Table 5.2. Crucially, the value of pre-photolysis [Cl_2O] in the FACSIMILE model was that determined from spectroscopic measurements.

The simulated [ClO] decay described by equation (5.iii) was always within 1% of that obtained from the FACSIMILE model, indicating the loss of sensitivity to channel (5.1c) at the concentration of Cl_2O used. Moreover, the fact that a simple four-reaction model could reproduce the results simulated using a more sophisticated model indicated a weak sensitivity to secondary chemistry and lent confidence to the extraction of $k_{5.1b}$

Reaction	k/cm^3 molecule^{-1} s^{-1}	reference
$Cl + Cl_2O \rightarrow Cl_2 + ClO$	$6.2\times10^{-11}\exp(130/T)$	[1]
$ClO + ClO \rightarrow Cl_2O_2$	$2\times10^{-15}\exp(1518/T)$	[6]
$Cl_2O_2 \rightarrow ClO + ClO$	$1.2\times10^{13}\exp(-7917/T)$ [a]	[6]
$ClO + ClO \rightarrow Cl + ClOO$	$3.0\times10^{-11}\exp(-2450/T)$	[1]
$ClO + ClO \rightarrow Cl_2 + O_2$	$k_{5.1b}$	*this work*
$ClO + ClO \rightarrow OClO + Cl$	$k_{5.1d}$	*this work*
$ClOO + Cl \rightarrow Cl_2 + O_2$	2.3×10^{-10} [b]	[1]
$ClOO + Cl \rightarrow ClO + ClO$	1.2×10^{-11} [b]	[1]
$ClO + OClO \rightarrow Cl_2O_3$	$1.9\times10^{-14}\exp(1250/T)$	[1]
$Cl_2O_3 \rightarrow ClO + OClO$	$1.2\times10^{13}\exp(-5905/T)$ [a]	[1]
$Cl + Cl_2O_2 \rightarrow Cl_2 + ClOO$	1.0×10^{-10} [b]	[1]
$Cl + OClO \rightarrow ClO + ClO$	$3.4\times10^{-11}\exp(160/T)$	[1]
$ClOO \rightarrow Cl + O_2$	$1.9\times10^{9}\exp(-1372/T)$ [a, c]	[1]
$Cl + O_2 \rightarrow ClOO$	$1.25\times10^{-15}\exp(1129/T)$ [c]	[1]

Notes:
[a] : units s^{-1}; [b] : k at T = 298 K; [c] : at p = 760 Torr

Table 5.2 : Reactions employed in the FACSIMILE model used in the present study

and $k_{5.1d}$. Attempts at measuring $k_{5.1c}$ were also made however, and are described in the following section.

Following generation of temporal profiles of ClO and OClO, both the simplified numerical integration model and the FACSIMILE model were fitted to $[ClO]_t$ and $[OClO]_t$ *simultaneously via* least-squares minimisation of residuals by optimising the values of $[ClO]_0$, $k_{5.1b}$ and $k_{5.1d}$. Gas flow-out from the reaction cell and the temporal averaging imparted to the recorded traces by the simultaneous illumination of 31 rows of the CCD detector (described in Section 3.4.4) were accounted for in both models. The two models returned optimised values of $k_{5.1b}$ and $k_{5.1d}$ in excellent agreement with one another, respectively within 3% and 1% at all temperatures. Figure 5.11 illustrates two typical kinetic traces along with their FACSIMILE fits and offset residuals.

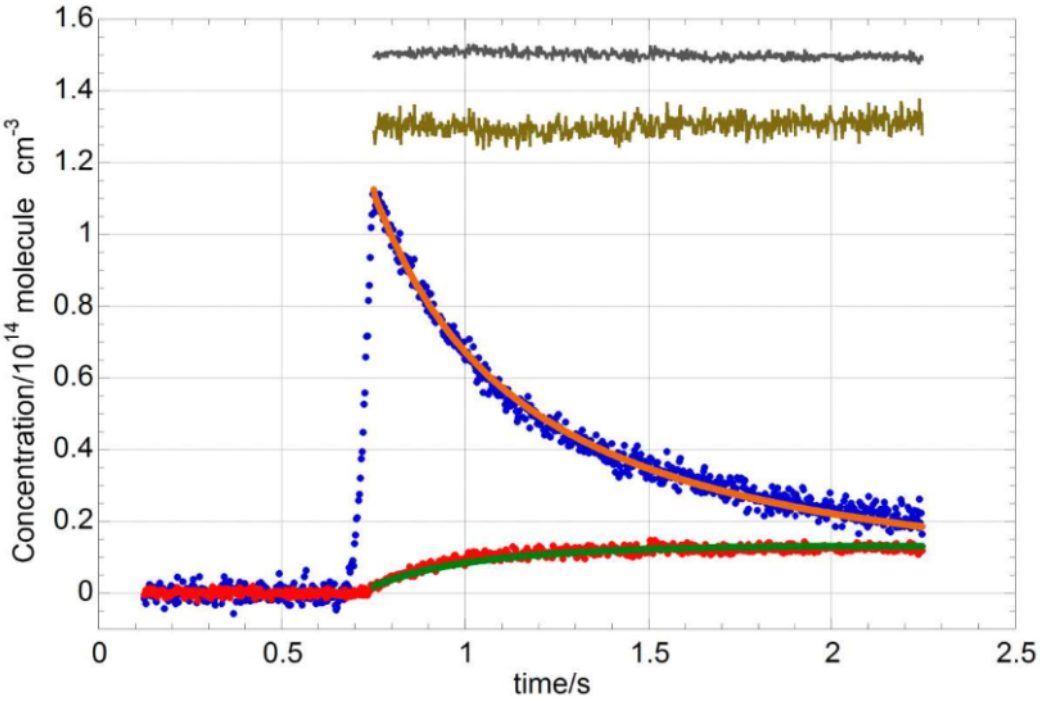

Figure 5.11 : Typical $[ClO]_t$ and $[OClO]_t$ decay traces recorded at T = 323 K (points) along with their respective FACSIMILE fits (solid lines). $[ClO]_t$ and $[OClO]_t$ residuals were offset by $+1.3\times10^{14}$ molecule cm^{-3} and $+1.5\times10^{14}$ molecule cm^{-3} respectively for clarity.

5.2.5 Investigation of $k_{5.1c}$

As discussed above, the observed ClO decay was insensitive to channel (5.1c) as a result of the rapid regeneration of ClO radicals from the two chlorine atoms effectively produced by channel (5.1c) under the experimental conditions used. However, as every Cl atom produced after the photolytic pulse rapidly undergoes reaction with Cl_2O, present in excess in the precursor mixture, the change in $[Cl_2O]$ following photolysis *should* retain kinetic information on channel (5.1c). The rate equation for the loss of Cl_2O is:

$$-\frac{d[Cl_2O]}{dt} = k_{5.3}[Cl][Cl_2O] \qquad (5.iv)$$

The temporal behaviour of the concentration of Cl atoms is described by:

$$\frac{d[\mathrm{Cl}]}{dt} = -k_{5.3}[\mathrm{Cl}][\mathrm{Cl_2O}] + (2k_{5.1c} + k_{5.1d})[\mathrm{ClO}]^2 \qquad (5.v)$$

Chlorine atoms can, under the experimental conditions used, be treated as reactive intermediates since the rate of their removal far exceeds the rate at which they are produced, as described in Section 2.1.1. The steady state approximation (SSA) can therefore be invoked and equation (5.v) is equated to zero:

$$\frac{d[\mathrm{Cl}]}{dt} = -k_{5.3}[\mathrm{Cl}][\mathrm{Cl_2O}] + (2k_{5.1c} + k_{5.1d})[\mathrm{ClO}]^2 \overset{\mathrm{SSA}}{\approx} 0 \qquad (5.vi)$$

By rearranging equation (5.vi), it follows that:

$$k_{5.3}[\mathrm{Cl}][\mathrm{Cl_2O}] \overset{\mathrm{SSA}}{\approx} (2k_{5.1c} + k_{5.1d})[\mathrm{ClO}]^2 \qquad (5.vii)$$

Substitution of equation (5.vii) into the expression for the rate of Cl_2O loss, equation (5.iv), shows that the temporal dependence of $[Cl_2O]$ is sensitive to the kinetics of channels (5.1c) and (5.1d):

$$-\frac{d[\mathrm{Cl_2O}]}{dt} = (k_{5.1c} + k_{5.1d})[\mathrm{ClO}]^2 \qquad (5.viii)$$

As the absorbance spectra recorded represent the change in absorbance brought about by photolysis and subsequent chemistry, the temporal traces obtained from the Beer-Lambert law also represent the changes in species concentrations relative to the pre-photolysis concentration. Therefore, if $\Delta[Cl_2O]_t$, defined as the change in concentration of $[Cl_2O]$ as a function of time relative to the pre-photolysis concentration, were monitored, it would in principle consist of an initial drop in the immediate post-photolysis, representing the Cl_2O consumed by the photolytically generated chlorine atoms and equal to $[ClO]_0$, followed by the further decay expressed by equation (5.viii), resulting from the Cl_2O reacting with chlorine atoms generated by channels (5.1c) and (5.1d), as illustrated in the simulated trace shown in Figure 5.12.

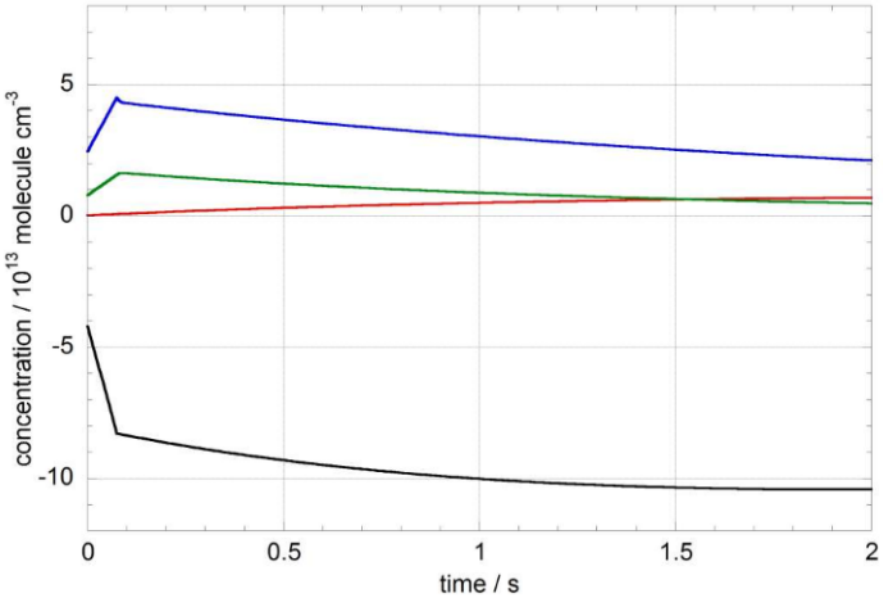

Figure 5.12 : Numerical integration simulation at T = 298 K showing expected temporal traces for ClO (blue), Cl_2O_2 (green), OClO (red) and $\Delta[Cl_2O]$ (black). Correction for gas flow-out and CCD averaging, as discussed in the text, were applied to all the traces shown.

Experiments were therefore undertaken to establish whether the signal from Cl_2O could be monitored. In this case, absorbance spectra were recorded at T = 298 K over the range λ = 235-300 nm, a spectral region encompassing both the peak in Cl_2O absorption ($\lambda \approx 255$ nm) and the vibronic bands of ClO ($\lambda > 265$ nm). A typical (time-averaged) spectrum recorded is shown in Figure 5.13.

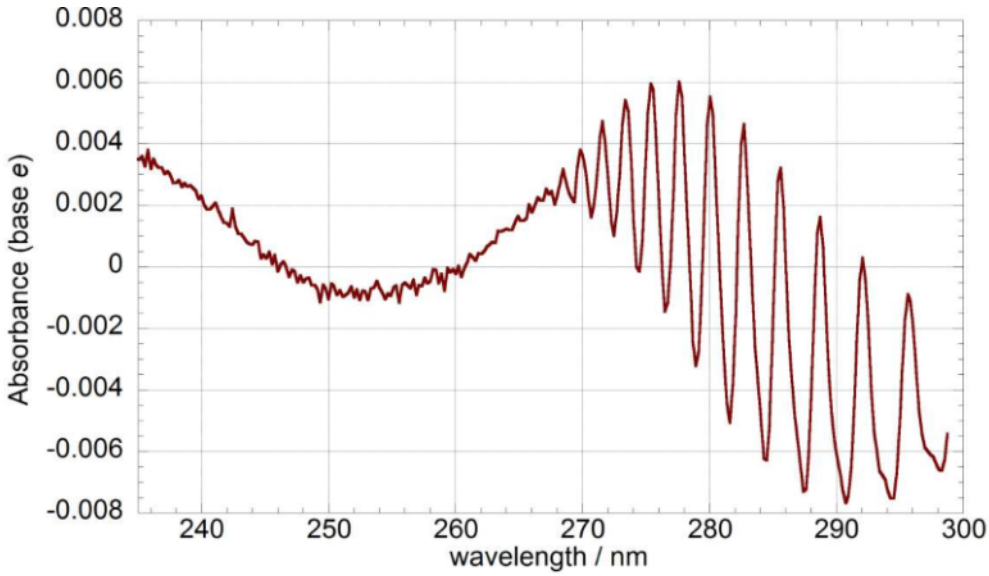

Figure 5.13 : Post-photolysis spectrum recorded at T = 298 K in the range λ = 235-300 nm at a resolution of 1.1 nm (FWHM) in an attempt to monitor $\Delta[Cl_2O]_t$.

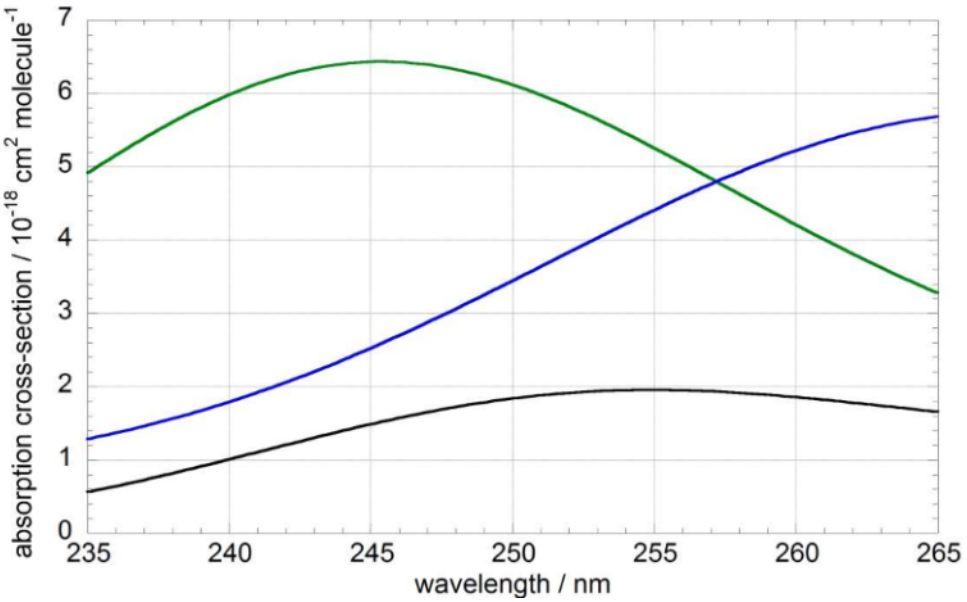

Figure 5.14 : Absorption cross-sections for ClO (blue), Cl_2O_2 (green) and Cl_2O (black) in the continuum (λ < 265 nm) region of the spectrum. The values for the cross-sections are those reported by JPL-NASA. [1]

The recorded absorbance in the continuum region of this spectrum (λ < 265 nm) results from the contribution of the individual absorbances of Cl_2O, Cl_2O_2 and ClO. These species all exhibit spectrally unstructured absorption cross-sections in the continuum wavelengths, as shown in Figure 5.14.

In principle, $[ClO]_t$ could be quantified accurately *via* differential fitting of the ClO cross-section to the structured part of the recorded absorbance. This would allow subtraction of the contribution of ClO from the continuum absorbance (λ < 265 nm), leaving a residual spectrum comprising of a positive absorption from Cl_2O_2 and a negative contribution from Cl_2O photolysis and subsequent removal. Subsequent fitting of the cross-sections of Cl_2O and Cl_2O_2 to the residual absorbance across the continuum region would then generate temporal concentration profiles of the remaining two absorbers.

This procedure required knowledge of the ClO differential cross-section in the structured region of the spectrum, as well as the absolute cross-sections of ClO, Cl_2O_2 and Cl_2O in the continuum region. The differential cross-section of ClO was obtained using the procedure outlined in Section 5.2.3 for the adopted instrumental resolution of

1.1 nm (FWHM). The cross-sections of Cl_2O and ClO (at continuum wavelengths) are well-characterised in the literature, with the majority of the reported studies within 10% of one another over the spectral range considered. The values of the cross-sections of Cl_2O and continuum ClO used in these experiments were those reported by JPL-NASA. [1] The Cl_2O_2 cross-sections were also taken from JPL-NASA, although it was noted that the uncertainty over the spectral range monitored is somewhat greater, with the latest JPL-NASA evaluation recommending an uncertainty of ± 35% at these wavelengths. [1]

An example of a multiple concentration-time profile obtained through the procedure outlined above is shown in Figure 5.15. Whilst the ClO and Cl_2O_2 traces seem consistent with the simulations, the temporal behaviour of Cl_2O shows some rather unexpected features: following the rapid consumption in the immediate post-photolysis (which would imply that Cl_2O was being accurately monitored), Cl_2O is apparently *regenerated* at longer timescales. No known gas-phase chemistry could account for this observation and it is therefore considered unlikely to be a real effect for the following reasons. Under the experimental conditions employed, the recombination of Cl with ClO would not compete with other Cl loss routes (predominantly reaction with excess Cl_2O). Furthermore, flow-out and flow-in of the gaseous mixture out/into the reaction

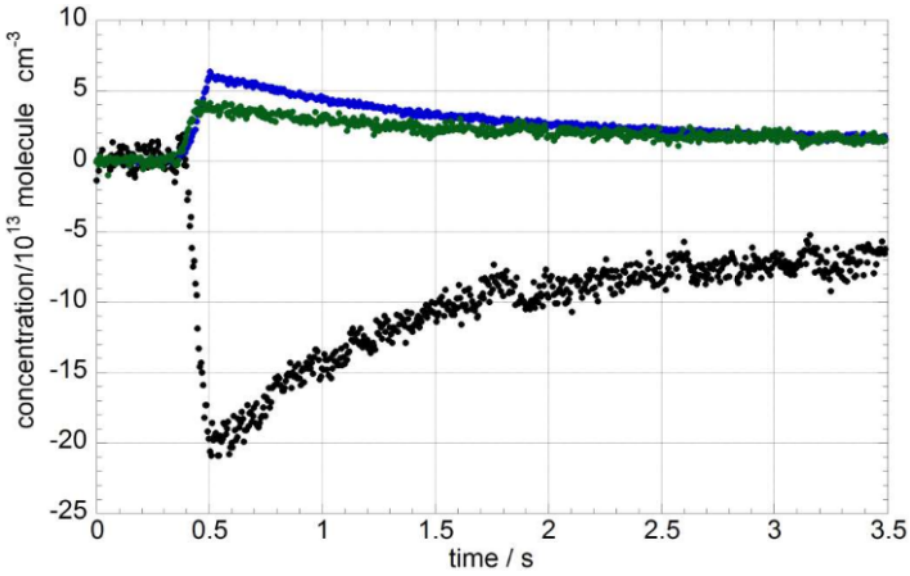

Figure 5.15 : Temporally-resolved [ClO] (blue), [Cl_2O_2] (green) and [Cl_2O] (black) obtained by differential fit of σ_{ClO} followed by fitting the two remaining absorbers to the residual absorbance, as discussed in the text.

cell could lead to an apparent recovery in $\Delta[Cl_2O]$ as a function of time, as the fraction of the gas mixture leaving the cell, which has been depleted of its Cl_2O content by photolysis, is replaced over the timescale of one experiment by a fresh mixture containing the original (pre-photolysis) Cl_2O partial pressure. However, the effects of gas flow-out were accounted for in the simulated trace showed in Figure 5.12 and cannot begin to reproduce the apparent increase in $\Delta[Cl_2O]$ obtained from spectral fitting. Moreover, as gas flow-out is mathematically included in the numerical integration model as a zeroth-order decay (in which the species lifetime corresponds to the residence time in the reaction cell), it could not reproduce the temporal behaviour of the apparent regeneration of Cl_2O.

Various other possibilities were considered. Although only a transient species in the reaction system employed, ClOO exhibits a very strong absorption over the wavelength range used in these experiments, reaching a maximum of $\sigma_{ClOO} = 2.98 \times 10^{-17}$ cm^2 molecule^{-1} at $\lambda = 246$ nm. [1] However, the lifetime of ClOO under the experimental conditions used is very short as it undergoes thermal dissociation very rapidly ($k_{5.4} = 1.9\times10^{11}$ s^{-1} at $T = 298$ K and $p = 1$ atm [1]). Numerical integration simulations run in FACSIMILE show that [ClOO] at any time would not exceed 4×10^6 molecule cm^{-3}, hence giving rise to a maximum absorbance of 1.2×10^{-8} absorbance units, thus far below the detection limit of the apparatus used.

The most probable source of this spurious signal was therefore attributed to a manifestation of the uncertainties associated with the literature cross-sections of the species at continuum wavelengths. Furthermore, given the similarities in the shapes of the three cross-sections at continuum wavelengths, notably Cl_2O and Cl_2O_2 as shown in Figure 5.14, the simultaneous independent fit of two such similar absorbers to the residual spectrum is apparently impractical. As a result, values of $k_{5.1c}$ could not be measured. The following section therefore illustrates the results on the kinetics of channels (5.1b) and (5.1d).

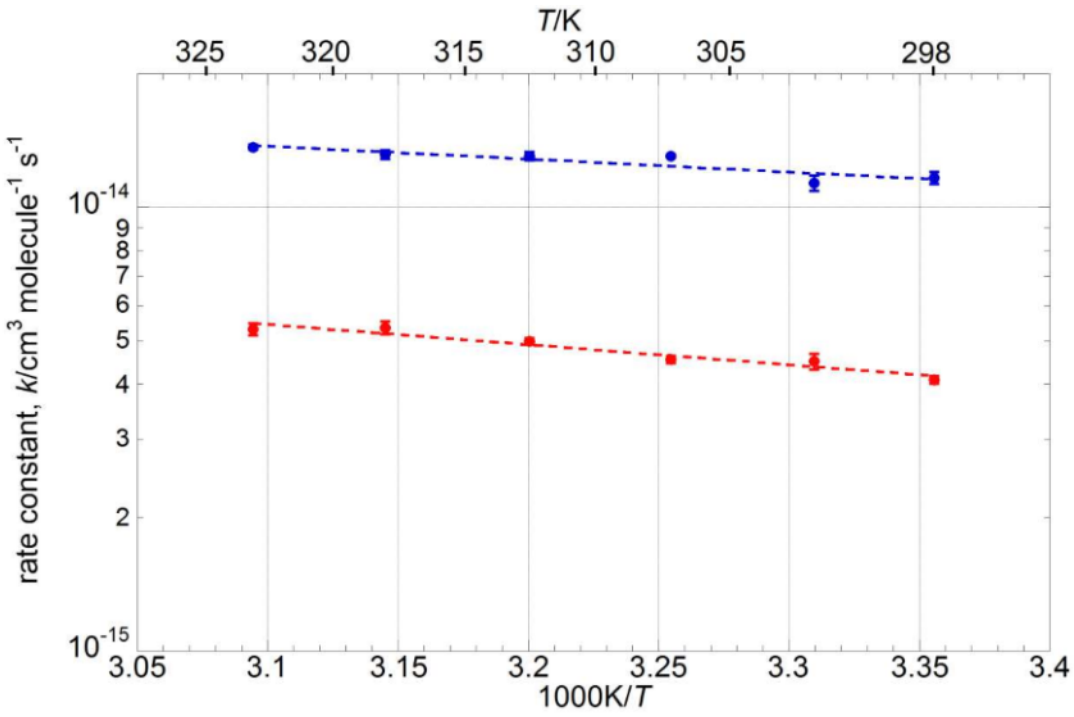

Figure 5.16 : Arrhenius plot for the values of $k_{5.1b}$ (in blue) and $k_{5.1d}$ (in red) obtained in the present work. Error bars are 2σ, statistical only.

5.3 Results

Values of $k_{5.1b}$ and $k_{5.1d}$ were obtained from the fitting procedure outlined in Section 5.2.4 at six different temperatures over the range T = 298-323 K. These values are given in Table 5.3 and are also shown in Arrhenius form in Figure 5.16.

T/K	$k_{5.1b}/10^{-15}$ cm^3 molecule^{-1} s^{-1}	$k_{5.1d}/10^{-15}$ cm^3 molecule^{-1} s^{-1}
298.0	11.6 ± 0.3	4.08 ± 0.07
302.0	11.3 ± 0.4	4.49 ± 0.2
307.0	13.03 ± 0.1	4.53 ± 0.08
312.5	13.03 ± 0.3	4.98 ± 0.09
318.0	13.15 ± 0.3	5.35 ± 0.18
323.0	13.66 ± 0.2	5.31 ± 0.16

Table 5.3 : Values of $k_{5.1b}$ and $k_{5.1d}$ obtained in this work. Errors are 2σ, statistical only.

The Arrhenius expressions obtained are $k_{5.1b}$= (1.15 ± 0.5) ×10^{-13}exp[−(686 ± 175)/T] cm^3 $molecule^{-1}$ s^{-1} and $k_{5.1d}$ = (1.4 ± 0.4) ×10^{-15}exp[−(1044 ± 134)/T]) cm^3 $molecule^{-1}$ s^{-1}, where the errors are 1σ from the Arrhenius fits.

5.4 Discussion

5.4.1 Sensitivity Analysis

Sensitivity of the results obtained for $k_{5.1b}$ and $k_{5.1d}$ to uncertainties in the secondary chemistry included in the numerical model was investigated by perturbing the reaction rate constants listed in Table 5.2 by a factor of two upwards and downwards sequentially. The FACSIMILE model with perturbed rate constants was then re-fitted to the [ClO] and [OClO] kinetic traces for a representative experiment at each temperature and the optimised $k_{5.1b}$ and $k_{5.1d}$ values were compared to those obtained from the unperturbed model. It was found that the deviation of $k_{5.1b}$ and $k_{5.1d}$ from the model containing unperturbed secondary chemistry kinetics was minimal (below 1%) at all temperatures for all reactions *excluding* the ClO dimerisation (reactions (5.1a), (−5.1a)).

ClO dimerisation was initially treated, in the "bimolecular" model, as secondary chemistry, hence values of $k_{5.1a}$ and $k_{–5.1a}$ obtained in the study described in Chapter 4 were perturbed by a factor of two for a sample fit at each temperature as above. However the values for $k_{5.1b}$ and $k_{5.1d}$ obtained indicated significant deviations from the values obtained with unperturbed dimerisation kinetics. The values returned for $k_{5.1b}$ and $k_{5.1d}$ at T = 298 K lay within 68% and 3% respectively of the values obtained from the "unperturbed" model. This divergence was less profound at T = 323 K, where $k_{5.1b}$ and $k_{5.1d}$ were within 16% and 0.1% of the values obtained from the unperturbed model. This analysis also indicated that $k_{5.1b}$ was particularly sensitive to the uncertainties in the parameters used for the ClO dimerisation, whereas $k_{5.1d}$ was only marginally affected. However, perturbing the kinetics of ClO dimerisation by a factor of two is arguably excessive as the current JPL-NASA [1] uncertainty factor is 1.32 (2σ) and the errors on the current study are somewhat smaller. The sensitivity analysis was therefore repeated by perturbing $k_{5.1a}$ and $k_{–5.1a}$ by 1.32. The returned $k_{5.1b}$ was within 25% of the

"unperturbed" value at T = 298 K and 6% at T = 323 K. On the other hand, $k_{5.1d}$ was within 2% of the unperturbed value at T = 298 K and 0.05% at T = 323 K. The effects of using $k_{5.1a}$ and $k_{-5.1a}$ from the JPL-NASA evaluation instead of the values reported in Chapter 4 [6] were also investigated. Values of $k_{5.1b}$ obtained from fits to the FACSIMILE model where the JPL-NASA rate constants for ClO dimerisation were used were found to be 13% smaller at T = 298 K and 1% smaller at T = 323 K than values of $k_{5.1b}$ resulting from fits where the kinetics of ClO dimerisation were based on the values reported in Chapter 4. Channel (5.1d) showed a less significant sensitivity to ClO dimerisation as fitting to the kinetic traces using JPL-NASA parameters for the dimerisation returned values of $k_{5.1d}$ decreased by a maximum of 0.2% over the temperature range studied compared to those obtained using the dimerisation kinetics reported in Chapter 4.

In order to measure $k_{5.1b}$ and $k_{5.1d}$ accurately, it was also crucial that each experiment was performed under excess [Cl_2O] so that channel (5.1c) was effectively masked and did not contribute to the observed [ClO] decay. Sensitivity to uncertainties and fluctuations in Cl_2O abundances in the precursor mixture was also therefore quantified by perturbing the value for [Cl_2O] input in the FACSIMILE model by a factor of two for the analysis of a sample trace at each temperature. Results show minimal deviations in the kinetic parameters for values of [Cl_2O] as low as 4.5×10^{15} molecule cm^{-3} (corresponding to half the typical Cl_2O concentration determined spectroscopically as discussed above), with the returned values of $k_{5.1b}$ and $k_{5.1d}$ lying within 0.4% of the values obtained using the actual calculated [Cl_2O].

The values of $k_{5.1b}$ and $k_{5.1d}$ obtained in the present study also depended critically on the concentrations of ClO and OClO, which in turn are strongly affected by the absorption cross-sections used to fit to the recorded spectra. Sensitivity to uncertainties in the ClO and OClO cross-sections used was therefore also investigated. In the determination of the ClO differential cross-section at the lower resolution (1.1 nm FWHM) used in this work, the parameterisation of $\sigma_{ClO\ diff}(T)$ the study of ClO dimerisation described in Chapter 4 was used to calibrate high resolution (0.8 nm FWHM) spectra which in turn were employed to quantify [ClO]. As no appreciable change in the decay of ClO was observed in the high resolution runs of the back-to-back experiments, as discussed

above, the main source of uncertainty was attributed to that reported for the value of the parameterised high-resolution $\sigma_{\mathrm{ClO\ diff}}(T)$. Errors in this expression for the high resolution differential cross-section of ClO were therefore propagated through the whole analytical procedure down to the low-resolution cross-sections so that, at every experimental temperature, upper and lower limits of the ClO cross-sections were determined. Differential fitting using the Beer-Lambert law was then repeated for a sample dataset at each temperature using the ClO cross-sections at the upper and lower limits of this uncertainty range. The traces obtained were then fitted to the FACSIMILE model and the returned values for the rate constants compared to those obtained using the unperturbed ClO cross-section. Results of this procedure reflect the temperature dependence of the uncertainties in the high-resolution $\sigma_{\mathrm{ClO\ diff}}$, which become more significant with increasing temperatures: at the lower end of the temperature range used (T = 298 K), the values for $k_{5.1b}$ and $k_{5.1d}$ obtained using σ_{ClO} at the upper limit of its uncertainty range are respectively 9% and 109% larger than those obtained from the unaltered ClO cross-section, whereas they increased by 35% and 141% respectively at T = 323 K. Similarly, when σ_{ClO} at the lower limit of its uncertainty range was employed, the values of $k_{5.1b}$ and $k_{5.1d}$ were smaller than their counterparts using unperturbed σ_{ClO} by 11% and 70% at T = 298 K and by 44% and 81% at T = 323 K. These potential effects of uncertainties in σ_{ClO}, although stemmed from a rigorous statistical propagation of errors, do however appear to be a considerable overestimate in the light of the consensus on the low resolution $\sigma_{\mathrm{ClO\ diff}}$ at T = 298 K shown, for example, in Figure 5.7. Therefore the uncertainty in $\sigma_{\mathrm{ClO\ diff}}$ (T = 298 K) was redefined, for the purposes of this analysis, as two standard deviations (95% confidence) resulting from the scatter of the three values of $\sigma_{\mathrm{ClO\ diff}}$ available at that temperature. The relative error in σ_{ClO} thus decreased from 0.45(1σ) from the propagation of the errors in the high-resolution parameterisation of σ_{ClO} to 0.23 (2σ). The relative error in σ_{ClO} at T = 323 K was now estimated as 0.29, allowing for a 25% increase as a consequence of the temperature dependence of the uncertainties in the high-resolution $\sigma_{\mathrm{ClO\ diff}}$. The effects of these smaller errors on the returned rate constants were somewhat more modest, as expected: at T = 298 K, the values of $k_{5.1b}$ from perturbed traces were within 5% of the value obtained from the traces using unperturbed σ_{ClO}, whereas those of $k_{5.1d}$ fell within 50%. Similarly, at T = 323 K, the values of $k_{5.1b}$ were within 20% of the value from the traces obtained using unperturbed σ_{ClO}, whereas those of $k_{5.1d}$ fell within 60%.

Uncertainty in the absorption cross-section of OClO from Wahner *et al*. [22] was also taken into account. These authors report an error of $\pm 4\times10^{-19}$ cm^2 molecule^{-1} for every point in the spectrum, stemmed principally from baseline shifts. However these baseline effects are not expected to affect as profoundly the quantification of [OClO] carried out in this study since differential fitting was employed. A baseline shift would affect the peaks and the troughs of the spectrum in equal manner so that the peak-to-trough differential cross-section remained unchanged. As a "worst-case" scenario, it was however decided to study how an error equal in magnitude to the one quoted by Wahner *et al*. would affect the rate constants $k_{5.1b}$ and $k_{5.1d}$ when this error was applied to the *differential* OClO cross-section. The cross-section difference between the a(15) peak at λ = 322.78 nm and the trough at higher wavelength (λ = 326.1 nm) was calculated for σ_{OClO} at T = 298 K and perturbed by $\pm 4\times10^{-19}$ cm^2 molecule^{-1}. The whole spectrum was then scaled to match the altered differential cross-section. The [OClO] traces generated using the perturbed σ_{OClO} gave OClO concentrations within 7% of the [OClO] trace obtained from the unmodified $\sigma_{OClO.}$ The values of $k_{5.1b}$ and $k_{5.1d}$ from the FACSIMILE fit to these traces were within respectively 1.6% and 7% of the values resulting from fitting to the traces obtained using unperturbed σ_{OClO}, and it is concluded that the sensitivity to uncertainties in σ_{OClO} is therefore minimal.

Sensitivity of values of $k_{5.1b}$ and $k_{5.1d}$ to the uncertainties in the gaseous mixture flow-out from the reaction cell was also investigated. This was important, due to the very slow timescale (seconds) of these reactions. This was achieved by perturbing the flow-out (calculated as the sum of each individual gas flow) by ± 10%. The effects of the altered flow-out were not significant as the returned $k_{5.1b}$ and $k_{5.1d}$ lay respectively within 3% and 0.5% of the values obtained using the notional total gas flow-out, which is in any case known to within a few percent from flowmeter calibration experiments, as discussed in Appendix 1.

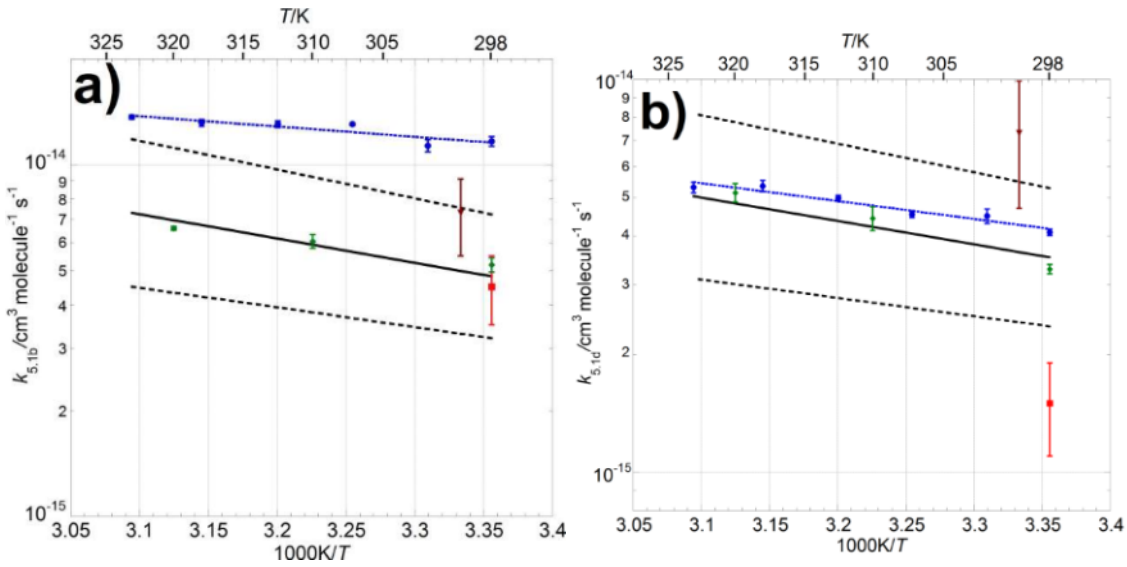

Figure 5.17 : Arrhenius plots for a) $k_{5.1b}$ and b) $k_{5.1d}$. Values from this work are shown as filled blue circles and the resulting parameterisation as a blue dotted line; errors from this work are 2σ, statistical only. JPL-NASA [1] recommended values are illustrated as a solid black line, with associated uncertainty limits represented by black dashed lines. Data from Nickolaisen *et al.* [3] are shown as green diamonds. Data from Cox and Derwent [14] are shown as red squares, whereas the values from Simon *et al.* [17] are represented as brown inverted triangles.

5.4.2 Comparison with previous studies

The rate constants for channels (5.1b) and (5.1d) obtained in this study are plotted in Arrhenius form in Figure 5.17, along with the results from previous work. Whilst the values of $k_{5.1d}$ from this work are in general good agreement with previous work by Nickolaisen *et al.* [3], and consequently with the JPL-NASA recommendation [1] based upon it, the measured $k_{5.1b}$ from this study is larger than that reported by Nickolaisen *et al.* at all temperatures. Furthermore, the temperature dependence of $k_{5.1b}$ and $k_{5.1d}$ determined in the present work is somewhat less pronounced than that reported by Nickolaisen *et al.* [3] The Arrhenius expressions obtained from fitting to $k_{5.1b}$ and $k_{5.1d}$ in the present work were:

$k_{5.1b}$/cm^3 molecule^{-1} s^{-1} $= (1.15 \pm 0.5) \times 10^{-13} \exp[-(686 \pm 175)/T]$

cf. $k_{5.1b}$/cm^3 molecule^{-1} s^{-1} $= (1.01 \pm 0.12) \times 10^{-12} \exp[(-1590 \pm 100)/T]$ from Nickolaisen *et al.* [3]

$k_{5.1d}$ /cm^3 molecule^{-1} s^{-1} = (1.4 ± 0.4) ×10^{-15}exp[−(1044 ± 134)/T])

cf. $k_{5.1d}$/cm^3 molecule^{-1} s^{-1} = (3.50 ± 0.31) ×10^{-13} exp[(−1370 ± 150)/T] from Nickolaisen *et al*. [3]

This work thus found values of $k_{5.1b}$ and $k_{5.1d}$ to increase by approximately 17% and 30% respectively over the temperature range studied (T = 298-323 K), whereas the parameterisations of $k_{5.1b}$ and $k_{5.1d}$ from Nickolaisen *et al*. show an increase of 51% and 43% respectively over the same temperature range.

In contrast to the present work, Nickolaisen *et al*. [3] obtained values of $k_{5.1b}$ and $k_{5.1d}$ mainly from fitting a FACSIMILE model uniquely to $[OClO]_t$ traces at nine temperatures in the range T = 300-380 K. In the present study, seven vibronic bands of OClO in the range λ = 340-400 nm were monitored at a spectral resolution of 0.18 nm (FWHM). Validation to this procedure was obtained by monitoring ClO in experiments otherwise identical to those in which OClO was monitored, at only two temperatures of the experimental range considered (T = 340 and 370 K) and using five vibronic bands over the range λ = 270-280 nm with the same spectral resolution. The values of $k_{5.1b}$ and $k_{5.1d}$ from the two sets of experiments reported by Nickolaisen *et al*. are within ≤ 10% of one another.

As discussed extensively above, in the sensitivity analysis, the kinetic parameters used to account for the ClO dimerisation ($k_{5.1a}$ and $k_{-5.1a}$) have a significant effect on the measured $k_{5.1b}$ (and a minor – negligible – effect on $k_{5.1d}$) at the lower temperatures used in the present work. Nickolaisen *et al*. used different values of $k_{5.1a}$ and $k_{-5.1a}$ than those employed in the current study when fitting to the kinetic traces with FACSIMILE. Nickolaisen *et al*. measured their own $k_{5.1a}$[M] as a function of temperature from experiments performed in the presence of excess chlorine atoms and calculated $k_{-5.1a}$ from their $k_{5.1a}$[M] combined with K_{eq} for the ClO dimerisation from the 1992 JPL-NASA evaluation. [24] When the values of $k_{5.1a}(T)$ and $k_{-5.1a}(T)$ obtained in Chapter 4 were replaced by those used by Nickolaisen *et al*. in the FACSIMILE model used in the current study, a markedly stronger temperature dependence was observed for $k_{5.1b}(T)$

and the following Arrhenius expression was obtained, which is in very good agreement with that obtained by Nickolaisen *et al.*:

$k_{5.1b}/\text{cm}^3\ \text{molecule}^{-1}\ \text{s}^{-1} = (8 \pm 0.2) \times 10^{-13}\exp[(-1290 \pm 225)/T]$

cf. $k_{5.1b}/\text{cm}^3\ \text{molecule}^{-1}\ \text{s}^{-1} = (1.01 \pm 0.12)\times 10^{-12}\exp[(-1590 \pm 100)/T]$ from Nickolaisen *et al.* [3]

$k_{5.1d}$ was, on the other hand, only marginally affected by the choice of dimerisation kinetics. However, as discussed in the sensitivity analysis above, $k_{5.1d}$ is affected by σ_{ClO} to a greater extent than $k_{5.1b}$. The reference cross-sections used by Nickolaisen *et al.* to quantify [ClO] and [OClO] were obtained by comparing peak-to-trough differential absorbances of vibrational bands in their recorded spectra to the relative differential cross-sections of the same bands taken from a previous study by Sander and Friedl [25] for the ClO spectrum and from Wahner *et al.* [22] for the OClO spectrum. A direct comparison between the differential ClO cross-section used in the present study and the one determined by Sander and Friedl is not straightforward however as the value for only the *absolute* ClO cross-section at the (12, 0) peak of ClO is reported in the paper by Sander and Friedl. Data points from the work of Sander and Friedl were also reported in the JPL-NASA evaluation [1] but were averaged over 1 nm intervals and therefore cannot be used to determine the differential cross-section at the instrumental resolution used.

The study by Simon *et al.* [17] determined the absolute rate constants of the ClO + ClO bimolecular channels by fitting FACSIMILE models to the traces recorded at three wavelengths, λ = 240, 257.7 and 292 nm. As the former two wavelengths lie in the *continuum* (unstructured) part of the ClO spectrum, uncertainty in the contributions of other absorbers over the same spectral region (Cl_2O_2 and Cl_2O) is expected to affect the accuracy of this determination. A further experiment in the same work employed broadband monitoring of OClO over the range λ = 281-361 nm to optimise the value of $k_{5.1d}$. However, only $k_{5.1d}$ was allowed to vary in the fitting procedure while $k_{5.1b}$ and $k_{5.1c}$ were held fixed at the values determined from the single-wavelength part of the study. This procedure may therefore have biased the fitting procedure to agree with the value of $k_{5.1d}$ obtained from single-wavelength measurements.

Previous studies by Wongdontri-Stuper *et al.* [15] and Horowitz and co-workers [18, 19] monitored the chlorine photosensitised decomposition of ozone which allowed the determination of the branching ratios for channels (5.1b)-(5.1d) without characterising the absolute rate constants. It follows that a direct comparison between the results of these studies and those from the present work is not possible as the masking of channel (5.1c) achieved in the current laser photolysis study ruled out the possibility of determining the total k_{bi} and, consequently, the branching ratios. However, it is still possible to *estimate* values for the branching ratios based on $k_{5.1b}$ and $k_{5.1d}$ from the present work by making assumptions on the value of $k_{5.1c}$. The studies by Burrows and Cox [20], Simon *et al.* [17] and Nickolaisen *et al.* [3] are in good agreement with regards to the value of $k_{5.1c}$ and their findings average to $k_{5.1c} = (7.5 \pm 0.5)\times10^{-15}$ cm^3 molecule^{-1} s^{-1} at $T = 298$ K, where the error is 1σ. This value is in good agreement (and the basis of) the current JPL-NASA [1] recommendation ($k_{5.1c} = 8.0\times10^{-15}$ cm^3 molecule^{-1} s^{-1} at $T = 298$ K), based solely on the work of Nickolaisen *et al.* Using the average $k_{5.1c}$ from previous studies and the values of $k_{5.1b}$ and $k_{5.1d}$ from the present work leads to the following branching ratios, shown in the form of $k_{5.1b}/k_{bi}$: $k_{5.1c}/k_{bi}$: $k_{5.1d}/k_{bi}$ = 0.50:0.32:0.18 at T = 298 K. These values confirm channel (5.1d) as the minor reaction pathway of the ClO + ClO bimolecular channels but indicate that channel (5.1b) is the major contributor to the bimolecular decay of ClO, in disagreement with the studies by Wongdontri-Stuper *et al.* [15] and Horowitz and co-workers [18, 19] which reported channel (5.1c) as the most efficient channel. The branching ratios estimated from the rate constant obtained in the present study are in good agreement with those from Cox and Derwent [14] although the absolute rate constants determined by Cox and Derwent are about a factor of two smaller than those obtained in the present work. One of the reasons for this discrepancy can be attributed to the fact that the FACSIMILE model used by Cox and Derwent to fit to the kinetic traces optimised the values of $k_{5.1b}$, $k_{5.1c}$, $k_{5.1d}$ and $k_{-5.1a}$. The optimised value for $k_{-5.1a}$ at $T = 298$ K and $p = 1$ atm was $k_{-5.1a} = 110 \pm 50$ s^{-1} which is about 156% higher than that obtained from the current JPL-NASA recommendation of $k_{-5.1a} = 43$ s^{-1}. As discussed above, the ClO + ClO bimolecular model is very sensitive to the rate of dissociation of the ClO dimer: calculations showed that, at $T = 298$ K, a value of $k_{-5.1a}$ twice as large as the current JPL-NASA recommendation would result in a decrease of $k_{5.1b}$ by approximately 35%.

5.5 Conclusions

This study has characterised the rate constants of two of the three bimolecular channels of the ClO self-reaction, namely channels (5.1b) and (5.1d), producing Cl_2 + O_2 and OClO + Cl respectively, at six temperatures over the range T = 298-323 K and at atmospheric pressure. The Arrhenius expressions obtained for both channels show a weaker temperature dependence than those reported in previous studies. $k_{5.1d}(T)$ determined in the present work is in good agreement with the current recommendation of JPL-NASA over the experimental temperature range, whereas the measured $k_{5.1b}(T)$ falls above the JPL-NASA uncertainty upper limit at these temperatures. Experiments were also undertaken to attempt to measure $k_{5.1c}$ by monitoring the amount of Cl_2O consumed by the chlorine atoms generated by channels (5.1c) and (5.1d). These attempts however proved unsuccessful, attributed to the overlapping and similar spectra of absorbing species over the same spectral window.

High-resolution measurement of the absorption cross-section of Cl_2 over the structured region λ = 510-570 nm [26] became available only after the completion of the experiments on the ClO bimolecular channels reported here. Although the Cl_2 absorption cross-section in this region is very weak (in the order of 10^{-22} cm^2 molecule^{-1}), the presence of structured vibronic bands could in principle allow the use of differential fitting procedures and therefore lead to the unequivocal quantification of Cl_2 regardless of any underlying absorbers, thus avoiding the complications arising when operating with overlapping unstructured absorbers, as discussed extensively in Section 5.2.5. The possibility of monitoring the temporal behaviour of Cl_2 in the post-photolysis temporal domain would then allow extraction of kinetic information on channel (5.1c), as the chlorine atoms generated by this channel react with the excess Cl_2O to regenerate ClO and a Cl_2 molecule. Therefore the temporal behaviour of [Cl_2], excluding the initial amount of Cl_2 photolysed by the laser pulse and that generated by reaction (5.3) in the immediate post-photolysis, would be described by the following rate equation:

$$\frac{d[\mathrm{Cl_2}]}{dt} = (k_{5.1b} + 2k_{5.1c} + k_{5.1d})[\mathrm{ClO}]^2 \qquad (5.ix)$$

This provides potentially interesting material for future work, but the feasibility of these measurements will depend crucially on the signal-to-noise ratio of the recorded absorbance over the structured region of the Cl_2 spectrum. As the values of the Cl_2 cross-section in this region are very small, an implementation of the existing experimental apparatus to include, for example, multipass absorption spectroscopy, thus increasing the optical pathlength of the system, would be necessary.

5.6 References

1. S.P. Sander, J. Abbatt, J.R. Barker, J.B. Burkholder, R.R. Friedl, D.M. Golden, R.E. Huie, C.E. Kolb, M.J. Kurylo, G.K. Moortgat, V.L. Orkin, P.H. Wine, *Chemical Kinetics and Photochemical Data for Use in Atmospheric Studies*, Evaluation No. 17, **2011**, JPL Publication 10-6, Jet Propulsion Laboratory, Pasadena, United States
2. R.A. Cox, G.D. Hayman, *Nature*, **1988**, 332, 796
3. S.L. Nickolaisen, R.R. Friedl, S.P. Sander, *J. Phys. Chem.*, **1994**, 98, 155
4. W.J. Bloss, S.L. Nickolaisen, R.J. Salawitch, R.R. Friedl, S.P. Sander, *J. Phys. Chem. A*, **2001**, 105, 11226
5. G. Boakes, W.H. Hindi Mok, D.M. Rowley, *Phys. Chem. Chem. Phys.*, **2005**, 7, 4102
6. V. Ferracci, D.M. Rowley, *Phys. Chem. Chem. Phys.*, **2010**, 12, 11596
7. G. Porter, F.J. Wright, *Discuss. Faraday Soc.*, **1953**, 14, 23
8. F.H.C. Edgecombe, R.G.W. Norrish, B.A. Thrush, *Proc. R. Soc. Lond. Ser. A*, **1957**, 243, 24
9. S.W. Benson, J.H. Buss, *J. Chem. Phys.*, **1957**, 27, 1382
10. H.S. Johnston, E.D. Morris, J. Van den Bogaerde, *J. Am. Chem. Soc.*, **1969**, 91, 7712
11. M.A.A. Clyne, J.A. Coxon, *Proc. R. Soc. Lond. Ser. A*, **1968**, 303, 207
12. M.A.A. Clyne, I.F. White, *Trans. Faraday Soc.*, **1971**, 67, 2068
13. M.A.A. Clyne, D.J. McKenny, R.T. Watson, *J. Chem. Soc. Faraday Trans. I*, **1975**, 71, 322
14. R.A. Cox, R.G. Derwent, *J. Chem. Soc. Faraday Trans. I*, **1979**, 75, 1635

15. W. Wongdontri-Stuper, R.K.M. Jayanty, R. Simonaitis, J. Heicklen, *J. Photochem.*, **1979**, 10, 163
16. G.D. Hayman, J.M. Davies, R.A. Cox, *Geophys. Res. Lett.*, **1986**, 13, 1347
17. F.G. Simon, W. Schneider, G.K. Moortgat, J.P. Burrows, *J. Photochem. Photobiol. A: Chem.*, 1990, 55, 1
18. A. Horowitz, D. Bauer, J.N. Crowley, G.K. Moortgat, *Geophys. Res. Letters*, **1993**, 20, 1423
19. A. Horowitz, J.N. Crowley, G.K. Moortgat, *J. Phys. Chem.*, **1994**, 98, 11924
20. J.P. Burrows, R.A. Cox, *J. Chem. Soc. Faraday Trans. I*, **1981**, 77, 2465
21. C.N. Hinshelwood, C.R. Prichard, *J. Chem. Soc.*, **1923**, 123, 2730
22. A. Wahner, G.S. Tyndall, A.R. Ravishankara, *J. Phys. Chem*, **1987**, 91, 2134
23. A.R. Curtis, W.P. Sweetenhan, FACSIMILE, **1987**, AERE Harwell Publication, Oxford
24. W.B. DeMore, S.P. Sander, D.M. Golden, R.F. Hampson, M.J. Kurylo, C.J. Howard, A.R. Ravishankara, C.E. Kolb, M.J. Molina, *Chemical Kinetics and Photochemical Data for Use in Stratospheric Modelling*, Evaluation No. 10, **1992**, JPL Publication 92-20, Jet Propulsion Laboratory, Pasadena, United States
25. S.P. Sander, R.R. Friedl, *J. Phys. Chem.*, **1989**, 93, 4764
26. I.A.K. Young, C. Murray, C.M. Blaum, R.A. Cox, R.L. Jones, F.D. Pope, *Phys. Chem. Chem. Phys.*, **2011**, 13, 15318

Chapter 6
Kinetic Studies of the Temperature Dependence of the BrO Self-Reaction

6.1 Introduction

Characterising the reactivity of bromine monoxide radicals, BrO, is of crucial importance to understand recent changes in the Earth's atmosphere. BrO radicals play a critical role in ozone-depleting events, both in Polar Regions and at mid-latitudes. In the stratosphere, for instance, a cycle involving the BrO + ClO reaction is one of the major contributors to catalytic ozone destruction observed during Polar Springtime. [1] In the troposphere, ozone depletion has been detected in the Arctic Marine Boundary Layer and has been associated with enhanced BrO mixing ratios and the self-reaction of BrO, [2, 3] as illustrated in Figure 6.1.

Many studies have shone light on the origins and chemistry of atmospheric bromine. It is now known that, whilst the vast majority of atmospheric chlorine originates from anthropogenic sources, a considerable fraction of the bromine present in the atmosphere

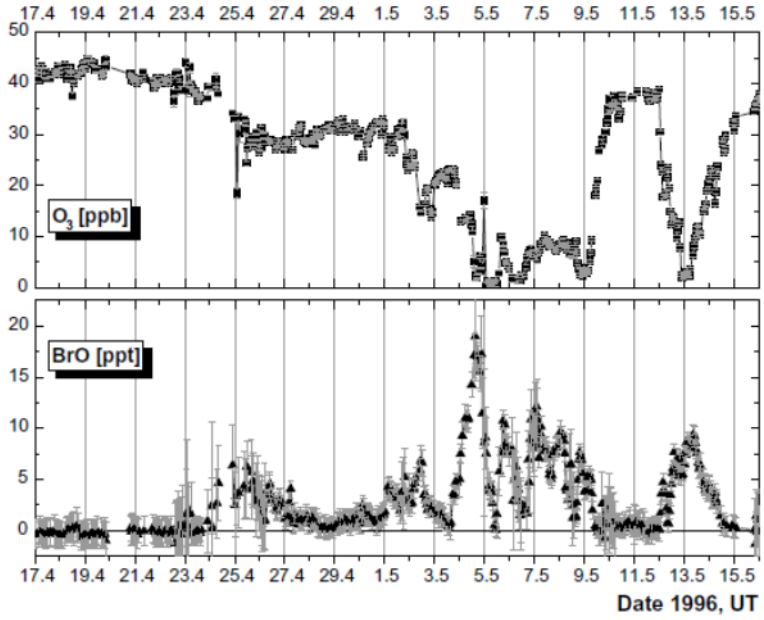

Figure 6.1 : Abundances of ozone and BrO as measured by Tuckermann *et al.* [4] in the Arctic Marine Boundary Layer, clearly showing the anticorrelation between the concentrations of the two species. The diagram was taken from reference 3.

is emitted by natural, biogenic sources, such as phytoplankton. Moreover, despite the lower atmospheric abundance of bromine compared to chlorine, [5] bromine-driven ozone destruction is more efficient than chlorine on a per atom basis. This is because the active forms of bromine, Br and BrO, are more thermodynamically and photolytically preferred to their "reservoir" (inactive) forms compared to their chlorine counterparts.[6, 7]

The BrO self-reaction occurs in the atmosphere at suitably high BrO mixing ratios. The current understanding of this reaction is that it comprises of two channels: [8, 9]

$$BrO + BrO \rightarrow 2Br + O_2 \quad (6.1a)$$

$$\rightarrow Br_2 + O_2 \quad (6.1b)$$

At ambient temperature the reaction is dominated by channel (6.1a), which, in the presence of ozone, leads to ozone removal *via* reaction (6.2):

$$Br + O_3 \rightarrow BrO + O_2 \quad (6.2)$$

Therefore, for every Br atom produced by channel (6.1a), one ozone molecule is consumed by reaction (6.2), which in turn catalytically regenerates BrO. In sunlight, the product Br_2 from channel (6.1b) would be rapidly photolysed to Br atoms, again leading to ozone loss. The BrO self-reaction is therefore not only atmospherically important as a key step in its own right as a catalytic ozone-depleting cycle, but it must be also taken into account when studying, in the laboratory, other atmospherically important reactions such as BrO + HO_2 and BrO + ClO.

6.1.1 Previous Studies

A number of studies have focused on the kinetics and branching of the BrO self-reaction [6, 8-22] using a variety of techniques, from temperatures as low as T = 202 K [20] up to T = 573 K. [10] Most of these studies are in relatively good agreement at T = 298 K, and their results at ambient temperature are summarised in Table 6.1. Somewhat fewer studies [6, 8, 9, 13, 14, 17, 20, 22] have investigated the temperature dependence of the BrO self-

Reference	Technique [a]	T/K	p/Torr	$k_{6.1}/10^{-12}$ cm^3 molecule^{-1}s^{-1}	$k_{6.1a}/10^{-12}$ cm^3 molecule^{-1}s^{-1}	$k_{6.1b}/10^{-13}$ cm^3 molecule^{-1}s^{-1}	$\alpha = k_{6.1a}/k_{6.1}$
Clyne and Cruse [10]	DF/UV	293-573	1	5.2 ± 0.6			
Basco and Dogra [11]	FP/UV	298	400-760	1.1 ± 0.2			
Clyne and Watson [12]	DF/MS	298		3.2 ± 0.7			
Jaffe and Mainquist [8]	PD	258-333					0.84 ± 0.01
Sander and Watson [9]	FP/UV	223-338	50-475	2.17 ± 0.68		3.46 ± 0.68 [b] 4.12 ± 1.99 [b]	0.84 ± 0.3 [b] 0.81 ± 0.46 [b]
Cox *et al*. [13]	MM/UV	278-338				6.9 ± 1.4[c]	0.84 ± 0.5[c]
Turnipseed *et al*. [14]	DF/MS	253-400	2	2.45 ± 0.26 [d]			0.88 ± 0.04[d]
Lançar *et al*. [15]	DF/MS	298	1-2	3.2 ± 0.5	2.7 ± 0.5	4.7 ± 1.5	0.85 ± 0.3
Bridier *et al.*[16]	FP/UV	298	760	3.1 ± 0.4[e]		4.9 ± 0.6	
Mauldin *et al*. [6]	FP/UV	220, 298	75-600	2.7 ± 0.5	2.3 ± 0.3	4.4 ± 0.8	0.84 ± 0.01
Rattigan *et al*. [17]	CP/UV	298-343	343-647			3.38 ± 0.33	
Rowley *et al.*[18]	FP/UV	298	760	2.98 ± 0.42	2.42 ± 0.42	4.69 ± 0.68	0.85 ± 0.03
Laszlo *et al*.[19]	LP/UV	295	200	2.8 ± 0.5 [f]			
Gilles *et al*.[20]	LP/UV	204-388	500	3.5 ± 0.35			
Bedjanian *et al*.[21]	DF/MS	298	1	2.75 ± 0.35	2.35 ± 0.4	4.0 ± 0.5	0.84 ± 0.03
Harwood *et al*.[22]	FP-LP/UV	222-298	100-760	2.90 ± 0.28	2.59 ± 0.28	3.1 ± 0.2	0.89 ± 0.13
IUPAC [23]				3.2 ± 0.3	2.7 ± 0.3	4.8 ± 0.5	0.85 ± 0.11
JPL-NASA [24]				3.25 ± 0.45	2.74 ± 0.4	5.02 ± 0.7	0.84 ± 0.11
This work	LP/UV	265-320	760	3.4 ± 0.08	2.8 ± 0.08	5.75 ± 0.07	0.83 ±0.03

Notes:

[a]: DF/UV = discharge flow/UV absorption spectroscopy; FP/UV = flashlamp photolysis/ UV absorption spectroscopy; DF/MS = discharge flow/mass spectrometry; PD = photosensitised decomposition; MM/UV = molecular modulation/UV spectroscopy; CP/UV = continuous photolysis/ UV absorption spectroscopy; LP/UV = laser photolysis/ UV absorption spectroscopy

[b]: Sander and Watson used two different methods to measure $k_{6.1b}$. The first consisted in monitoring BrO decay in excess O_3. The second involved measurements of the quantum yield of O_3 loss

[c]: at T = 303 K

[d]: at T = 304 K

[e]: calculated assuming α = 0.84

[f]: at T = 295 K

Table 6.1: Summary of the previous studies on the ambient temperature kinetics and branching of the BrO self-reaction. All rate constants and branching ratios reported are at T = 298 K except where noted.

reaction: the majority of these reported a negative temperature dependence for the overall rate constant and for channel (6.1b) along with a weaker, near-zero temperature dependence for channel (6.1a). However, these previous studies have also reported somewhat conflicting results with regard to the absolute values of the individual rate constants. The work of Sander and Watson [9] was the first to investigate the overall rate of reaction (6.1) at temperatures other than T = 298 K; these authors measured $k_{6.1}$ at three temperatures over the range T = 223-338 K. Cox *et al*. [13] reported values for $k_{6.1b}$ and for the branching ratio $\alpha = k_{6.1a}/k_{6.1}$ at four temperatures over the range T = 278-338 K, hence inferring $k_{6.1}$, and found greater rate constants than those reported by Sander and Watson as well as a weaker negative temperature dependence for $k_{6.1b}$. However, measurements of $k_{6.1}$ by Turnipseed *et al*. [14] at three temperatures over the range T = 253−400 K showed good agreement with the work of Sander and Watson. Mauldin *et al*. [6] determined the rate constants of both channels, hence the overall rate constant and the branching ratio, at T = 298 K and at T =220 K. Gilles *et al*. [20] measured $k_{6.1}$ at nine temperatures over the range T = 204-388 K, finding values of the overall rate constant greater than those of Sander and Watson [9] and Turnipseed *et al*. [14] Harwood *et al*. [22] measured $k_{6.1a}$ and $k_{6.1b}$ at five temperatures over the range T = 222−298K, and obtained smaller rate constants than previous work. A more in-depth account of previous studies on the BrO self-reaction is presented in Section 6.4.1 below.

Studies on the BrO self-reaction at low temperatures are complicated by the apparent contribution of a termolecular component to the observed BrO decay at T < 250 K, as reported by Mauldin *et al*. [6] and Harwood *et al*. [22] Both of these studies found that the overall rate constant for BrO loss was pressure-dependent at T = 220 K and T = 222 K respectively and reported an additional absorption in their spectra which was attributed to the BrO dimer. By contrast, Sander and Watson reported pressure-independent values of $k_{6.1}$ at a similar temperature (T = 223 K). In addition to this disagreement, most studies on the temperature dependence of the BrO self-reaction carry significant statistical uncertainties as measurements are typically only available at a small number of temperature points (with the exception of the work of Gilles *et al*. [20]).

JPL-NASA recommendations [24] for the kinetics and branching of the BrO self-reaction have remained unchanged since 1997. The recommended temperature dependence for

the overall rate constant of reaction (6.1), $k_{6.1}$, is based on the work of Sander and Watson, [9] Turnipseed *et al*. [14] and Gilles *et al*., [20] whereas the temperature dependence of the branching ratio α is based on the study of Mauldin *et al*. [6] (who measured the branching ratio at only two temperatures, T = 298 K and 220 K) and on an extrapolation of the data from Cox *et al*.[13], who measured the branching ratio only down to T = 277.5 K, to lower temperatures. Extrapolation of the data from Cox *et al*. to T = 220 K gives a value of α of 0.72, whereas Mauldin *et al.* measured a branching ratio of 0.68 at this temperature. It appears therefore that the branching of the two channels, whilst well-established at ambient temperature, is still poorly characterised at sub-ambient temperatures relevant to the upper troposphere and stratosphere, due to the paucity of studies performed at such temperatures.

This study aimed to measure the rate constants of both channels of the BrO self-reaction at sub-ambient temperatures (in this case down to T = 266.5 K) and to accurately characterise the temperature dependence of the branching ratio employing laser flash photolysis coupled with UV absorption spectroscopy. Many previous studies have employed this technique, most of them using a flashlamp as the photolysis source [6, 9, 11, 16, 18], others using a laser. [19, 20, 22] However the present study is the first to combine the advantages of laser photolysis (selective photolysis of precursor gases, reduced undesired secondary chemistry, reduced experimental noise) with those of CCD detection (*i.e*. simultaneous spectral *and* temporal resolution of recorded UV absorbances), as discussed in previous chapters.

6.2 Experimental

6.2.1 Radical Generation

BrO radicals were formed following laser photolysis of $Br_2/O_3/O_2/N_2$ gaseous mixtures. Photolysis of Br_2 at λ = 351 nm generated bromine atoms which reacted with excess ozone to produce BrO:

$$Br_2 + h\nu \rightarrow 2\,Br \qquad (6.3)$$

$$Br + O_3 \rightarrow BrO + O_2 \qquad (6.2)$$

Gaseous $Br_2/O_3/O_2/N_2$ mixtures were prepared in a gas flow using calibrated mass flow controllers (MKS). Bromine vapour was introduced into the gas mixture by passing a known flow of nitrogen gas through a bubbler containing liquid Br_2 (Acros, 99.8%) kept at 0°C inside a Dewar flask. The bromine content in the precursor mixture was calculated using flow rates and the vapour pressure of liquid Br_2 at T = 0°C and was typically (1-2) × 10^{16} molecule cm^{-3}. These concentrations were confirmed by fitting the JPL-NASA [24] recommended Br_2 cross-section to measurements of the Br_2 absorption spectrum in the region λ = 450-580 nm. Ozone was generated by flowing oxygen gas (BOC, 99.99%) through a commercial ozoniser (Ozonia Triogen 213). The ozone output from this ozoniser was measured *via* UV spectroscopy and quantified using the Beer-Lambert law, as described in Appendix 1. The typical conversion efficiency of the ozoniser was found to be approximately 6% and ozone concentrations in the precursor mixture were (1-2) × 10^{16} molecule cm^{-3}. These gases were mixed with a nitrogen (BOC, 99.998%) bath gas to balance to p = 1 atm in the mixing line from which they were delivered to the reaction cell *via* Teflon tubing.

The optimised experimental conditions which were designed using kinetic calculations and numerical integration modelling minimised the occurrence of secondary chemistry such that BrO radicals were promptly and exclusively formed from Br atoms. Post-photolysis bromine atom concentrations, $[Br]_0$, and therefore initial BrO concentrations, $[BrO]_0$, were typically in the range (5–6) × 10^{13} molecule cm^{-3} and were determined from fits to the kinetic traces, as discussed in Section 6.2.4 below.

6.2.2 Species monitoring

Species in the reaction mixture were monitored by means of their UV absorption spectra recorded over the range λ = 298-326 nm. A 600 grooves mm^{-1} diffraction grating was used along with a spectrograph entrance slit width of 75 μm, resulting in a resolution (FWHM) of 0.5 nm. Spectra were typically recorded at intervals of 100 μs.

The BrO spectrum exhibits structured absorption features over the range λ = 290-380

nm attributed to the ($A\ ^2\Pi_{3/2} \leftarrow X\ ^2\Pi_{3/2}$) vibronic transition, with the most intense bands appearing in the region λ = 317-339 nm. However, in the experimental set-up, the use of a dichroic reflector to direct the laser beam (λ = 351 nm) into the reaction cell meant that no transmitted light in the range λ = 330-420 nm reached the spectrograph, thus effectively limiting the monitoring to wavelengths λ < 330 nm. BrO was therefore monitored using the less intense vibronic peaks in the range λ = 298-326 nm.

Absorbance spectra were obtained, as described in Chapter 3, using Beer's Law and represented the *change* in the total absorbance of the reactive mixture post-photolysis. A typical absorbance spectrum for photolysis of $Br_2/O_3/O_2/N_2$ mixtures is shown in Figure 6.2. The spectrum recorded in the immediate post-photolysis (t = 3.5-8.5 ms) shows the distinctive vibronic peaks of BrO, indicating prompt radical formation upon photolysis. At longer timescales after photolysis (t = 53.5-58.5 ms), the intensity of the BrO signal decreased following radical decay *via* the BrO self-reaction and a negative contribution to the total absorbance was observed, attributed to ozone removal *via* reaction (6.2). Deconvolution of these spectra is described in detail in the following section.

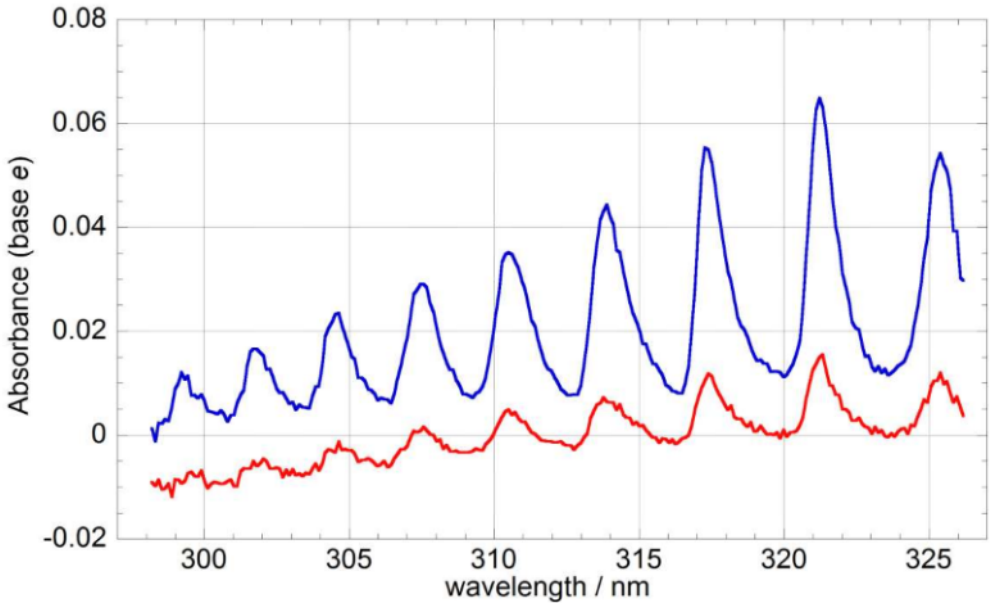

Figure 6.2 : Typical absorbance spectra of photolysed $Br_2/O_3/O_2/N_2$ mixtures recorded at T = 265.5 K in the immediate post-photolysis (shown in blue, averaged over t = 3.5-8.5 ms after photolysis) and at longer timescales after photolysis (shown in red, averaged over t = 53.5-58.5 ms after photolysis).

6.2.3 Determination of Species Concentrations

Time-resolved radical and other species concentrations were obtained by fitting reference cross-sections to the recorded absorbances *via* the Beer-Lambert Law. The BrO spectrum measured by Wilmouth *et al.* [7] was used as the reference BrO cross-section in this work. As the resolution of this spectrum was higher (0.4 nm FWHM) than that of the experimental spectra recorded in this work (0.5 nm FWHM), the cross-section from Wilmouth *et al*. was smoothed using, in this case, a 93-point Gaussian averaging kernel to match the lower experimental resolution of the present work, as described in Appendix 3. The absence of systematic features in the residuals obtained from spectral subtraction of the scaled reference spectrum from the experimental spectra added confidence to this smoothing procedure, as shown in Figure 6.3. Since the vibronic bands of BrO are also strongly dependent on temperature, the reference BrO cross-sections were interpolated to each experimental temperature again using the spectra recorded by Wilmouth *et al*. at T = 228 K and T = 298 K, assuming that σ_{BrO} varied linearly with temperature over this range. The validity of the linear temperature dependence of the BrO cross-section was supported by the study of Gilles *et al*., [20] who observed linear behaviour of both the absolute cross-section at the (7, 0) peak of BrO and of the differential cross-section (of the same peak to the red-shifted adjacent trough) at nine temperatures over the interval T = 204-388 K. The values of σ_{BrO} measured by Gilles *et al*. are in good agreement with those obtained in a previous study by Wahner *et al*. (at only two temperatures, T = 298 K and T = 223 K), therefore supporting the linearity of this temperature dependence. At each temperature, the absence of any residual structure following spectral fitting and subtraction confirmed the determination of BrO concentrations.

Differential fitting procedures were used to determine BrO concentrations. This technique, described in Chapter 3, allows unequivocal monitoring of absorbers exhibiting spectral structure. As BrO was the only such absorber in the gas mixture post-photolysis, the Beer-Lambert Law could therefore be expressed as:

$$A_{\text{diff }\lambda,t} = \sigma_{\text{diff BrO},\lambda}[\text{BrO}]_t l \qquad (6.i)$$

where $A_{\text{diff }\lambda,t}$ is the differential absorbance spectrum and $\sigma_{\text{diff BrO},\lambda}$ is the differential BrO cross-section. An example of differential fitting to the recorded absorbance is shown in Figure 6.3 and the resulting $[BrO]_t$ temporal trace, from fitting to each sequential spectrum, is shown in Figure 6.4.

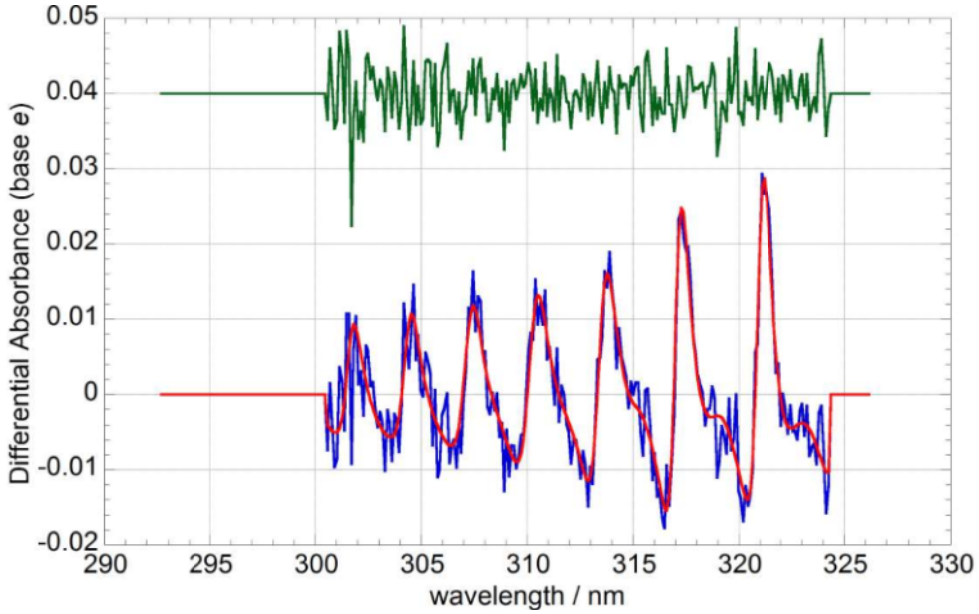

Figure 6.3 : Differential spectral fitting to a BrO spectrum recorded at T = 287.4 K and at t = 0.013 s after photolysis. The experimental differential spectrum is shown in blue and the scaled BrO differential cross-section is shown in red. Residuals, in green, have been offset by +0.04 absorbance units for clarity.

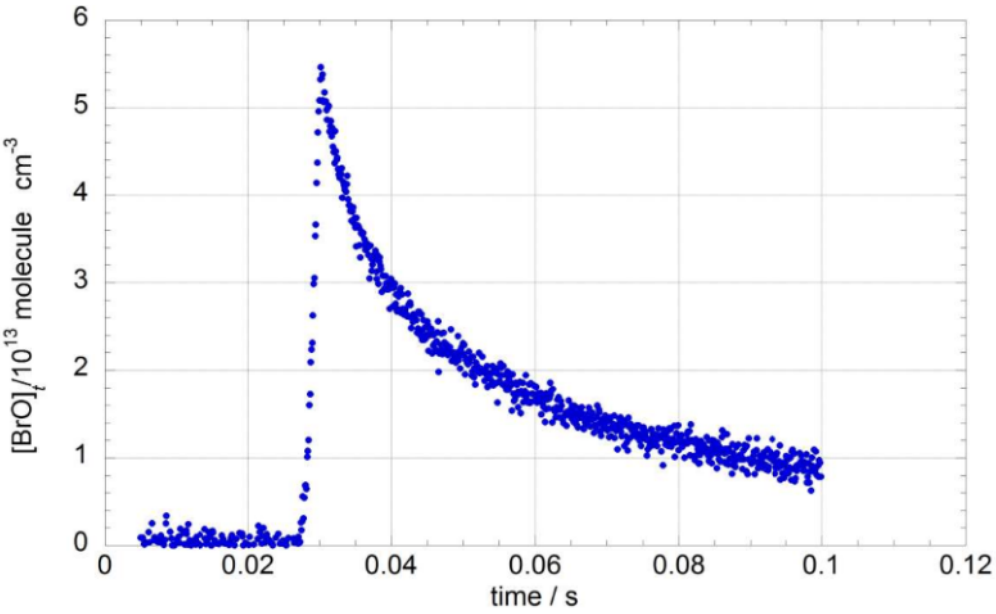

Figure 6.4 : [BrO] temporal trace at T = 287.4 K obtained from differential fitting routines.

Whilst unequivocal and accurate [BrO] monitoring was possible in these experiments, this monitoring alone was not sufficient to investigate both channels of reaction (6.1). Under the elevated ozone concentrations employed in the current work, the two bromine atoms produced by channel (6.1a) promptly regenerated BrO *via* reaction (6.2). The observed [BrO] decay was therefore only sensitive to channel (6.1b) and fitting a simulated [BrO] profile to the experimental trace would only allow determination of $k_{6.1b}$, as discussed in Section 6.2.4.

It was possible, however, to also monitor the ozone consumed by the regeneration of BrO *via* reaction (6.2) from the Br atoms generated in channel (6.1a). This was feasible thanks to the negative contribution from ozone removal to the recorded absorbance, as discussed in the previous section. Once BrO concentrations were quantified *via* differential fitting, the contribution of BrO from the recorded absorbance was subtracted. This procedure revealed the underlying negative absorbance arising from ozone removal and fitting a literature cross-section of ozone to this residual spectrum at each time point allowed quantification of the change in ozone concentrations, $\Delta[O_3]$, brought about by photolysis and subsequent chemistry, as illustrated in Figure 6.5.

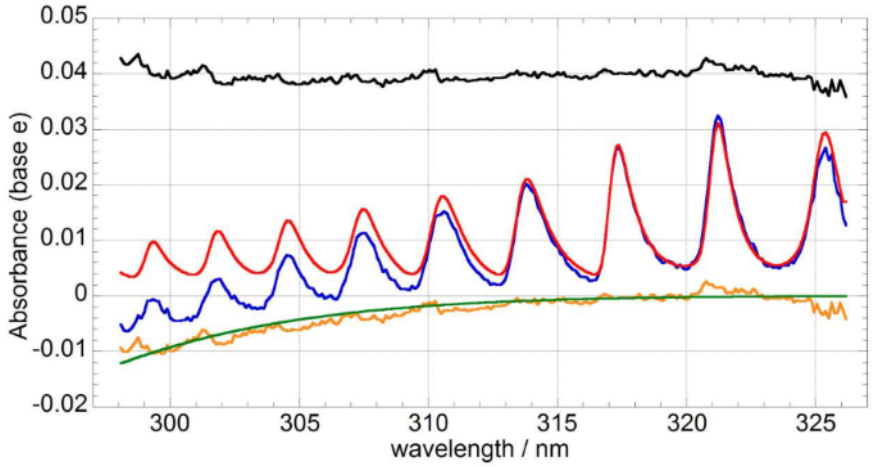

Figure 6.5 : Deconvolution of an absorbance spectrum recorded at T = 265.5 K following photolysis of $Br_2/O_3/O_2/N_2$ gas mixtures. The contribution of BrO absorption (in red, quantified *via* differential fitting routines) is subtracted from the recorded absorbance (in blue) leaving a negative residual (in orange) arising from ozone removal. Fitting a reference cross-section of ozone (in green) to this residual absorbance allows quantification of $\Delta[O_3]$. Residuals between the experimental and calculated absorbance (obtained as the sum of the contributions from BrO and O_3) are shown in black and have been offset by +0.04 absorbance units for clarity.

The values for the ozone cross-section used to fit to the residual spectra were those reported by JPL-NASA. [24] Unlike the BrO spectrum, ozone absorption in the near-UV, at the current experimental resolution, was devoid of significant structured features and therefore did not exhibit an appreciable dependence on spectral resolution. Smoothing of the reference ozone cross-section was therefore not required. Temperature effects on the ozone cross-section are also very weak. In any case, reference O_3 cross-sections were generated at each experimental temperature *via* an interpolation of the JPL-NASA temperature-dependent cross-sections in a manner similar to that used for the BrO spectrum.

A typical $\Delta[O_3]_t$ kinetic profile obtained from fitting to the residual spectra is shown in Figure 6.6.

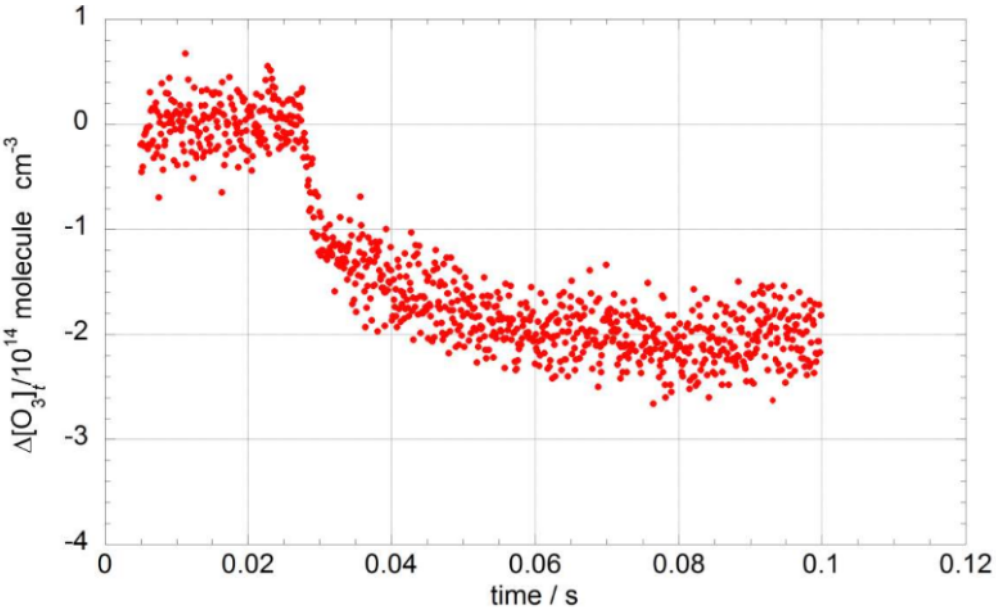

Figure 6.6 : $\Delta[O_3]$ temporal trace recorded at T = 287.4 K.

6.2.4 Kinetic Analysis

Under the elevated ozone concentrations used in the current work, all bromine atoms, whether generated directly by photolysis of Br_2 or by channel (6.1a), were promptly converted into BrO *via* reaction (6.2). As a result, the observed [BrO] decay was not sensitive to channel (6.1a). This can be shown using classical kinetics; in a simple

model consisting of reactions (6.1a), (6.1b) and (6.2), the rate of BrO loss can be expressed as:

$$-\frac{d[\mathrm{BrO}]}{dt} = 2k_{6.1a}[\mathrm{BrO}]^2 + 2k_{6.1b}[\mathrm{BrO}]^2 - k_{6.2}[\mathrm{Br}][\mathrm{O_3}] \qquad (6.ii)$$

Under the experimental conditions used, Br atoms are in steady state, *i.e.* the rate of removal far exceeds the rate of production. Therefore the steady state approximation, described in Chapter 2, can be applied to the rate equation for Br:

$$\frac{d[\mathrm{Br}]}{dt} = 2k_{6.1a}[\mathrm{BrO}]^2 - k_{6.2}[\mathrm{Br}][\mathrm{O_3}] \overset{\mathrm{SSA}}{\approx} 0 \qquad (6.iii)$$

Equation (6.ii) can therefore be simplified to:

$$-\frac{d[\mathrm{BrO}]}{dt} = 2k_{6.1b}[\mathrm{BrO}]^2 \qquad (6.iv)$$

This equation is readily integrated to give an expression for the observed BrO decay:

$$[\mathrm{BrO}]_t = \left(\frac{1}{[\mathrm{BrO}]_0} + 2k_{6.1b}\,t\right)^{-1} \qquad (6.v)$$

Thus, fitting a simulated [BrO] trace from equation (6.v) to the observed experimental BrO decay allowed extraction of the rate constant of channel (6.1b) but provided no kinetic information on channel (6.1a). An example of a fit of equation (6.v) to an experimental [BrO] trace recorded at $T = 287.4$ K is shown in Figure 6.7.

As described in the previous section, the acquisition of sequential broadband spectra allowed not only the determination of the [BrO] temporal trace, but also the quantification of the change in ozone concentrations following photolysis, $\Delta[O_3]$. It can be shown, [9] using the same classical kinetics model employed to derive equation (6.v), that $\Delta[O_3]_t$ is sensitive to *both* channels (6.1a) and (6.1b), thus allowing a full

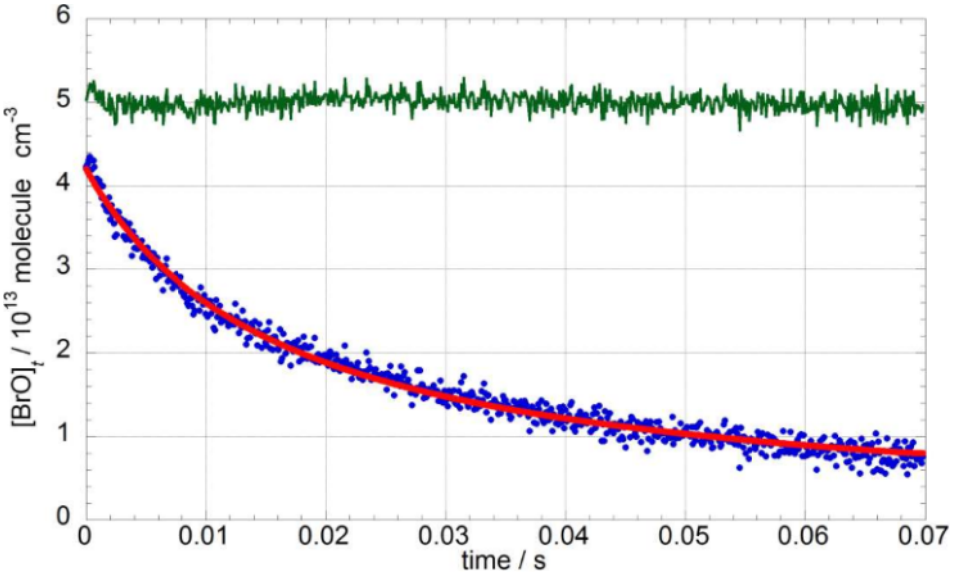

Figure 6.7 : Classical kinetic fit (in red) to a [BrO] trace recorded at T = 287.4 K (blue points). Residuals (in green) have been offset by $+5\times10^{13}$ molecule cm^{-3} for clarity.

characterisation of the kinetics of the BrO self-reaction. The rate of ozone removal *via* reaction (6.2) can be written as:

$$-\frac{d[O_3]}{dt} = k_{6.2}[Br][O_3] \qquad (6.vi)$$

Substituting equation (6.iii) into the equation above returns an expression for the rate of ozone removal in terms of $k_{6.1a}$ and [BrO]:

$$-\frac{d[O_3]}{dt} = 2k_{6.1a}[BrO]^2 \qquad (6.vii)$$

Substituting for [BrO] from (6.v):

$$-\frac{d[O_3]}{dt} = 2k_{6.1a}\left(\frac{1}{[BrO]_0} + 2k_{6.1b}t\right)^{-2} \qquad (6.viii)$$

Separating the variables and integrating both sides between time t = 0, defined as immediately after photolysis, and time t:

$$\int_{[O_3]_0}^{[O_3]_t} -d[O_3] = 2k_{6.1a}\int_0^t \frac{1}{\left(\frac{1}{[BrO]_0} + 2k_{6.1b}t\right)^2}dt \qquad (6.ix)$$

The right hand side of equation (6.ix) is in the form:

$$\int \frac{1}{(a+bx)^2}dx = -\frac{1}{b}\left(\frac{1}{a+bx}\right)$$

where in this case $a = 1/[BrO]_0$ and $b = 2k_{6.1b}$. Integration therefore results in:

$$-\left([O_3]_t - [O_3]_0\right) = -\frac{k_{6.1a}}{k_{6.1b}}\left[\frac{1}{\frac{1}{[BrO]_0} + 2k_{6.1b}t}\right]_0^t$$

$$\therefore [O_3]_t - [O_3]_0 = \frac{k_{6.1a}}{k_{6.1b}}\left\{\left(\frac{1}{\frac{1}{[BrO]_0} + 2k_{6.1b}t}\right) - [BrO]_0\right\} \qquad (6.x)$$

where $[O_3]_0$ is the concentration of ozone immediately following bromine photolysis *and* generation of BrO radicals, and $[O_3]_t$ is the subsequent ozone concentration reduced further by the catalytic destruction of ozone following reaction (6.1a). Equation (6.x) can be conveniently rearranged into:

$$[O_3]_t - [O_3]_0 = -2k_{6.1a}[BrO]_0^2\left(\frac{t}{1+2k_{6.1b}t[BrO]_0}\right) \qquad (6.xi)$$

Assuming $[O_3]_0 = [BrO]_0$ from the stoichiometry of BrO formation chemistry, equation (6.xi) becomes:

$$\Delta[O_3]_t = -[BrO]_0\left\{2k_{6.1a}[BrO]_0\left(\frac{t}{1+2k_{6.1b}t[BrO]_0}\right)+1\right\} \qquad (6.xii)$$

which is equivalent to the decay curve described by equation (6.xi) offset by $[BrO]_0$. As ozone is present in the precursor mixture, equation (6.xii) does not describe the temporal behaviour of ozone in terms of absolute concentrations, but rather in terms of the *change* in $[O_3]$ relatively to the pre-photolysis concentrations. The expression for $[O_3]_t$ on the left-hand side of equation (6.xii) was therefore replaced with the more correct $\Delta[O_3]_t$. Equation (6.xii) shows that ozone removal is sensitive to both $k_{6.1a}$ and $k_{6.1b}$ and hence fitting of this expression to experimental $\Delta[O_3]_t$ traces allows the determination of the branching ratio of the BrO self-reaction, defined for channel (6.1a) as $\alpha = k_{6.1a}/ k_{6.1}$.

Initially, equation (6.v) alone was fitted to the experimental $[BrO]_t$ trace *via* a least-squares minimisation routine optimising the values for $[BrO]_0$ and $k_{6.1b}$. Subsequently, equations (6.v) and (6.xii) were fitted *simultaneously* to the observed $[BrO]_t$ and $\Delta[O_3]_t$ traces respectively by optimising $[BrO]_0$, $k_{6.1a}$ and $k_{6.1b}$. The values of $[BrO]_0$ and $k_{6.1b}$ obtained from the simultaneous fit to $[BrO]_t$ and $\Delta[O_3]_t$ were respectively within 1% and 1.5% of those obtained by fitting uniquely to $[BrO]_t$ at all temperatures. Both sets of kinetic results are shown in Section 6.3. The simulated traces obtained from equations (6.v) and (6.xii) were corrected for gas flow-out from the reaction cell and for the averaging imparted to the recorded traces by the simultaneous illumination of 31 rows of the CCD detector before being fitted to experimental traces, as discussed in Section 3.4.4.

A typical fit to an experimental $\Delta[O_3]_t$ trace, obtained by fitting simultaneously equations (6.v) and (6.xii) to the $[BrO]_t$ and $\Delta[O_3]_t$ traces, is shown in Figure 6.8.

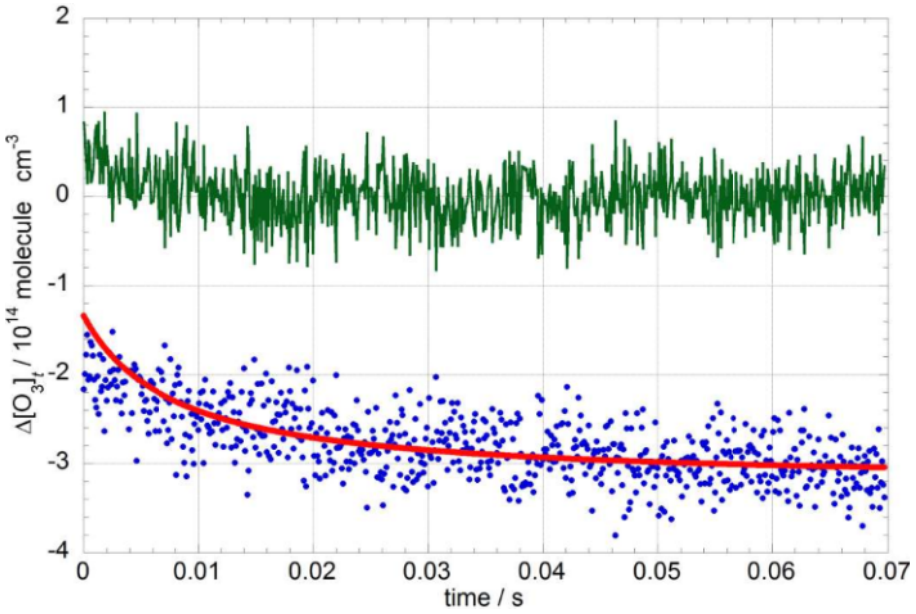

Figure 6.8 : Classical kinetic fit from equation (6.xii) (in red) to a $\Delta[O_3]_t$ trace recorded at T = 287.4 K (blue points). Residuals are shown in green.

As in the studies of the other halogen oxide reactions described in this thesis, a FACSIMILE [25] model was built for the BrO self-reaction. The numerical integration model included the reactions listed in Table 6.2 as well as expressions for gas flow-out (or flow-in) from/to the reaction cell and the temporal averaging of the signal imparted by the CCD detector.

Reaction	k/cm^3 molec^{-1} s^{-1}	reference
$Br + O_3 \rightarrow BrO + O_2$	$1.7\times10^{-11}\exp(-800/T)$	[24]
$BrO + BrO \rightarrow 2Br + O_2$	$k_{6.1a}$	*this work*
$BrO + BrO \rightarrow Br_2 + O_2$	$k_{6.1b}$	*this work*
$Br + BrO + M \rightarrow Br_2O + M$	$1.9\times10^{-14}\exp(1370/T)$ [a]	[22]
$Br_2O + Br \rightarrow BrO + Br_2$	4×10^{-11} [b]	[18]
$Br + Br + M \rightarrow Br_2 + M$	$4.8\times10^{-15}\exp(1136/T)$ [a]	[26]
$BrO + O_3 \rightarrow OBrO + O_2$	$7\times10^{-14}\exp(-3100/T)$	[27]

Notes:

[a]: at p = 760 Torr; [b]: at T = 298 K

Table 6.2 : Reactions employed in the FACSIMILE model used in the present study of the BrO self-reaction.

Initially, the FACSIMILE model was used to test for the effective masking of channel (6.1a) by fitting a simulated [BrO] trace to the experimental $[BrO]_t$ by optimising values of $[Br]_0$ and $k_{6.1b}$, while keeping $k_{6.1a}$ fixed at the value recommended by JPL-NASA. [24] The value of $k_{6.1a}$ was then perturbed by a factor of two (*i.e.*, doubled and halved) and the model fit to the same experimental BrO decay trace: the deviation of the optimised $k_{6.1b}$ from the value obtained from the FACSIMILE model with unperturbed $k_{6.1a}$ was minimal (< 2%) even at the smallest pre-flash ozone concentrations used in this work ($[O_3] = 1\times10^{16}$ molecules cm^{-3}). This confirmed the expected loss of sensitivity of the [BrO] trace to channel (6.1a). Furthermore, when the FACSIMILE model was used to fit *simultaneously* to sample $[BrO]_t$ and $\Delta[O_3]_t$ traces at each temperature, the returned values of $k_{6.1a}$ and $k_{6.1b}$ were respectively within 2.1% and 1.6% from those obtained from the simultaneous fitting of equations (6.v) and (6.xii) to experimental data.

The excellent agreement between the classical kinetic model and the numerical integration model indicates that the secondary reactions included in the FACSIMILE model, but neglected in the classical solutions for $[BrO]_t$ and $\Delta[O_3]_t$, ultimately have a minimal effect on the extracted kinetic parameters of the BrO self-reaction. The sensitivity to the secondary chemistry is however discussed in Section 6.4.1.

6.3 Results

The BrO self-reaction was studied at nine temperatures over the range T = 266.5-321.6 K and at ambient pressure (p = 760 Torr). Typically at least four experiments were performed at each temperature, each consisting of 20 photolysis events. As described in the previous section, two sets of data were obtained from the kinetic analysis: one in which $k_{6.1b}$ alone could be extracted from the analysis of the BrO decay, and one in which both $k_{6.1a}$ and $k_{6.1b}$ were obtained from simultaneous fitting to $\Delta[O_3]_t$ and $[BrO]_t$. The kinetic parameters resulting from the two different fitting procedures are shown in Tables 6.3 and 6.4.

T/K	$k_{6.1b}/10^{-13}$ cm^3 molecule^{-1} s^{-1}
265.5	6.84 ± 0.08
272.5	6.62 ± 0.03
279.9	6.19 ± 0.16
287.4	6.14 ± 0.10
298	5.69 ± 0.09
302.4	5.95 ± 0.09
309.5	6.34 ± 0.11
315.5	6.26 ± 0.11
320.6	5.91 ± 0.08

Table 6.3 : Values for $k_{6.1b}$ obtained from fitting to $[BrO]_t$ decay only. Errors are 2σ, statistical only.

T/K	$k_{6.1a}/10^{-12}$ cm^3 molecule^{-1} s^{-1}	$k_{6.1b}/10^{-13}$ cm^3 molecule^{-1} s^{-1}	$k_{6.1}/10^{-12}$ cm^3 molecule^{-1} s^{-1}	$k_{6.1a}/k_{6.1}$
265.5	3.14 ± 0.3	6.93 ± 0.1	3.83 ± 0.3	0.82 ± 0.01
272.5	3.22 ± 0.3	6.73 ± 0.04	3.90 ± 0.3	0.83 ± 0.01
279.9	2.99 ± 0.33	6.29 ± 0.02	3.62 ± 0.3	0.82 ± 0.02
287.4	3.00 ± 0.2	6.21 ± 0.1	3.62 ± 0.2	0.83 ± 0.007
298	2.81 ± 0.09	5.75 ± 0.07	3.39 ± 0.08	0.83 ± 0.005
302.4	2.32 ± 0.4	6.03 ± 0.1	2.92 ± 0.4	0.79 ± 0.02
309.5	3.30 ± 0.6	6.40 ± 0.2	3.94 ± 0.6	0.83 ± 0.02
315.5	3.56 ± 0.4	6.30 ± 0.2	4.20 ± 0.4	0.85 ± 0.01
320.6	2.55 ± 0.5	5.91 ± 0.1	3.14 ± 0.5	0.81 ± 0.03

Table 6.4 : Kinetic results from simultaneous fitting to both $[BrO]_t$ and $\Delta[O_3]_t$ traces. Errors are 2σ, statistical only.

Both channels showed a negative temperature dependence of the kinetic parameters and exhibited a linear Arrhenius behaviour, as shown in Figure 6.9. The Arrhenius expression for $k_{6.1b}$ obtained from fitting solely to the observed BrO decay was:

$$k_{6.1b}/\text{cm}^3 \text{ molecule}^{-1} \text{ s}^{-1} = (3.4 \pm 1.0) \times 10^{-13} \exp[(182 \pm 91)/T]$$

Simultaneous fitting to both $[BrO]_t$ and $[\Delta O_3]_t$ allowed characterisation of both channels as a function of temperature. The Arrhenius expressions resulting from this fitting procedure were:

$$k_{6.1a}/\text{cm}^3\ \text{molecule}^{-1}\ \text{s}^{-1} = (1.92 \pm 1.54) \times 10^{-12}\exp[(126 \pm 214)/T]$$

$$k_{6.1b}/\text{cm}^3\ \text{molecule}^{-1}\ \text{s}^{-1} = (3.4 \pm 0.8) \times 10^{-13}\exp[(181 \pm 70)/T]$$

This allowed the determination of an expression for the overall rate constant, $k_{6.1}$:

$$k_{6.1}/\text{cm}^3\ \text{molecule}^{-1}\ \text{s}^{-1} = (2.3 \pm 1.5) \times 10^{-12}\exp(134 \pm 185/T)$$

cf. JPL-NASA [24]: $k_{6.1}/\text{cm}^3\ \text{molecule}^{-1}\ \text{s}^{-1} = 1.5 \times 10^{-12}\exp(230/T)$

The branching ratio for channel (6.1a) was therefore calculated as:

$$\alpha = k_{6.1a}/k_{6.1} = (0.84 \pm 0.09)\exp[(-7 \pm 32)/T]$$

cf. JPL-NASA [24]: $k_{6.1a}/k_{6.1} = 1.6\exp(-190/T)$

In all cases, errors are 1σ, from the Arrhenius fit. The temperature dependence of $k_{6.1}$, $k_{6.1a}$ and $k_{6.1b}$ is illustrated in Arrhenius form in Figure 6.9, whereas that of the branching ratio for channel (6.1a), α, is shown in Figure 6.10.

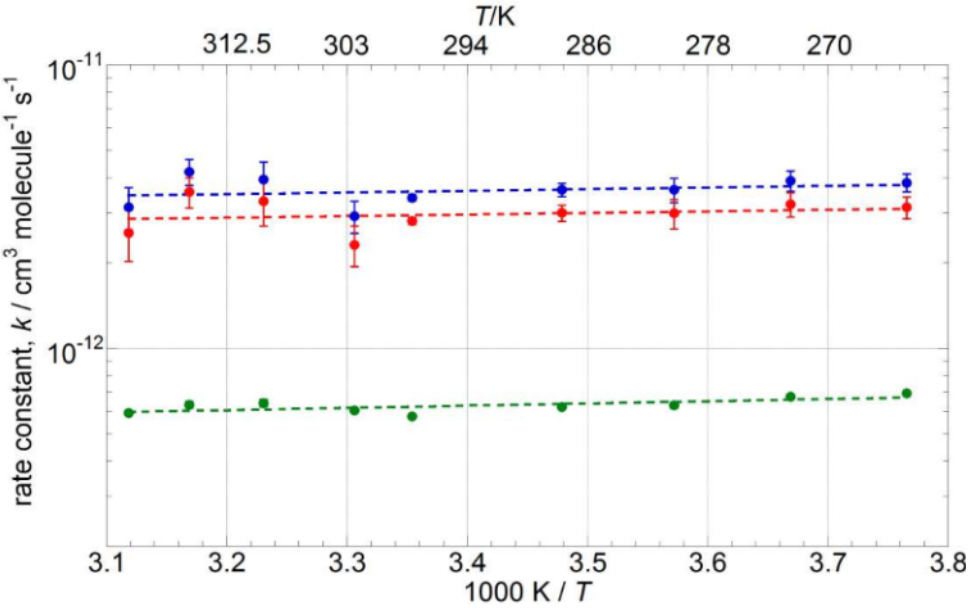

Figure 6.9 : Arrhenius plot for the values of $k_{6.1}$ (in blue), $k_{6.1a}$ (in red) and $k_{6.1b}$ (in green) obtained in the present work. The values of $k_{6.1b}$ plotted are those obtained from the simultaneous fit to $[BrO]_t$ and $[\Delta O_3]_t$. The parameterisations resulting from the experimental results are shown as dashed lines. Error bars are 2σ, statistical only.

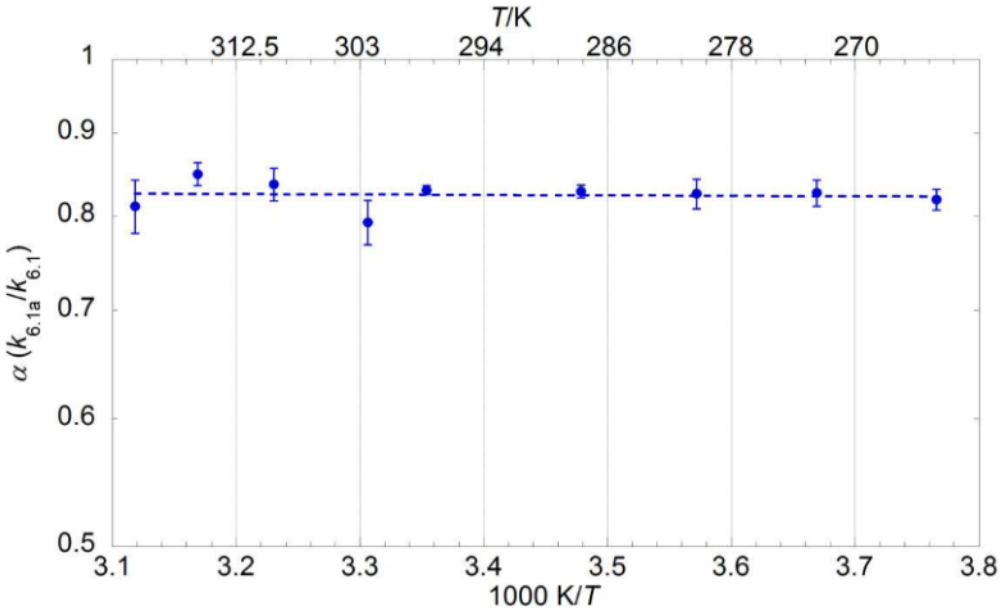

Figure 6.10 : Temperature dependence of the branching ratio for channel (6.1a), $\alpha = k_{6.1a}/k_{6.1}$, presented in Arrhenius form along with the resulting parameterisation (dashed line). Error bars arise from the propagation of the errors in $k_{6.1a}$ and $k_{6.1}$.

6.4 Discussion

6.4.1 Sensitivity Analysis

As discussed above, the sensitivity of $k_{6.1a}$, $k_{6.1b}$ and α to secondary chemistry appeared minimal. However, sensitivity of the values of $k_{6.1a}$, $k_{6.1b}$ and α to the uncertainties in the absorption cross-sections of BrO from Wilmouth *et al.*[7] and those of ozone from JPL-NASA [24] was investigated, as the extracted rate constants depended critically on the absolute concentrations of BrO and O_3. Wilmouth *et al.* report an error of ±11% for the differential cross-section of the (7, 0) band (λ = 338.5 nm) at T = 298 K; similarly, the recommended uncertainty for the O_3 cross-section from JPL-NASA is ±10%. The effect of perturbing the cross-section of one species by a certain factor was equivalent to scaling the temporal trace of the concentration of that species by the reciprocal of the same factor. This is particularly important for second order reactions where the absolute concentrations affect the derived kinetics. Thus, sample [BrO] and $\Delta[O_3]$ traces at T = 298 K were perturbed by 11% and 10% respectively, in sequence, and fitted simultaneously to equations (6.v) and (6.xii). The values of $k_{6.1a}$, $k_{6.1b}$ and α obtained from the simultaneous fit to the perturbed [BrO] trace and to the unperturbed

$\Delta[O_3]$ trace were within respectively 24%, 11% and 2% of the values resulting from fitting to the unperturbed [BrO] trace. Similarly, when only the ozone trace was perturbed, the returned values of $k_{6.1a}$, $k_{6.1b}$ and α were within 12%, 0.3% and 2% respectively of those obtained with the unaltered $\Delta[O_3]$ trace.

It was also noted that the structured Huggins bands of the ozone spectrum overlapped with the spectral region monitored in this work, as illustrated in Figure 6.11. Although the residual absorbance following subtraction of the differentially fitted BrO spectrum did not exhibit any structured features (Section 6.2.3), it was suspected that the presence of an underlying structured absorber, albeit weak, may have interfered with the fitting of the BrO cross-section to the recorded spectra. To address this, a number of spectra were re-analysed using the ozone cross-section from Brion *et al.*, [28] which accounted for the presence of the Huggins bands, in the place of that from JPL-NASA, which was devoid of any structured features. Brion *et al*. reported the absorption cross-section of ozone at high resolution (0.012 nm FWHM) over a wide spectral range (λ = 195-345 nm) and at five temperatures over the range T = 218-295 K. Analogously to the BrO cross-section, the high-resolution ozone spectrum from Brion *et al*. was therefore degraded to the lower experimental resolution employed in this study (0.5 nm FWHM) using a 93-point

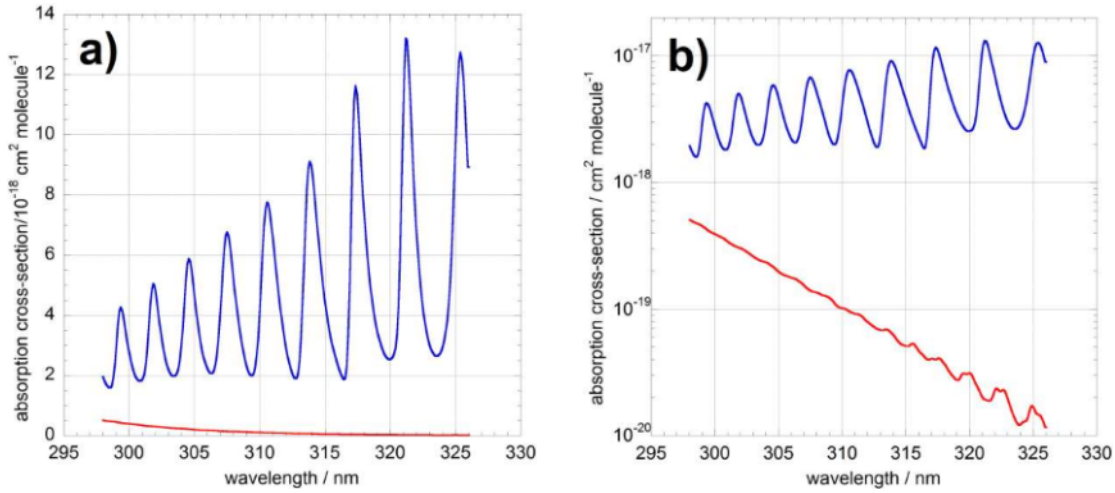

Figure 6.11 : BrO (in blue) and ozone (in red) cross-sections on a linear (a) and on a logarithmic (b) *y*-axis, revealing the presence of the Huggins bands of ozone over the spectral range monitored in this work. Both cross-sections were convolved to the experimental resolution used in the current study (0.5 nm FWHM). The BrO cross-section shown is taken from Wilmouth *et al*., [7] the O_3 cross-section is taken from Brion *et al*. [28]

Gaussian averaging kernel. Initially, the ozone cross-section from Brion *et al*. was fitted to the residual absorbance following removal of the BrO contribution to the total absorbance, as described in Section 6.2.3. The resulting $\Delta[O_3]$ traces, along with the corresponding [BrO] decay, were then fitted to the classical kinetics solutions, equations (6.v) and (6.xii). The resulting values of $k_{6.1a}$, $k_{6.1b}$ and α were respectively within 3%, 0.2% and 1% of those returned from traces obtained from fitting the JPL-NASA ozone cross-section to the residual absorbance. This was taken to show that the presence and inclusion of the ozone Huggins bands did not have a significant effect on the $\Delta[O_3]$ trace obtained from fitting to the residual absorbance after the removal of BrO absorption. Finally, to assess the possible effects of the Huggins bands on the *differential* fitting procedure of the BrO cross-section to the recorded spectra, a linear combination of the differential BrO cross-section and the differential ozone cross-section from Brion *et al*. was fitted to the recorded absorbance. The returned BrO trace did not deviate at all significantly (typically < 0.4%) from that obtained from the differential fit of the BrO cross-section alone which is unsurprising considering the relative magnitude of these cross-sections. The absence of a spectral signature arising from the Huggins bands, both in the differential fitting of the BrO cross-section and in fitting to the residual spectrum following subtraction of the BrO contribution to the total absorbance, was attributed principally to the small value of the ozone cross-section at λ > 310 nm, to the low spectral resolution and to the magnitude of the $\Delta[O_3]$ trace recorded.

Sensitivity studies were also undertaken to assess the impact of uncertainty in the secondary chemistry onto the extracted rate constants for the BrO self-reaction. As discussed above in Section 6.2.4, the excellent agreement between the classical kinetic solutions to the rate equations and the FACSIMILE model including secondary chemistry indicated a weak sensitivity to secondary BrO (and O_3) decay pathways other than reactions (6.1a) and (6.1b). This was confirmed by performing a sample FACSIMILE fit, one at each experimental temperature, in which the rates of the secondary reactions were perturbed sequentially by a factor of two. The effects on the returned kinetic parameters were minimal, with values of $k_{6.1a}$, $k_{6.1b}$ and α lying within 2.5%, 1.6% and 0.5% respectively of the values obtained from fitting to the unperturbed

models. Perturbation of the modelled gas flow-out by ±10% also had a negligible effect (< 0.01%) on the optimised values of $k_{6.1a}$ and $k_{6.1b}$.

Sufficiently high ozone concentrations in the precursor gas mixture were crucial in order to achieve the masking of channel (6.1a), which is a critical assumption in the derivation of the classical solutions, equations (6.v) and (6.xii). Ozone abundances in the precursor mixture were conveniently quantified by means of UV absorption spectroscopy and were found to be in the range of $[O_3] = 1\text{-}2 \times 10^{16}$ molecule cm^{-3}. Sensitivity to the uncertainty in precursor $[O_3]$ was investigated by performing FACSIMILE fits to sample traces in which the precursor $[O_3]$ was altered as follows. Values of $k_{6.1a}$ and $k_{6.1b}$ returned from fits in which the concentration of ozone was set to half the minimum concentration observed ($[O_3] = 0.5\times10^{16}$ molecule cm^{-3}) were respectively within 1.9% and 0.5% of those obtained from the model with unaltered precursor $[O_3]$. Analogously, when the precursor (model) ozone was set equal to double the maximum concentration observed ($[O_3] = 4\times10^{16}$ molecule cm^{-3}), the values of $k_{6.1a}$ and $k_{6.1b}$ obtained were respectively within 0.6% and 1.6% of those resulting from the unperturbed precursor $[O_3]$.

Harwood *et al*. [22] observed a pressure dependence of the overall rate constant $k_{6.1}$ at temperatures below $T = 250$ K. This behaviour was attributed to the termolecular BrO dimerisation reaction, analogous to the ClO dimerisation reaction:

$$BrO + BrO + M \quad \leftrightarrows \quad Br_2O_2 + M \qquad (6.4, -6.4)$$

As the lowest temperature in the present study is $T = 265.5$ K, it is however unlikely for reactions (6.4, −6.4) to occur, on the basis of these previous studies.

6.4.2 Comparison with Previous Studies

Arrhenius parameters (pre-exponential factor A and effective activation energy $-E_a/R$) for $k_{6.1a}$ and $k_{6.1b}$ are summarised in Table 6.5 along with the IUPAC [23] and JPL-NASA [24] recommendations and results from previous studies.

	$k_{6.1a}$		$k_{6.1b}$	
	$A/10^{-12}$ cm^3 molecule^{-1} s^{-1}	$-E_a/R$ /K	$A/10^{-14}$ cm^3 molecule^{-1} s^{-1}	$-E_a/R$ /K
JPL-NASA [24]	2.4	40	2.8	860
IUPAC [23]	2.7	0 ± 200	2.9	840 ± 200
Harwood *et al.* [22]	5.31 ± 1.17	211 ± 59	1.13 ± 0.47	983 ± 111
Cox *et al.* [13]			29^{+28}_{-14}	259 ± 208
This work (Fit to $[BrO]_t$ alone)			34 ± 10	182 ± 91
This work (Simultaneous fit to $[BrO]_t$ and $\Delta[O_3]_t$)	1.92 ± 1.54	126 ± 214	34 ± 8	181 ± 70

Table 6.5 : Arrhenius parameters (pre-exponential factor A and activation energy $-E_a/R$) for $k_{6.1a}$ and $k_{6.1b}$ from the current work and previous studies.

The two sets of results obtained for $k_{6.1b}$ from different fitting methods were (unsurprisingly) in excellent agreement with one another, with values of the rate constant at each temperature agreeing well within error range as shown in Tables 6.3 and 6.4. Consequently, the Arrhenius parameters for the temperature dependence of $k_{6.1b}$ derived from the two independent analyses were almost identical, as illustrated in Table 6.5, implying that the extraction of $k_{6.1b}$ from ozone traces gave identical values to those from BrO traces. The consistency of the results for $k_{6.1b}$ obtained from these two datasets therefore added confidence to this work.

Results for $k_{6.1}$, $k_{6.1a}$ and $k_{6.1b}$ from this work are compared to those from previous studies in the Arrhenius plots shown in Figures 6.12, 6.13 and 6.14 respectively. The values plotted for $k_{6.1b}$ for this work are those obtained from the simultaneous fit to $[BrO]_t$ and $[\Delta O_3]_t$. Comparison of the branching ratio α from this work with previous studies is also shown in Arrhenius form in Figure 6.15.

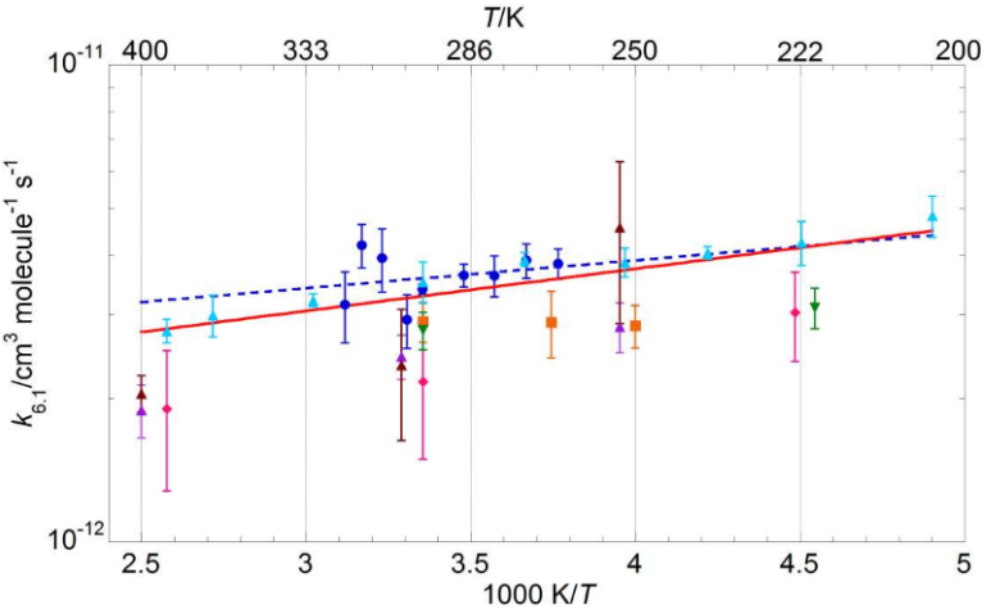

Figure 6.12 : Arrhenius plot for $k_{6.1}$ ($k_{6.1} = k_{6.1a} + k_{6.1b}$): this work (blue circles and blue dashed linear fit), Harwood *et al.* [22] (orange squares), Turnipseed *et al.* [14] using O + Br_2 (brown triangles), Turnipseed *et al.* using Br + O_3 [14] (purple triangles), Sander and Watson [9] (pink diamonds), Mauldin *et al.* [6] (green inverted triangles), Gilles *et al.* [20] (light-blue triangles) along with JPL-NASA recommendation [24] (red line). Errors from Harwood *et al.* are 1σ, as stated by the authors. Errors from this work are 2σ, statistical only.

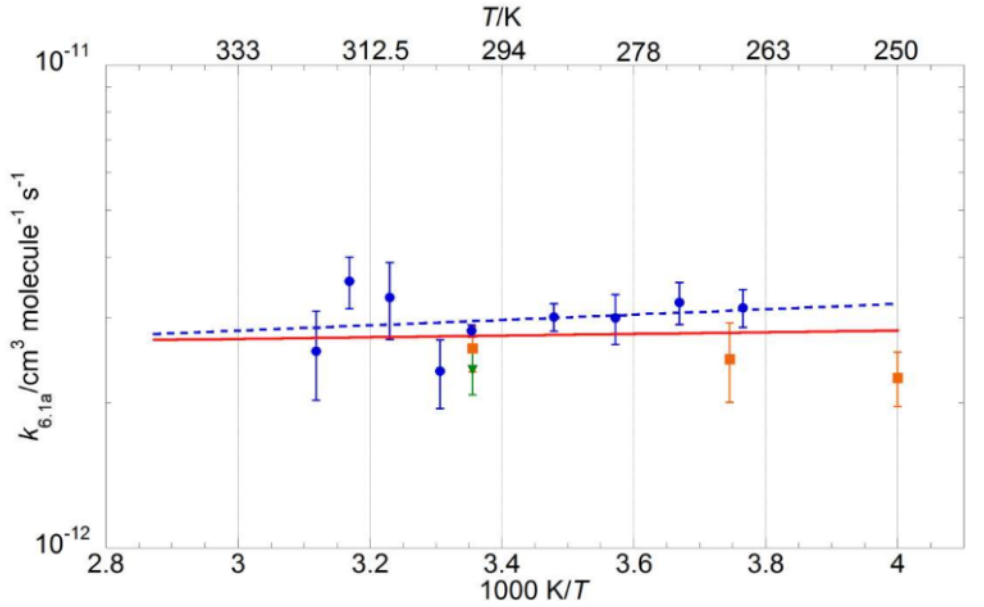

Figure 6.13 : Arrhenius plot for $k_{6.1a}$: this work (blue circles and blue dashed linear fit), Harwood *et al.* [22] (orange squares), Mauldin *et al.* [6] (green inverted triangles) along with JPL-NASA recommendation [24] (red line). Errors from Harwood *et al.* are 1σ, as stated by the authors. Errors from this work are 2σ, statistical only.

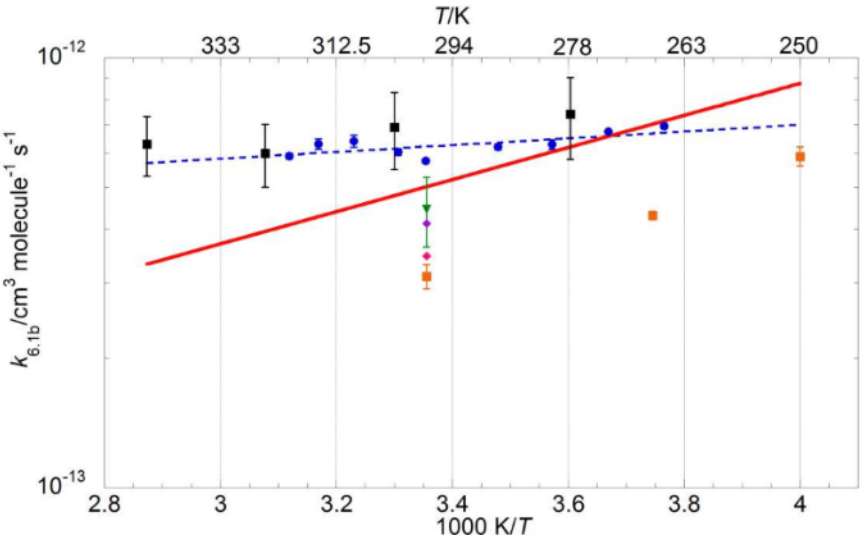

Figure 6.14 : Arrhenius plot for $k_{6.1b}$: this work (blue circles and blue dashed linear fit), Harwood *et al.* [22] (orange squares), Sander and Watson from measurements of second-order BrO decay [9] (pink diamonds), Sander and Watson from measurements of quantum yield of O_3 destruction [9] (purple triangle), Cox *et al.* [13] (black squares), Mauldin *et al.* [6] (green inverted triangles) along with JPL-NASA recommendation [24] (red line). Errors from Harwood *et al*. are 1σ, as stated by the authors. Errors from this work are 2σ, statistical only.

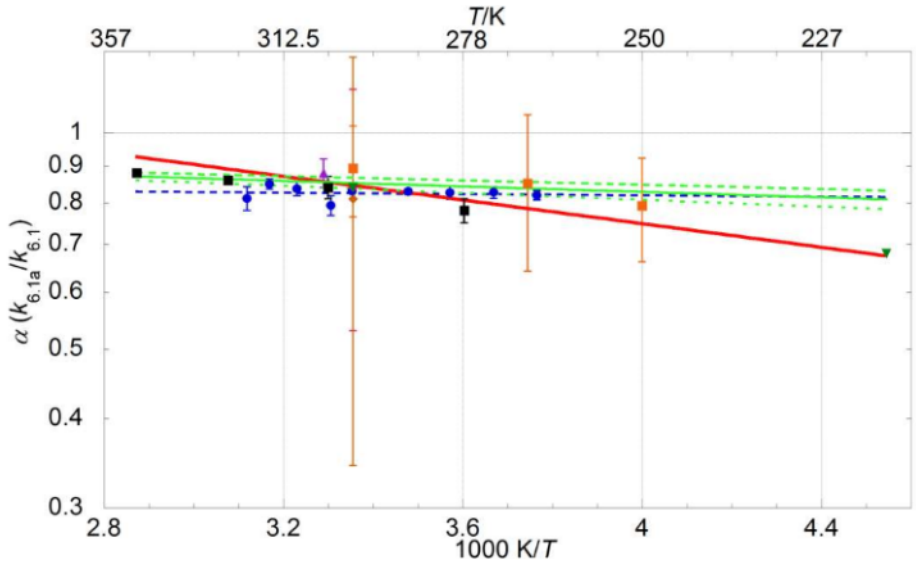

Figure 6.15 : Branching ratio for channel (6.1a) as a function of temperature: this work (blue circles and blue dashed linear fit), Harwood *et al.* [22] (orange squares), Turnipseed *et al.* [14] (purple triangles), Sander and Watson from measurements of second-order BrO decay [9] (pink diamonds), Sander and Watson from measurements of quantum yield of O_3 destruction [9] (purple triangle), Cox *et al.* [13] (black squares), Jaffe and Mainquist [8] (green solid line with upper and lower uncertainty limits in green dashed lines) Mauldin *et al*. (green inverted triangles) along with JPL-NASA recommendation [24] (red line). Errors from this work are 2σ, statistical only.

Early studies of the BrO self-reaction [10, 11, 12] only focused on the overall rate coefficient of the reaction, $k_{6.1} = k_{6.1a} + k_{6.1b}$. These results generally show poor agreement with one another, reflecting the uncertainties that were still surrounding the mechanism and products of the BrO self-reaction at the time. Jaffe and Mainquist [8] were the first to study the branching ratio $\alpha = k_{6.1a}/k_{6.1}$ of the BrO self-reaction by measuring the quantum yield of bromine photosensitised decomposition of ozone over the temperature range T = 258-333 K. These authors showed that channel (6.1a) was the dominating pathway over the experimental temperature range used, with a branching ratio of α = 0.84 ± 0.01 at T = 298 K. Sander and Watson [9] used flash photolysis coupled with UV absorption spectroscopy to measure $k_{6.1}$ at three temperatures (T = 223 K, 298 K and 388 K) and over the pressure range p = 50-475 Torr. A negative temperature dependence was reported for the overall reaction rate constant and no pressure dependence was observed at any of the temperatures used. $k_{6.1b}$ was also measured by Sander and Watson at T = 298 K, thus allowing determination of the branching ratio at room temperature giving α = 0.84 ± 0.3, in excellent agreement with the findings of Jaffe and Mainquist. Cox *et al*. [13] employed modulated photolysis coupled with UV absorption spectroscopy under excess ozone to monitor $k_{6.1b}$ over the range T = 278-338 K. Greater rate constants than those reported by Sander and Watson were determined along with a weaker negative temperature dependence. The temperature dependence of the branching ratio was also obtained by Cox *et al*. from analysis of the bromine sensitised decomposition of ozone and resulted in values of α ranging from 0.78 ± 0.03 at T = 277.5 K to 0.88 ± 0.01 at T = 348 K. Turnipseed *et al*. [14] carried out a study of the BrO self-reaction at low pressure (p = 2 Torr) using discharge flow coupled with mass spectrometry over the range T = 253-400 K, obtaining values of $k_{6.1}$ in good agreement with those of Sander and Watson. The same technique was used by Lançar *et al*. [15] to measure both $k_{6.1}$ and $k_{6.1b}$ at T = 298 K, corroborating the findings of Turnipseed *et al*. Bridier *et al*. [16] utilised flash photolysis coupled with UV absorption spectroscopy to monitor the rate of BrO decay through the self-reaction at T = 298 K. However, the reaction conditions employed in their work (excess ozone) only allowed determination of $k_{6.1b}$, hence they inferred the total rate of reaction $k_{6.1}$ assuming α = 0.84. The value obtained for $k_{6.1}$ from Bridier *et al*. was in good agreement with that reported by Lançar *et al*. but more than 40% higher than that of Sander and Watson, who used the same experimental technique. Mauldin *et al*. [6] measured the rate

coefficients of both channels of the BrO self-reaction using flash photolysis coupled with UV absorption spectroscopy. In the Mauldin *et al*. study, $k_{6.1a}$ and $k_{6.1b}$ were determined at two temperatures, T = 220 K and 298 K, over the pressure range p = 75–600 Torr with a variety of bath gases (He, N_2 and SF_6). The overall rate coefficient $k_{6.1}$ was found to be independent of pressure at T = 298 K but dependent on pressure at T = 220 K. On the other hand, the branching ratio α was found to be independent of pressure at both temperatures and was found to be 0.84 ± 0.01 at T = 298 K and 0.68 ± 0.05 at T = 220 K. Rattigan *et al*. [17] used continuous photolysis of bromine/ozone mixtures with UV absorption spectroscopy, measuring $k_{6.1b}$ over the temperature range T = 293-343 K. Their values are amongst the lowest to date and this is the only study indicating a positive temperature dependence for channel (6.1b). Rowley *et al*. [18] employed flash photolysis with the inclusion, for the first time in a gas kinetics study, of a two-dimensional charge-coupled device (CCD) detector for monitoring both wavelength and time resolved absorptions. The rate constants obtained in their work agree well with the studies of Mauldin *et al*. [6] and of Lançar *et al*. [15] Both Laszlo *et al*. [19] and Bedjanian *et al*. [21] studied the BrO self-reaction at ambient temperature, the first using laser flash photolysis with UV absorption spectroscopy, the second employing discharge flow coupled with mass spectrometry. Their findings are in good agreement with each other and previous work. Gilles *et al*. [20] used laser photolysis coupled with UV absorption spectroscopy to measure the overall rate constant $k_{6.1}$ over the temperature range T = 204-388 K and at pressures p = 6-15 Torr. A negative temperature dependence for $k_{6.1}$ was observed, with higher values of the rate constant than those of Sander and Watson and Turnipseed *et al*. The study by Harwood *et al*. [22] is the most extensive to date, considering the temperature (T = 222-298 K) and pressure (p = 100-760 Torr) ranges over which the BrO self-reaction was characterised. Similarly to the work of Rowley *et al.*, flash photolysis with UV absorption spectroscopy using CCD detection was used to measure the rate constants of both channels. A negative temperature dependence of the rate constants was observed throughout, in agreement with almost all previous work. In addition, the overall rate coefficient $k_{6.1}$ was found to be dependent on pressure at temperatures below T = 250 K. This finding disagrees with those of Sander and Watson, who observed no pressure dependence at T = 223 K but agrees with those of Mauldin *et al*., who reported a pressure-dependent $k_{6.1}$ at T = 220 K.

The overall rate constant of the BrO self-reaction, $k_{6.1}$, from this work is in good agreement with the findings of Gilles *et al.* [20] Unsurprisingly, the current JPL-NASA recommendation [24] (partly based on the work of Gilles *et al.*, as discussed in Section 6.1.1) lies within the error range of the values obtained in this study at most experimental temperatures but does exhibit a stronger temperature dependence which therefore becomes more evident at higher temperatures. However, extrapolation of data from this work to temperatures more relevant to polar regions is in good agreement with the JPL-NASA evaluation.

On the other hand, the values obtained for the rate constant of channel (6.1a), $k_{6.1a}$, in this work show a slightly more pronounced temperature dependence than those reported in the current JPL-NASA evaluation. [24] The parameterisation from the present work suggests larger values of $k_{6.1a}$ at low temperatures: extrapolation of data from the present work to T = 250 K results in $k_{6.1a}$ 13% higher than JPL-NASA and 42% higher than Harwood *et al.* [22] The divergence between the two temperature dependences becomes more manifest at T = 220 K, where extrapolation of data from the present work is approximately 20% higher than the JPL-NASA recommendation. The scatter of the points in the Arrhenius plot for $k_{6.1a}$ arises principally from the lower signal-to-noise ratio of the ozone kinetic traces, compared to those for BrO. However results from this study lie within current JPL-NASA uncertainty limits.

The temperature dependence of $k_{6.1b}$ obtained in this study is in very good agreement with that of Cox *et al.* [13] but it is noticeably weaker than both the JPL-NASA recommendation and previous work from Sander and Watson, [9] Mauldin *et al.* [6] and Harwood *et al.* [22] Over the relatively narrow experimental range used in this work (of about 55 K), values of $k_{6.1b}$ vary by a factor of 1.1 whereas the JPL-NASA recommended values vary, over the same temperature range, by a factor of 1.7. The JPL-NASA recommended value for $k_{6.1b}$ at T = 250 K is 25% greater than the value extrapolated from this work.

Unsurprisingly, as $k_{6.1a}$ measured in this work is greater than the JPL-NASA recommendation at low temperatures and $k_{6.1b}$ shows a much weaker negative

temperature dependence than that evaluated by JPL-NASA, the branching ratio from this work reflects a net dominance of channel (6.1a) over channel (6.1b) not only at ambient temperature, but also at temperatures typical of the Arctic Boundary Layer. The JPL-NASA recommendation is based on data from Cox *et al.* [13] and those of Mauldin *et al.*; [6] the evaluation for α is 0.84 at T = 298 K and 0.68 at T = 220 K. Most studies, including the present one, therefore agree on the partitioning at ambient temperature. However, extrapolation of results from the present work to T = 220 K gives a value of α = 0.81, indicating a significantly less pronounced temperature dependence of the branching ratio and a different partitioning of the products of the BrO self-reaction at temperatures typical, for example, of the Arctic Boundary Layer, as discussed below. However, given the evidence of a termolecular component to the BrO self-reaction at T < 250 K (at the concentrations used in this and other laboratory studies), the assumption of a branching ratio based on a two-channel mechanism may be inappropriate, indicating the need for further studies at low temperatures.

The study from Jaffe and Mainquist [8] reports a parameterisation of the temperature dependence of the ratio $k_{6.1a}/k_{6.1b}$ from the analysis of bromine photosensitised decomposition of ozone in the range T = 258-333 K. Their values of $k_{6.1a}/k_{6.1b}$ are obtained from the quantum yields for ozone decomposition based on the assumption that Br atoms are in steady state. The branching ratio for channel (6.1a) expressed above is related to $k_{6.1a}/k_{6.1b}$ *via*:

$$\alpha = \frac{k_{6.1a}}{k_{6.1}} = \left[1 + \left(\frac{k_{6.1a}}{k_{6.1b}}\right)^{-1}\right]^{-1} \qquad \text{(6.xiii)}$$

Values for α were calculated from $k_{6.1a}/k_{6.1b}$ from Jaffe and Mainquist using equation (6.xiii) and are plotted in Figure 6.15. The branching ratios measured in this work agree well with those obtained from the measurements of Jaffe and Mainquist.

The values of $k_{6.1}$ from this study are higher than those reported by Sander and Watson [9], Turnipseed *et al.* [14] and Harwood *et al.* [22] Data from Sander and Watson were recorded at three temperatures between T = 223 K and T = 388 K, data from Turnipseed

et al. at three temperatures over the range T = 253-400 K, data from Harwood *et al.* at three temperatures in the range T = 250-298 K. Harwood *et al.* also recorded data at two temperatures below T = 250 K. However, since the same authors observed that Arrhenius behaviour is lost below T = 250 K, these two data points have been excluded from the present discussion. The temperature dependence from Sander and Watson only relies on three points, one of which lies below T = 250 K: these authors observed no pressure dependence at T = 223 K, whereas both Mauldin *et al.* and Harwood *et al.* reported pressure-dependent rate constants at very similar temperatures (T = 220 K and T = 222 K respectively). The temperature dependences observed by both Harwood *et al.* [22] and Turnipseed *et al.* [14] also carry noteworthy statistical uncertainty since they rely on three temperature measurements only.

The current study has measured the kinetic parameters of both channels of the BrO self-reaction at nine temperatures and it is similar in extent to the work of Gilles *et al.*, [20] whose values of $k_{6.1}$ are in very good agreement with those reported here. Gilles *et al.* studied the BrO self-reaction at nine temperatures but over a much broader T range (T = 204-388 K) than the present work. The narrower temperature range used in this work (T = 265.5-320.6 K) was dictated by several reasons discussed below. Harwood *et al.* observed pressure-dependent rate constants below 250 K and attributed the deviation from linear Arrhenius behaviour to the termolecular association channel leading to the dimerisation of BrO. To avoid the onset of potential complicating non-bimolecular BrO decay, T = 265.5 K was therefore chosen as the lowest temperature. The upper temperature limit was dictated by physical limitations of the thermostatting unit set-up.

Since the second-order nature of BrO decay gave rate constants which were dependent upon absolute concentrations, and hence absorption, of BrO radicals, discussion of the BrO cross-section employed in previous studies [6, 9, 22] where BrO was monitored using UV absorption spectroscopy is necessary. Both Harwood *et al.* [22] and Mauldin *et al.* [6] used the BrO cross-section measured by Wahner *et al.* [26] Direct comparison of the σ_{BrO} measured by Wahner *et al.* and Wilmouth *et al.*, [7] whose cross-section was used in the present work, is possible as both reported σ_{BrO} at a spectral resolution of 0.40 nm FWHM. Wahner *et al.* reported a value for σ_{BrO} at the (7,0) vibronic peak (λ = 338.5 nm) of 1.55×10^{-17} cm^2 molecule^{-1}, whereas Wilmouth *et al.* measured a very slightly

higher cross-section of 1.58×10^{-17} cm^2 molecule^{-1} for the same spectral band at the same resolution.

Accounting for the different cross-sections in second-order kinetic studies also allows scaling of correct kinetic parameters to equivalent cross-sections. The values of $k_{6.1}$ reported by Harwood *et al*. and by Mauldin *et al*. are respectively *ca.* 14% and 18% lower than $k_{6.1}$ from this work at $T = 298$ K. When scaled up to the cross-section from Wilmouth *et al*., these values are very slightly different, and respectively 13% and 16% lower than $k_{6.1}$ from this work.

Sander and Watson [9] measured the BrO cross-section at the (7, 0) band at all experimental temperatures (T = 223, 298 and 388 K) at a resolution of 0.09 nm (FWHM). Their value of σ_{BrO} at $T = 298$ K is $(1.14 \pm 0.14) \times 10^{-17}$ cm^2 molecule^{-1}, somewhat lower than the ones reported by both Wahner *et al.* [25], $(1.55 \pm 0.13) \times 10^{-17}$ cm^2 molecule^{-1}, and by Wilmouth *et al.* [7], 1.58×10^{-17} cm^2 molecule^{-1}, both reported at a lower resolution (0.4 nm FWHM). This is unexpected since, as the peaks of structured spectra become sharper at higher resolution and the cross-section reported by Sander and Watson might on this basis be expected to exceed those measured by Wahner *et al.* and Wilmouth *et al*. at lower resolutions. Both Wahner *et al*. and Gilles *et al*. argue that Sander and Watson did not actually measure σ_{BrO} at the peak of the (7, 0) band, which is reported at $\lambda = 338.5$ nm: Sander and Watson actually measured the BrO cross-section at $\lambda = 339$ nm, hence potentially missing the peak and recording a noticeably lower BrO cross-section. For comparison purposes, σ_{BrO} at $\lambda = 339$ nm reported by Wilmouth *et al*. (obtained from the reported spectrum) is 1.27×10^{-17} cm^2 molecule^{-1}, in good agreement with Sander and Watson despite the lower resolution (which affects the tails of spectral peaks to a lesser extent than the peak itself). The same comparison holds for the other two temperatures reported by Sander and Watson: at $T = 223$ K, Sander and Watson measured $\sigma_{BrO} = (1.56 \pm 0.14) \times 10^{-17}$ cm^2 molecule^{-1} (*cf*. 1.47×10^{-17} cm^2 molecule^{-1} at $\lambda = 339$ nm, interpolated from Wilmouth *et al*.) and at $T = 388$ K, Sander and Watson measured $\sigma_{BrO} = (0.96 \pm 0.12) \times 10^{-17}$ cm^2 molecule^{-1} (*cf*. 1.02×10^{-17} cm^2 molecule^{-1} at $\lambda = 339$ nm, interpolated from Wilmouth *et al*.), lending confidence to a potential wavelength miscalibration in the Sander and Watson study.

The BrO cross-section determined by Gilles *et al.* [20] at a resolution of 0.5 nm FWHM for the (7,0) band (1.63×10^{-17} cm^2 molecule^{-1}) is in good agreement with that of Wilmouth *et al.* [7] degraded to the lower resolution (1.56×10^{-17} cm^2 molecule^{-1}). At T = 298 K, the value of $k_{6.1}$ reported by Gilles *et al.* is 3.6% higher than the one obtained in this work using the cross-section from Wilmouth *et al.*; after scaling the [BrO] traces recorded at T = 298 K to the cross-section determined by Gilles *et al*, the value of $k_{6.1}$ obtained is within 0.8% of that from Gilles *et al*.

Turnipseed *et al.* [14] measured $k_{6.1}$ using discharge flow coupled with mass spectrometry. Their method therefore did not rely on the determination of the BrO cross-section. Turnipseed *et al*. obtained two values for $k_{6.1}$, one from the O + Br_2 system and one from the Br + O_3 system. These values of $k_{6.1}$ at T = 304 K are respectively *ca.* 31% and 34% lower than interpolation from the results of the present study to the same temperature. The reason for this discrepancy remains uncertain.

6.5 Atmospheric Implications

Despite being of relatively minor significance in the stratosphere due to low BrO mixing ratios (typically of a few pptv), the BrO self-reaction is very important in the troposphere, especially in the Arctic Marine Boundary Layer during springtime, when BrO concentrations are relatively high (as much as 30 pptv). This work has measured a significantly weaker temperature dependence of the partitioning of channels (6.1a) and (6.1b) than the current JPL-NASA [24] recommendation. Our findings imply that channel (6.1a), which directly depletes ozone, dominates the branching of reaction (6.1) at temperatures typical of the Arctic Boundary Layer to a greater extent than currently thought. Therefore the partitioning between active (Br) and inactive bromine (Br_2) could be shifted towards the former, leading to a potential increased ozone-depleting efficiency of the BrO catalytic cycle.

6.6 Conclusions

The BrO self-reaction has been characterised as a function of temperature in the regime relevant to the lower troposphere. Arrhenius expressions for both channels of the BrO self-reaction and for the overall reaction (6.1) were derived. The temperature dependence of the extrapolated overall rate of reaction (6.1) is in good agreement with the current JPL-NASA recommendation; [24] they agree within 6% at T = 250 K. However, the branching of the BrO self-reaction towards Br atoms determined in this work shows a weaker temperature dependence than previously reported with consequent potential implications for the ozone-depleting efficiency of the BrO self-reaction in regions such as the Polar Boundary Layer.

6.7 References

1. WMO (World Meteorological Organization), *Scientific Assessment of Ozone Depletion: 2010, Global Ozone Research and Monitoring Project*, Report No. 52, **2011**, Geneva, Switzerland
2. M. Hausmann, U. Platt *J. Geophys. Res.: Atm.*, **1994**, 99, 25399
3. U. Platt, G. Hönninger *Chemosphere*, **2003**, 52, 325
4. M. Tuckermann, R. Ackermann, C. Gölz, H. Lorenzen-Schmidt, T. Senne, J. Stutz, B. Trost, W. Unold, U. Platt, *Tellus*, **1997**, 49B, 533
5. Y. Bedjanian, G. Poulet, *Chem. Rev.* **2003**, 103, 4639
6. R. L. Mauldin III, A. Wahner, A. R. Ravishankara, *J. Phys. Chem.*, **1993**, 97, 7585
7. D.M. Wilmouth, T.F. Hanisco, N.M. Donahue, J.G. Anderson, *J. Phys. Chem. A*, **1999**, 103, 8935
8. S. Jaffe, W.K. Mainquist, *J. Phys. Chem.*, **1980**, 84, 3277
9. S.P. Sander, R.T. Watson, *J. Phys. Chem.*, **1981**, 85, 4000
10. M.A.A. Clyne, H.W. Cruse, *Trans. Faraday. Soc.*, **1970**, 66, 2214
11. N. Basco, S.K. Dogra, *Proc. Soc. London, Ser. A*, **1971**, 323, 417
12. M.A.A. Clyne, R.T.J Watson, *Chem. Phys. Faraday Trans.*, **1975**, 71, 336
13. R.A. Cox, D.W. Sheppard, M.P. Stevens, *J. Photochem.*, **1982**, 19,189
14. A.A. Turnipseed, J.W. Birks, J.G. Calvert, *J. Phys. Chem.*, **1991**, 95, 4356

15. I.T. Lançar, G. Laverdet, G. LeBras, G. Poulet, *Int. J. Chem. Kinet.*, **1991**, 23, 37
16. I. Bridier, B. Veyret, R. Lesclaux, *Chem. Phys. Lett.*, **1993**, 201, 563
17. O.V. Rattigan, R.A. Cox, R.L. Jones, *Chem. Phys. Lett.*, **1994**, 230, 121
18. D.M. Rowley, M.H. Harwood, R.A. Freshwater, R.L. Jones, *J. Phys. Chem.*, **1996**, 100, 3020
19. B. Laszlo, R.E. Huie, M.J. Kurylo, *J. Geophys. Chem.*, **1997**, 102, 1523
20. M.K. Gilles, A.A. Turnipseed, J.B. Burkholder, A.R. Ravishankara, S. Solomon, *J. Phys. Chem. A*, **1997**, 101, 5526
21. Y. Bedjanian, G. LeBras, G. Poulet, *J. Phys. Chem.*, **1998**, 102, 10501
22. M.H. Harwood, D.M. Rowley, R.A. Cox, R.L. Jones, *J. Phys. Chem. A*, **1998**, 102, 1790
23. R. Atkinson, D.L. Baulch, R.A. Cox, J.N. Crowley, R.F. Hampson, R.G. Hynes, M.E. Jenkin, M.J. Rossi, J. Troe, Evaluated kinetic and photochemical data for atmospheric chemistry: Volume III – gas phase reactions of inorganic halogens, *Atmos. Chem. Phys.*, **2007**, 7, 981
24. S.P. Sander, J. Abbatt, J.R. Barker, J.B. Burkholder, R.R. Friedl, D.M. Golden, R.E. Huie, C.E. Kolb, M.J. Kurylo, G.K. Moortgat, V.L. Orkin, P.H. Wine, *Chemical Kinetics and Photochemical Data for Use in Atmospheric Studies*, Evaluation No. 17, **2011**, JPL Publication 10-6, Jet Propulsion Laboratory, Pasadena, United States
25. A.R. Curtis, W.P. Sweetenhan, FACSIMILE, **1987**, AERE Harwell Publication, Oxford
26. D.L. Baulch, J. Duxbury, S.J. Grant, D.C. Montague, *J. Phys. Chem. Ref. Data*, **1981**, 10
27. O.V. Rattigan, R.A. Cox, R.L. Jones, *J. Chem. Soc. Faraday Trans.*, **1995**, 91, 4189
28. J. Brion, A. Chakir, D. Daumont, J. Malicet, C. Parisse, *Chem. Phys. Lett.*, **1993**, 213, 610

Chapter 7
Kinetic Studies of the BrO + ClO Cross-Reaction

7.1 Introduction

The BrO + ClO cross-reaction couples the chemistry of (principally) stratospheric bromine and chlorine [1] and initiates a catalytic ozone-destroying cycle responsible for up to ~50% of the observed ozone depletion in the Antarctic vortex during polar springtime. [2, 3] The BrO + ClO reaction consists of three known channels:

$$BrO + ClO \rightarrow BrCl + O_2 \quad (7.1a)$$

$$\rightarrow ClOO + Br \quad (7.1b)$$

$$\rightarrow OClO + Br \quad (7.1c)$$

The chlorine peroxy radical produced by channel (7.1b) rapidly undergoes thermal dissociation so that channel (7.1b) effectively regenerates atomic halogens, Cl and Br, both of which react with ozone:

$$Cl + O_3 \rightarrow ClO + O_2 \quad (7.2)$$

$$Br + O_3 \rightarrow BrO + O_2 \quad (7.3)$$

In sunlight, channel (7.1a) also leads to ozone loss upon photolysis of BrCl; on the other hand, photolysis of OClO produced by channel (7.1c) into O + ClO leads to a null cycle as ozone is regenerated upon termolecular recombination of the O atom with O_2. At nighttime, measured OClO abundances are often used as a marker for BrO, since the BrO + ClO cross-reaction is the primary source of stratospheric OClO. In the absence of sunlight, OClO concentrations depend crucially on the branching of reaction (7.1): as channel (7.1a) sequestrates BrO into its nighttime reservoir form BrCl, OClO production is terminated once all BrO is locked into BrCl. [4, 5]

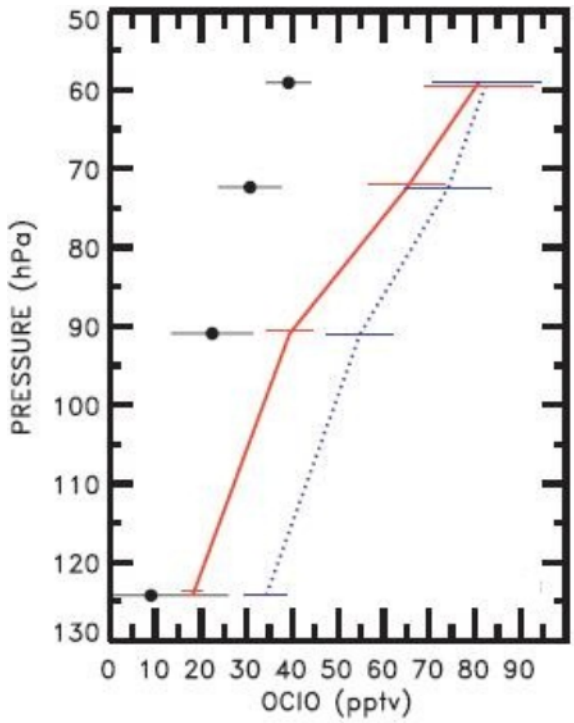

Figure 7.1 : Modelled OClO abundances using the recommended kinetic parameters for the BrO + ClO cross-reaction (photochemical steady state model shown as the blue dotted curve and isentropic trajectory model shown as the red solid curve) taken from the work of Canty *et al.* [5] Also plotted is the OClO concentration (black data points) measured above Kiruna (Northern Sweden) on 23rd Jan 2000 using lunar occultation and a balloon-borne UV spectrometer. Taken from reference 5.

Recent studies have highlighted the considerable uncertainties still affecting the product partitioning of reaction (7.1). Analysis of nighttime OClO measurements by Canty and co-workers [5] showed that atmospheric models based on the kinetic parameters currently reported by JPL-NASA [6] overestimate measured OClO abundances, as illustrated in Figure 7.1. To account for the observed discrepancy, Canty *et al.* questioned the current channel partitioning recommended for reaction 7.1 and suggested a higher value for the branching ratio of channel (7.1a) and a corresponding smaller one for that of channel (7.1c) than current recommendations at temperatures typical of Polar vortices. Moreover, simulations by Kawa *et al.* [7] showed that uncertainties in the branching of the BrO + ClO cross-reaction have a profound impact on the modelling of stratospheric ozone depletion, second only to the uncertainties in the photolysis rate of the ClO dimer, thus calling for a better definition of the product partitioning, as well as the kinetics, of the BrO + ClO cross-reaction at low temperatures.

7.1.1 Previous Studies

The BrO + ClO cross-reaction has been the object of several studies [8, 9, 10, 11, 12, 13, 14, 15] over a wide range of temperatures spanning from T = 220 K [12, 13] up to T = 408 K [11]. Early studies came to conflicting conclusions due to uncertainties on the very nature of

the reaction mechanism and channels: a flash photolysis study by Basco and Dogra [8] concluded that BrCl was the only product of reaction (7.1), whereas Clyne and Watson [9] found no evidence for channel (7.1a) and identified channel (7.1b) and (7.1c) as the product channels with equal partitioning using discharge flow with mass spectrometry. Toohey and Anderson [10] were the first to fully elucidate the full mechanism of the BrO + ClO cross-reaction by identifying the three product channels (7.1a-7.1c) at T = 298 K using a discharge flow system coupled with mass spectrometry. They also found that BrCl was potentially produced from BrO + ClO in a vibrationally excited state. The study of Hills *et al*. [11] represented the first attempt to characterise the temperature dependence of reaction (7.1) and that of its product branching. By means of discharge flow/mass spectrometry, these authors found a zero temperature dependence of the kinetics over the range T = 241-408 K and reported the lowest values to date for the overall rate constant of reaction (7.1), $k_{7.1}$.

Friedl and Sander studied reaction (7.1) employing two different techniques over the same temperature range, T = 220-400 K. The results from their discharge flow/mass spectrometry study [12] and their flash photolysis/UV absorption spectroscopy study [13] are in excellent agreement with one another, reporting a value of $k_{7.1}$ at T = 298 K approximately 60% greater than that reported by Hills *et al*. Moreover, Friedl and Sander observed a marked negative temperature dependence for the rate constants of all channels of the BrO + ClO cross-reaction, with the overall rate constant $k_{7.1}$ increasing by about 70% over the temperature range studied. The temperature dependence of the branching ratios showed that channel (7.1a) was a minor pathway with $\alpha = k_{7.1a}/k_{7.1}$ = 0.08 at T = 400 K and α = 0.06 at T = 220 K. Both studies of Friedl and Sander reported channel (7.1c) to be the dominant channel at T = 220 K.

Poulet *et al*. [14] studied the kinetics and products of the BrO + ClO cross-reaction at T = 298 K by means of discharge flow/mass spectrometry. These authors reported a value of $k_{7.1}$ in good agreement with that measured in both studies by Friedl and Sander. To this date, Poulet *et al*. are the only authors to have directly measured the BrCl yield of reaction (7.1), reporting a branching ratio of α = 0.12, higher than that measured by Friedl and Sander.

Turnipseed *et al*. [15] measured $k_{7.1}$ and the branching ratios of channels (7.1a) and (7.1c) over the range T = 234-406 K using discharge flow/mass spectrometry. Their results are in overall good agreement with both studies by Friedl and Sander, showing a negative temperature dependence of all reaction channels. However, Turnipseed *et al*. measured a slightly stronger (negative) temperature dependence of the overall reaction rate constant than that reported in the studies of Friedl and Sander. Turnipseed *et al*.

Reference	technique [a]	T/K	p/Torr	$k_{7.1}$ / 10^{-11} cm^3 molecule^{-1} s^{-1}	$\alpha = k_{7.1a}/k_{7.1}$	$\beta = k_{7.1b}/k_{7.1}$	$\gamma = k_{7.1c}/k_{7.1}$
Basco and Dogra[8]	FP/UV	298	760	0.25	1[b]		
Clyne and Watson [9]	DF/MS	298	0.75	1.34 ± 0.2	0	0.5 ± 0.18	0.5 ± 0.18
Toohey and Anderson[10]	DF/RS/ LMR	298	1-2	1.4 ± 0.2			0.45
Hills *et al*.[11]	DF/MS	241-408		0.82 ± 0.1	< 0.02	0.45 ± 0.1	0.55 ± 0.1
Friedl and Sander[12]	DF/MS	220−400	1	1.29 ± 0.2	0.08 ± 0.03		0.48 ± 0.07
Sander and Friedl[13]	FP/UV	220−400	50−700	1.29 ± 0.16			0.59 ± 0.1
Poulet *et al*.[14]	DF/MS	298	0.6-1	1.13 ± 0.15	0.12 ± 0.05		0.43 ± 0.10
Turnipseed *et al*.[15]	DF/MS	234-406	2	1.08 ± 0.2[c]	0.09 ± 0.02[c]		0.48 ± 0.07[c]
IUPAC[16]				1.4	0.07	0.44	0.49
JPL-NASA[6]				1.26	0.08	0.44	0.48
This work	LP/UV	246-314	760	1.86 ± 0.11			0.59 ± 0.06

Notes:

[a]: FP/UV = flash photolysis/ UV absorption spectroscopy; DF/UV = discharge flow/UV absorption spectroscopy; DF/RF/LMR = discharge flow/resonance fluorescence/laser magnetic resonance; LP/UV = laser photolysis/ UV absorption spectroscopy

[b]: assumed

[c]: at T = 304 K

Table 7.1 : Summary of previous studies on the kinetics of the BrO + ClO cross-reaction. All rate constants and branching ratios reported are at T = 298 K except where noted.

also reported a value of the branching ratio for channel (7.1a) at low temperatures (α = 0.10) higher than that at ambient temperature (α = 0.09), contrary to the trend observed by Friedl and Sander.

Results from previous studies of the BrO + ClO reaction are summarised in Table 7.1. Current IUPAC [16] and JPL-NASA [6] recommendations are based on the discharge flow mass spectrometry studies of Friedl and Sander and of Turnipseed *et al*.

7.2 Experimental

The aims of this study were to characterise the kinetics and branching of the BrO + ClO cross-reaction as a function of temperature using laser flash photolysis of suitable gas mixtures coupled with broadband time-resolved UV absorption spectroscopy. The unique properties of charge-coupled device (CCD) detection allowed real-time monitoring of the two reagent radicals, BrO and ClO, and one of the products, OClO, thus enabling an accurate characterisation of the total rate constant, $k_{7.1}$, and of the branching for channel (7.1c), $\gamma = k_{7.1c}/ k_{7.1}$.

7.2.1 Radical Formation

Laser photolysis of $Cl_2/Cl_2O/Br_2/O_3/O_2/N_2$ precursor mixtures was used to initiate reactions resulting in the formation of BrO and ClO radicals. Atomic halogens were the principal product of the photolysis of the precursor gases at the laser wavelength, λ = 351 nm:

$$Cl_2 + h\nu \rightarrow 2Cl \qquad (7.4)$$

$$Br_2 + h\nu \rightarrow 2Br \qquad (7.5)$$

As discussed in Chapters 4 and 5, the photolysis of Cl_2O into Cl + ClO represented a minor photolysis pathway given the relatively small absorption cross-section of Cl_2O at λ = 351 nm compared to that of Cl_2 (σ_{Cl_2} and σ_{Br_2} are respectively ~ 25 and ~6 times

greater than σ_{Cl_2O} at the laser wavelength [6]). Under the experimental conditions used in this work of excess Br_2 over Cl_2O and O_3, chlorine atoms were rapidly and effectively converted into bromine atoms *via* reaction (7.6):

$$Cl + Br_2 \rightarrow BrCl + Br \qquad (7.6)$$

Hence the main sources of BrO and ClO radicals were the reactions of Br atoms with the Cl_2O and O_3 precursors respectively:

$$Br + Cl_2O \rightarrow ClO + BrCl \qquad (7.7)$$

$$Br + O_3 \rightarrow BrO + O_2 \qquad (7.3)$$

The chlorine counterparts of reactions (7.7) and (7.3)

$$Cl + Cl_2O \rightarrow ClO + Cl_2 \qquad (7.8)$$

$$Cl + O_3 \rightarrow ClO + O_2 \qquad (7.2)$$

were found to be minor pathways, as competing reaction (7.6) rapidly consumed the atomic chlorine available ($k_{7.6}$ = 3.6 ×10^{-10} cm^3 molecule^{-1} s^{-1} [17] *cf.* $k_{7.8}$ = 9.6 ×10^{-11} cm^3 molecule^{-1} s^{-1} [6] and $k_{7.2}$ = 1.2 ×10^{-11} cm^3 molecule^{-1} s^{-1} [6] at T = 298 K).

As a result of the complex nature of the radical formation chemistry, the initial concentrations of ClO and BrO, $[ClO]_0$ and $[BrO]_0$, depended crucially on the relative concentrations of the precursor species. Extensive numerical modelling was undertaken using FACSIMILE (see Section 7.2.4) to design the experimental conditions and to ensure that the flux of radicals through the complex network of reactions was understood and optimised for the investigation of the BrO + ClO kinetics. $[Br_2]$ and $[Cl_2]$ were kept at a typical value of (1-2) × 10^{16} molecule cm^{-3} to ensure formation of sufficient atomic halogens following photolysis; on the other hand, as Cl_2O and O_3 are both strong absorbers at λ < 280 nm, values of $[Cl_2O]$ and $[O_3]$ greater than ~5 × 10^{15} molecule cm^{-3} resulted in poor signal at those wavelengths and had to be limited, as

discussed in the following section. Under typical conditions, the $[Cl_2O]/[O_3]$ ratio in the precursor mixture became critical in determining the relative magnitude of $[ClO]_0$ and $[BrO]_0$. Further numerical integration modelling showed that, by increasing the $[Cl_2O]/[O_3]$ ratio, reaction (7.7) was favoured over reaction (7.3), leading to initial BrO concentrations below the detection limit. On the other hand, by making $[Cl_2O]/[O_3]$ too small, BrO production *via* reaction (7.3) dominated over reaction (7.7), thus inhibiting ClO formation. This was confirmed by a series of exploratory experiments performed under constant $[O_3]$ (~2.5×10^{15} molecule cm^{-3}) but at different $[Cl_2O]$ in order to vary the $[Cl_2O]/[O_3]$ ratio. Spectra from these experiments are shown in Figure 7.2 and illustrate the formation of excess BrO over ClO at low (< 0.7) $[Cl_2O]/[O_3]$ ratios, whereas the signal of ClO dominates at high (> 4) $[Cl_2O]/[O_3]$ ratios.

In the current study, given that a number of reactions ((7.6) followed by (7.7), (7.8) and

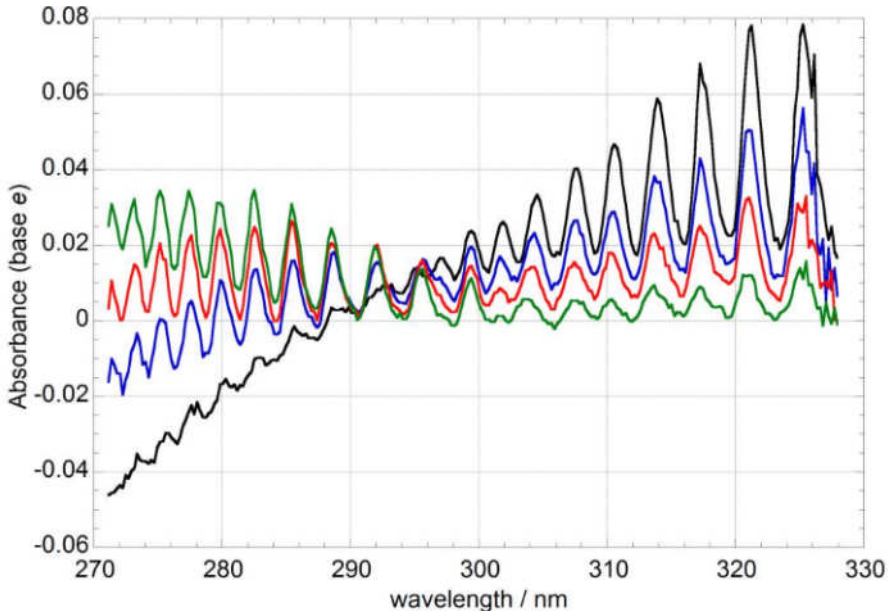

Figure 7.2 : Spectra recorded in the immediate post-photolysis of $Cl_2/Cl_2O/Br_2/O_3/O_2/N_2$ mixtures (averaged over t = 0.4-1.3 ms after photolysis) at different $[Cl_2O]/[O_3]$ ratios: $[Cl_2O]/[O_3]$ = 3.8 (in black), $[Cl_2O]/[O_3]$ = 2.1 (in blue), $[Cl_2O]/[O_3]$ = 1.2 (in red) and $[Cl_2O]/[O_3]$ = 0.7 (in green). The BrO signal (peaks at λ > 300 nm) decreases as the $[Cl_2O]/[O_3]$ ratio is increased. Conversely, the ClO signal (peaks at λ < 300 nm) becomes more intense as the $[Cl_2O]/[O_3]$ ratio increases. The negative contribution to the total spectrum observed at lower wavelengths originates from ozone removal *via* reaction (7.3) and becomes weaker as the $[Cl_2O]/[O_3]$ ratio is increased, as expected from reaction (7.7) dominating over reaction (7.3).

(7.2)) led to the regeneration of ClO radicals from atomic products, it was considered prudent to maintain conditions of excess ClO over BrO. In this case the observed [BrO] decay would exhibit pseudo-first order kinetics, as described in Section 7.2.4. However, to still obtain an appreciable (and therefore detectable) amount of BrO radicals, $[Cl_2O]/[O_3]$ ratios in the range of 1.5-2 were employed. This gave rise typically to $[ClO]_0 = 1 \times 10^{14}$ molecule cm^{-3} and $[BrO]_0 = 3 \times 10^{13}$ molecule cm^{-3}.

All precursor gases were delivered *via* Teflon tubing to a Pyrex mixing line where they mixed with the nitrogen (BOC, >99.98%) carrier flow. The flow rates of nitrogen and oxygen (>99.99%, BOC) were set using mass flow controllers (MKS), whereas that of Cl_2 (BOC, supplied as 5% by volume in N_2; purity >99%) was controlled using needle valves and measured using a calibrated glass ball meter. Cl_2O was produced *in situ* using the method originally described by Hinshelwood and Pritchard [18], consisting of passing a known flow of the diluted Cl_2 gas through a trap containing solid dried yellow mercuric (II) oxide (HgO, Sigma-Aldrich, >99%). This method is described in detail in Section 4.2.1. Bromine vapour was introduced into the gas mixture by passing a small flow of nitrogen through a bubbler containing liquid Br_2 (Acros, 99.8%) kept at $T = 0$ °C inside a Dewar flask. The bromine content in the precursor mixture was quantified spectroscopically by fitting Br_2 absorption cross-sections from JPL-NASA [6] to the absorbance recorded in static (*i.e.*, in the absence of photolysis) experiments over the range $\lambda = 450$-580 nm. Calculations using flow rates and the vapour pressure of liquid bromine at $T = 0$ °C were in good agreement with the bromine abundances determined in the gas mixtures spectroscopically. Ozone was generated by flowing oxygen gas through, in this case, a cell incorporating a mercury "pen-ray" lamp. Production of O_3 using this method was calibrated as a function of oxygen flow through the cell and ozone abundances were quantified *via* UV spectroscopy, as described in Appendix 1.

Typical concentrations of precursor gases in the pre-photolysis mixture were as follows: $[Cl_2] = 1$-1.6×10^{16} molecule cm^{-3}; $[Cl_2O] = 4.5$-5×10^{15} molecule cm^{-3}; $[Br_2] = 1.5$-2.0×10^{16} molecule cm^{-3}; $[O_3] = 2$-2.5×10^{15} molecule cm^{-3}; $[O_2] = 1 \times 10^{18}$ molecule cm^{-3}; $[N_2]$ = balance to 1 atm. Static (non photolysed) spectra of the precursor gas mixture also revealed the presence of a small OClO impurity, typically corresponding to $[OClO] = 5$-10×10^{13} molecule cm^{-3}, as shown in Figure 7.3.

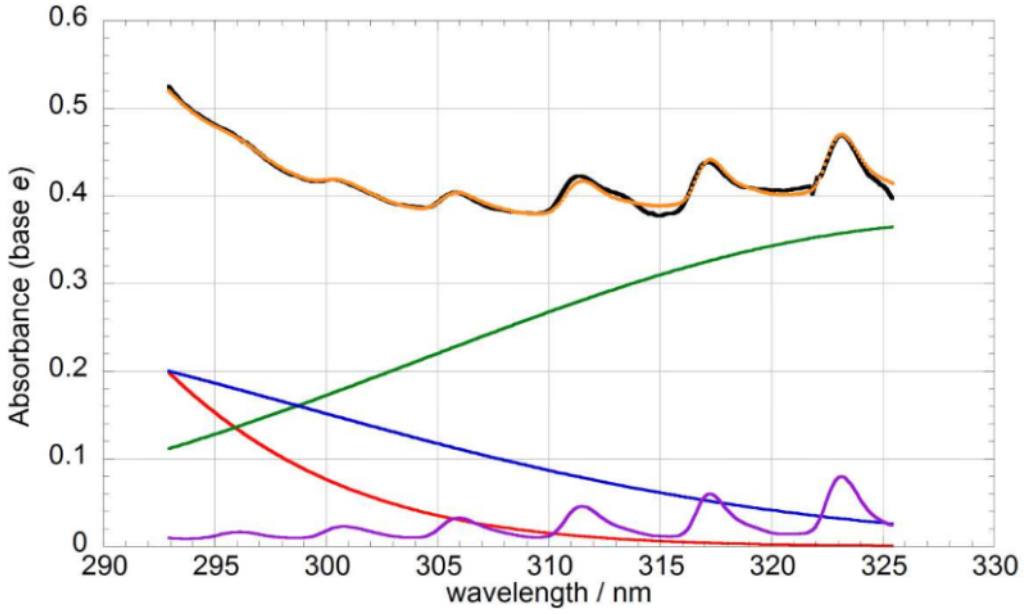

Figure 7.3 : Absorbance spectrum of the precursor $Cl_2/Cl_2O/Br_2/O_3/O_2/N_2$ mixture (in black) exhibiting the presence of structured features attributed to OClO at longer wavelengths. The contributions of ozone (in red), Cl_2O (in blue), Cl_2 (in green) and OClO (in purple) to the total calculated absorbance (orange points), as determined by least-squares fitting, are also shown.

As such impurities typically arise from the presence of water vapour in vessels containing chlorine gas, the trap containing mercuric oxide was cleaned and dried for 48 hours, then re-assembled with fresh HgO. However, despite this, the characteristic peaks resulting from the OClO spectrum were still observed at $\lambda > 310$ nm. As no reaction between the species in the precursor mixture is known to generate OClO, it was suspected that water vapour back-diffusing into the system was the cause of the impurity. To address this, a dry nitrogen flow was left running for 12-24 hours prior to experiments but the OClO signal was still observed. It was also thought that the presence of the Huggins bands of the ozone spectrum might have given rise to the peaks observed experimentally; however it was found that the shape of the recorded peaks bore scant resemblance to those of the Huggins bands. Furthermore, the difference in precursor $[O_3]$ obtained from fitting an ozone cross-section accounting for the presence of the Huggins bands (taken from Brion *et al.* [19]) instead of one devoid of structured features (*e.g.* from JPL-NASA [6]) to static spectra such as the one shown in Figure 7.3, was negligible (< 3%). Following further experiments, it was observed that the peaks attributed to OClO in the precursor mixture disappeared once the ozone flow had been switched off. This suggested a correlation between ozone and the observed OClO

impurity. A similar unexpected and unexplained OClO signal was observed in the discharge flow/mass spectrometry study of the BrO + ClO cross-reaction by Friedl and Sander. [12] These authors reported a large background signal for OClO at m/z =67 for a reactive mixture including Cl_2O and ozone and attributed it to an as then unidentified chemical process. To this day, no reaction of ozone with either Cl_2 or Cl_2O yielding OClO has been reported.

The presence of OClO in the precursor mixture did not however constitute a significant hindrance *per se* to the experiments and was in any case taken into account in the analysis of the results. The photolysis of the OClO impurity also contributed to the formation of the desired radicals:

$$OClO + h\nu \rightarrow O + ClO \qquad (7.9)$$

As well as directly producing the ClO radical, photolysis of OClO also generated O atoms whose fate was mainly to react with the excess Br_2 and Cl_2O precursor gases to produce BrO and ClO respectively:

$$O + Br_2 \rightarrow BrO + Br \qquad (7.10)$$

$$O + Cl_2O \rightarrow ClO + ClO \qquad (7.11)$$

From rate calculations using $k_{7.10}$ reported by Harwood *et al.* [20] and $k_{7.11}$ from JPL-NASA [6] along with the precursor concentrations used in the current work, it was calculated that approximately 92% of O atoms generated by the photolysis of OClO would be expected to react through reaction (7.10) with the remaining 8% reacting through reaction (7.11) at T = 298 K.

7.2.2 Radical Monitoring

Species in the reaction mixture were monitored by means of UV absorption spectroscopy with charge-coupled device (CCD) detection. A 300 grooves mm^{-1} diffraction grating was employed and the width of the entrance slit was set to 75 μm,

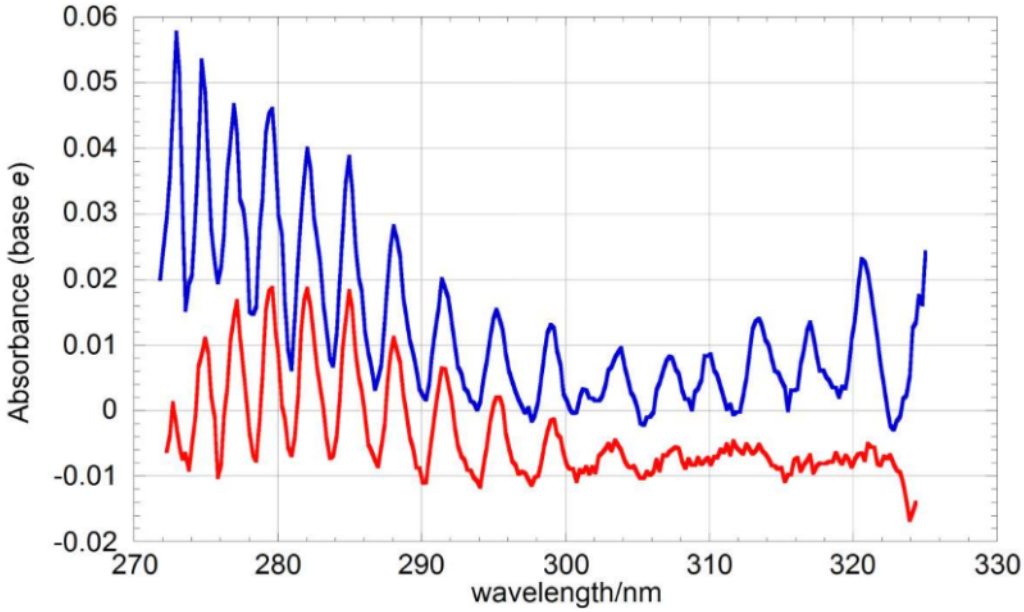

Figure 7.4 : Temporally averaged spectra recorded in the immediate (t = 150-350 μs after photolysis, in blue) and late (t = 2.4-2.6 ms after photolysis, in red) post-photolysis.

resulting in a spectral resolution of 1.1 nm (FWHM). Typically the spectral range λ = 270-325 nm was monitored in the photolysis experiments carried out in the current work.

The temporal resolution of the experiment was dictated by the time elapsed between each charge transfer event (*shift time*), which was set to 5 μs in the current work.

Absorbance spectra of the reactive mixture were obtained using Beer's law, as discussed in Chapter 3; these spectra represented the changes in absorbance of the reactive mixture brought about by photolysis. Figure 7.4 illustrates two examples of temporally averaged spectra recorded at different times following photolysis: the spectrum shown in blue was recorded immediately following photolysis (t = 150-350 μs after photolysis) and is dominated by the vibronic features of ClO (λ = 270-310 nm) and BrO (λ = 310-325 nm) radicals produced upon photolysis as described in Section 7.2.1. The spectrum shown in red, recorded at longer timescales after photolysis (t = 2.4-2.6 ms after photolysis), also shows strong ClO structure at the short wavelength end of the spectrum but, by contrast, is devoid of BrO vibronic peaks. This was a consequence of the experimental set-up employed in this work: precursor concentrations were designed to generate excess ClO over BrO and also to minimise BrO regeneration from the

atomic halogens produced by channels (7.1b) and (7.1c), by favouring reaction (7.7) over reaction (7.3). As a result, when all BrO had reacted away, ClO was still present in the reaction mixture. The characteristic peaks of the OClO spectrum were expected to be visible in the spectral region at $\lambda < 310$ nm at long timescales after photolysis, as OClO is one of the products of reaction (7.1). However, these features do not appear so obvious in the spectrum shown in Figure 7.4 due to the presence of the OClO impurity in the precursor mixture. Photolysis of said impurity gave rise to a negative OClO signal in the immediate post-photolysis and, following OClO production *via* channel (7.1c), the concentration of OClO returns to approximately pre-photolysis values, hence leaving no significant spectral signature at longer timescales. This implied that a negative OClO absorbance is underlying all the sequential spectra recorded directly after photolysis. This could be easily verified: stripping a (differential) spectrum recorded in the immediate post-photolysis from the contributions of ClO and BrO (quantified by differential fitting routines described in the following section) reveals the presence of a negative OClO signal, as shown in Figure 7.5.

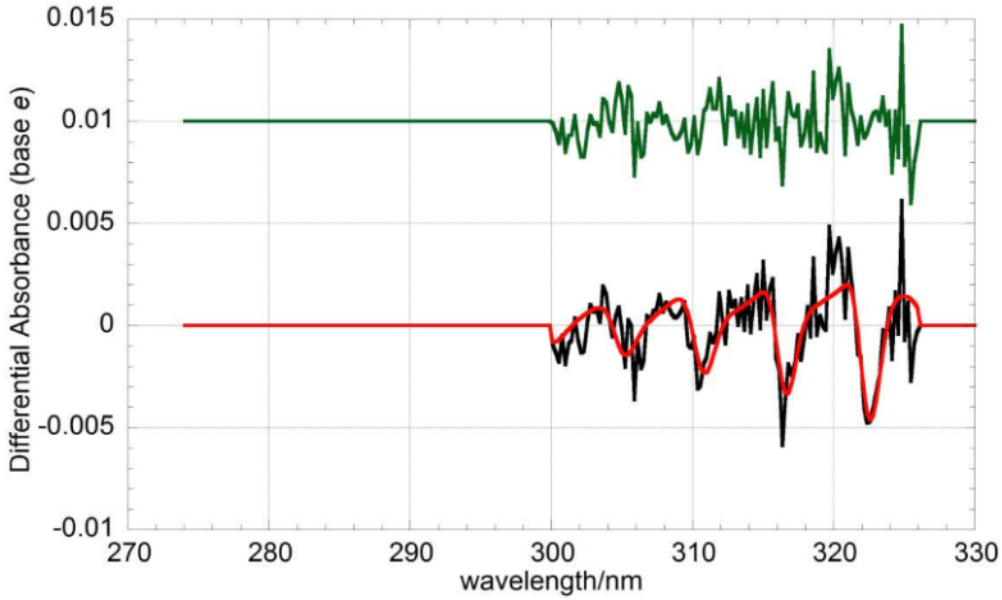

Figure 7.5 : Residual differential absorbance (black), averaged over t = 110-190 μs in the immediate post-photolysis, following subtraction of the contributions of BrO and ClO to the total differential absorbance. Fitting an appropriately scaled OClO differential cross-section (red) to the residual spectrum reveals the presence of negative OClO absorbance arising from the photolysis of the OClO impurity present in the precursor mixture. Residuals from this fit (green) were offset by +0.01 absorbance units for clarity.

7.2.3 Determination of species concentrations

The concentrations of ClO, BrO and OClO were obtained by differentially fitting the cross-sections of these species to the recorded absorbance spectra *via* the Beer-Lambert Law, as described in Chapter 3. This procedure required accurate knowledge of the absorption cross-sections of the species of interest.

The ClO cross-section used was that derived for the work on the ClO + ClO bimolecular channels presented in Chapter 5 at the same spectral resolution (1.1 nm FWHM). These cross-sections were obtained by degrading the high resolution (0.8 nm FWHM) ClO differential cross-section, $\sigma_{\text{ClO diff}}$, at the (12, 0) peak (λ = 275.2 nm), measured in the study of ClO dimerisation [21] presented in Chapter 4, to the lower resolution (1.1 nm FWHM) used in the present study. The procedure employed has been described previously in Chapter 5 and in the literature. [22] ClO cross-sections at a resolution of 1.1 nm (FWHM) were obtained at eight temperatures over the range T = 283-324 K. In the current study of the BrO + ClO cross-section, low-resolution ClO cross-section were extrapolated to the experimental temperature for T < 283 K.

The cross-sections of BrO and OClO were taken from previous work of Wilmouth *et al*. [23] and of Wahner *et al*. [24] respectively. The high-resolution (0.4 nm and 0.25 nm FWHM respectively) cross-sections reported in those studies were degraded to match the lower resolution employed in present study (1.1 nm FWHM) by applying Gaussian averaging kernels (specifically, a 93-point kernel for σ_{BrO} and a 29-point kernel for σ_{OClO}), a procedure extensively described in Appendix 3. In addition, to account for the temperature dependence of vibronic absorption bands, the reference cross-sections were interpolated to each experimental temperature using the spectra recorded at T = 228 K and T = 298 K for σ_{BrO} and at T = 204 K and T = 296 K for σ_{OClO}. This procedure assumed a linear temperature dependence of the cross-sections of halogen oxides, the validity of which is confirmed by previous studies. [25]

The absence of any residual structure at each temperature following spectral fitting and subtraction (as shown in Figures 7.5 and 7.6) added confidence to spectral smoothing

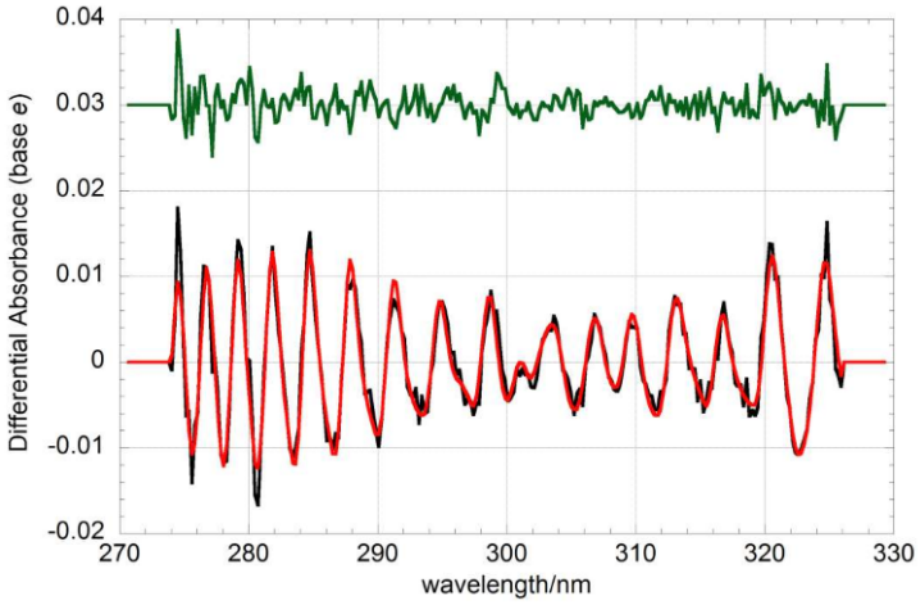

Figure 7.6 : Typical differential spectrum (black) and fit (red) averaged over t = 110-190 μs after photolysis. The fit consists of a linear combination of appropriately scaled ClO, BrO and OClO cross-sections. Residuals (green) were offset by 0.03 absorbance units for clarity.

and to the linear interpolation of the reference cross-sections over the temperature range used.

As ClO, BrO and OClO are all absorbers with spectral structure, differential fitting procedures were employed in fitting to the recorded spectra. This method, described in detail in Chapter 3, allows unequivocal monitoring of such absorbers by virtue of high-pass filtering to obtain the spectrally structured absorptions alone. A typical differential fit is shown in Figure 7.6.

A typical concentration plot for [ClO], [BrO] and [OClO] is shown in Figure 7.7. As explained above, photolysis of the OClO present in the precursor mixture gives rise to the negative apparent OClO concentration in the immediate post-photolysis period. At long timescales following photolysis, [OClO] (which should more correctly be termed Δ[OClO]) recovers to approximately its pre-photolysis values, resulting in the absence of significant OClO signal in the absorbance spectra recorded at these timescales, discussed above.

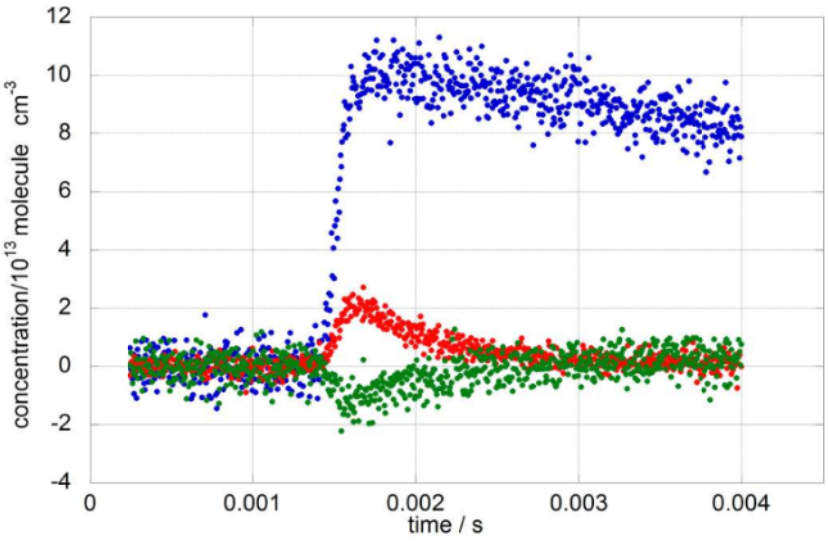

Figure 7.7 : Typical [ClO] (in blue), [BrO] (in red) and [OClO] (in green) temporal traces obtained from photolysis of $Cl_2/Cl_2O/Br_2/O_3/O_2/N_2$ mixtures at T = 298 K, with photolysis initiated at t = 0.0014 s.

7.2.4 Kinetic Analysis

Reaction conditions were designed so that ClO was present in excess throughout the BrO decay and that the atomic halogens produced by some of the channels of reaction (7.1) *only* regenerated ClO. In this manner BrO regeneration was minimised and the sole loss mechanism for BrO was reaction (7.1). Under these conditions, the rate of loss of BrO could be approximated to a pseudo-first order decay:

$$-\frac{d[\mathrm{BrO}]}{dt} = k_{7.1}[\mathrm{BrO}][\mathrm{ClO}] \approx k_{7.1}'[\mathrm{BrO}] \qquad (7.\mathrm{i})$$

where $k_{7.1} = k_{7.1a} + k_{7.1b} + k_{7.1c}$ and $k_{7.1}' = k_{7.1}[\mathrm{ClO}]$. The BrO temporal decay was therefore described by:

$$[\mathrm{BrO}]_t = [\mathrm{BrO}]_0 \exp(-k_{7.1}'\, t) \qquad (7.\mathrm{ii})$$

Similarly, OClO build-up *via* channel (7.1c) could be expressed as:

$$\frac{d[\mathrm{OClO}]}{dt} = k_{7.1c}[\mathrm{BrO}][\mathrm{ClO}] \approx k_{7.1c}'[\mathrm{BrO}] \qquad (7.\mathrm{iii})$$

where $k_{7.1c}' = k_{7.1c}[\mathrm{ClO}]$. Substituting (7.ii) into (7.iii) gives:

$$\frac{d[\mathrm{OClO}]}{dt} = k_{7.1c}'[\mathrm{BrO}]_0 \exp(-k_{7.1}'t) \qquad (7.\mathrm{iv})$$

Separating the variables, invoking stoichiometry and integrating results in:

$$\int_{[\mathrm{OClO}]_0}^{[\mathrm{OClO}]_t} d[\mathrm{OClO}] = k_{7.1c}'[\mathrm{BrO}]_0 \int_0^t \exp(-k_{7.1}'t)dt \qquad (7.\mathrm{v})$$

Solving the integral gives:

$$[\mathrm{OClO}]_t - [\mathrm{OClO}]_0 = \frac{k_{7.1c}'[\mathrm{BrO}]_0}{k_{7.1}'}\{1 - \exp(-k_{7.1}'t)\} \qquad (7.\mathrm{vi})$$

$[\mathrm{OClO}]_0$, defined as the concentration of OClO immediately after photolysis, is not zero because of the presence and photolysis of OClO in the precursor mixture. $[\mathrm{OClO}]_0$ therefore corresponds to the amount of OClO removed from the gaseous mixture by photolysis and is, by definition, negative. The temporal behaviour of [OClO] is thereafter described by:

$$[\mathrm{OClO}]_t = \frac{k_{7.1c}'[\mathrm{BrO}]_0}{k_{7.1}'}\{1 - \exp(-k_{7.1}'t)\} + [\mathrm{OClO}]_0 \qquad (7.\mathrm{vii})$$

Traces simulated using equations (7.ii) and (7.vii) were fitted to the experimental $[\mathrm{BrO}]_t$ and $[\mathrm{OClO}]_t$ traces by least-squares routines optimising the values of $[\mathrm{BrO}]_0$, $[\mathrm{OClO}]_0$, $k_{7.1}'$ and $k_{7.1c}'$. The optimised values of $k_{7.1}'$ and $k_{7.1c}'$ were then divided by the average [ClO] to obtain $k_{7.1}$ and $k_{7.1c}$. This pseudo-first order model returned excellent fits to BrO and OClO temporal traces at near-ambient temperatures ($T \geq 283$ K), as shown in Figure 7.8. However this model failed to reproduce the behaviour of $[\mathrm{OClO}]_t$ observed at lower temperatures ($T < 283$ K). All previous studies on the BrO + ClO cross-reaction are in agreement in observing a negative temperature dependence for the rate constant of channel (7.1c). [12, 13, 15] Therefore the OClO build-up following photolysis was expected to become faster at lower temperatures. However, as shown in Figure 7.9, the opposite trend was observed in the current study and the [OClO] trace, after the

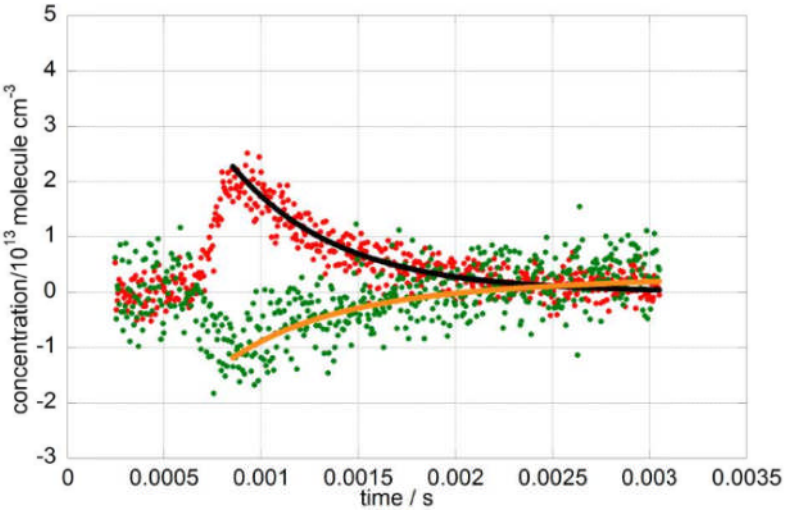

Figure 7.8 : Typical pseudo-first order fits (solid lines) to [BrO] (red data points) and [OClO] (green data points) traces recorded at T = 298 K with photolysis initiated at t = 0.0007 s.

initial depletion due to photolysis, actually exhibited a slower build-up at lower temperatures. Experiments performed at T = 246 K also indicated further removal of OClO from the reaction mixture following initial photolysis instead of OClO production, suggesting the presence of complicating secondary chemistry.

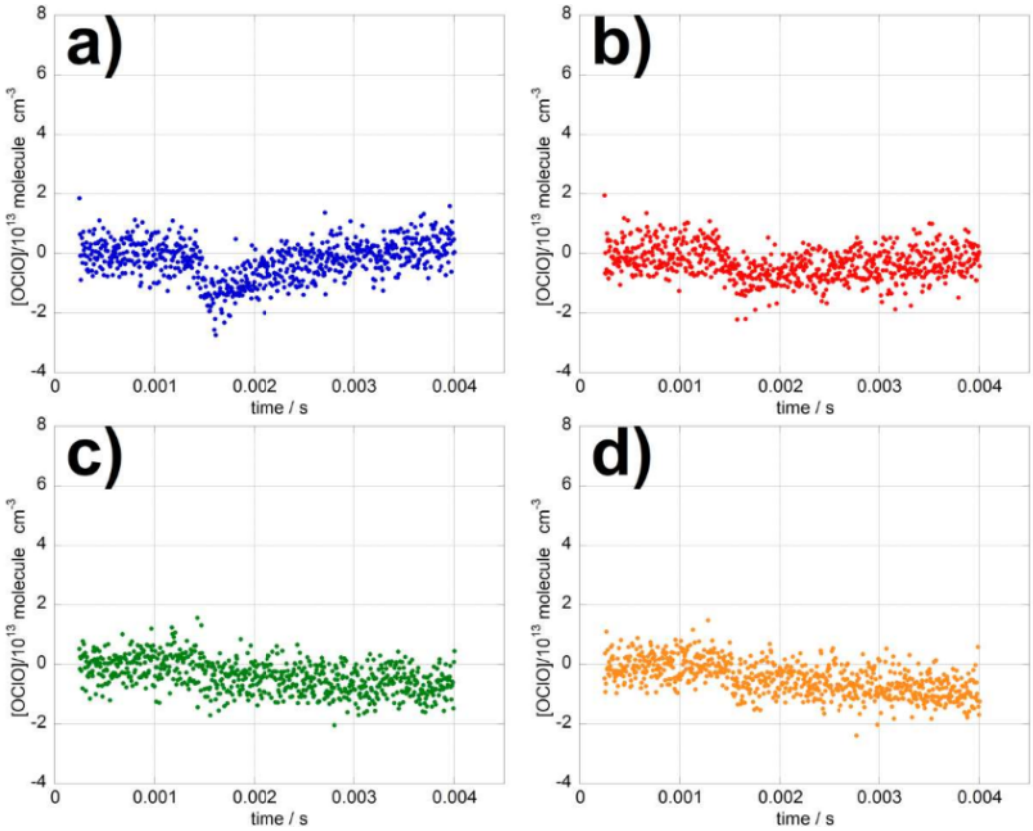

Figure 7.9 : [OClO] temporal traces from photolysis of $Cl_2/Cl_2O/Br_2/O_3/O_2/N_2$ mixtures at a) T = 298 K; b) T = 269 K; c) T = 257 K; d) T = 246 K, with photolysis initiated at t = 0.0014 s.

The simple first-order model, consisting of equations (7.ii) and (7.vii), could evidently not account for such secondary chemistry arising at low temperatures. Furthermore, considering the rapid timescale over which the reaction took place, the possibility of the decay chemistry not being entirely decoupled from the formation chemistry could not be ignored. For these reasons, numerical integration was invoked and a FACSIMILE [26] model was developed, including all the known reactions of the species contained in the reaction mixture. These reactions are listed in Table 7.2 along with the Arrhenius expression for their kinetics where available.

Reaction	k/cm^{3}molecule^{-1}s^{-1}	***Reference***
$Br + Cl_2O \rightarrow BrCl + ClO$	$2.1 \times 10^{-11}\exp(-470/T)$	[6]
$Cl + Cl_2O \rightarrow Cl_2 + ClO$	$6.2 \times 10^{-11}\exp(130/T)$	[6]
$Br + O_3 \rightarrow BrO + O_2$	$1.7 \times 10^{-11}\exp(-800/T)$	[6]
$Cl + O_3 \rightarrow ClO + O_2$	$2.3 \times 10^{-11}\exp(-200/T)$	[6]
$Cl + Br_2 \rightarrow BrCl + Br$	$2.3 \times 10^{-10}\exp(135/T)$	[17]
$BrO + ClO \rightarrow BrCl + O_2$	$k_{7.1a}$	*this work*
$BrO + ClO \rightarrow Br + ClOO$	$k_{7.1b}$	*this work*
$BrO + ClO \rightarrow Br + OClO$	$k_{7.1c}$	*this work*
$ClOO \rightarrow Cl + O_2$	$2.4 \times 10^{9}\exp(-1452/T)$ [a, b]	[6]
$ClO + ClO \rightarrow Cl_2O_2$	$3.5 \times 10^{-14}\exp(700/T)$ [b]	[21]
$Cl_2O_2 \rightarrow ClO + ClO$	$1.0 \times 10^{14}\exp(-8505/T)$ [a, b]	[21]
$ClO + ClO \rightarrow Cl_2 + O_2$	$1.0 \times 10^{-12}\exp(-1590/T)$	[22]
$ClO + ClO \rightarrow Cl + ClOO$	$3.0 \times 10^{-11}\exp(-2450/T)$	[6]
$ClO + ClO \rightarrow OClO + Cl$	$3.5 \times 10^{-13}\exp(-1370/T)$	[22]
$BrO + BrO \rightarrow Br_2 + O_2$	$2.8 \times 10^{-14}\exp(860/T)$	[27]
$BrO + BrO \rightarrow 2Br + O_2$	$2.4 \times 10^{-12}\exp(40/T)$	[6]
$Br + Cl_2 \rightarrow BrCl + Cl$	1.7×10^{-15} [c]	[28]
$Br + BrCl \rightarrow Cl + Br_2$	3.3×10^{-15} [c]	[29]
$Cl + BrCl \rightarrow Cl_2 + Br$	1.45×10^{-11} [c]	[30]
$ClO + OClO \rightarrow Cl_2O_3$	$3.1 \times 10^{-14}\exp(1095/T)$ [b]	[6]
$Cl_2O_3 \rightarrow ClO + OClO$	$1.9 \times 10^{13}\exp(-6059/T)$ [a, b]	[6]
$Cl + OClO \rightarrow ClO + ClO$	$3.4 \times 10^{-11}\exp(160/T)$	[6]
$Br + OClO \rightarrow BrO + ClO$	$2.6 \times 10^{-11}\exp(-1300/T)$	[6]
$Cl + BrO \rightarrow Br + ClO$	2×10^{-10} [c]	[10]
$Cl + ClO \rightarrow Cl_2 + O$	$1.7 \times 10^{-12}\exp(-4590/T)$	[29]
$O + ClO \rightarrow Cl + O_2$	$2.8 \times 10^{-11}\exp(85/T)$	[6]
$O + BrO \rightarrow Br + O_2$	$1.9 \times 10^{-11}\exp(230/T)$	[6]

$O + OClO \rightarrow ClO + O_2$	$2.4 \times 10^{-12}\exp(-960/T)$	[6]
$O + Cl_2O \rightarrow ClO + ClO$	$2.7 \times 10^{-11}\exp(-530/T)$	[6]
$ClOO + O \rightarrow ClO + O_2$	5.0×10^{-11} [c]	[31]
$O + BrCl \rightarrow BrO + Cl$	2.10×10^{-11} [c]	[32]
$Br_2 + O \rightarrow BrO + Br$	$5.1 \times 10^{-13}\exp(989/T)$	[20]
$O + O_3 \rightarrow O_2 + O_2$	$8.0 \times 10^{-12}\exp(-2060/T)$	[6]
$O + Cl_2 \rightarrow ClO + Cl$	$7.4 \times 10^{-12}\exp(-1650/T)$	[33]
$O + O_2 \rightarrow O_3$	$8.4 \times 10^{-16}\exp(844/T)$ [b]	[6]
$O + OClO \rightarrow ClO_3$	$8.9 \times 10^{-13}\exp(367/T)$ [b]	[6]

Notes: [a]: units s^{-1}; [b]: at p = 760 Torr; [c]: at T = 298 K

Table 7.2 : Reactions included in the FACSIMILE model used in this study of the BrO + ClO cross-reaction with their rate constants expressed in the Arrhenius form, $k = A\exp(-E_a/RT)$ where possible.

Simulated traces generated using FACSIMILE were fitted to the recorded temporal traces of ClO, BrO and OClO *via* least-squares minimization of the residuals by optimizing $[Cl]_0$, $[Br]_0$, $[OClO]_0$, $k_{7.1}$ and $k_{7.1c}$. Typical FACSIMILE fits at different temperatures are shown in Figures 7.10 and 7.11. The FACSIMILE model successfully reproduced the observed temporal behaviour of all species including [OClO] at low temperatures and resulted in excellent fits to the recorded traces at all temperatures, as

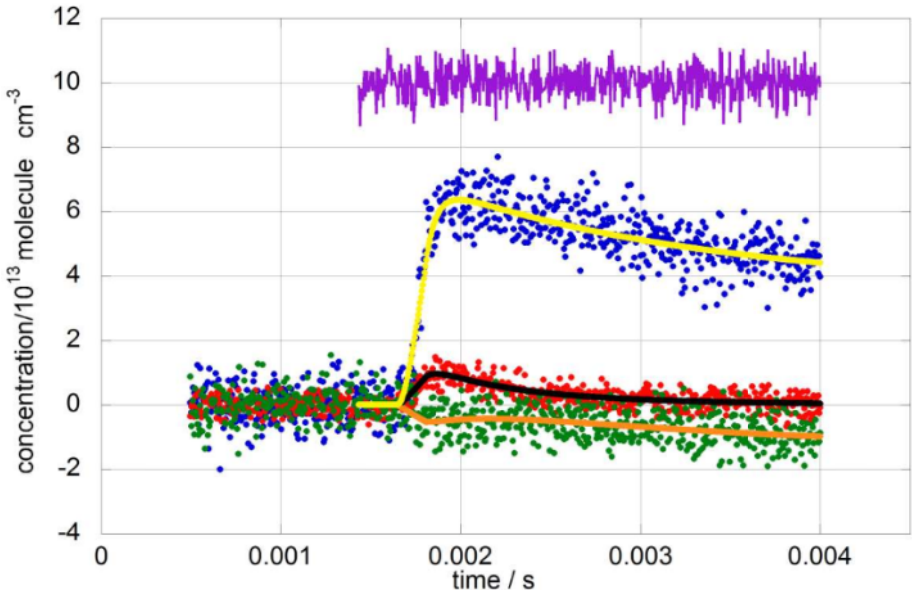

Figure 7.10 : Experimental [ClO] (in blue), [BrO] (in red) and [OClO] (in green) temporal traces recorded for the BrO + ClO study at T = 246 K along with their FACSIMILE fits (in yellow, black and orange respectively). The residuals of the fit to the [OClO] trace (in purple) were offset by $+10^{13}$ molecule cm^{-3} for clarity. Photolysis was initiated at t = 0.0017 s.

shown in Figure 7.10.

The numerical integration model also allowed investigation into the cause of the apparently anomalous behaviour of [OClO] at low temperatures. It was found that the reversible reaction of ClO and OClO:

$$ClO + OClO + M \quad \leftrightarrows \quad Cl_2O_3 + M \qquad (7.12, -7.12)$$

played a critical role. This equilibrium between OClO, ClO and Cl_2O_3 shifts towards the products as the temperature is lowered, so that whilst OClO is produced *via* channel (7.1c) it is, at the same time, undergoing association with ClO (present in excess) resulting in OClO being sequestered into Cl_2O_3. In the absence of OClO in the precursor mixture, reactions (7.12, −7.12) would be expected to have a smaller effect on the temporal behaviour of OClO. However, as an OClO impurity was unavoidably present in the gaseous mixture before photolysis, the rate of the forward reaction (7.12) became comparable to that of the OClO build-up at low temperatures, thus imparting a diversion from the expected pseudo-first order behaviour of $[OClO]_t$.

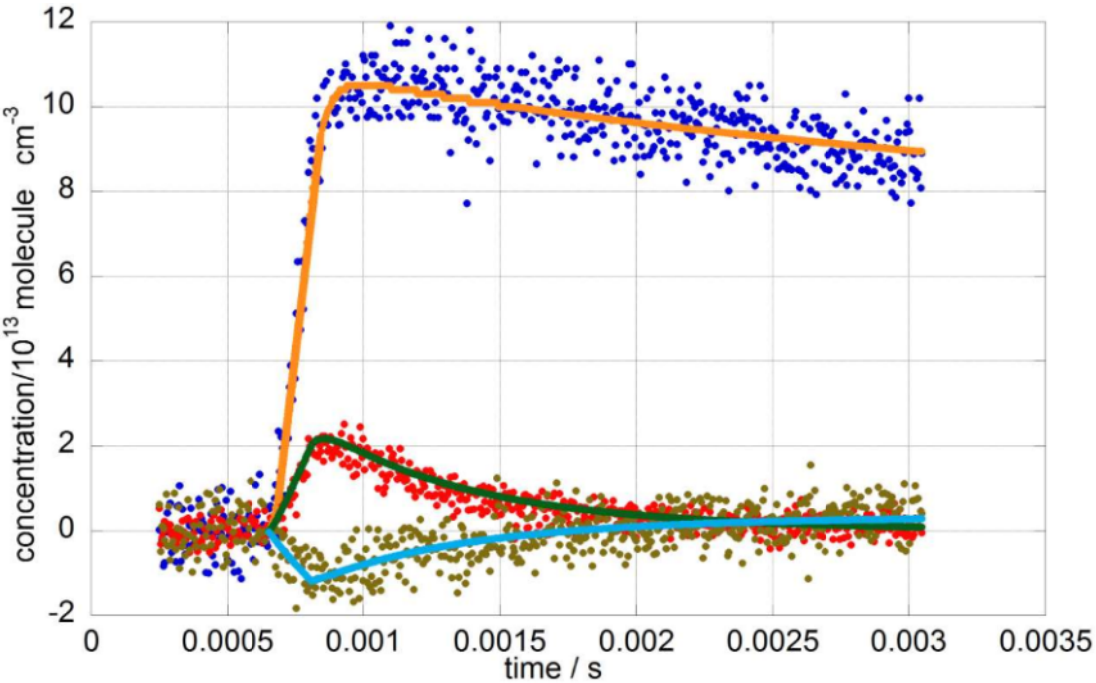

Figure 7.11 : Typical [ClO] (in blue), [BrO] (in red) and [OClO] (in green) traces recorded in the study of the BrO + ClO cross-reaction at T = 298 K along with their FACSIMILE fits (respectively, in orange, green and light blue), with photolysis initiated at t = 0.0007 s.

Gas flow-out from (and flow-in to) the reaction cell and the averaging imparted to the recorded traces by the simultaneous illumination of 31 rows of the CCD detector were also accounted for in both the pseudo-first order model and the FACSIMILE model, as described previously. As the [BrO] trace was only marginally affected by Cl_2O_3 formation, and as [ClO] remains relatively constant over the timescale of BrO decay, even at low temperatures, the pseudo-first order model could still be used to obtain values of $k_{7.1}$ at $T < 283$ K.

Values of $k_{7.1}$ and of $k_{7.1c}$ (at $T \geq 283$ K) from the pseudo-first order model were in excellent agreement with those obtained from the FACSIMILE fits, within a maximum of 10% of one another. This agreement added confidence to the sensitivity of the experimental conditions principally to the BrO + ClO cross-reaction.

The possibility of the (unknown) mechanism forming OClO in the precursor mixture having an effect on the measured [OClO] and, consequently, on the extracted kinetics of channel (7.1c) was also investigated. Photolysis experiments were performed in the absence of Br_2 but under otherwise identical conditions to those described above. The observed [OClO] trace consisted of a negative step function, showing no appreciable OClO recovery following photolysis. This was consistent with FACSIMILE simulations, showing that (as expected) OClO production *via* one of the bimolecular channels of the ClO self-reaction would be too slow to be detected over the fast timescales used. It was therefore concluded that the mechanism forming OClO in the precursor mixture, although unidentified, did not significantly affect the [OClO] temporal trace.

Since the reaction mixture was designed to regenerate ClO radicals from the atomic halogens produced by some of the channels of reaction (7.1), the ClO decay profile exhibited sensitivity to only some of these channels. Specifically, channel (7.1c) would not be expected to contribute to the observed ClO decay as the Br atom produced therein would regenerate ClO *via* reaction (7.7). Channel (7.1b), on the other hand, would actually be expected to result in ClO production following the rapid thermal dissociation of the product ClOO. Channel (7.1a) would conversely result in ClO loss. Therefore analysis of the ClO decay profile, also taking into account other ClO loss

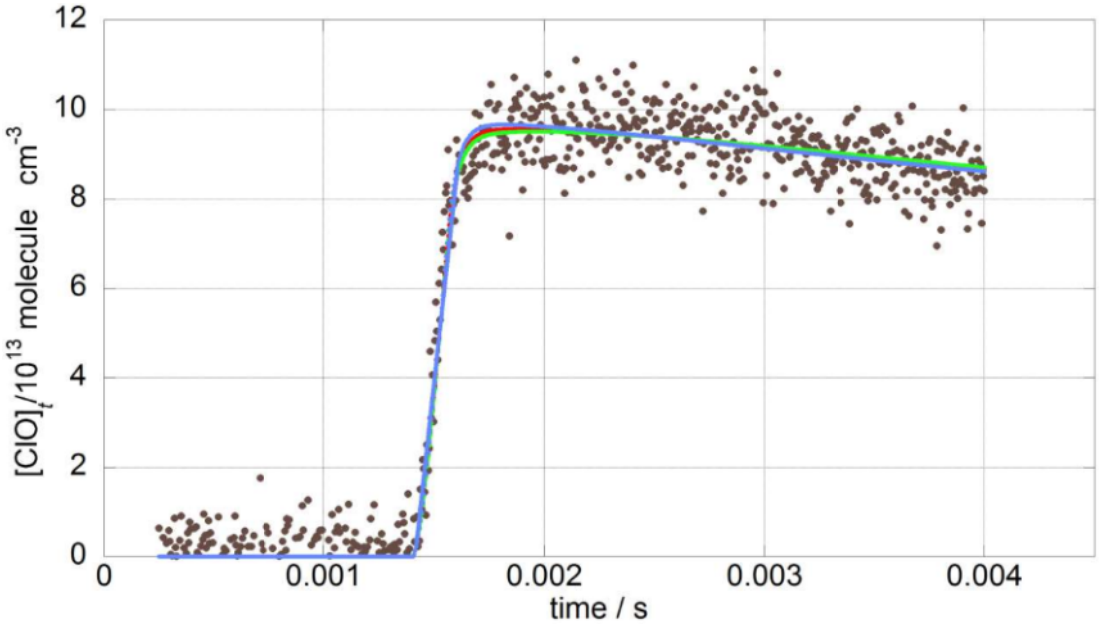

Figure 7.12 : Experimental $[ClO]_t$ (brown data points) and modelled $[ClO]_t$ traces using values of the $k_{7.1b}/k_{7.1a}$ ratio of 5.07 (in red), 10.14 (in green) and 2.535 (in light blue), with photolysis initiated at t = 0.0014 s. Pre-photolysis data points below [ClO] = 0 were omitted for clarity.

processes (notably ClO dimerisation), should in principle reveal sensitivity to (the difference between) $k_{7.1a}$ and $k_{7.1b}$. In practice, however, numerical modelling using FACSIMILE indicated that channel (7.1a) was too slow to provide sufficient sensitivity to quantify $k_{7.1a}$ especially given the noise associated with the [ClO] trace. This is illustrated in Figure 7.12, which shows a fitted [ClO] trace at T = 298 K using different values of the ratio $k_{7.1b}/k_{7.1a}$: initially, the simulated trace was fitted to the data by constraining the $k_{7.1b}/k_{7.1a}$ ratio to the value of 5.07, in accordance to the current JPL-NASA recommendation. The fixed ratio was then perturbed by a factor of two, *i.e.* doubled ($k_{7.1b}/k_{7.1a}$ = 10.14) and halved ($k_{7.1b}/k_{7.1a}$ = 2.535). The clear similarities between the simulated traces expose the lack of sensitivity associated with the [ClO] temporal trace to significant changes in $k_{7.1a}$.

Furthermore, even if some degree of sensitivity to $k_{7.1a}$ were present, it would be critically dependent on any secondary chemistry exhibited by the ClO radical. This would become particularly problematic at low temperatures, where the poorly characterised association of ClO + OClO, reactions (7.12, −7.12), becomes increasingly significant. It was therefore not possible to reliably determine $k_{7.1a}$ alone with the radical monitoring system employed; the values of $k_{7.1a}$ and $k_{7.1b}$ obtained from fitting

the FACSIMILE model to the experimental trace were therefore only considered meaningful when combined into ($k_{7.1a} + k_{7.1b}$).

The possibility of measuring $k_{7.1a}$ from the temporal behaviour of BrCl was also explored in a separate set of experiments. Molecular halogens (Cl_2, Br_2) and the mixed halogen species (BrCl) exhibit smooth absorption cross-sections in the UV/visible region of the electromagnetic spectrum, as illustrated in Figure 7.13. These spectra can be reproduced using semi-logarithmic Gaussians, as described extensively by Maric and co-workers. [34, 35, 36, 37] However, independent monitoring of the main absorption band of BrCl, peaking at $\lambda \approx 375$ nm, would present difficulties as the BrCl spectrum largely overlaps with the Br_2 spectrum, as shown in Figure 7.13. As the concentration of Br_2 is not constant in the reaction mixture used in the current work, and as Br_2 is a stronger absorber than BrCl, the BrCl signal in this region would be masked by an intense overlying Br_2 absorbance. As described in Section 5.2.5, spectral fitting of multiple overlapping smooth spectra makes species monitoring more problematic and can give rise to unrealistic concentration profiles.

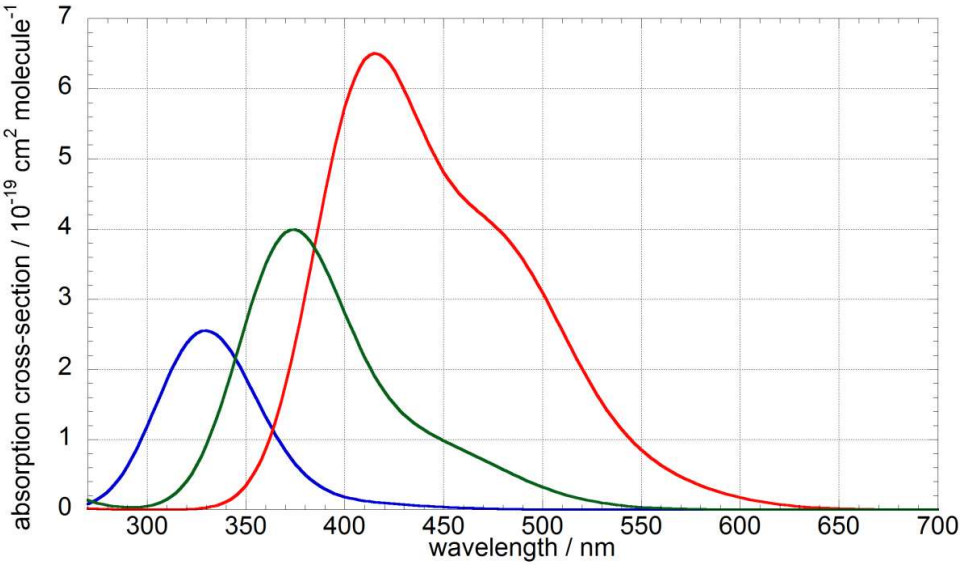

Figure 7.13 : Absorption cross-sections for Cl_2 (in blue), BrCl (in green) and Br_2 (in red), taken from the latest JPL-NASA recommendation. [6]

However, all of the spectra shown in Figure 7.13 also exhibit vibronic bands at the higher wavelength end of the main absorption band, as originally shown by the work of Maric *et al.* [34, 35] The presence of vibronic peaks in an absorbance spectrum allows in principle the use of differential fitting routines, which in turn provide a series of

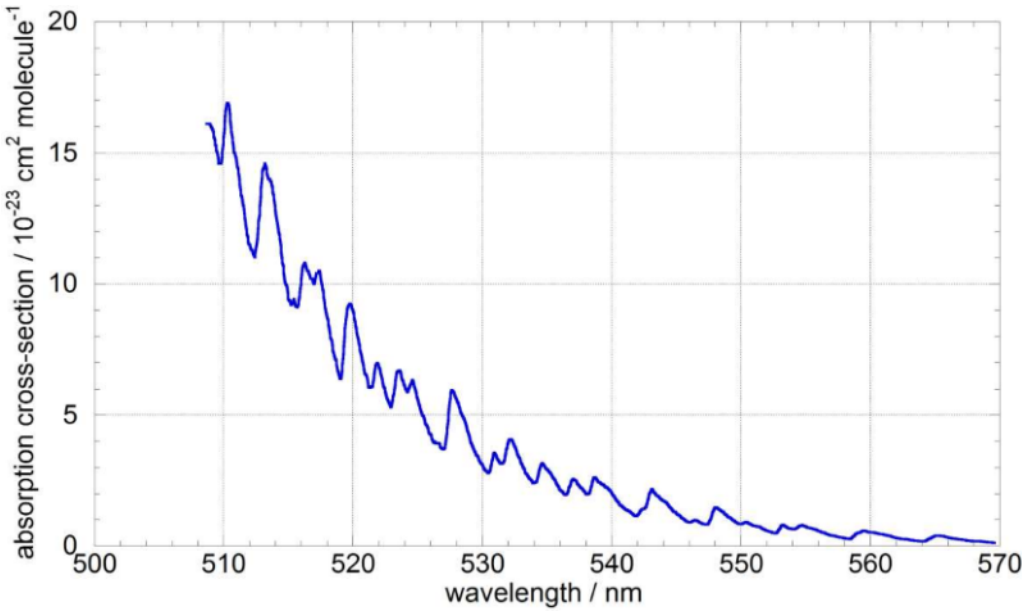

Figure 7.14 : Absorption cross-section of Cl_2 over the structured region of the spectrum, as measured by Young *et al*. [38] at an instrumental resolution of 0.36 nm (FWHM) at T = 298 K.

advantages including unequivocal quantification of the structured absorber and possibility of monitoring multiple absorbing species. A recent study by Young *et al*. [38] has characterised the structured region of the Cl_2 absorption spectrum over the range λ = 509-570 nm at four temperatures between T = 197-298 K as illustrated in Figure 7.14. Similarly, Schneider and von Helden [39] have reported the Br_2 cross-section over the

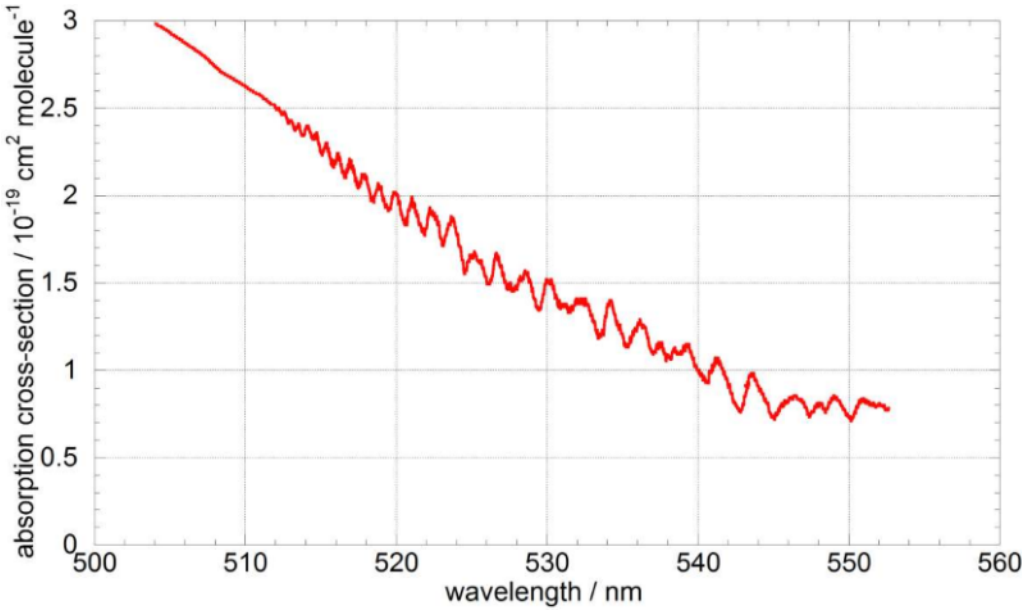

Figure 7.15 : Absorption cross-section of Br_2 over the structured region of the spectrum, as measured by Schneider and von Helden [39] at a resolution of 0.04 nm (FWHM) at T = 294 K.

range λ = 504-553 nm, encompassing the bromine vibronic structure, as shown in Figure 7.15.

To this date, no high-resolution study of the BrCl cross-section, analogous to those studies of Young *et al*. and of Schneider and von Helden, has been reported. As BrCl is formed by mixing Cl_2 and Br_2, any spectral characterisation of its spectrum relies first on the subtraction of the chlorine and bromine contribution to absorption.

Experiments involving the photolysis of $Cl_2/Cl_2O/Br_2/O_3/O_2/N_2$ precursor mixtures, identical to those described in the previous sections, were carried out to investigate the possibility of BrCl monitoring. However, in this series of experiments, changes in absorbance over the spectral region λ = 450-650 nm were monitored. A typical spectrum recorded at T = 298 K is shown in Figure 7.16a: distinct peaks in the recorded absorbance were observed in the region λ = 540-640 nm.

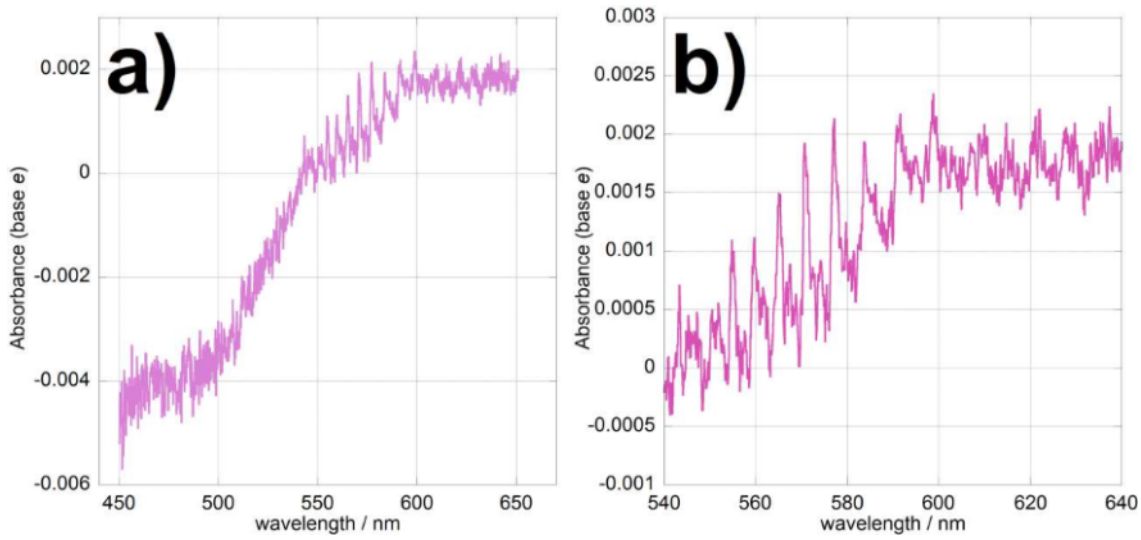

Figure 7.16 : Change in absorbance following photolysis of $Cl_2/Cl_2O/Br_2/O_3/O_2/N_2$ gaseous mixtures at T = 298 K a) over the spectral region λ = 450-650 nm and b) over the region λ = 540-640 nm where structured features were observed.

As Cl_2, Br_2 and BrCl all undergo changes in their concentration following photolysis, the observed peaks could in principle arise from any of them or from a combination of them. The FACSIMILE model described above was used to simulate temporal profiles for the changes in concentration of the three molecular halogens: as shown in Figure 7.17, changes in $[Cl_2]$ mainly arise from photolysis but, considering the small

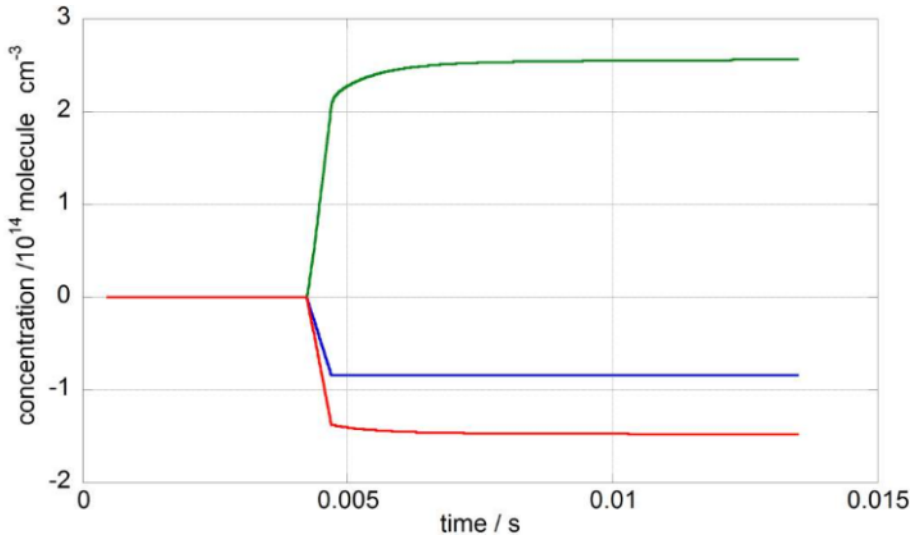

Figure 7.17 : Temporal profiles for $\Delta[Cl_2]$ (in blue), $\Delta[Br_2]$ (in red) and [BrCl] (in green) obtained from FACSIMILE simulations of photolysis of $Cl_2/Cl_2O/Br_2/O_3/O_2/N_2$ mixtures at $T = 298$ K.

magnitude of the Cl_2 cross-section in the region λ = 540-640 nm, it is highly unlikely that the observed peaks shown in Figure 7.16 arose from Cl_2. On the other hand, Br_2 molecules are photolysed and also consumed by reaction (7.6) in the immediate post-photolysis (by the Cl atoms formed upon photolysis of Cl_2) and subsequently by the Cl atoms generated by channel (7.1b). BrCl is formed by reactions (7.6) and (7.7) immediately following photolysis; over longer timescales BrCl is formed directly *via* channel (7.1a) and *via* further reactions (7.6) and (7.7) involving the Br and Cl atoms produced by channels (7.1b) and (7.1c).

Br_2 and BrCl were therefore the likely candidates to explain the structured absorbance observed at $\lambda > 540$ nm. As the Br_2 cross-section from Schneider and von Helden was only available over the range λ = 504-553 nm, it could not be fitted over the entire region λ = 540-640 nm to the recorded spectra. To overcome this, the absorbance spectrum of Br_2 vapour was recorded over the range λ = 540-570 nm, thus overlapping the high-wavelength end of the available literature Br_2 cross-section and the low wavelength end of the observed spectral bands. The Br_2 absorbance was scaled differentially to the literature cross-section from Schneider and von Helden, after this had been degraded to the lower instrumental resolution employed in this study, as shown in Figure 7.18.

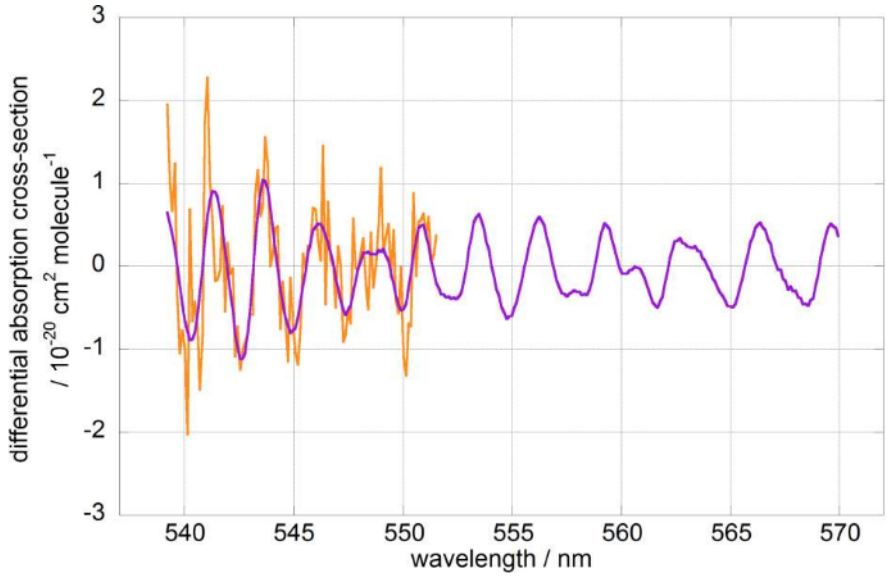

Figure 7.18 : Differential fit of a scaled Br_2 absorbance spectrum (in purple) to the Br_2 absorption cross-section determined by Schneider and von Helden [39] (in orange).

The differential Br_2 cross-section obtained was then fitted to the structured absorbance recorded in sequential spectra at $\lambda > 540$ nm. This resulted in a very noisy temporal profile albeit consistent with the one simulated *via* FACSIMILE, showing a negative $\Delta[Br_2]$ after photolysis. The fitted contribution of Br_2 to the recorded (differential) absorbance was then subtracted from the absorbance itself: structured features were still present in this residual and these were attributed to BrCl. As no BrCl cross-section was available over the spectral region of interest, the average spectral residual was fitted to the residual at each time point, resulting in an uncalibrated concentration trace showing a sharp rise following photolysis, consistent with BrCl formation. This seems to indicate that the peaks observed in the spectrum arise from a combination of a positive contribution of the BrCl spectrum and a negative contribution of the Br_2 spectrum. However, the absence of an absolute reference cross-section for BrCl and the level of noise associated with both traces was such that it precluded any further kinetic analysis. The poor quality of the signal stemmed from the magnitude of the Br_2 and BrCl absolute *and* differential cross-sections, which resulted in the low signal-to-noise ratio obtained.

The overall rate coefficient $k_{7.1}$, along with that of channel (7.1c), $k_{7.1c}$, were however determined over the temperature range T = 246-324 K as reported in the following section.

7.3 Results

The BrO + ClO cross-reaction was studied at six temperatures over the range T = 246-314 K. The data collected consisted of experiments of at least a hundred photolysis events at each temperature. The values of $k_{7.1}$ and $k_{7.1c}$ obtained from fitting the FACSIMILE model to the experimental traces are shown in Table 7.3, along with values of the branching ratio for channel (7.1c), $\gamma = k_{7.1c}/ k_{7.1}$. These are also presented in Arrhenius form in Figures 7.19 and 7.20.

T/K	$k_{7.1}$ / 10^{-11} cm^3 molecule^{-1} s^{-1}	$k_{7.1c}$ / 10^{-11} cm^3 molecule^{-1} s^{-1}	$\gamma = k_{7.1c}/ k_{7.1}$
246	3.1 ± 0.1	1.52 ± 1	0.48 ± 0.31
257	2.7 ± 0.3	1.26 ± 0.5	0.46 ± 0.15
269	2.74 ± 0.03	1.26 ± 0.4	0.46 ± 0.14
283	2.58 ± 0.01	1.3 ± 0.3	0.50 ± 0.10
298	1.86 ± 0.11	1.11 ± 0.14	0.59 ± 0.06
314	1.83 ± 0.04	1.15 ± 0.15	0.63 ± 0.07

Table 7.3 : Values of $k_{7.1}$, $k_{7.1c}$ and $\gamma = k_{7.1c}/k_{7.1}$ obtained in this work from fitting the FACSIMILE model to the experimental temporal traces. Errors correspond to 2σ, statistical only.

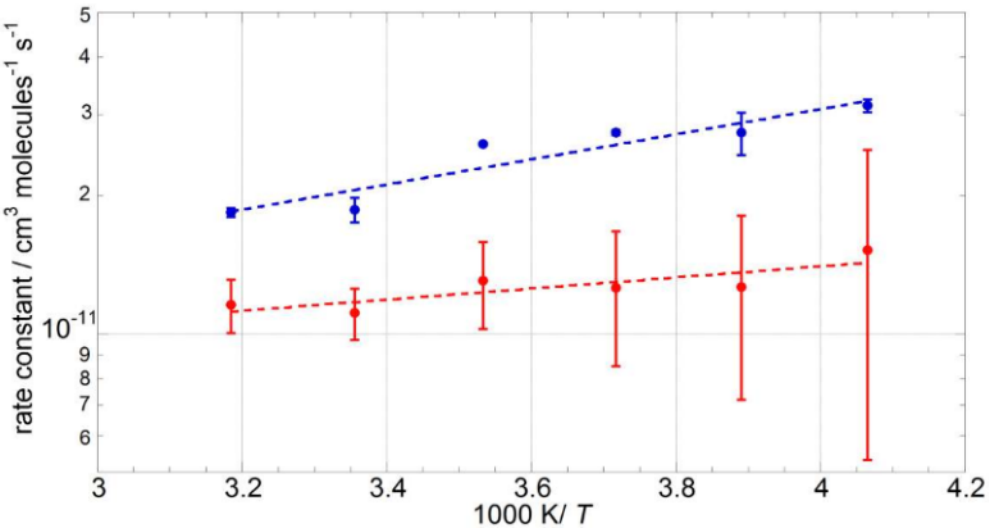

Figure 7.19 : Arrhenius plot for $k_{7.1}$ (in blue) and $k_{7.1c}$ (in red) obtained in the present work. The Arrhenius fits to these data are shown as dashed lines. Error bars are 2σ, statistical only.

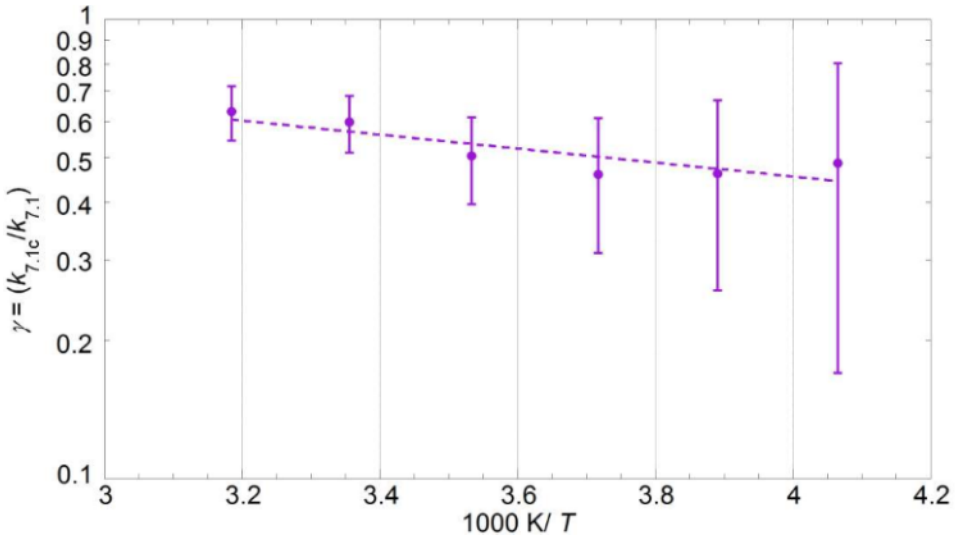

Figure 7.20 : Temperature dependence of the branching ratio for channel (7.1c), $\gamma = k_{7.1c}/k_{7.1}$, presented in Arrhenius form along with the resulting parameterisation (dashed line). Error bars are 2σ, statistical only.

The Arrhenius expressions obtained from this study are reported below, along with those from the latest JPL-NASA evaluation. [6] The errors reported are 1σ, statistical only from the Arrhenius fits. Table 7.4 reports the Arrhenius parameters for reaction (7.1) and channel (7.1c) from previous studies, from the JPL-NASA and the IUPAC [16] recommendations, and from the present work.

$$k_{7.1} / \text{cm}^3 \text{ molecule}^{-1} \text{ s}^{-1} = (2.5 \pm 1.1) \times 10^{-12} \exp[(630 \pm 120)/T]$$
$$k_{7.1c} / \text{cm}^3 \text{ molecule}^{-1} \text{ s}^{-1} = (4.6 \pm 1.5) \times 10^{-12} \exp[(280 \pm 90)/T]$$

cf. JPL-NASA:

$$k_{7.1} / \text{cm}^3 \text{ molecule}^{-1} \text{ s}^{-1} = 3.3 \times 10^{-12} \exp(400/T)$$
$$k_{7.1c} / \text{cm}^3 \text{ molecule}^{-1} \text{ s}^{-1} = 9.5 \times 10^{-13} \exp(550/T)$$

This work measured a stronger temperature dependence of the overall reaction rate $k_{7.1}$, but a weaker temperature dependence of the rate of channel (7.1c), along with greater absolute values for both $k_{7.1}$ and $k_{7.1c}$ than previously reported. Comparison with previous studies is discussed in Section 7.4.2.

	$k_{7.1c}$		$k_{7.1}$	
	$A/10^{-13}$ cm^3 molecule^{-1} s^{-1}	$-E_a/R$ /K	$A/10^{-12}$ cm^3 molecule^{-1} s^{-1}	$-E_a/R$ /K
Friedl and Sander [12]	16 ± 4	426 ± 50	4.7 ± 0.5	320 ± 60
Sander and Friedl [13]	18	431	6.1 ± 1.2	240 ± 60
Turnipseed *et al.* [15]	6.7 ± 1.0	622 ± 94	2.59 ± 0.36	445 ± 84
JPL-NASA [6]	9.5	550	3.3	400
IUPAC [16]	16	430	4.7	320
this work	46 ± 15	280 ± 90	2.5 ± 1.1	630 ± 120

Table 7.4 : Arrhenius parameters for the BrO + ClO reaction kinetics. Errors from this work are ±1σ, those from previous studies ±2σ. Note that the values obtained for $k_{7.1c}$ from the study of Sander and Friedl [13] are based on only two data points, hence their errors are not reported.

7.4 Discussion

7.4.1 Sensitivity analysis

The uncertainties in the reaction rates of the radical formation chemistry and of the subsequent secondary chemistry propagated into uncertainty in the final values of $k_{7.1}$ and $k_{7.1c}$ obtained from fitting the numerical integration model to the experimental traces. To quantify these effects, the rate constants of the reactions in the FACSIMILE model were sequentially perturbed upwards and downwards by a factor of two and the modified model was fitted to the experimental traces. This analysis was carried out for a sample trace at three temperatures: initially at T = 298 K, then at the two extremes of the temperature range studied, namely T = 314 K and T = 246 K.

This analysis gave similar results for the sensitivity at T = 298 K and T = 314 K: the perturbation of most reactions had minimal (< 1%) effects on the values of $k_{7.1}$ and $k_{7.1c}$, with the exception of the formation reactions (7.3), (7.6), (7.7), (7.10), (7.11), the ClO dimerisation and the BrO self-reaction. This investigation showed that the values of $k_{7.1}$ and $k_{7.1c}$ obtained from fitting FACSIMILE models to temporal traces were most sensitive to reactions (7.3) and (7.7): the runs in which these reactions were perturbed returned values of $k_{7.1}$ and $k_{7.1c}$ respectively within 40% and 10% of those obtained from the unmodified model. The sensitivity to reactions (7.6), (7.10) and (7.11) was more

modest, with the perturbation of their rate constants giving rise to a deviation from the values of $k_{7.1}$ and $k_{7.1c}$ resulting from the unperturbed model of 2% and 1% respectively. Perturbation of the rate constants of the ClO dimerisation and of the BrO self-reaction had a negligible effect on $k_{7.1c}$ (<1%) but returned values of $k_{7.1}$ within 5% and 2% respectively from those obtained from the unaltered model. However, the perturbation of the rate constants of these reactions by a factor of two appeared to be an overestimate in the light of the uncertainty factors reported in the latest JPL-NASA evaluation [6] and indeed the current work. Therefore a new series of sensitivity runs was performed for sample traces at T = 298 K and T = 314 K, taking into account only those reactions whose perturbation had led to a deviation in $k_{7.1}$ and/or $k_{7.1c}$ greater than 1%. Rate constants for these reactions were perturbed by the uncertainty factors recommended by JPL-NASA. As these uncertainty factors were all lower than the factor of two previously used, deviations from the kinetic parameters returned from the unperturbed model were far less pronounced than in the previous runs. Only the perturbation of the rates of reactions (7.3) and (7.7) resulted in deviations greater than 1%, more specifically of 10% for $k_{7.1}$ and 3% for $k_{7.1c}$. Perturbation of the rate constants for the ClO dimerisation produced no significant deviation in the returned value of $k_{7.1c}$, and the returned value of $k_{7.1}$ was within 2% of that obtained from the unperturbed model.

The results of the sensitivity analysis performed at the lowest temperature of this study, T = 246 K, were notably different from those obtained at higher temperatures. Whilst perturbation of reactions other than formation chemistry and the XO (X = Cl, Br) self-reactions by a factor of two had negligible (< 1%) effects on the returned values of $k_{7.1}$ and $k_{7.1c}$ at T =298 K and T = 314 K, the same treatment at T = 246 K led to a higher deviation (typically ~ 2 %) from the values obtained *via* the unperturbed model. This behaviour was rationalised on account of the negative temperature dependence of some of these reactions: as their rate constants increase at low temperatures, this secondary chemistry starts to compete more efficiently with reaction (7.1) and therefore has a greater effect on $k_{7.1}$ and $k_{7.1c}$ when their rate constants are perturbed. However, this evidently does not apply to those reactions in the FACSIMILE model with positive temperature dependence. The observed enhanced sensitivity to secondary chemistry could also arise from the poorer signal-to-noise ratio observed for the temporal traces recorded at T = 246 K, which affected the capacity of the perturbed model to converge

to values of $k_{7.1}$ and $k_{7.1c}$ that did not deviate from those obtained with the unperturbed secondary chemistry. The poorer signal recorded at low temperatures was partly due to lower radical concentrations caused by the slower formation reactions (7.3) and (7.7) as a result of the positive temperature dependence of their rate constants. The concentrations of chlorine monoxide and bromine monoxide radicals in the immediate post-photolysis, $[ClO]_0$ and $[BrO]_0$, at T = 246 K were respectively 20% and 55% lower than those observed at T = 314 K. In addition to this, species that absorb strongly over the spectral window used in this study (mainly Cl_2O_2 and Cl_2O_3) produced by secondary reactions are more thermally stable at T = 246 K than at ambient temperature, thus leading to a significant decrease in light transmitted through the reactive mixture at lower temperatures. In common with the results of the sensitivity analysis at T = 298 K and T = 314 K, perturbation of formation reactions and of the XO self-reactions by a factor of two produced the largest deviations from the values of $k_{7.1}$ and $k_{7.1c}$ obtained with the unaltered model; however the magnitude of such deviations was larger at T = 246 K than that observed at higher temperatures. Perturbation of formation reactions (7.3) and (7.7) by a factor of two returned values of $k_{7.1}$ and $k_{7.1c}$ which deviated from those obtained with the unperturbed model by as much as 80% for both rate constants. Perturbation of reactions (7.6), (7.10) and (7.11) produced somewhat smaller (< 10%) deviations, whilst values of $k_{7.1}$ and $k_{7.1c}$ obtained from models with perturbed rate constants for the ClO dimerisation and for the BrO self-reaction lay within 5% of those from unperturbed models. As discussed for the sensitivity analysis to secondary chemistry at higher temperatures, an uncertainty factor of two is usually larger than current uncertainties estimated by JPL-NASA. [6] However, most of the uncertainty factors reported in the JPL-NASA evaluation are temperature-dependent and they increase above and below T = 298 K. At T = 246 K these uncertainties are approximately equal to two for reaction (7.7) and for the BrO self-reaction. Sensitivity procedures were therefore re-run for the reactions whose uncertainty factors were lower than two at T = 246 K. Perturbation of reaction (7.3) led to deviations in $k_{7.1}$ and $k_{7.1c}$ of 40% and 60% respectively, perturbation of (7.6), (7.10), (7.11) and of the ClO dimerisation all led to smaller deviations (< 5% in most cases).

The sensitivity of the FACSIMILE model for the BrO + ClO cross-reaction to the ClO + OClO termolecular association was negligible at the high end of the temperature range

used, but became very pronounced at T = 246 K due to the enhanced thermal stability of the Cl_2O_3 adduct at low temperatures. Deviation of the unperturbed values of $k_{7.1}$ and $k_{7.1c}$ caused by the perturbation of the equilibrium constant described by reactions (7.12, −7.12) increased from < 1% at T = 298 K and T = 314 K to approximately 90% at T = 246 K, using the JPL-NASA uncertainty factor of 1.4 instead of a value of two. It became clear that sequestration of OClO into Cl_2O_3 affected the observed temporal behaviour of [OClO], thus interfering critically with the extraction of the rate constant for channel (7.1c). In addition to this, experimental noise on the kinetic traces at T = 246 K made it extremely hard to decouple the OClO build-up *via* channel (7.1c) from equilibration (7.12, −7.12), to the point that the model would not readily converge to a unique value of $k_{7.1c}$. As a consequence, the errors in $k_{7.1c}$, and consequently in its branching ratio γ, reported in Table 7.3 increase as the temperature is lowered.

The effects of the sensitivity to secondary chemistry, of the lower initial radical concentrations and the poorer signal at low temperatures were used to define the low temperature limit for the current study of reaction (7.1). On the other hand, the upper limit of the temperature range used in the current study was dictated by the instrumental limitation of the thermostatting set-up.

The absorption cross-sections of ClO, BrO and OClO were evidently crucial in the determination of the temporal concentration traces and, therefore, in the extraction of kinetic information for the BrO + ClO reaction. To ascertain the effect of uncertainties in the cross-sections used on the final values of $k_{7.1}$ and $k_{7.1c}$, each cross-section was perturbed using the recommended errors (discussed below) so that an upper and a lower limit were determined for each cross-section at each experimental temperature. The analytical procedure leading to the quantification of the absorbers, outlined in Section 7.2.3, was therefore repeated using each modified cross-section at a time, for all experimental data. The temporal traces were then fitted to the FACSIMILE model and the returned values of $k_{7.1}$ and $k_{7.1c}$ were compared to those obtained using unperturbed cross-sections.

As discussed previously in Chapter 5 and in the literature, [22] uncertainty in σ_{ClO} was defined by two standard deviations from three values of the ClO cross-sections

measured at $T = 298$ K; this gave rise to a relative error in σ_{ClO} of 0.23 at $T = 298$ K, of 0.26 at $T = 314$ K and of 0.15 at $T = 246$ K. The temperature dependence of the relative errors reflected the uncertainties in the high-resolution differential ClO cross-sections derived in Chapter 4 and employed to obtain σ_{ClO} at the lower resolution of the current study (see Section 7.2.3). The errors in the ClO cross-sections were propagated through the analytical procedure and the values of $k_{7.1}$ and $k_{7.1c}$ resulting from perturbed cross-sections lay within 12% and 28% of those obtained using unperturbed cross-sections at $T = 314$ K. Similarly, at $T = 246$ K, values of $k_{7.1}$ and $k_{7.1c}$ were within 8% and 13% of those obtained using unperturbed cross-sections.

This work employed the BrO cross-sections measured by Wilmouth *et al.*; [23] these authors reported an error of 11% for the differential cross-section of the (7, 0) vibronic band at $\lambda = 338.5$ nm at $T = 298$ K. In this sensitivity analysis, BrO cross-sections at all experimental temperatures were therefore perturbed by a factor of 1.11 and then fitted to the recorded absorbance spectra to generate [BrO] traces. These traces were then fitted to the FACSIMILE model and the returned values for $k_{7.1}$ and $k_{7.1c}$ lay within respectively 5% and 3% of the values obtained using the unperturbed σ_{BrO} at $T = 314$ K and by 8% and 5% at $T = 246$ K.

The OClO cross-sections used in the current work are those reported by Wahner *et al.* [24] These authors identified baseline shifts as the main source of error in their measurement and recommended an uncertainty of $\pm 4 \times 10^{-19}$ cm^2 molecule^{-1} for each point of the spectrum. However, a baseline shift would not affect the spectral fit carried out in the current work as differential fitting procedures are adopted. As described previously in Chapter 5, the differential cross-section of the a(15) peak at $\lambda = 322.78$ nm was however perturbed by $\pm 4 \times 10^{-19}$ cm^2 molecule^{-1} and the whole spectrum was scaled to match the altered differential cross-section at all experimental temperatures. Perturbed OClO cross-sections were then employed in the quantification of OClO *via* the Beer-Lambert Law and the traces thus generated were fitted to the FACSIMILE model. The returned values of $k_{7.1}$ and $k_{7.1c}$ at $T = 314$ K were within 1% and 4% respectively of the values obtained from unaltered cross-sections; these deviations increased to 10% and 9% respectively at $T = 246$ K.

Errors in the absorption cross-sections of all three species monitored were combined to give an upper and a lower limit to $k_{7.1}(T)$ and $k_{7.1c}(T)$, expressed in Arrhenius form:

$$k_{7.1\ \mathrm{upper}}/\ \mathrm{cm^3\ molecule^{-1}\ s^{-1}} = 2.7 \times 10^{-12}\exp(636/T)$$
$$k_{7.1\ \mathrm{lower}}/\ \mathrm{cm^3\ molecule^{-1}\ s^{-1}} = 2.5 \times 10^{-12}\exp(587/T)$$
$$k_{7.1c\ \mathrm{upper}}/\ \mathrm{cm^3\ molecule^{-1}\ s^{-1}} = 9.7 \times 10^{-12}\exp(130/T)$$
$$k_{7.1c\ \mathrm{lower}}/\ \mathrm{cm^3\ molecule^{-1}\ s^{-1}} = 2.5 \times 10^{-12}\exp(390/T)$$

The sensitivity of the values obtained for $k_{7.1}$ and $k_{7.1c}$ to the concentrations of precursor species was also investigated. As illustrated in Section 7.2.1, the concentration of species in the precursor mixture was quantified by means of UV absorption spectroscopy. Sensitivity of the rate constants to uncertainties in the precursor species concentrations was studied by perturbing the values for [Br_2], [Cl_2], [Cl_2O] and [OClO] input in the FACSIMILE model by ±10%, one at a time, at T = 298 K and T = 246 K. At T = 298 K, the rate constants obtained from the model with perturbed [Br_2] and [Cl_2] were respectively within 0.7% and 0.3% from those returned from the unaltered model. As the [Cl_2O]/[O_3] ratio dictated the partitioning of Br between reaction (7.7) and reaction (7.3), fluctuations in the concentrations of Cl_2O and O_3 had a more appreciable effect than those in Br_2 and Cl_2 on the returned rate constant, which were in any case within 6% of those obtained from the unperturbed model. Perturbation of the concentration of the OClO impurity present in the precursor mixture by 10% had minor effects (< 1%) on the returned rate constants. When the same procedure was repeated at T = 246 K, an enhanced sensitivity to [Cl_2O] and [O_3] was observed, with perturbed models returning values of $k_{7.1}$ and $k_{7.1c}$ within 15% of those from unaltered models. By contrast, perturbation of precursor [OClO] had a non-negligible effect at this low temperature, resulting in deviations from the rate constants obtained from the unperturbed model of approximately 25 %.

The effects of the uncertainty in the flow-out of the gaseous mixture from the reaction cell were also investigated. The values of $k_{7.1}$ and $k_{7.1c}$ returned from a FACSIMILE model in which the flow-out had been perturbed by 10% lay within <0.5% from those obtained from the unperturbed model at T = 298 K and within 1.5% at T = 246 K, indicating that uncertainty in the flow-out was a minor source of error. This behaviour

was expected as gas flow-out was minimal over the fast timescale at which the BrO + ClO cross-reaction took place.

In conclusion, for such an inherently complex reaction system, care has to be taken to ensure that sensitivity to the target reactions is maximised, whilst sensitivity to the uncertainties in the secondary reaction kinetics, precursor concentrations and cross-sections is minimised. This study has found that uncertainty in some parameters (the kinetics of the formation chemistry, ClO dimerisation, BrO self-reaction, Cl_2O_3 formation, as well as the absorption cross-sections of the three species monitored and precursor [Cl_2O] and [O_3]) do exhibit an effect on the inference of kinetic parameters reported here, whilst others do not.

7.4.2 Comparison with previous work

Figures 7.21, 7.22 and 7.23 illustrate the values of $k_{7.1}$, $k_{7.1c}$ and γ obtained from this work in Arrhenius form, along with the results from previous studies and the current JPL-NASA recommendations. [6]

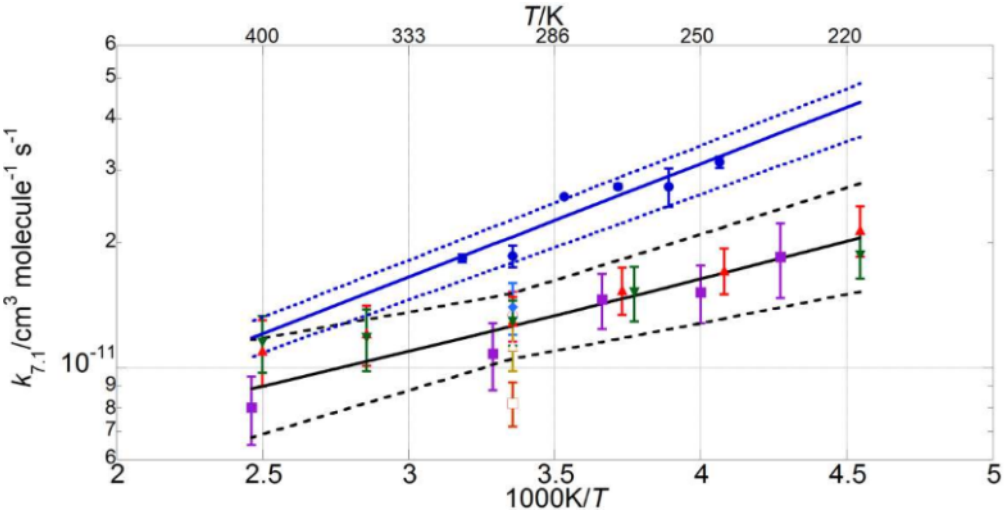

Figure 7.21 : Arrhenius plot for $k_{7.1}$. Data from this work are shown as blue circles, along with the resulting parameterisation (blue line) and the uncertainty limits (dashed blue lines) as discussed in Section 7.4.1. Also shown are the data from Clyne and Watson [9] (pink open circles), Toohey and Anderson [10] (blue diamonds), Hills *et al.* [11] (open orange squares), Friedl and Sander [12] (red triangles), Sander and Friedl [13] (inverted green triangles), Poulet *et al.* [14] (open green triangles), Turnipseed *et al.* [15] (purple squares). The current JPL-NASA [6] recommendation is shown as a black line along with its uncertainty range (dashed black lines).

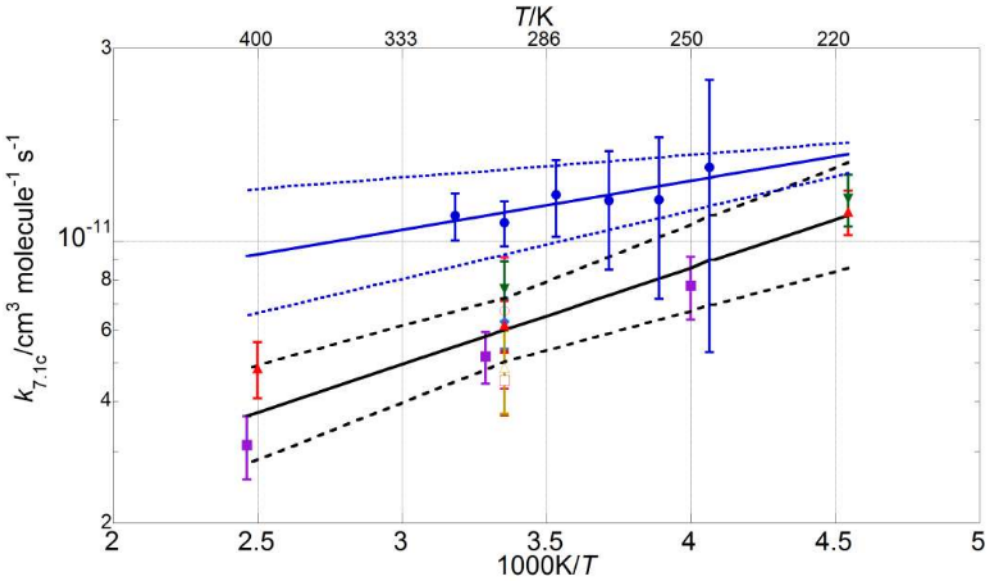

Figure 7.22 : Arrhenius plot for $k_{7.1c}$. Data from this work are shown as blue circles, along with the resulting parameterisation (blue line) and the uncertainty limits (dashed blue lines) as discussed in Section 7.4.1. Also shown are the data from Clyne and Watson [9] (pink open circles), Toohey and Anderson [10] (blue diamonds), Hills *et al.* [11] (open orange squares), Friedl and Sander [12] (red triangles), Sander and Friedl [13] (inverted green triangles), Poulet *et al.* [14] (open green triangles), Turnipseed *et al.* [15] (purple squares). The current JPL-NASA [6] recommendation is shown as a black line along with its uncertainty range (dashed black lines).

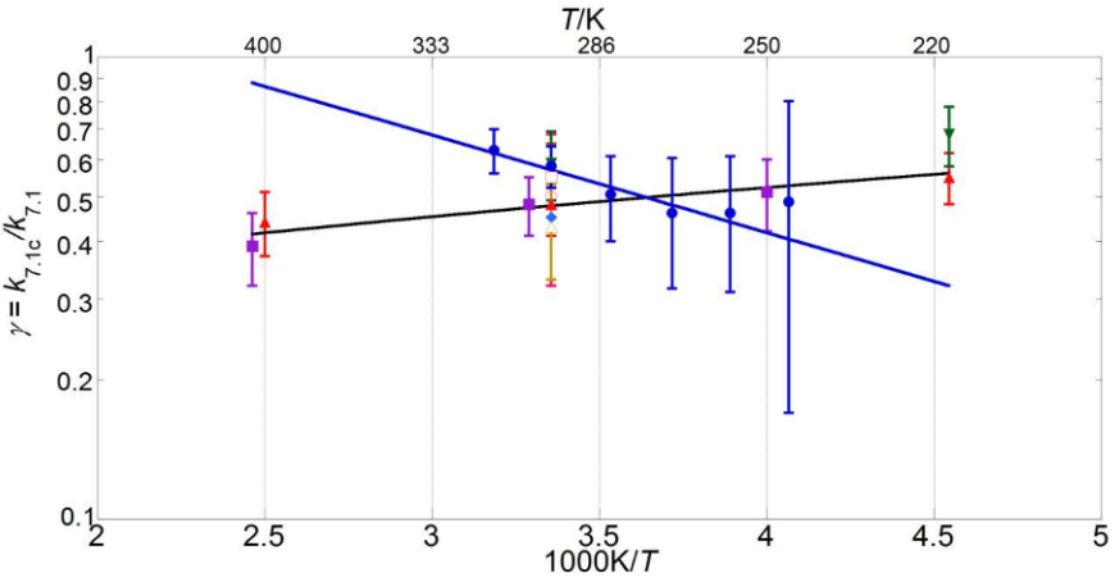

Figure 7.23 : Branching ratio for $k_{7.1c}$ presented in Arrhenius form. Data from this work are shown as blue circles, along with the resulting parameterisation (blue line). Also shown are the data from Clyne and Watson [9] (pink open circles), Toohey and Anderson [10] (blue diamonds), Hills *et al.* [11] (open orange squares), Friedl and Sander [12] (red triangles), Sander and Friedl [13] (inverted green triangles), Poulet *et al.* [14] (open green triangles), Turnipseed *et al.* [15] (purple squares) and the current JPL-NASA [6] recommendation (black line).

The values of $k_{7.1}$ from the present study are approximately 70% greater than the current JPL-NASA recommendation over the whole temperature range studied here, and they also fall outside the JPL-NASA upper uncertainty limit at all temperatures (Figure 7.21). The temperature dependence of $k_{7.1}$ from this work was also slightly more (negatively) pronounced than that reported by previous studies (Table 7.4). This work also measured values of the rate constant of channel (7.1c) greater than the current JPL-NASA recommendation (Figure 7.22), along with a weaker temperature dependence of $k_{7.1c}$ than those from previous studies and JPL-NASA (Table 7.4). The branching ratio for channel (7.1c), γ, as a result of the temperature dependences of $k_{7.1c}$ and $k_{7.1}$ observed in this work, therefore became smaller as the temperature was lowered, contrary to the findings of previous studies (Figure 7.23). However, as discussed in the previous section, uncertainties in the secondary chemistry of OClO and the reduction in signal quality at low temperatures due to the formation of stable absorbers (Cl_2O_2, Cl_2O_3), resulted in the considerable uncertainty in $k_{7.1c}$ and, consequently, γ at $T < 283$ K.

The simultaneous broadband time-resolved monitoring of [ClO], [BrO] and [OClO] as a function of time, along with the employment of differential fitting techniques, constitute an enormous advantage of the current work over, for example, the dual-wavelength study by Sander and Friedl. Sander and Friedl used flash photolysis of Br_2/Cl_2O mixtures to generate ClO and BrO radicals, then simultaneously monitored ClO at the (12,0) peak at λ = 275.2 nm and BrO at the (7, 0) peak at λ = 338.5 nm. However, multiple underlying absorbances are significant at both wavelengths. Sander and Friedl applied a correction to the absorbance recorded at λ = 275.2 nm to account for the (negative) contribution to the total absorbance arising from the Cl_2O consumed in the formation chemistry. However, FACSIMILE simulations using the reaction conditions described by Sander and Friedl showed that the ClO dimer, Cl_2O_2, would also give a non negligible contribution to the total absorbance at λ = 275.2 nm under conditions of low temperature and high pressure. At T = 220 K and p = 700 Torr, respectively the lowest temperature and the highest pressure used by Sander and Friedl, approximately 10% of the total simulated absorbance (averaged over the timescale of BrO decay, approximately Δt = 1-1.5 ms after photolysis) at λ = 275.2 nm would be expected to arise from the presence of Cl_2O_2. This contribution to the total absorbance fell to 3% at

T = 298 K and <1% at T = 400 K, and was fully negligible at all temperatures in the low pressure regime (p = 50 Torr) as a consequence of the temperature and pressure dependence of the ClO + ClO equilibration. However, not accounting for the contributions of Cl_2O_2 to the total absorbance in the work of Sander and Friedl could therefore have led to an overestimate of [ClO] at low temperatures and high pressures which propagated into an underestimate of $k_{7.1}$, as $k_{7.1} = k_{7.1}'/[ClO]$ under the pseudo-first order assumption derived from excess ClO over BrO. This is consistent with the values of $k_{7.1}$ (T) from the current work diverging from those obtained by Sander and Friedl at low temperatures: whilst the two studies are in good agreement at T = 400 K, with the extrapolated $k_{7.1}$ from this study lying within 4% of the measurement from Sander and Friedl, the extrapolated $k_{7.1}$ at T = 220 K from this study is more than twice that measured by Sander and Friedl at the same temperature.

Similarly, underlying absorbers could potentially have interfered with the monitoring of BrO at λ = 338.5 nm in the Sander and Friedl study. Sander and Friedl obtained the pseudo first-order rate constant for reaction (7.1), $k_{7.1}'$, from the slopes of plots of the logarithm of the absorbance recorded at λ = 338.5 nm against time. Production of BrCl directly *via* channel (7.1a) and indirectly from Br and Cl atoms from channels (7.1b) and (7.1c) undergoing reactions (7.6) and (7.7) would also have an effect on the absorbance recorded at λ = 338.5 nm, giving rise to an apparent slower decay of the absorbance. Simulations were run in FACSIMILE to assess the potential magnitude of this effect; neglect of underlying absorbers always resulted in an underestimate of the $k_{7.1}'$, but the extent to which this may have affected the values of $k_{7.1}$ from Sander and Friedl could not be quantified precisely due to lack of experimental details of their work.

Sander and Friedl determined the branching ratio of channel (7.1c), γ, as the ratio between the [OClO] yield measured after the [BrO] decay had proceeded to completion and the initial concentration of BrO, $[BrO]_0$. [OClO] and $[BrO]_0$ were obtained by Sander and Friedl in consecutive experiments conducted under identical conditions at two temperatures only, T = 220 K and T = 298 K. OClO spectra were recorded 2 ms after photolysis, with a 1 ms exposure. $[BrO]_0$ was obtained by back-extrapolating logarithmic plots of the absorbance at λ = 338.5 nm to t = 0 and then converting the

initial absorbance into $[BrO]_0$ using a value of the BrO cross-section at λ = 338.5 nm determined in the same study. As discussed above, the presence of underlying absorbers at λ = 338.5 nm may lead to an underestimate of the slope of such plots and, in turn, of the absorbance at t = 0. This would lead to an overestimate in γ. As the pressure range of the experiments on the branching ratio is not specified, it is not possible to assess whether the ClO + OClO termolecular association interfered with the [OClO] build-up at T = 220 K. However if that were the case, it would result in a significant underestimate of the value reported by Sander and Friedl of γ = 0.68 at T = 220 K as some OClO genuinely produced by the BrO + ClO reaction would have been sequestered into Cl_2O_3.

All previous studies agree on the negative temperature dependence of the total rate constant, $k_{7.1}$, and of the individual channels, with the exception of the work of Hills *et al*. [11] Results from Hills *et al*. are in stark contrast to those from all other previous studies as they report a near-zero temperature dependence and a value of $k_{7.1}$ smaller than the current JPL-NASA recommendation by approximately 35% at T = 298 K and by 60% at T = 220 K. Friedl and Sander [12] attributed this disagreement to the neglect of secondary chemistry; more specifically, Hills *et al*. did not account for bromine atoms generated by reactions (7.1) and (7.6) which regenerated BrO *via* reaction (7.3) with the ozone present in the gas flow. Regeneration of BrO would have affected the observed kinetics of BrO, giving rise to an apparent slower decay.

All discharge flow/mass spectrometry studies of the BrO + ClO cross-reaction reported in the literature were performed under conditions of excess ClO over BrO. In these studies, Cl atoms were produced from Cl_2 by microwave discharge and ClO radicals were generated either *via* Cl + OClO [10, 14] or Cl_2O + Cl, [15] or both. [11, 12] In these studies, the concentration of Cl atoms produced was either in excess over or equal to that of OClO and Cl_2O, to ensure full consumption of precursor chlorine oxides and allow direct detection of OClO produced by channel (7.1c). However, the absence of Cl_2O in the flow tube studies also prevented scavenging of bromine atoms (as occurs in the photolysis system, *via* reactions (7.3) and (7.7)) and hence allowed the reaction:

$$Br + OClO \rightarrow BrO + ClO \qquad (7.13)$$

to occur. In discharge flow experiments, bromine atoms were formed as products of the BrO + ClO cross-reaction as well as by-products of BrO production as reported in the studies of Friedl and Sander [12] and Turnipseed *et al.* [15] (where the reaction O + Br_2 was employed to generate BrO) and in the work of Poulet *et al.* [14] (who used excess Br atoms with O_3). Poulet *et al.* noted that, subsequently, reaction (7.13) did occur, necessitating the correction of OClO concentrations to determine the branching ratio for channel (7.1c). The rate constant for reaction (7.13) is, however, not well known, with the current JPL-NASA quoting an uncertainty (at the 1σ level) of 100% at T = 298 K and of 185% at T = 220 K. Absent or flawed correction for reaction (7.13) would affect $k_{7.1}$ and $k_{7.1c,}$ as a result of distorted [BrO] and [OClO] temporal profiles. As reaction (7.13) regenerates BrO from Br atoms, the kinetics of the observed [BrO] decay would return a smaller pseudo-first order $k_{7.1}'$.

The presence of OClO in the precursor mixture observed in the current work was attributed to unknown chemistry involving ozone with Cl_2O and/or Cl_2. Friedl and Sander [12] also reported the presence of a background OClO signal in their discharge flow study under excess ozone conditions. Similar reaction conditions of excess ozone to generate BrO *via* reaction (7.3) were also employed by Turnipseed *et al.* but these authors did not detect or report any anomalous OClO signal. This indicates that two of the three studies that have investigated the temperature dependence of the BrO + ClO cross-reaction might have been affected by the presence of OClO in the precursor mixture, which may in turn have led to an overestimate of the branching ratio for channel (7.1c), γ. Despite the potential presence of OClO in the precursor mixture, Cl_2O_3 formation *via* reaction (7.12) is unlikely to have occurred in flow systems even at low temperatures (T < 250 K) due to the low pressure at which these studies were performed (p = 1 Torr for Friedl and Sander and p = 2 Torr for Turnipseed *et al.*).

Crucially, all previous studies on the BrO + ClO cross-reaction [9-12, 14, 15] were performed at low pressures (p < 2 Torr), with the exception of the work of Sander and Friedl. [13] The discrepancy between the temperature dependences of $k_{7.1}$ and $k_{7.1c}$ observed in this work and those measured by Sander and Friedl has been discussed extensively and can be rationalised in terms of the neglect of additional absorbers and secondary chemistry by Sander and Friedl. On the other hand, the disagreement between the present work

and previous studies using discharge flow/mass spectrometry could potentially arise from the contribution of a termolecular association channel operating at high pressures, leading to the production of a stable $BrClO_2$ adduct. The different temperature dependences of $k_{7.1}$ shown in the Arrhenius plot in Figure 7.21 are consistent with this mechanism as the discrepancy between high-pressure (this study) and low-pressure (Friedl and Sander, Turnipseed *et al.*) values of $k_{7.1}$ becomes more significant at low temperatures, where formation of the adduct would be expected to be more efficient. However, the existence of a termolecular component to the BrO + ClO cross-reaction could only be established by further experiments performed over a wide range of pressures as well as temperatures.

Results from the current study indicate that the OClO-producing pathway of the BrO + ClO cross-reaction, channel (7.1c) is less efficient than previously reported at temperatures typical of the polar stratosphere. This result could potentially account for the discrepancy highlighted by Canty *et al.* [5] between field measurements of stratospheric OClO abundances and atmospheric models.

7.5 Conclusions

The temperature dependences of the rate constants of the overall reaction (7.1), $k_{7.1}$, and of the OClO producing channel, $k_{7.1c}$, of the BrO + ClO reaction were determined by means of laser flash photolysis at six temperatures over the range T = 246-314 K. Three species in the reaction mixture (ClO, BrO, OClO) were monitored simultaneously by means of their UV absorption spectra, and the use of differential fitting techniques allowed unequivocal quantification of these absorbing species in spite of the presence of additional absorbers over the same spectral range. The possibility of characterising the kinetics of channel (7.1a) was also investigated in a separate series of exploratory experiments, by attempting to monitor the BrCl product using the vibronic bands of the BrCl spectrum. This attempt showed promising initial results, but a major drawback was the lack of high-resolution BrCl cross-sections available in the literature, necessary to quantify the observed signal.

Both $k_{7.1}$ and $k_{7.1c}$ exhibited negative temperature dependences, but the absolute values

of both rate constants were larger than previous studies at all temperatures. This discrepancy can only be partially explained in terms of systematic errors in the current work (notably, in the species absorption cross-sections). However, the principal reason for the discrepancy is thought to lie in secondary chemistry occurring in this and other work, arising in the complicated reacting mixture, especially from the presence of OClO in the precursor mixture, observed here and in some previous studies.

7.6 References

1. M.B. McElroy, R.J. Salawitch, S.C. Wofsy, J.A. Logan, *Nature*, **1986**, 321, 759
2. WMO (World Meteorological Organization), *Scientific Assessment of Ozone Depletion: 2010, Global Ozone Research and Monitoring Project*, Report No. 52, **2011**, Geneva, Switzerland
3. K. Frieler, M. Rex, R.J. Salawitch, T. Canty, M. Streibel, R.M. Stimpfle, K. Pfeilsticker, M. Dorf, D.K. Weisenstein, S. Godin-Beekmann, *Geophys. Res. Lett.*, **2006**, 33, L10812
4. R.P. Wayne, G. Poulet, P. Biggs, J.P. Burrows, R.A. Cox, P.J. Crutzen, G.D. Hayman, M.E. Jenkin, G. Le Bras, G.K. Moortgat, U. Platt, R.N. Schindler, *Atmos. Environ.*, **1995**, 29, 2677
5. T. Canty, E.D. Rivière, R.J. Salawitch, G. Berthet, J.-B. Renard, K. Pfeilsticker, M. Dorf, A. Butz, H. Bösch, R.M. Stimpfle, D.M. Wilmouth, E.C. Richard, D.W. Fahey, P.J. Popp, M.R. Schoeberl, L.R. Lait, T.P. Bui, *J. Geophys. Chem.*, **2005**, 110, D01301
6. S.P. Sander, J. Abbatt, J.R. Barker, J.B. Burkholder, R.R. Friedl, D.M. Golden, R.E. Huie, C.E. Kolb, M.J. Kurylo, G.K. Moortgat, V.L. Orkin, P.H. Wine, *Chemical Kinetics and Photochemical Data for Use in Atmospheric Studies*, Evaluation No. 17, **2011**, JPL Publication 10-6, Jet Propulsion Laboratory, Pasadena, United States
7. S.R. Kawa, R.S. Stolarski, P.A. Newman, A.R. Douglass, M. Rex, D.J. Hofmann, M.L. Santee, K. Frieler, *Atmos. Chem. Phys.*, **2009**, 9, 8651
8. N. Basco, S.K. Dogra, *Proc. Roy. Soc. Lond. A.*, **1971**, 323, 417
9. M.A.A. Clyne, R.T. Watson, *J. Chem. Soc., Faraday Trans. I*, **1977**, 73, 1169
10. D.W. Toohey, J.G. Anderson, *J. Phys. Chem.*, **1988**, 92, 1705

11. A.J. Hills, R.J. Cicerone, J.G. Calvert, J.W. Birks, *J. Phys. Chem.*, **1988**, 92, 1853
12. R.R. Friedl, S.P. Sander, *J. Phys. Chem.*, **1989**, 93, 4756
13. S.P. Sander, R.R. Friedl, *J. Phys. Chem.*, **1989**, 93, 4764
14. G. Poulet, I.T. Lançar, G. Lavardet, G. Le Bras, *J. Phys. Chem.*, **1990**, 94, 278
15. A.A. Turnipseed, J.W. Birks, *J. Phys. Chem.*, **1991**, 95, 4356
16. R. Atkinson, D.L. Baulch, R.A. Cox, J.N. Crowley, R.F. Hampson, R.G. Hynes, M.E. Jenkin, M.J. Rossi, J. Troe, Evaluated kinetic and photochemical data for atmospheric chemistry: Volume III – gas phase reactions of inorganic halogens, *Atmos. Chem. Phys.*, **2007**, 7, 981
17. Y. Bedjanian, G. Laverdet, G. Le Bras, *J. Phys. Chem. A*, **1998** 102, 953
18. C.N. Hinshelwood, C.R. Prichard, *J. Chem. Soc.*, **1923**, 123, 2730
19. J. Brion, A. Chakir, D. Daumont, J. Malicet, C. Parisse, *Chem. Phys. Lett.*, **1993**, 213, 610
20. M.H. Harwood, D.M. Rowley, R.A. Cox, R.L. Jones, *J. Phys. Chem. A*, **1998**, 102, 1790
21. V. Ferracci, D.M. Rowley, *Phys. Chem. Chem. Phys.*, **2010**, 12, 11596
22. V. Ferracci, D.M. Rowley, *Int. J. Chem. Kinet.*, **2012**, 44, 386
23. D.M. Wilmouth, T.F. Hanisco, N.M. Donahue, J.G. Anderson, *J. Phys. Chem. A*, **1999**, 103, 8935
24. A. Wahner, G.S. Tyndall, A.R. Ravishankara, *J. Phys. Chem.*, **1987**, 91, 2134
25. M.K. Gilles, A.A. Turnipseed, J.B. Burkholder, A.R. Ravishankara, S. Solomon, *J. Phys. Chem. A*, **1997**, 101, 5526
26. A.R. Curtis, W.P. Sweetenhan, FACSIMILE, **1987**, AERE Harwell Publication, Oxford
27. V. Ferracci, K. Hino, D. M. Rowley, *Phys. Chem. Chem. Phys.*, **2011**, 13, 7997
28. D.A. Dolson, S.R. Leone, *J. Phys. Chem.*, **1987**, 91, 3543
29. D.L. Baulch, J. Duxbury, S.J. Grant, D.C. Montague, *J. Phys. Chem. Ref. Data*, **1981**, 10, 1
30. M.A.A. Clyne, H.W. Cruse, *J. Chem. Soc. Faraday Trans. 2*, **1972**, 68, 1377
31. N. Basco, S.K. Dogra, *Proc. Roy. Soc. Lond. A.*, **1971**, 323, 29

32. M.A.A. Clyne, P.B. Monkhouse, L.W. Townsend, *Int. J. Chem. Kinet.*, **1976**, 8, 425

33. P.H. Wine, J.M. Nicovich, A.R. Ravishankara, *J. Phys. Chem.*, **1985**, 89, 3914

34. D. Maric, J.P. Burrows, R. Meller, G.K. Moortgat, *J. Photochem. Photobiol. A: Chem.*, **1993**, 70, 205

35. D. Maric, J.P. Burrows, G.K. Moortgat, *J. Photochem. Photobiol. A: Chem.*, **1994**, 83, 179

36. D. Maric, J.P. Burrows, *J. Phys. Chem*., **1996**, 100, 8645

37. D. Maric, J.N. Crowley, J.P. Burrows, *J. Phys. Chem. A*, **1997**, 101, 2561

38. I.A.K. Young, C. Murray, C.M. Blaum, R.A. Cox, R.L. Jones, F.D. Pope, *Phys. Chem. Chem. Phys.*, **2011**, 13, 15318

39. W. Schneider, G. von Helden, unpublished work, **1989**, later reported in E.-P. Röth, R. Ruhnke, G. Moortgat, R. Meller, W. Schneider, *Berichte des Forschungszentums Jülich*, **1997**, jül-3340

Chapter 8
Concluding Remarks

The experiments reported in this thesis have elucidated the kinetics and thermochemistry of a number of halogen monoxide radical reactions by means of laser photolysis coupled with UV absorption spectroscopy with CCD detection, obtaining channel-specific kinetic information on the known product channels whenever possible.

The results reported here demonstrate the immense power of time-resolved broadband UV absorption spectroscopy in the investigation of the reactions of halogen monoxide radicals, XO (X = Cl, Br). The use of CCD detection, allowing the acquisition of sequential spectra of a photolysed gas mixture, is in many ways an electronic analogue, with improvements, of the photographic plate detection method originally used by Porter and Wright in the first flash photolysis experiments carried out in the 1950s. [1] The simultaneous temporal *and* spectral resolution afforded by the CCD confers many clear advantages over single-wavelength techniques. The most obvious of these is the unequivocal identification of species in the gas mixture, allowing the potential additional observation of unexpected absorbing species. Furthermore, since all halogen monoxide radicals exhibit strong vibronic bands in their absorption spectra, broadband species monitoring allows to extract a "fingerprint" of that structured absorption by means of differential spectroscopy. This signal provides an indication of the time-dependent concentration of the absorber exhibiting spectral structure alone, irrespective of any changes in the underlying absorbance, many of which may, in this and in other work, have resulted from unidentified absorbing species. The recording of sequential broadband spectra also allows, crucially, simultaneous monitoring of multiple absorbing species.

Careful optimisation of the reaction conditions employed maximised the sensitivity of the system towards the target reaction. This was clearly shown, for each reaction system used, by fitting not only numerical integration simulations, generated by compiling all the possible reactions occurring in the gaseous mixture in a model, but also simpler classical rate equation solutions to the experimentally observed concentration temporal profiles. Nevertheless, extensive sensitivity analysis routines

were performed to ascertain and quantify the principal sources of uncertainty in the kinetic and thermochemical parameters obtained in each reaction system.

All of the reactions investigated in this thesis are involved in atmospheric ozone depletion: therefore the results reported in Chapters 4-7 will have atmospheric implications, which can only be quantified accurately *via* modelling studies. A very recent study by Sumińska-Ebersoldt *et al*. [2] observed, for example, that the nighttime abundances of ClO in the Arctic stratosphere would not be consistent with a ClO/Cl_2O_2 thermal equilibrium constant significantly higher than the one proposed by Plenge *et al*. [3] The values of the equilibrium constant for ClO dimerisation reported in the current thesis do, however, exceed those reported by Plenge *et al.*; moreover, the present work has highlighted a consensus amongst "optical" methods for the study of this equilibration [4] (following careful re-analysis of the dataset from Cox and Hayman [5]), as opposed to the results of mass-spectrometric measurements (Plenge *et al*.). The reason for this discrepancy might lie in the very nature of the ClO dimer, interpretation of which would affect the results of the Third Law analysis for ClO dimerisation. This hypothesis, although speculative, seems plausible as recent *ab initio* studies from Barker *et al*. [6] suggest the existence of an alternative structure of the ClO dimer. Barker *et al*. observed a minimum in the PES for ClO dimerisation corresponding to the formation of a cyclic ClO dimer. If ClO dimerisation did proceed by one or two (or indeed more) pathways, with likely different thermochemistry, the interpretation of the results of laboratory studies would be profoundly affected as well as those of field measurements, crucially dependent upon the atmospheric fate of a non-peroxide ClO dimer.

Indeed, the rationale behind some of the research presented in this thesis was the necessity for better characterisation of kinetic and/or thermochemical reaction parameters often highlighted by significant discrepancies reported between field measurements and models based on the results of previous laboratory studies. These disagreements often strike a nerve in the study of atmospheric chemistry, more fundamentally whether kinetic and thermochemical information inferred/deduced from field observations is more reliable than that obtained in the laboratory. On the one hand, field observations are evidently made under "real" atmospheric conditions (temperature, pressure, species concentrations), but these do not allow the same degree

of control over the reaction system of interest than that afforded by laboratory studies. On the other hand, laboratory studies allow a great deal of control over the reaction system used but, on account of the limited sensitivity of detection or the difficulty in generation of reactive species, the resulting kinetic parameters often require long extrapolations to be utilised in atmospheric models. ClO dimerisation is an apt example. As shown in the work reported in Chapter 4, sensitivity to the thermal decomposition of the ClO dimer is lost below $T = 250$ K, thus precluding the possibility of measuring K_{eq} at temperatures typical of the Antarctic polar vortex ($T < 200$ K). Effectively, under the experimental conditions used, ClO equilibration reverts to pure second order at $T < 250$ K. This is ultimately a consequence of the ClO concentrations used in laboratory studies, which are 3-4 orders of magnitude greater than those observed during ozone depleting events. Improvements in the instrumental sensitivity, for example by means of Chemical Ionisation Mass Spectrometry (CIMS), a method already used in field measurements, [7] may therefore, eventually, allow to operate under more realistic species concentrations, thus allowing measurement of K_{eq} at lower temperatures.

The work reported in this thesis on the "bimolecular" channels of the ClO self-reaction was the first to simultaneously monitor reactant ClO and the product OClO. The reaction conditions used only allowed the determination of the kinetics of two of the three reaction channels. Despite the use of broadband monitoring, the presence of three absorbers devoid of spectral structure unfortunately precluded any further investigation of the channel producing ClOO. By contrast, in the reaction system used to study the BrO self-reaction, it was possible to monitor the BrO vibronic signal using differential spectroscopy and also the spectrally smooth absorption of ozone, after subtraction of the contribution of BrO to the total observed absorbance. This was possible as the ozone signal was the only known absorption underlying the BrO signal, in contrast to the multiple smooth absorbers observed in the work on the ClO self-reaction. The capacity to monitor BrO and O_3 simultaneously allowed determination of the kinetics and product branching of the BrO self-reaction. The results obtained in this work on the kinetics and branching of the BrO self-reaction are in good agreement with the previous studies at $T = 298$ K. However, this work measured a very weak temperature dependence for the branching ratio of the channel producing atomic bromine, implying

a greater partitioning towards atomic bromine at low temperatures than that reported in previous studies and in the current JPL-NASA evaluation. [8] Recommended kinetics and branching of the BrO self-reaction were last updated by JPL-NASA in 1997: furthermore, the recommended expression for the temperature dependence of the partitioning between the two known product channels is apparently based on only two studies, one of which reports values of the branching ratio for the channel producing atomic bromine only at $T = 298$ K and $T = 220$ K. As a termolecular component of the BrO self-reaction, analogous to ClO dimerisation, has also been observed at temperatures $T < 250$ K, the inclusion of a data point at $T = 220$ K in this recommendation appears somewhat impractical.

Characterisation of the termolecular component of the BrO self-reaction is therefore desirable in order to ascertain the stability and spectroscopy of the BrO dimer. However, a study of the termolecular association of two BrO radicals becomes more complicated than its chorine analogue as, in the BrO self-reaction, both termolecular *and* bimolecular components exhibit a negative temperature dependence. Therefore it would not be possible to entirely decouple the pressure-dependent association channel from the bimolecular products in the same way as in the studies carried out on the ClO self-reaction.

Comparison of the present study of the BrO self-reaction with previous work also highlights some of the advantages of CCD detection over single-wavelength techniques. As discussed extensively in Chapter 6, Sander and Watson [9] aimed to monitor BrO at the (7, 0) vibronic peak but monitored the signal at $\lambda = 339$ nm instead of the reported peak wavelength of $\lambda = 338.5$ nm, which may have affected their results on the kinetics of the BrO self-reaction profoundly. Such incorrect wavelength calibration can be extremely problematic in single-wavelength studies, but it represents only a minor inconvenience with CCD detection, on account of the presence and exploitation of the vibronic features of, in this case, BrO. The power of the broadband monitoring technique was particularly evident in the study of the BrO + ClO cross-reaction reported in Chapter 7. Here, the ability to monitor ClO, BrO *and* the OClO product simultaneously and accurately using differential spectroscopy was unique to this work and proved a highly constrained determination of the kinetics and branching of the BrO

+ ClO cross-reaction. Moreover, optimisation of the radical source chemistry allowed effective operation under pseudo-first order conditions of BrO decay in excess ClO, greatly simplifying the kinetic analysis. This work measured a greater overall rate constant for the BrO + ClO cross-reaction than previous studies, along with a decreasing contribution of the OClO producing channel to this reaction at lower temperatures. The atmospheric implications of these results are complex given the multiple product channels of this reaction. However, simplistically, these results suggest that the role of the BrO + ClO cross-reaction is currently underestimated in atmospheric models.

Broadband absorbance spectra of the precursor mixture in the BrO + ClO system revealed the presence of an OClO impurity in the reaction cell even in the absence of photolysis. This species, the origin of which was attributed to a yet unknown process, led to complicating secondary chemistry at lower temperatures, compromising the quality of the OClO signal monitored. Future studies might attempt at minimising this (termolecular) secondary chemistry by operating, for example, under reduced pressure.

As proved in the current work, the advantages of flash photolysis/UV absorption spectroscopy with CCD detection are most evident when monitoring transient species whose absorbance spectra show structural features. Hence future investigation into other gas phase reactions involving halogen monoxide radicals with other radical families (*e.g.* ClO + CH_3O_2) and those of other structured absorbers, such as NO_2 (*e.g.*, BrO + NO_2) would be expected to extend and improve the current kinetic database.

In conclusion, the results presented in this thesis provide significant new data on halogen monoxide free radical reactions of importance in the atmosphere, as well as evidence for a number of unresolved issues which point the way to future studies. The results also illustrate the clear advantages of time-resolved broadband UV spectroscopy in the investigation of the kinetics of these reactions, as provided by the unique CCD detection system. This perhaps leads the way for future developments led by availability in opto-electronic technology. The next step could be, for example, the exploitation of further technical advances, *e.g.* in IR spectroscopy, to allow the

simultaneous monitoring of other species and the eventual understanding of this complex, fascinating and atmospherically important gas phase radical chemistry.

References

1. R.G.W. Norrish, G. Porter, *Nature*, **1949**, 164, 658
2. O. Sumińska-Ebersoldt, R. Lehmann, T. Wegner, J.-U. Grooß, E. Hösen, R. Weigel, W. Frey, S. Griessbach, V. Mitev, C. Emde, C.M. Volk, S. Borrmann, M. Rex, F. Stroh, M. von Hobe, *Atmos. Chem. Phys.*, **2012**, 12, 1353
3. J. Plenge, S. Kuhl, B. Vogel, R. Muller, F. Stroh, R. Flesch, E. Ruhl, *J. Phys. Chem. A*, **2005**, 109, 6730
4. V. Ferracci, D.M. Rowley, *Phys. Chem. Chem. Phys.*, **2010**, 12, 11596
5. R.A. Cox, G.D. Hayman, *Nature*, **1988**, 332, 796
6. J. R. Barker, private communication
7. J.A. Neuman, R.S. Gao, M.E. Schein, S.J. Ciciora, J.C. Holecek, T.L. Thompson, R.H. Winkler, R.J. McLaughlin, M.J. Northway, E.C. Richard, D.W. Fahey, *Rev. Sci. Inst.*, **2000**, 71, 3886
8. S.P. Sander, J. Abbatt, J.R. Barker, J.B. Burkholder, R.R. Friedl, D.M. Golden, R.E. Huie, C.E. Kolb, M.J. Kurylo, G.K. Moortgat, V.L. Orkin, P.H. Wine, *Chemical Kinetics and Photochemical Data for Use in Atmospheric Studies*, Evaluation No. 17, **2011**, JPL Publication 10-6, Jet Propulsion Laboratory, Pasadena, United States
9. S.P. Sander, R.T. Watson, *J. Phys. Chem.*, **1981**, 85, 4000

Appendix 1
Calibration Procedures

A1.1 Mass Flow Controllers

Mass flow controllers (MFCs) were routinely calibrated between experiments by measuring the time taken for a set flow of gas to sweep out a known volume, determined using of a modified burette. MFCs were connected to a burette *via* a tube fitted with a T-piece. Soapy water was injected into the flow of gas from the MFC *via* the T-piece, and the time taken for a meniscus to pass through a known volume in the burette was recorded. The procedure was repeated at different mass flow settings on each MFC, in random order, and, following corrections for standard conditions of temperature and pressure, calibration plots, such as that shown in Figure A1.1, were used to determine the actual flow of gas by linear regression.

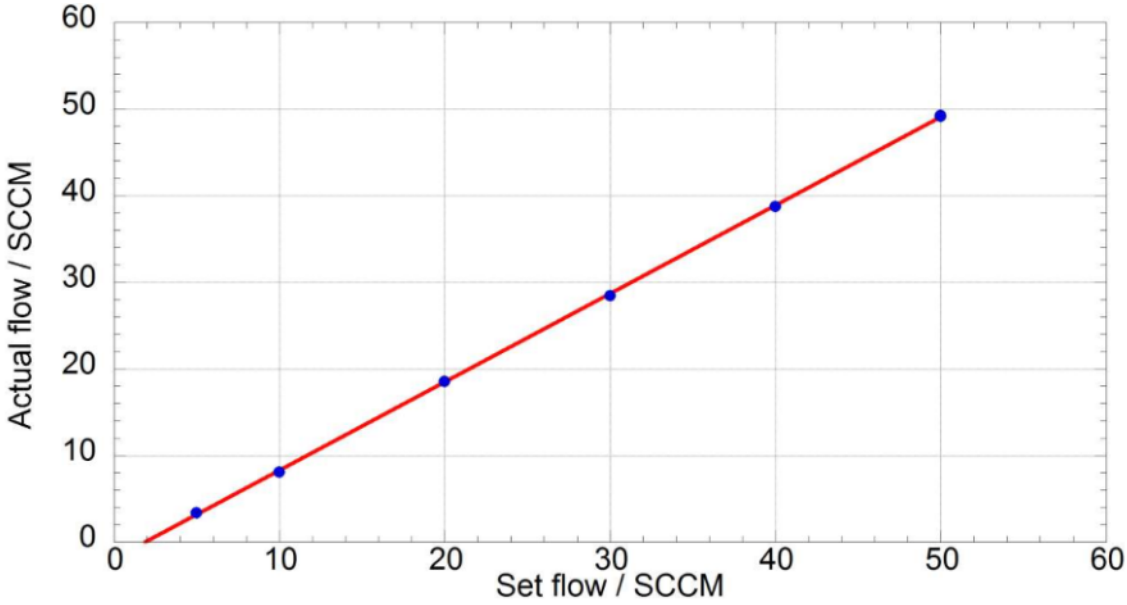

Figure A1.1 : Typical calibration plot for mass flow controllers, showing in this case an offset of approximately +1.9 on the displayed (set) flow.

A1.2 Rotameter

The rotameter, used to measure flows of corrosive gases such as Cl_2 (diluted in N_2), was calibrated by passing known flows of pure N_2, from a calibrated MFC, through the

rotameter and noting the ball height. A calibration plot, such as that shown in Figure A1.2, was produced, and a polynomial equation was least-squares fitted to the data to allow determination of the actual flow rate of the gas from the ball height of the rotameter. The procedure was repeated at several flow rates in random order.

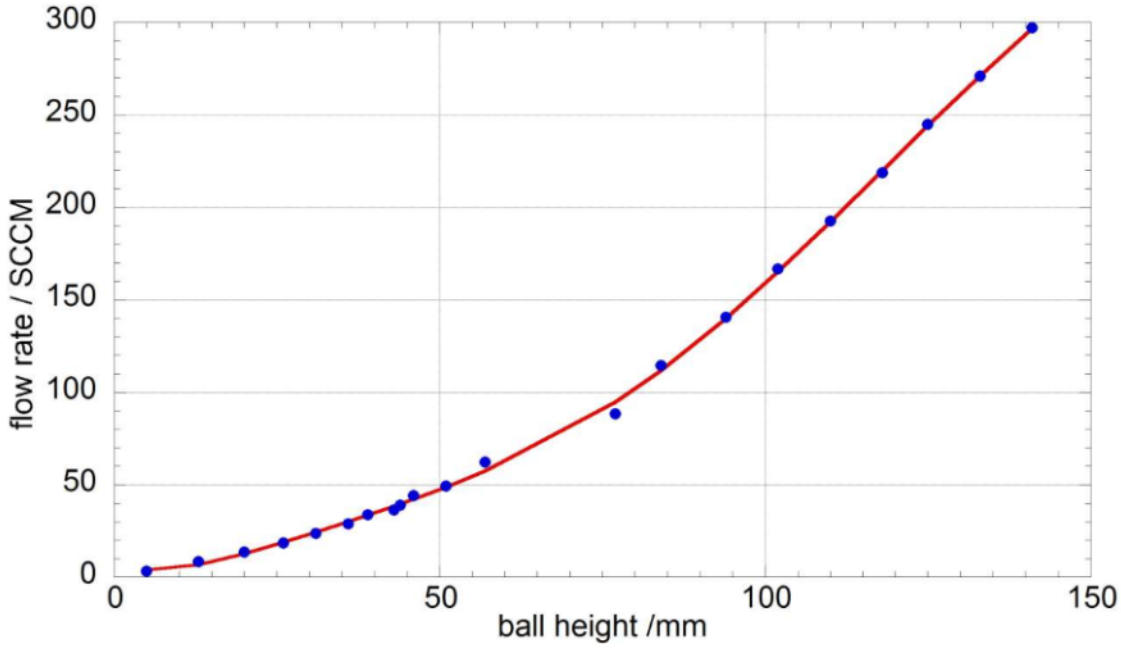

Figure A1.2 : Calibration plot for the rotameter used to monitor flow rates of corrosive gases.

A1.3 Wavelength

Precise wavelength calibration of recorded spectra was crucial to ensure that the correct absorption cross-sections were fitted to the experimentally observed absorbances. Wavelength calibration was conducted for each set of experiments, under identical spectral settings to the kinetics experiments. Calibration was achieved by recording an emission spectrum of a low-pressure mercury "pen-ray" lamp. As shown in Figure A1.3, the Hg spectrum has well-defined sharp features: by recording the CCD pixel number at which the mercury peaks occur and knowing the exact wavelength at which these peaks occur (well defined in the literature [1]) a calibration plot was produced, as illustrated in Figure A1.4. The resulting linear regression is in the form:

$$\lambda = \text{dispersion} \times (\text{pixel number}) + \lambda_0 \qquad \text{(A1.i)}$$

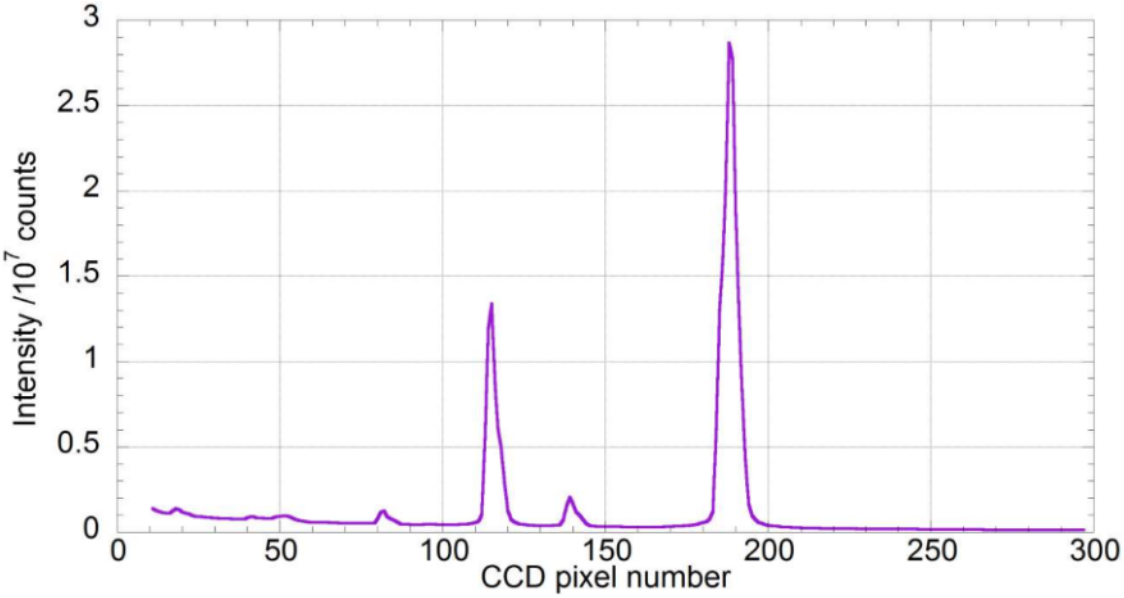

Figure A1.3 : Typical light intensity spectrum emitted by a mercury "pen-ray" lamp (approximately corresponding to the spectral range λ = 270-337 nm).

and allows determination of the dispersion of the diffraction grating used, along with the initial wavelength recorded, λ_0. Typical values of the dispersion were 0.1122 nm pixel^{-1} for the 600 grooves mm^{-1} diffraction grating, 0.2226 nm pixel^{-1} for the 300 grooves mm^{-1} diffraction grating and 0.4446 nm pixel^{-1} for the 150 grooves mm^{-1} diffraction grating.

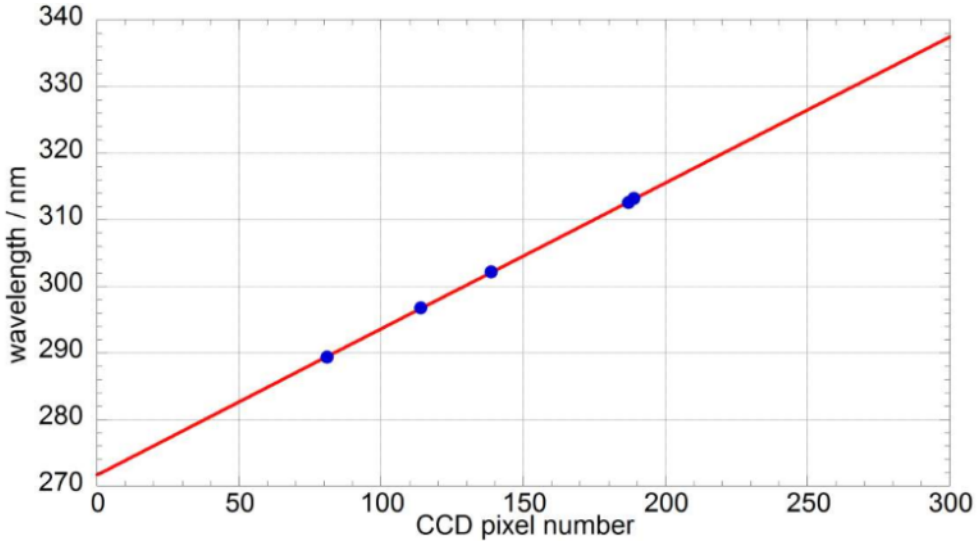

Figure A1.4 : Plot of known mercury peak wavelength *versus* CCD pixel number (blue points) for the 300 grooves mm^{-1} diffraction grating. The linear parameterisation of this plot (red line) is used to wavelength calibrate experimentally recorded spectra.

Evidently, a wavelength calibration requires at least two points; however, in some cases, only one mercury peak could be observed over the wavelength range monitored. In these cases, the dispersion measured from other experiments with the same diffraction grating was employed and the value of λ_0 obtained from equation (A1.i) using the single peak available.

Many of the absorbers monitored in this work, such as ClO, BrO and OClO, exhibit vibronic bands in their spectra. The wavelengths at which these structured spectral features occur are also well-characterised in the literature, [2] and therefore provided a second way by which to wavelength calibrate spectra. A typical calibration plot including the peak positions of the mercury emission spectrum as well as those of the vibronic bands of the BrO absorption spectrum is shown in Figure A1.5.

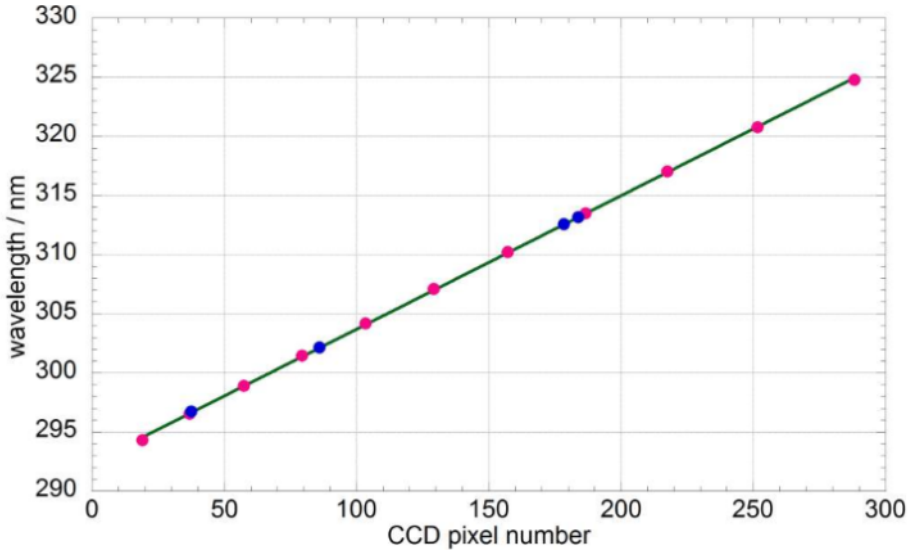

Figure A1.5 : Calibration plot for the 600 grooves mm^{-1} diffraction grating using the positions on the CCD wavelength axis of peaks from the emission spectrum of mercury (in blue) and those of the vibronic bands of the BrO absorption spectrum (in pink).

A1.4 HgO trap

The presence of Cl_2O in the precursor mixture was necessary in most of the experiments reported in this thesis as this species acts as a precursor of the ClO radical. Cl_2O was typically produced *in situ* by flowing diluted Cl_2 gas through a trap containing solid

dried yellow mercuric (II) oxide (HgO, Sigma-Aldrich, > 99%), resulting in the reaction: [3]

$$2Cl_2(g) + HgO(s) \rightarrow Cl_2O(g) + HgCl_2(s) \qquad (A1.1)$$

When fresh HgO was employed, the Cl_2/Cl_2O conversion efficiency was very high (> 90%), leaving very little Cl_2 available for direct photolysis. To obtain more control over the conversion of molecular chlorine into Cl_2O, a T-junction was placed upstream of the trap containing HgO so that part of the Cl_2 flow was sent through a side arm leading directly into the mixing line. The side arm was equipped with a needle valve, so that the amount of chlorine *not* going through the HgO trap, and therefore *not* being converted into Cl_2O, was regulated by opening or closing the needle valve. The conversion efficiency of this set-up was calibrated for different degrees of opening of the needle valve by recording static (*i.e.* in the absence of photolysis) spectra of the gaseous mixture in a N_2 carrier flow of typically 900 SCCM over the range λ = 235-300 nm and fitting reference Cl_2O and Cl_2 cross-sections [2] to the recorded absorbance *via* a least-squares method. A typical recorded absorbance with optimised Cl_2O and Cl_2 contributions is shown in Chapter 5, Figure 5.10. The calibration resulting from an input flow of 30 SCCM of Cl_2 (5% diluted in N_2) is given in Figure A1.6. The degree

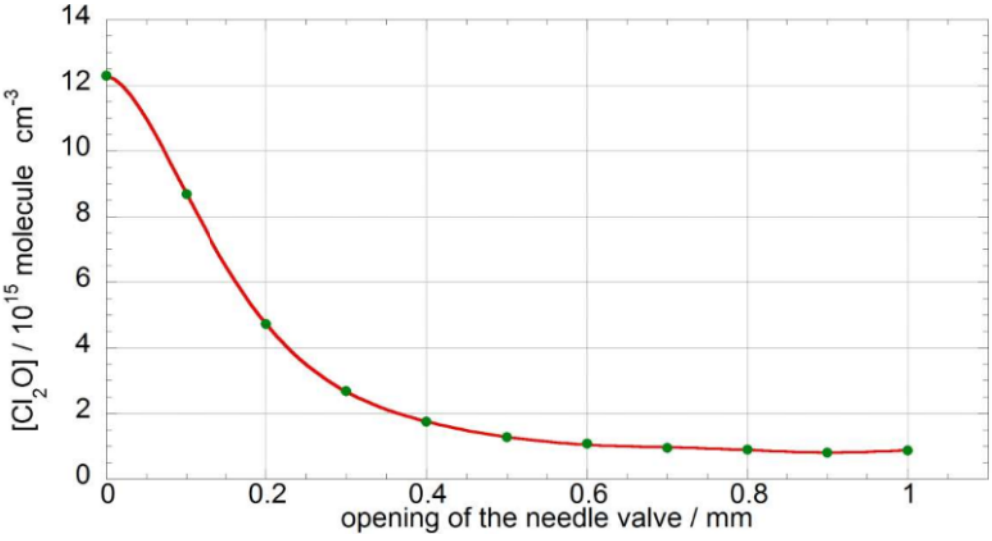

Figure A1.6 : Calibration of the $[Cl_2O]$ output from a trap containing mercuric oxide (II) for an incoming flow of 30 SCCM of Cl_2 (5% diluted in N_2) at different degrees of opening of the needle valve.

of opening of the needle valve was measured using the scale on the valve itself, with the value of 0 mm corresponding to the valve fully shut (*i.e.*, all Cl_2 sent through the HgO trap).

A1.5 Ozonisers

Ozone was generated using one of two methods, depending on the concentration required. Ozone was produced by passing a known oxygen flow either through a commercial ozoniser (Ozonia Triogen 213) when high concentrations (> 10^{16} molecule cm^{-3}) were needed, or through a cell incorporating a mercury "pen-ray" lamp when lower concentrations (< 5×10^{15} molecule cm^{-3}) were required. In both cases, the ozone output in a N_2 carrier flow of typically 900 SCCM was calibrated against different input O_2 flows by recording static (*i.e.* in the absence of photolysis) spectra of the gaseous mixture over the range λ = 230-295 nm and fitting reference O_3 cross-sections [2] to the recorded absorbance *via* a least-squares method. The calibration plot for the commercial ozoniser is shown in figure A1.7 and that for the mercury lamp cell is shown in Figure A1.8.

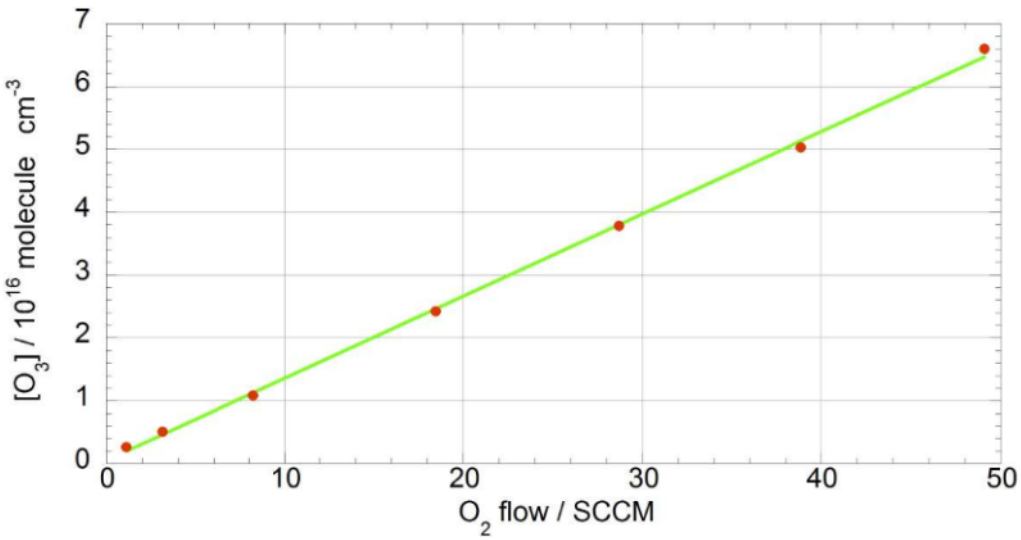

Figure A1.7 : Calibration plot for the O_3 output from an industrial ozoniser, measured in a nitrogen carrier flow of 900 SCCM for different input O_2 flows.

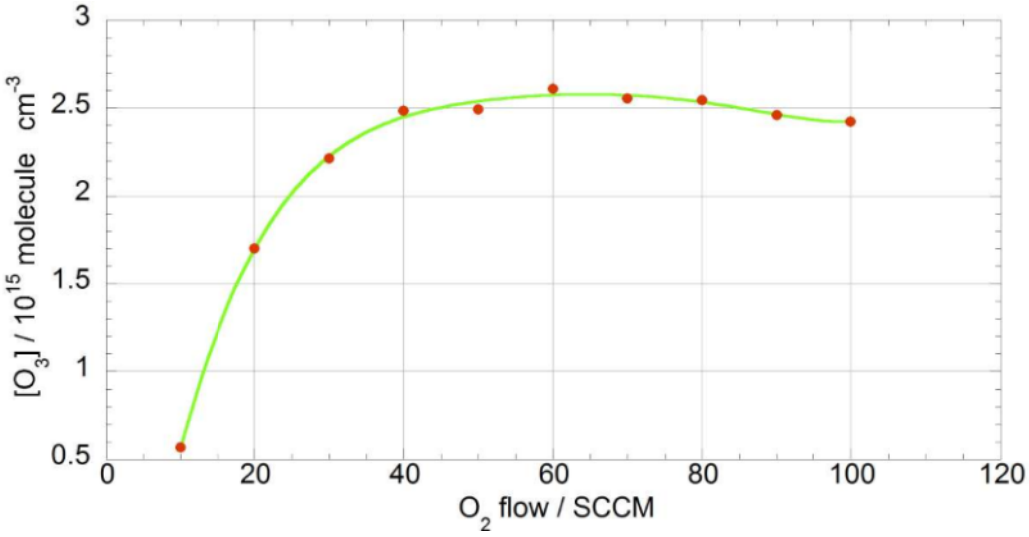

Figure A1.8 : Calibration plot for the O_3 output of a cell incorporating a "pen-ray" mercury lamp, measured in a nitrogen carrier flow of 900 SCCM for different input O_2 flows.

A1.6 References

1. J.E. Sansonetti, W.C. Martin, S.L. Young, *NIST Handbook of Basic Atomic Spectroscopic Data*, web version http://www.nist.gov/pml/data/handbook/index2.cfm
2. S.P. Sander, J. Abbatt, J.R. Barker, J.B. Burkholder, R.R. Friedl, D.M. Golden, R.E. Huie, C.E. Kolb, M.J. Kurylo, G.K. Moortgat, V.L. Orkin, P.H. Wine, *Chemical Kinetics and Photochemical Data for Use in Atmospheric Studies*, Evaluation No. 17, **2011**, JPL Publication 10-6, Jet Propulsion Laboratory, Pasadena, United States
3. C. N. Hinshelwood, C. R. Prichard, *J. Chem. Soc.*, **1923**, 123, 2730

Appendix 2
Concentration Gradient Studies

Because of the longitudinal path of the photolysis laser beam, the presence of an optically thick precursor mixture at the laser wavelength gives rise to a concentration gradient of photolysis products within the reaction cell. It can be easily envisaged how, if the concentration of photolabile precursor species is sufficiently high, the laser beam will be significantly absorbed in the initial part of the precursor mixture (where the laser enters) and therefore significantly attenuated when it reaches the opposite end. This could lead to spurious kinetics being observed, since high (fast reacting) concentrations of photogenerated species in one region of the reaction vessel would be averaged along the absorption pathlength with low concentrations in another.

Calculations were performed to investigate this effect. In all the reaction systems used in the experiments described in this thesis, the formation of free radicals was initiated by the photolysis of molecular halogens, X_2 (X = Cl, Br). It is therefore possible to simulate the attenuation of the laser beam through the cell for a precursor mixture containing a specific amount of species X_2, given that the cross-section of X_2 and the laser output as it first enters the reaction cell are known. The cell is then split in ten notional sections, each of 10 cm in length, and the laser light transmitted from one section to the subsequent one can be obtained by rearranging the Beer-Lambert law:

$$I_t = I_0 \left\{1 - \exp\left(-\sigma_{X_2}[X_2]l\right)\right\} \qquad \text{(A2.i)}$$

where I_t is the light intensity transmitted through each section, I_0 is the intensity of the incoming light, σ_{X_2} is the absorption cross-section of X_2, $[X_2]$ is the concentration of X_2 and l is the optical pathlength through each section of the cell (10 cm by definition). I_0 corresponds to the full laser output for the first section of the cell, and the values of I_t calculated for one particular section of the cell are used as the I_0 for the subsequent section. Calculation of the number of photons absorbed in each section per unit volume allows the determination of the initial concentration of photolysis products, $[X]_0$. For the purpose of these simulations, it was assumed that $[X]_0 = [XO]_0$, which is a solid

assumption considered that precursor concentrations were optimised so that all halogen atoms formed from photolysis of X_2 were converted rapidly into XO radicals. Once values of $[XO]_0$ were known for each section of the cell, ten second order [XO] decay traces were simulated using the initial value of [XO] and reference rate coefficients. The ten resulting simulated traces were then averaged to represent the line-of-sight view along the reaction cell and analysed to give a distortion (enhancement in the determined rate constant) from the known input kinetic parameters. The degree of distortion as a function of optical depth (absorbance) for a simulated system involving photolysis of Br_2 is shown in Figure A2.1 below.

The optical densities of the precursor mixtures employed in the experiments reported in this thesis were always below 0.5, leading to negligible (< 1%) predicted distortions in the extracted kinetics.

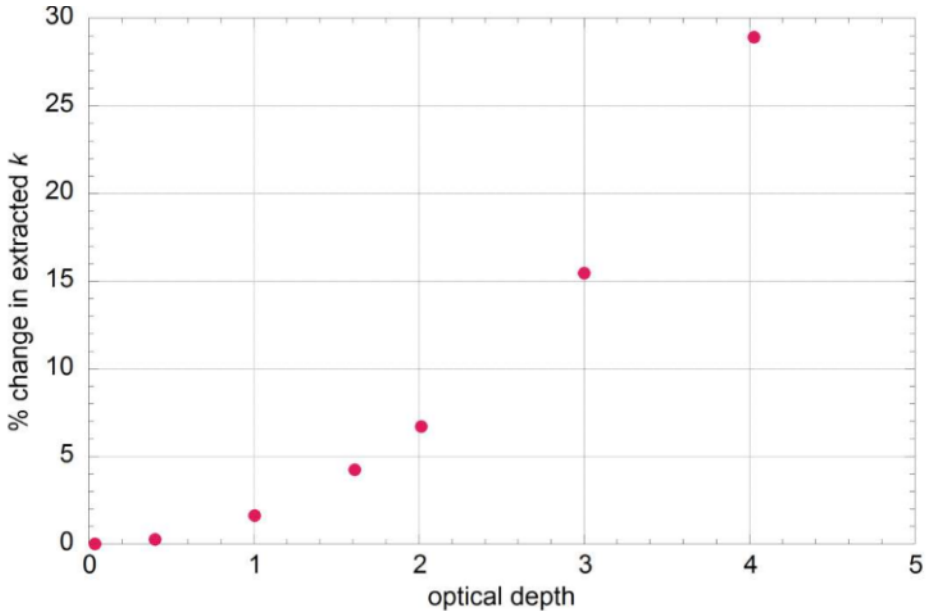

Figure A2.1 : Percentage change in k_{output} relative to k_{input} as a function of optical depth, showing the distortion to the kinetics resulting from an increase in optical depth.

Appendix 3
Effects of Instrumental Resolution on Absorbance Spectra

A3.1 Measuring the instrument function (resolution)

According to Heisenberg's uncertainty principle the observed radiation associated with any electronic (or vibronic) transition has a natural line width. If this radiation is observed using a dispersive detection system, as for the experiments reported in this thesis, the magnitude and shape of this line width will be additionally influenced by the instrument function of the detection system. Consequently, even monochromatic light passed through a diffraction spectrograph will be spread over a range of wavelengths governed by this instrument function. The width of this spread is in turn dependent upon the spectral resolution. For the spectrograph/CCD detection system employed in this work, the entrance slit width and dispersion of the spectrograph determines the spectral resolution.

Mercury lamp emission spectra were used to determine the resolution of the spectrograph over the range of slit widths 20-100 μm. Following dispersion, the monochromatic mercury peaks appeared as Gaussian curves as a function of wavelength at the detector and the resolution was determined as the *full-width half maximum* (FWHM) of a Gaussian function fitted to the recorded peak. These functions were defined as:

$$y = I_{\max}\exp\left\{-a\left(\lambda-\lambda_{\max}\right)^2\right\} \qquad \text{(A3.i)}$$

where $I_{\max}$ is the maximum intensity of the Gaussian, a is the width parameter and $\lambda_{\max}$ is the centre wavelength. The condition at half maximum is:

$$y = \frac{I_{\max}}{2} \qquad \text{(A3.ii)}$$

From this constraint an expression for the resolution can be found:

$$\text{resolution (FWHM)} = 2\left\{\lambda_{max}{}^2 - \left[\lambda_{max}{}^2 + \frac{1}{a}\ln\frac{1}{2}\right]\right\}^{0.5} \qquad \text{(A3iii)}$$

A plot of resolution against the entrance slit width is shown in Fig A3.1.

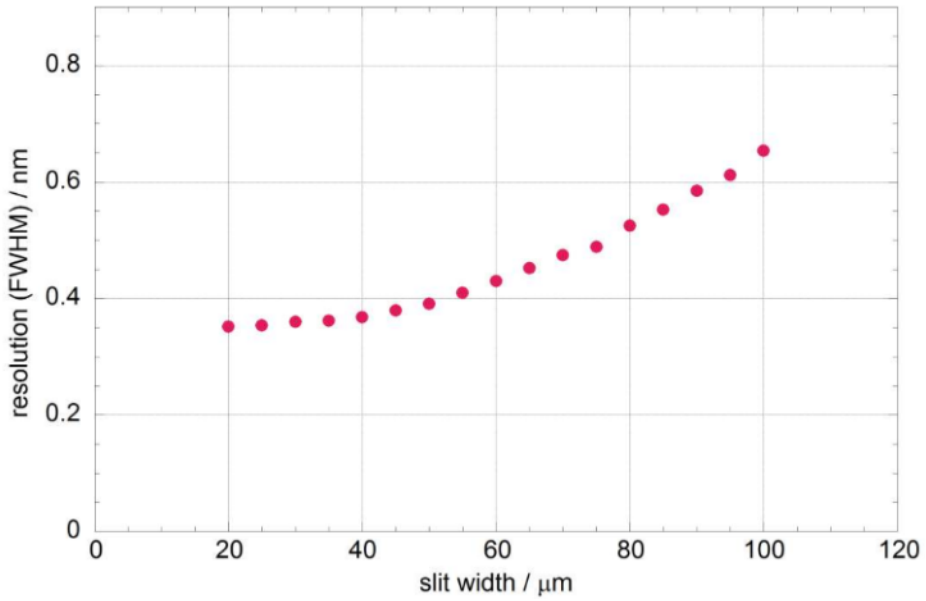

Figure A3.1 : Variation in resolution of the spectrograph as a function of slit width for the 600 grooves mm^{-1} diffraction grating.

A3.2 Spectral Convolution

If the spectral resolution of a detection system is decreased this will be accompanied by an increase in the apparent line width of any observed spectral features. This effect becomes most significant in spectra exhibiting vibronic structure, where a progression of individually resolved peaks is observed corresponding to transitions from the electronic ground state to discrete vibrational states in the first excited electronic state below the dissociation threshold. The magnitude of such structural features is readily affected by the instrument function, since the natural line widths are somewhat smaller than the magnitude of the spectral resolution. Consequently, the magnitude and shape of the experimentally determined absorption spectra are directly dependent upon the resolution of the apparatus used. In addition, the cross-sections determined from such

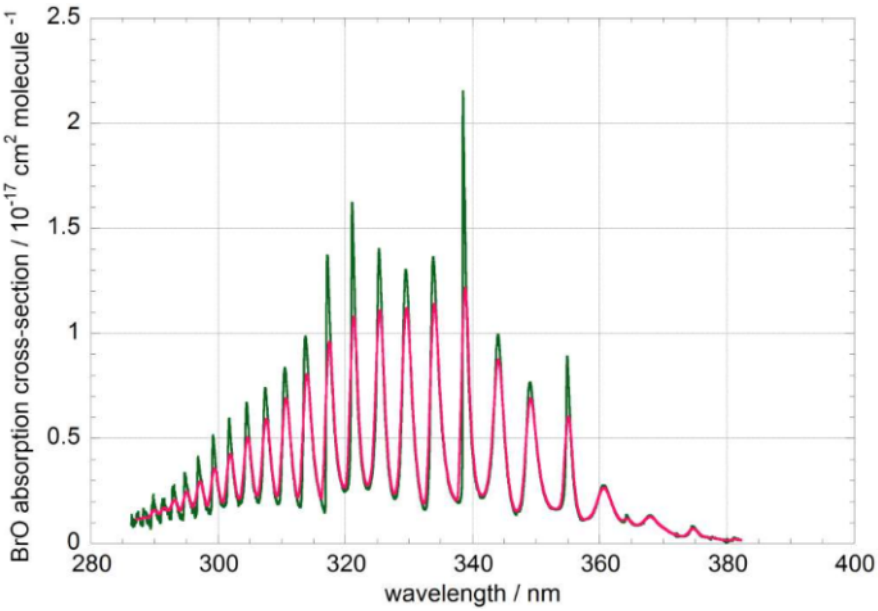

Figure A3.2 : BrO absorption cross-sections illustrating the effect of spectral resolution on structured absorption spectra. The green spectrum was recorded at 0.4 nm (FWHM) by Wilmouth *et al.* [1] and the pink spectrum was convolved from the reference spectrum from Wilmouth *et al*. to the experimental resolution of 1.1 nm (FWHM) used in the experiments on the BrO + ClO cross-reaction.

spectra, or used to quantify absorbing species contributing to such spectra must also be dependent upon the resolution of the detection system, as illustrated in Figure A3.2.

Since differential routines were used to determine radical concentrations by fitting the structural magnitude of the reference cross-sections to that of the recorded absorption spectra, it was vital that the respective resolutions were matched to ensure accurate determination of radical concentrations and subsequent kinetic parameters. Reference absorption cross-sections taken from the literature are typically recorded at higher resolutions than those achieved in this work. These literature cross-sections therefore required smoothing before their use to quantify absorbing species present in the experimental spectra.

Cross-sections were smoothed to appropriate lower resolutions using sliding average routines. As the instrument function of the apparatus employed in this study is well described by a Gaussian function, the smoothing kernel used in the averaging routine consisted of a Gaussian function, the width of which reflected the spectral resolution required.

A3.3 References

1. D.M. Wilmouth, T.F. Hanisco, N.M. Donahue, J.G. Anderson, *J. Phys. Chem. A*, **1999**, 103, 8935

Appendix 4
Gaussian Fitting to Literature Absorption Cross-Sections

Absorption cross-sections are often reported in the literature at intervals of 5 or 10 nm. In many instances encountered in this thesis, it was necessary to know the value of a cross-section at a wavelength within the given interval, or on a different wavelength grid. In the case of spectrally smooth, unstructured absorption cross-sections, it was possible to reproduce the literature cross-section using a linear combination of semilogarithmic Gaussian functions of the form:

$$y = \sigma_{max} \exp\left\{ -a \left[\ln\left(\frac{\lambda_{max}}{\lambda} \right) \right]^2 \right\} \qquad \text{(A4.i)}$$

where σ_{max} is the value of the Gaussian function at its peak, a is the width parameter and λ_{max} is the wavelength at which the maximum absorption occurs. The use of Gaussian functions is justified as follows: smooth, unstructured spectra arise from transitions from a ground electronic state to one or more dissociative (repulsive) excited states, as described in Section 2.5.1. Therefore the shape of these spectra mainly reproduces the shape of the wavefunction of the ground state, which is typically Gaussian.

An example of this procedure is given below for the absorption cross-section of Cl_2O. This is reported in the JPL-NASA evaluation [1] at intervals of 10 nm over the range λ = 200-640 nm. A linear combination of three Gaussian functions was fitted to the literature spectrum *via* a least squares routine, optimising the values of the σ_{max}, a and λ_{max} parameters of each Gaussian.

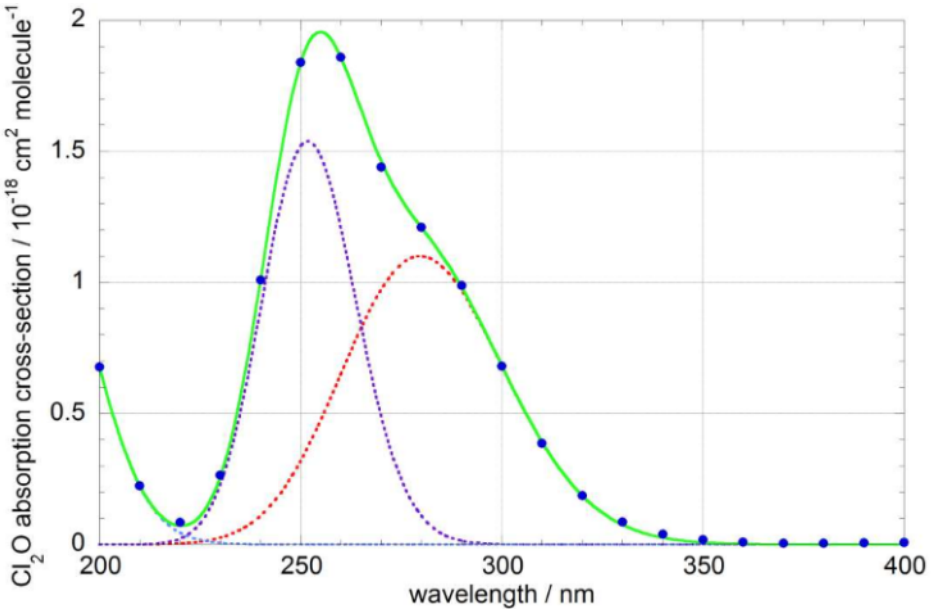

Figure A4.1 : Absorption cross-section of Cl_2O reported by JPL-NASA [1] (blue points) along with the three fitted Gaussians (dashed blue, violet and red lines) and the sum of the fitted Gaussians (solid green line).

A4.1 References

1. S.P. Sander, J. Abbatt, J.R. Barker, J.B. Burkholder, R.R. Friedl, D.M. Golden, R.E. Huie, C.E. Kolb, M.J. Kurylo, G.K. Moortgat, V.L. Orkin, P.H. Wine, *Chemical Kinetics and Photochemical Data for Use in Atmospheric Studies*, Evaluation No. 17, **2011**, JPL Publication 10-6, Jet Propulsion Laboratory, Pasadena, United States